INM
Leibniz Institute
for New Materials

UNIVERSITÄT
DES
SAARLANDES

Electrofluids Vol. 1:

Electrical and mechanical networks in carbonaceous particle suspensions and their potential as liquid electronic components

Dominik Sebastian Schmidt

Saarbrücken

2025

Electrofluid

Electrofluids Vol. 1:

Electrical and mechanical networks in carbonaceous particle suspensions and their potential as liquid electronic components

Dissertation
Zur Erlangung des akademischen Grades
des Doktors der Naturwissenschaften
der Naturwissenschaftlich-Technischen Fakultät
der Universität des Saarlandes

von
Dominik Sebastian Schmidt

Saarbrücken

2025

Tag des Kolloquiums: 31.03.2026

Dekan: Prof. Dr.-Ing. Dirk Bähre

Berichterstatter: Jun.-Prof. Dr. Lola González-García
Prof. Dr. Guido Kickelbick

Vorsitz: Prof. Dr.-Ing. Gianluca Rizzello

Akad. Mitglied: Dr. Juan Pablo Segovia Gutiérrez

Abstract

Stretchable and flexible conductors are essential for applications ranging from wearable strain sensors to soft robotic stable interconnects. Conventional materials often fail under large mechanical deformations, while alternatives such as liquid metals overcome breakage but present other limitations. This thesis introduces *Electrofluids*, a new class of materials composed of conductive filler particles dispersed in non-conductive liquid matrices. Their design leverages filler–matrix affinity to control particle agglomeration and network formation, enabling electrical conductivity at reduced filler loadings. Based on mismatching affinities, conductive emulsions demonstrate volume-exclusion effects that lower electrical percolation thresholds, strategies known for solid composites to liquid systems. Furthermore, the role of the filler is addressed by using different carbonaceous fillers (carbon black, carbon nanotubes, and graphene flakes). Key properties of the fillers, such as aspect ratio, oxygen content, and bending stiffness, are identified as critical for tuning the electromechanical behavior of electrofluids. Finally, it is demonstrated how, by rational selection of filler and matrix, electrofluids can be engineered as strain sensors and stable conductors, offering a versatile platform for next-generation soft electronics.

Zusammenfassung

Dehnbare und flexible Leiter sind essenziell für verschiedenste Anwendungen, die von tragbaren Dehnungssensoren bis zu stabilen Verbindungsstücken für weiche Robotik reichen. Konventionelle Materialien versagen bei großer mechanischer Verformung, während Alternativen wie Flüssigmetalle dieses Versagen vermeiden, jedoch andere Einschränkungen aufweisen. Diese Arbeit stellt Elektrofluide vor, eine neue Materialklasse, die aus leitfähigen Füllstoffpartikeln besteht, dispergiert in nicht-leitfähigen flüssigen Matrizen. Ihr Design nutzt die Affinität zwischen Füllstoff und Matrix zur Steuerung von Agglomeration und Netzwerkbildung, wodurch elektrische Leitfähigkeit bei geringerer Füllstoffmenge erreicht wird. Basierend auf unterschiedlichen Affinitäten zeigen leitfähige Emulsionen Volumenausschlusseffekte, die elektrische Perkolationsschwellen senken; Strategien, die von Kompositen auf Flüssigsysteme übertragen werden. Zudem wird die Rolle des Füllstoffs durch den Einsatz verschiedener kohlenstoffhaltiger Füller (Ruß, Kohlenstoffnanoröhren, Graphenflocken) untersucht. Wichtige Eigenschaften wie Aspektverhältnis, Sauerstoffgehalt und Biegesteifigkeit erweisen sich als entscheidend für die Abstimmung des elektromechanischen Verhaltens. Schließlich wird gezeigt, wie Elektrofluide durch gezielte Auswahl von Füllstoff und Matrix als Dehnungssensoren und stabile Leiter entwickelt werden können und daher eine vielseitige Plattform für die nächste Generation weicher Elektronik darstellen.

Publications & Contributions

Publications relevant to this thesis

Chapter 3 is based on a manuscript published in the journal ACS Applied Materials and Interfaces.

- **D.S. Schmidt**, T. Kraus, and L. González-García. "Electrofluids with tailored rheoelectrical properties: liquid composites with tunable network structures as stretchable conductors." ACS Applied Materials & Interfaces 16.33 (2024): 43942-43950.

Chapter 4 is based on a manuscript published in the Journal of Physics: Materials.

- **D.S. Schmidt**, D. Perius, and L. González-García. "Conductive emulsions with selective filler distribution as volume exclusion strategy in electrofluids." Journal of Physics: Materials 9.1 (2026): 015019.

Chapter 5 is based on a manuscript under review in the journal Advanced Materials Technologies.

- **D.S. Schmidt**, P. Fortugno, C.-F. López-Cámara, H. Wiggers, and L. González-García. “Morphology-Driven Electromechanical Performance of Graphene-Based Electrofluids for Emerging Soft Electronic Systems.” (Under review in Advanced Materials Technologies, 2026).

Other publications

- Zhang, L., **Schmidt, D. S**., González-García, L., & Kraus, T. (2022). Microscopic Softening Mechanisms of an Ionic Liquid Additive in an Electrically Conductive Carbon-Silicone Composite. *Advanced Materials Technologies*, *7*(11), 2101700.
- Lago-Garrido, S., **Schmidt, D. S**., Martín-Alfonso, M. J., & González-García, L. (2025). Multi-Walled Carbon Nanotubes Suspensions as Liquid Conductors: Electrical and Mechanical Network Interplay. *Advanced Electronic Materials*, 2400917.
- Haghipour, A., Arnold, S., Oehm, J., **Schmidt, D.**, Gonzalez-Garcia, L., *et al.*. (2025). Optimized Preparation and Potential Range for Spinel Lithium Titanate Anode for High-Rate Performance Lithium-Ion Batteries. *Advanced Energy and Sustainability Research*, *6*(1), 2400239.
- Fehlberg, M., **Schmidt, D. S**., Saikumar, S., Cavdan, M., Drewing, K., & Bennewitz, R. (2025). A Touch of Stribeck-Finger-Pad Friction in Viscous Liquid Spreading. *Tribology letters*, *73*(3), 91.
- C. Muñoz-Núñez, A. Barco-Martín, K. Deshpande, **D. S. Schmidt** and L. González-García, S. Trujillo, A. Muñoz-Bonilla, M. Fernández-García (2025). "Tuning the biological scaffolds’ performance by the combination of two antioxidant and antimicrobial chitosan derivatives." Carbohydrate Polymer Technologies and Applications: 101069.
- C. Muñoz-Núñez, A. Barco-Martín, K. Deshpande, **D. S. Schmidt** and L. González-García, S. Trujillo, A. Muñoz-Bonilla, M. Fernández-García (2025). Incorporation of imidazolium chitosan derivative yields scaffolds with enhanced antioxidant, antimicrobial, and immunomodulatory properties. (accepted manuscript in the Journal of Regenerative Biomaterials)

“Science is not about why, it’s about why not?”

-Senku Ishigami

Acknowledgements

Many people have supported me throughout the journey of my PhD, and I am deeply grateful for their contributions. This section of my thesis is dedicated to acknowledging those who have guided, encouraged, and inspired me along the way. Without their help—whether through academic advice, technical assistance, or emotional support—this work would not have been possible.

First and foremost, I would like to express my deepest gratitude to my supervisor, Lola González-García. Inviting me to continue from my master's thesis into a PhD while simultaneously building a new research group from the ground up was no small challenge. Thank you for your guidance, patience, and unwavering support throughout this journey, and for always having my back during difficult times. I could not have wished for a better mentor—someone who not only helped me grow as a scientist but also as a person every single day.

I would also like to extend my sincere thanks to Prof. Dr. Guido Kickelbick, who kindly agreed to serve as the second corrector of my thesis. I truly appreciate his willingness to read, evaluate, and provide his assessment of my work with no hesitation.

Dominik and David, my time in INM would not have been the same without you. The legendary D^3 events, the depression sessions, and our countless random discussions meant so much to me. Both of you contributed enormously—scientifically and personally—to the success of this thesis, and I am truly grateful for that.

A big thank you goes to my research group, Electrofluids—a small family that I am truly grateful to have been part of. Beyond countless after-work activities, your honest and constructive feedback, on everything I did, had a real impact and helped improve this work. Sergio, thank you for always being available in times of need and for showing me the "contaminated" area of Huelva. Niclas, thanks for being a fellow German in the group and for introducing me to the world of coffee. Srishti, thank you for organizing those (un)forgettable house parties and for teaching me tricks about rheology I didn't know. Gun Woo, I appreciate your patience and generosity in sharing your knowledge. Antonio, thanks for giving me 10% of your sauce business! Simon, thank you for your daily support in the lab, and Josef, for always being positive and working for the team.

Special thanks also to Quan, Xue, and Philip, who spent many hours preparing samples as HiWis, and to all the students I had the pleasure of supervising during this time: David, Quan, Hendrik, Sergio, and Niclas. You were great students, always challenging me and helping me grow as a scientist. Finally, thanks to everyone who has been part of the Electrofluids family at any point; you all made this journey unforgettable.

I would be remiss not to mention another group that had a significant impact on this journey: my sincere thanks to Tobias Kraus and the whole Structure Formation group

for welcoming me first as a master's student and now as a postdoc. I am grateful to all past and present members for helping me overcome experimental challenges and for making daily life more enjoyable, especially in the coffee kitchen. However, there are some names I must highlight: Indra, thank you for being my first supervisor in the group. Thomas, I appreciate your effort in building the mercury setup in the rheometer lab—even if it made my hair age faster than expected! Long, thank you for your support, especially at the start of my PhD; many things went more smoothly thanks to your guidance.

To my loyal office colleagues—Björn, Bart-Jan, Makara, and David—thank you for sharing countless moments. Knapp, thank you for leading the PhD head task force, Curto, thanks for leading the crime investigation unit, and Anja, for keeping the lab organized.

I would also like to express my gratitude to all members of the INM–Leibniz Institute for New Materials, across research, administration, IT, workshop, library, service groups, and facility management. Your support has been invaluable in making this work possible. A special mention goes to Ralf for his outstanding IT assistance and for always being ready to solve problems quickly. Of course, I want to thank Robert Drumm for his help with the tensile machine and for always being available whenever an issue arose in the lab. To everyone who contributed—whether by keeping things running smoothly behind the scenes or by lending a helping hand during challenging moments—thank you for making my time at INM both productive and enjoyable.

Last, and most importantly, I want to express my heartfelt gratitude to my parents, my sister, and my friends for their unwavering support throughout this journey. Thank you for your patience, encouragement, and for always being there when I needed strength and perspective. This achievement would not have been possible without you.

Motivation

Many aspects of modern life are dominated by the use of electronic materials. These include common devices like displays, smartphones, or computers, but also human-machine interfaces that bring their functionality closer to the human body. Sensors, smart textiles, and other wearable technologies have been developed to equip daily life objects with functionality. This includes measurements of physiological parameters of the body or heat up your jacket or gloves during the winter period. While the first prototypes focused on functionality, a trend towards design and adaptability emerges. Devices should integrate with the body and match its mechanical properties, making wearables almost unnoticed in daily life.

This trend urges for the development of soft, skin-like materials, away from classical, rigid electronic components. A key challenge for the design of such soft materials is the integration of different material properties. As for a material to be considered soft, the degree of deformability in multiple directions to a significant extent, must be ensured. This is realized by, for example, flexible and stretchable polymer foils, onto which electric circuits are printed. On one hand, conductive materials are often rigid with limited deformability. On the other hand, stretchable and flexible materials often have poor electrical conductivity.

Panta rhei – everything flows – dated back to Heraclitus from Samos around 500 B.C., gives an idea of a truly soft material. A liquid adapts to every shape and follows every deformation that is imposed on it. If a conductive functionality is added to this liquid, without changing the property of adaptability, new perspectives for soft electronics are opened. At this point, electrofluids – concentrated, conductive suspensions – come into play. An electrofluid is composed of conductive particles, dispersed in a non-conductive, liquid matrix. At a certain amount of filler particles, they come in contact to each other and form networks, capable of transporting charges. Due to their liquid state, the particles remain mobile, allowing them to reconfigure and adapt to external deformation, and remain conductive due to the continuous reformation of particle contacts. In contrast to liquid metals, i.e., low melting point metals or alloys, the electrical and mechanical properties of electrofluids are highly adjustable by changing concentration or composition.

The formation of conductive structures within such electrofluids and how the resulting network affects the electrical and mechanical properties is part of the discussion in this thesis. In the first chapter, a comprehensive review of the state of the art of concentrated suspensions and current materials for the use in flexible and stretchable electronics is given, followed by the main questions that are addressed in this thesis. In chapter 3, the concept of electrofluids is introduced using carbon black as conductive filler and studying the effect of the polarity of the liquid matrix. The fourth chapter exploits the affinity of conductive carbon black with different matrices to direct particle distribution with a volume exclusion strategy. The use of different conductive filler materials is investigated in the fifth chapter. Here, the role of the morphology of different 2D carbonaceous fillers on the properties of electrofluids is discussed. Distinct electromechanical properties depending on the type of filler are discussed. A general discussion on electrofluids follows, including the topics of electrical and mechanical network formation in different filler-matrix systems, sensing properties as well as time dependent behavior. A conclusion on the main findings and an outlook for future work closes this thesis.

Table of content

1. State of the art

Within the following sections, a brief overview of the current state of research in the framework of flexible and stretchable electronics and in the field of particle gels and concentrated suspensions is given. This short review discusses strategies for the design of such electronic materials including conductive polymers and liquid metals (LM) with a special focus on conductive polymer composites (CPCs), i.e. polymers filled with conductive particles. Different matrix materials, commonly used in CPCs, alongside conductive fillers are introduced. Among those, carbon fillers are the main interest within this thesis. A special focus lays on the electrical and mechanical properties caused by the formation of the filler networks within the composite materials.

1.1. Soft electronics

Flexible and stretchable electronics are a type of material that inherits electronic functionality while being able to be mechanically deformed, a combination of properties that is not found in classic electronic components. The deformation may be applied in form of bending and twisting (flexible), or stretching and compressing (stretchable). The key challenge is to keep the electronic functionality of the material, while allowing many degrees of freedom in deformation. Several strategies have been employed to address this problem, resulting in many different types of materials. Conductive polymers present both flexibility and electrical conductivity, making them a straightforward choice. An alternative is to make use of liquid metals, that provide high intrinsic conductivity and, due to their flowability, adapt to any type of stretchable encapsulant. Also, CPCs have been explored, as many combinations of polymers and conductive fillers are possible, and allow for a high degree of tunability. In the following sections, each of these approaches is discussed in detail.

1.1.1. Conductive Polymers

Polymers are essential to the nowadays technology and lifestyle and are predominantly used due to their cheap production and outstanding mechanical properties. In 1977, Shirakawa *et al*. synthesized the first, intrinsically conductive polymer (polyacetylene).[1] Conductive polymers are rendered conductive due to their unique backbone chain consisting of conjugated bonds. The electrons in those bonds, the so-called π-electrons play a crucial role in the conduction mechanism, since in a conjugated configuration they are delocalized allowing for charge transfer.[2] Typical conductivities of conductive polymers can reach values of 10^{-2} S/cm (compared to 10^{-14} S/cm for insulating polymers).[3] To further enhance the conductivity (up to 10^{3} S/cm)[2], conductive polymers are often doped, meaning enriching or depleting of electrons. Among conductive polymers, the most prominent examples are polypyrrole (PPy), Polyanilin (PA), poly(3,4-ethylenedioxythiophene) polystyrene sulfonate (PEDOT:PSS), and poly(3-hexylthiophene-2,5-diyl) (P3HT). These polymers are attractive for soft electronics, not only due to the conductivity, but also since they can be shaped into electric conductors (see Figure 1.1A) by spray coating or screen-printing.[4] Some recent fields of application include supercapacitors,[5] organic light-emitting devices (OLEDs),[6] or stretchable conductors.[7] Conductive polymers are typically limited by their solubility, brittleness, and difficult processing.[8]

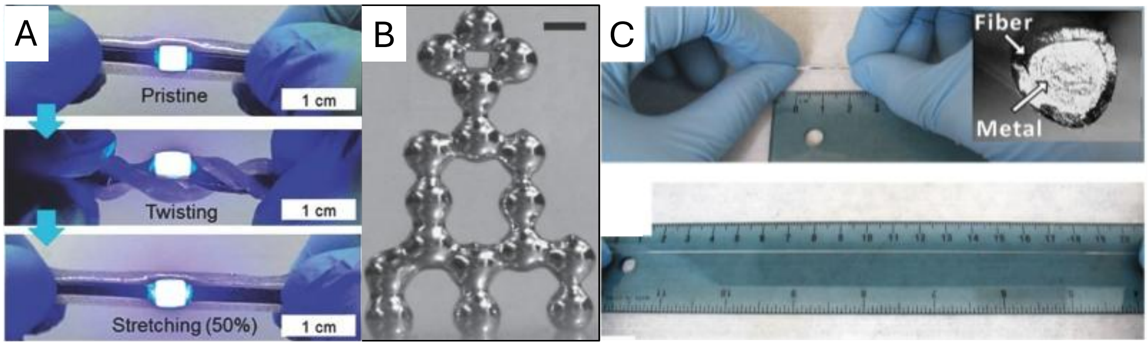

Figure 1.1. A: A conductive polymer (PEDOT:PSS) encapsulated into a stretchable polymer (PDMS) and connected to an electric circuit. The LED incorporated into the polymer remains active despite mechanical deformation. Adapted with permission from reference.[4] B: 3D structure fabricated by dispensing EGaIn droplets on top of each other. The formation of an oxide layer, when exposed to air, is sufficient to provide mechanical stability to the droplets. Scale bar represents 0.5 mm. Reproduced with permission from reference.[9] C: Liquid metal (EGaIn) inside an elastomeric tube (poly[styrene-b-(ethylene-co-butylene)-b-styrene], (SEBS). A strain of 1000% is applied manually without breaking the tube nor the electrical conduction. Reproduced with permission from reference.[10]

1.1.2. Liquid metals

Liquid metals (LMs) are those that have a melting point close to or below room temperature, making them intrinsically conductive while flowing.[11] Prominent examples are mercury or caesium. Mercury, commonly used in the past for metal extraction, dental fillings, electronic switches, and a well-known component of thermometers, is inherently toxic and, therefore, not safe to use in devices that are in contact with the human body or the environment.[12] A recent decision by the European Union in 2017, forbidding the use of mercury in thermometers, shows the need for alternatives. Alkali metals are highly reactive when exposed to humidity, making them uninteresting for many applications under standard conditions. More realistic options are gallium or its alloys with indium or tin.[11]A 1:5 atomic ratio of indium to gallium results in an eutectic alloy (EGaIn) with a melting point of 15.7 °C and an electrical conductivity of $3\cdot10^6$ S/m.[13] If tin is added to this mixture, changing the atomic ratios to 68.5% gallium, 21.5% indium, and 10% tin, an alloy (Galinstan) forms that has an even lower melting point of -19 °C with just slightly reduced electrical conductivity of $2.3\cdot10^6$ S/m.[14] The combination of high conductivity and flow properties makes these alloys suitable for soft electronic applications. Although the main components, gallium and indium, are generally considered safe, there are still ongoing studies regarding the specific toxicity of these alloys.[15]

If both EGaIn or Galinstan are exposed to oxygen, an oxide layer forms on their surface. This layer prevents flowing under rest and provides the material a sufficient yield stress to stabilize certain 3D structures (see Figure 1.1B).[13] While beneficial for 3D printing techniques, the processability is hindered for other methods. In many cases, LMs are encapsulated to avoid excessive exposure to air and for device integration. Due to their liquid nature, their stretchability is only limited by the mechanical properties of the encapsulant, reaching high strain retaining electrical conductivity (see Figure 1.1C). Another strategy to exploit their liquid nature integrates LMs into elastomers to provide self-healing properties.[16] In the work of Markvicka *et al.*, LM droplets are integrated into an elastomer to allow for self-healing properties by recreation of destroyed conductive LM paths.[17] The intrinsic conductivity allows for stable conductive interconnects, since the change in resistance is only dependent on the geometrical changes during elongation.[10] This also implies that high sensitivity cannot be achieved by simple encapsulation. More complex structures, like LM foams[18] or LM inclusions,[19] are required to reach higher sensitivities, limiting the use of LMs in sensor applications.

1.2. Conductive composites

Conductive polymer composites (CPCs) are composed of conductive filler particles in an insulating polymer matrix.[20] Due to the extensive variety of polymers and fillers that can be combined, CPCs offer a great degree of tunability to create flexible and stretchable electronic materials with tailored properties. As electrofluids can be defined as liquid composites, they share some characteristics with their solid counterparts. Therefore, this section discusses CPCs in more detail.

When adding conductive particles to a matrix, they can form a continuous network (see cross-section of a CPC in Figure 1.2A), responsible for carrying the electrical conductivity, while the polymer confers to the composite sufficient mechanical stability and flexibility. Among other structures, the creation of highly stretchable conductive interconnects (see Figure 1.2B) and wearable strain sensors (Figure 1.2C) was demonstrated.[21, 22] As both matrix and filler are determinative for the final electrical and mechanical performance of the CPCs, their properties and use are discussed in the following sections.

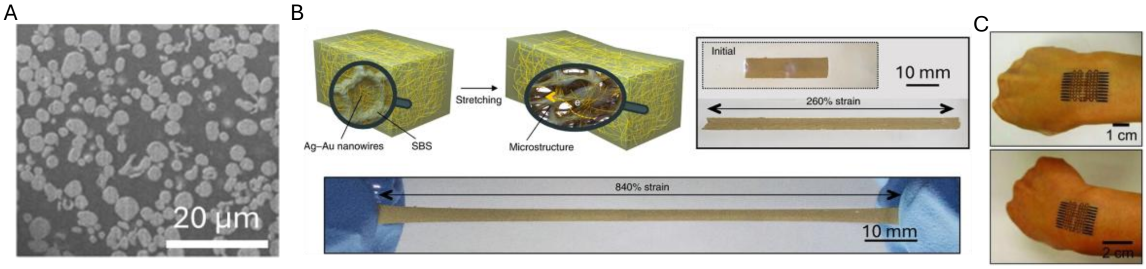

Figure 1.2. A: Scanning electron microscopy (SEM) image of a focused-ion beam (FIB) cross section of a silver-polydimethylsiloxane (PDMS) composite. Reproduced with permission under creative commons license BB CY from reference.[23] B: Composite of silver-gold nanowires in poly(styrene-butadiene-styrene) (SBS) polymer. Mechanical deformation of up to 840% without failure was reported. Adapted with permission from reference.[21] C: Printed structures of a PDMS-carbon nanotube (CNTs) composite, embedded in a PDMS matrix. The composite acts as a sensor for human motion detection. Reproduced with permission from reference.[22]

1.2.1. Matrix materials

For stretchable composites, polymers are the most promising class of materials to serve as a matrix, due to their inherit mechanical properties. Polymers are distinguished by their type and degree of crosslinking into three main categories, thermoplastics, thermosets, and elastomers. For stretchable CPCs only thermoplastics and elastomers are of relevance, since thermosets are characterized by a very high crosslinking density between the polymer chains, making them very rigid (see Figure 1.3A).[24] Thermoplastic polymers are composed of linear chains and are only physically crosslinked making them meltable and easy to process (see Figure 1.3B). In elastomers, the mesh of crosslinks is very loose giving them the ability to stretch and deform elastically (see Figure 1.3C). A special type of polymeric matrix materials are hydrogels. Hydrogels are, physically or chemically crosslinked[25] polymers that can entrap water in between the chains and, as a result, swell (see Figure 1.3D).[26] This characteristic makes them useful especially for biological applications. This chapter will discuss these three types of polymers and their use as matrix material in CPCs.

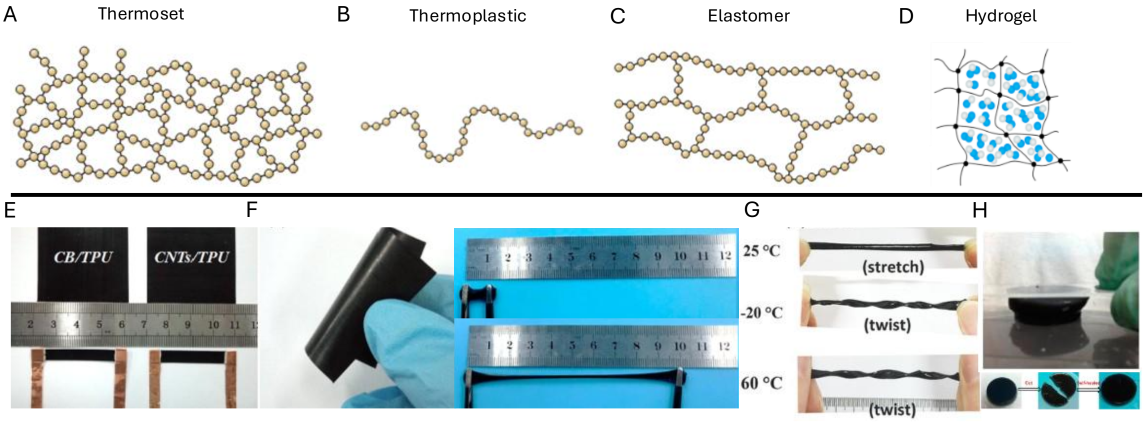

Figure 1.3. A: Schematic structure of a thermoset polymer. The crosslinking density is high, making this type of polymer very hard. B: Schematic representation of thermoplastic polymer. Linear chains only provide physical interactions and entanglements. C: Schematic structure of an elastomer. Linear polymer chains are connected via chemical crosslinks. The crosslinking density is low, providing a certain degree of flexibility in the chain. Panels A-C reproduced with permission from reference.[24] D: Schematic representation of a hydrogel. Water molecules fill the spaces between crosslinked polymer chains. Adapted with permission under creative commons license CC BY from reference.[27] E: Composite material containing thermoplastic polyurethan and either carbon black or carbon nanotubes. Both types of composites are conductive and flexible. Adapted with permission from reference.[28] F: Conductive composite made from silicone polymer and carbon black. High stretchability of up to 1000% strain was achieved. Adapted with permission from reference. [29] G: Glycerol-water hydrogel with 10 wt.% CNTs. The conductive hydrogel can undergo different deformation modes at different temperatures without breaking. Adapted with permission from reference.[30] H: Compressible conductive hydrogel based on graphite in a polyacrylamide (PAM) hydrogel. After cutting in half the hydrogel can be healed by bringing the two halves back into contact. Adapted with permission from reference.[31]

Thermoplastic polymers

Due to the presence of only physical interactions between the polymer chains, the mechanical properties of thermoplastic polymers depend strongly on the temperature. At low temperatures, the chains are “frozen”, resulting in solidification of the polymer. With elevating temperature, the chains increase their mobility, making the polymer viscoelastic. This point is defined as glass transition temperature (T_g). At even higher temperatures, the thermal energy exceeds the physical interaction energy, and the polymer is melting (melting temperature, T_m) i.e., liquifying.[24] The temperature windows differ depending on the type and crystallinity of the polymer. In this molten state, thermoplastics can be shaped into complex geometries by using different processing techniques like molding, injection, or extrusion.[32] Thermoplastics are often used as flexible substrates[33] or for conductive composites.[34] The filler is typically dispersed in the polymer in its molten state. Once cooled down, the fillers are embedded within the solidified polymer matrix. One of the most often used polymers for stretchable CPCs is thermoplastic polyurethane (TPU). This is because within the thermoplastic polymers, neat TPU was reported to sustain up to 600% strain before breaking.[35] In the work of Zheng *et al.*, carbon nanotubes were added to a TPU matrix to create a strain sensor with a sensing range of up to 135% strain (see Figure 1.3E).[28] Besides extension, also sensors for compressive strain were developed. Zhai *et al.* fabricated a TPU foam with carbon black filler that was compressible up to 80%. The elastic properties of the TPU allowed for fast recovery and stable electrical signals over time.[36]

Elastomers

A low degree of crosslinking, allowing the polymer chains to slide among each other to a certain extent, confers the elastomers their elastic properties.[32] This crosslinking may either be of chemical or of physical nature.[37] The former one requires a chemical reaction that links the chains together, creating strong bonds between them, while the latter one is based on van der Waals (vdW) interactions between the chains. The degree of crosslinking determines the mechanical properties. A commonly used class of polymers are polysiloxanes, for example, polydimethylsiloxane (PDMS). These polymers are biocompatible, inert, transparent, and highly stretchable up to strains of more than 1800%.[38, 39] Even composites made out of silicone polymers can undergo deformation up to 1500% (see Figure 1.3F).[29] Some polymers contain chains that are composed of a mixture of different chain segments that create different interaction forces to tune the mechanical properties.[37] Typical examples include poly(styrene-butadiene-styrene) (SBS) or poly(styrene-co-ethylenebutylene-co-styrene) (SEBS).[37] One of the biggest differences between chemically and physically crosslinking polymers regarding their use in composites is the amount of filler that can be incorporated. If the filler concentration exceeds a certain point, the chemical crosslinking reaction is hindered and the movement of the polymer chains limited, deteriorating the mechanical properties.[40] It has been reported that the addition of silica particles to a SBR polymer reduces the cross-linking density with increasing filler loading.[41] Since physical crosslinked polymers do not undergo a crosslinking reaction, even high amounts of filler are able to be used.[40]

Hydrogels

Hydrogels are built up from crosslinked, hydrophilic polymers,[42] with a high water uptake capacity,[43] making them swell when coming into contact with it. Initially, the development of such hydrophilic polymer networks was fostered by the need for a replacement for traditional contact lenses for more soft alternatives.[44] Commonly used polymers for hydrogels are among others poly2-hydroxyethylmethacrylate (pHEMA), polyvinyl alcohol (PVA), polyethylene glycol (PEG), polyacrylic acid (PAA), or polyacryl amide (PAM).[44] The polymer chains are crosslinked either physically or chemically.[45] Nevertheless, the stiffness and the shape stability of hydrogels are typically low.[46] The preparation of nanocomposites by adding conductive fillers to the hydrogel improves their mechanical properties, creating CPCs.[44] When adding 10 wt.% of carbon nanotubes (CNTs) into a hydrogel of PAA and PAM, high stretchability (up to 700%) and flexibility was reported at different temperatures (see

Figure 1.3G).[30] The amount of CNT filler was sufficient to render the hydrogel conductive with 8.2 S/m.[30] Das *et al.*, used graphene flakes in a PAM hydrogel to create compressible hydrogels with self-healing properties (see Figure 1.3H) and a conductivity up to 0.012 S/m.[31]

Even though all the presented matrix materials are used for CPCs, each of them has their own limitations in terms of stretchability and break at a certain deformation. As electrofluids are designed to remain in their fluid state, such limitations do not exist as a material property. In the following subsection, the different types of fillers that are incorporated into the matrix, will be discussed.

1.2.2. Filler materials

To create a CPC from a non-conductive matrix material, electrically conductive filler particles need to be dispersed into it. High conductivity is often achieved with metals like copper ($5.96\cdot10^7$ S/m), gold ($4.42\cdot10^7$ S/m), or silver, which has the highest conductivity among them ($6.3\cdot10^7$ S/m).[47] Silver is predominantly used for flexible and stretchable electronics applications since copper is not stable and oxidizes rapidly and gold is very expensive.[48] Silver has been successfully used to create transparent strain sensors, by using nanowires in a PDMS matrix,[49] or flexible e-skins based on silver nanoparticles in a polyimine matrix.[50] Nevertheless, for many applications the use of silver is expensive and not reasonable from an economic perspective. An alternative type of filler, although less conductive, are carbon-based fillers. Especially when a high conductivity is not required, the cheap and easy production as well as being mostly inert, make them a promising candidate for CPCs. Due to their low density (up to 2.23 g/cm^3, as the density of graphite) carbon materials are beneficial for the use in electrofluids to avoid fast sedimentation. The most used carbon fillers are carbon black (CB), carbon nanotubes (CNTs), and graphene flakes (GP),[51] which are discussed below in more detail.

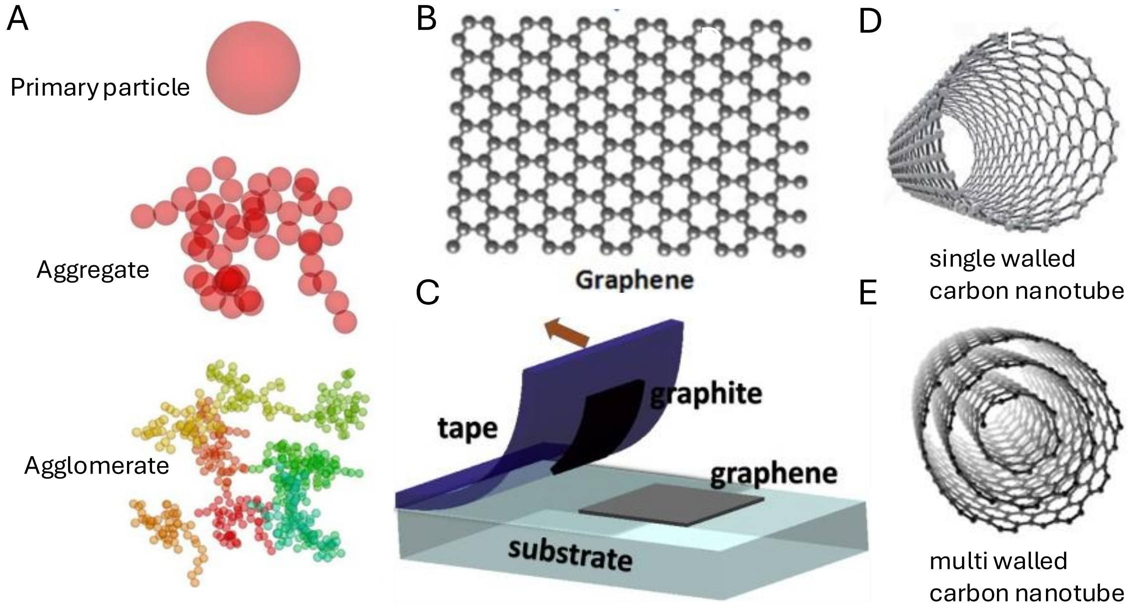

Figure 1.4. A: Hierarchical structure of carbon black. Spherical primary particles build larger aggregates. Multiple aggregates stick together via van der Waals (vdW) forces, forming larger agglomerates. Reproduced with permission from reference.[52] B: Schematic representation of a 2D graphene lattice. Adapted with permission from reference.[53] C: Synthesis method of single- and few layered graphene via adhesive tape method. Reproduced with permission from reference.[54] D: Schematic representation of a single-walled carbon nanotube (SWCNT) and E: a multi-walled carbon nanotubes (MWCNT). Adapted with permission from reference.[53]

Carbon black

Carbon black is by far the most used carbon-based filler with an annual production of 15.2 million tons in 2023.[55] Most of it is used as filler material for plastics and rubbers for reinforcement and antistatic properties.[56] CB is produced by thermal combustion of oil feedstock. There are different methods depending on the type of furnace or gas used to decompose the feedstock. Among all these methods, acetylene black typically creates CB with high purity and very little contamination.[57] The resulting CB exhibits a hierarchical structure, described by three levels (see Figure 1.4A). The smallest units are the primary particles that are formed at the beginning of the combustion process. They typically are in the size range of 18 to 285 nm[56] and composed of multiple layers of graphitic carbon lattices forming the so-called carbon onion structure. These primary particles fuse together due to collisions during the fabrication process and form the second hierarchical level, the aggregates. They are considered the smallest dispersion unit since separation of the primary particles from the aggregates is only possible when applying high energy (for example during ball milling). Depending on the aggregation process, aggregates with lower (closed) or higher (open) structure form. The aggregate configuration also determines the surface area of the CB, which is lower for low structured and higher for high structured CBs, leading to surface areas between 25 and 1500 m^2/g, respectively.[58] As the aggregates come into close contact to each other, physical interactions (van der Waals (vdW) forces), act as driving force to create the third hierarchical level, agglomerates. They are loose structures that grow depending on the aggregate concentration and their tendency to cluster together. Due to the weak interactions, temporal separation of the agglomerates requires less energy, for example by ultrasound or shear deformation. Adjusting the size and distribution of agglomerates is important as they are responsible for the final properties of the composite.

One of the main reasons why carbon materials are used as conductive filler in CPCs is the fact that they facilitate electron conduction. The conduction mechanism of CB can be divided into two mechanisms. First, the intraparticle conduction, which is mediated by the graphitic lattice structure within the primary particles. In such a structure, each carbon atom has a free π bond that causes electrons to delocalize and conduct current.[59] Second, the interparticle conduction, which is mainly due to tunneling that takes place when the distance between two particles is small enough.[60] Although it is one of the oldest type of conductive fillers, CB still remains an important material for a variety of modern applications like flow batteries[61] or sensors.[62] Due to its complex hierarchical structure, the network formation at the different levels is still discussed.[63]

Graphene Flakes

Graphene, first experimentally prepared in 2004 by Novoselov *et al.*,[64] recently became a popular 2D filler material due to its outstanding mechanical and electrical properties.[65] A single graphene sheet (see Figure 1.4B) consists of only one layer of a honeycomb orientated carbon lattice. Electron conduction is mediated also via delocalized π electrons throughout the lattice. While this, in-plane conductivity can be as high as 10^8 S/m,[66] it is only achievable for monolayer graphene. As more sheets are stacked, the out-of-plane conductivity limits the maximum conductivity as the conduction mechanism here is based on electron tunneling. Although originally prepared via a simple scotch tape delamination of graphite (see Figure 1.4C),[64] the yield of this method is too low to be relevant for a large scale production.[67] Synthesis routes of graphene can be classified by either top-down or bottom-up processes.[68] Top-down processes use graphite or graphite oxide as precursor material, which subsequently undergoes exfoliation procedures for example by mechanical exfoliation. In a recent approach, Mardlin *et al.* prepared graphene flakes via a solvent-free thermomechanical exfoliation process with varying surface area depending on the degree of exfoliation.[69] Solvent-based methods include the chemical exfoliation method. Here, small molecules are intercalated between the graphene layers of graphite, which increase the distance between them. Hence, their interlayer adhesion force is reduced, making it easier to separate.[68] Vacuum process techniques, like chemical vapor deposition (CVD) or gas-phase plasma synthesis, are bottom-up approaches and are used to create single or few-layered graphene. Both methods are not reliant on strong chemicals that potentially create defects in the graphene lattice and reduce their electrical properties.[70] Due to their high electrical conductivity and optical transparency, graphene finds application in solar cells[71] and supercapacitors,[72] but also for wearables and strain sensors.[73]

Carbon Nanotubes

Carbon Nanotubes (CNTs) are 1D fillers and can be described as a folded sheet of graphene forming a tube with several nanometers in diameter. Depending on the number of sheets, single-walled and multi-walled carbon nanotubes (SWCNT and MWCNT) are distinguished (see Figure 1.4D and E). Routes of production include arc discharge, chemical vapor deposition, or laser ablation.[74, 75] As the other two carbon species, the carbon lattice in CNTs is sp^2 hybridized, rendering them electrically conductive. Due to the possibility of reaching high aspect ratio up to 1000,[76] conductive composites with very low filler concentrations down to 0.04 vol.% have been reported.[77-79] Besides their high intrinsic conductivity (up to 10^6 S/cm)[80] and their mechanical strength (Youngs modulus up to 3.5 TPa),[81] the incorporation of CNTs into a polymeric matrix is challenging due to the high vdW forces creating bundles of CNTs.[80] One way to disassemble these bundles is to use ultrasonication. Due to the high energy at the interface of the CNTs, they separate and disperse in the surrounding medium.[80] This method is less effective in more viscous solvents, which is especially limiting for the direct dispersion in polymer melts or concentrated polymer solutions. Furthermore, a long and intensive treatment may cause defects in the structure of the CNTs, which reduces their electrical conductivity[82] or breaks them and reduces their aspect ratio.[83] Another approach, often used to better disperse CNTs, is their functionalization. This reduces the attractive force between individual CNTs either by disturbing the π-π conjugation or due to induced defects in the lattice structure. Due to the change in surface chemistry, the interactions with the matrix can be increased leading to a preferential dispersion instead of bundling. Alternatively, polymers or surfactants can be attached to the CNTs via vdW forces creating a layer around the CNTs that prevents their bundling but also reduces electron conduction.[80]

1.3. Electrical properties

The basic requirement for polymer composites to become conductive is the creation of an electrical network of fillers that can transport electrons through the material. The random formation of conductive networks can be described by the so-called percolation theory, a mathematical model to describe the connectivity of objects within a given volume. The network structure that is formed determines the electrical conductivity of the composite. A brief introduction to the percolation model and the role of filler contacts for the electrical properties of CPCs is addressed in this section.

1.3.1. Network formation

Originally introduced by Broadbent and Hammersly in 1957,[84] percolation describes transport phenomena through a porous medium. This general description finds application in describing the flow of fluid through a porous material like a sponge or sandstone but can also be applied to other transport phenomena such as electrons through a conductive network like the one formed by fillers in CPCs.[85] A simple model to describe percolation is the so-called "site percolation" model. For simplicity, a 2D cubic lattice is assumed that contains bonds (lines) and sites (intersection points) as shown in Figure 1.5A. Now, sites are added randomly to this lattice. If two sites are adjacent to each other they form a bond, indicated by a thick solid line in Figure 1.5B. Sites are subsequently added until a continuous path of bonds is formed from one side of the lattice to the other (Figure 1.5C). The fraction of sites required to form this path is defined as the percolation threshold.[86] For the case of a 2D cubic lattice, a fraction of 0.593 of all sites need to be occupied to reach this threshold.[87] This number reduces to 0.312 in a 3 dimensional, simple cubic configuration.[88] Now, one can define the existence of a site as electrically conductive and the absence of a site as electrically insulating. In such a case, the creation of a continuous path of bonds is equivalent to a steady flow of electrons through the lattice, i.e., a transition from an insulator to a conductor.[85] For CPCs, conductive filler particles are the sites and particle-particle contacts are the bonds, meaning that the minimal required amount of filler particles to render the composite conductive defines the percolation threshold in CPCs. As each particle occupies a certain volume within the composite, the filler concentration is often given as a volume fraction. A corresponding curve of the logarithm of electrical conductivity against the filler volume fraction for a CPC is shown in Figure 1.5D. At low concentrations, the filler particles are not connected. With increasing concentration, more clusters form, and the number of connected fillers increases until a critical concentration, at which one conductive pathway is formed. In this percolation region, conductivity increases by several orders of magnitude with very little addition of filler. Further increase in concentration increases also conductivity, but to a smaller extent. The determination of the critical concentration based on a percolation curve like in Figure 1.5D is done by fitting Equation 1.1 defined for 3D conductive networks:[87]

$$\sigma \propto A(\phi - \phi_c)^t, \phi > \phi_c \tag{1.1}$$

where σ is the electrical conductivity, A is a constant, ϕ the filler fraction, ϕ_c the critical threshold concentration, and t the critical exponent (note that the condition $\phi > \phi_c$ must be fulfilled, since it is only defined above the percolation threshold). Percolation thresholds of CPCs can be as low as 0.005 wt.% for single-walled CNTs in an epoxy matrix[89] or as high as 78 wt.% for silver particles in epoxy resin.[90] For CPCs, it is crucial to reach percolation with as few filler particles as possible to a) limit the costs and resource consumption for the fabrication and, b) minimize their impact on the mechanical properties of the selected matrix (this point is addressed in section **1.4. Mechanical Properties** in more detail).

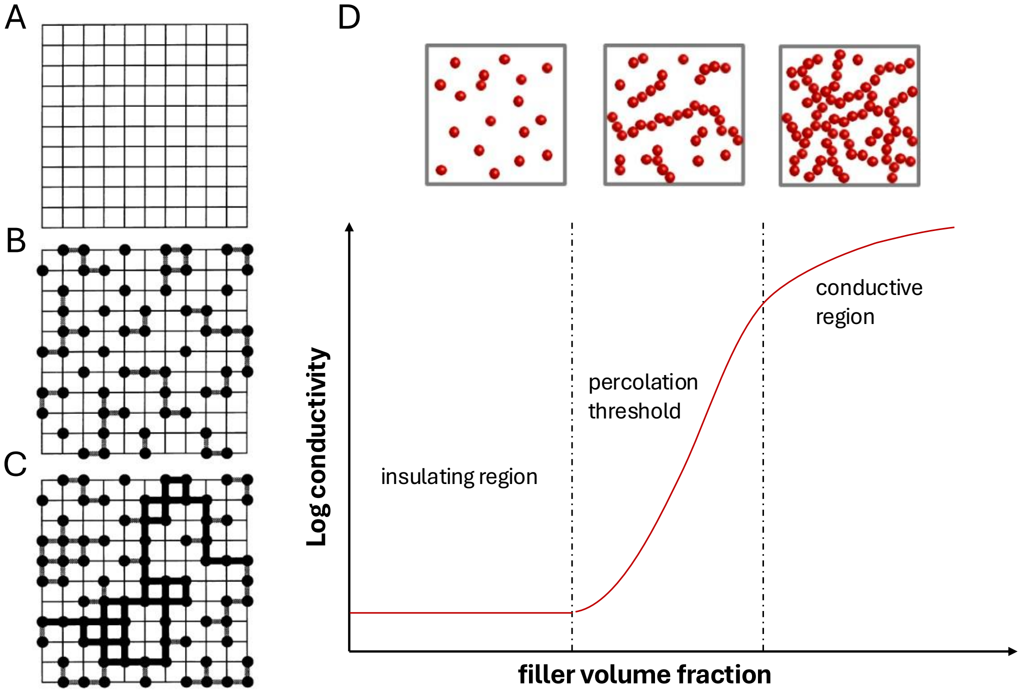

Figure 1.5. A-C: 2D lattice model to describe the percolation transition. No connected sites in A. Isolated clusters of connected sites in B. Isolated clusters of connected nodes and lattice spanning cluster of connected sites in C. Thin lines represent connections in isolated clusters and thick lines represent connections contributing to a connected cluster. Reproduced with permission from reference.[86] D: Example of an electrical percolation curve indicating three different regions. An insulating region at filler concentrations below the percolation threshold, a percolation transition, and a conductive region at filler concentrations above the percolation threshold.

Influence of the filler

In several studies, the influence of the filler's aspect ratio on the percolation threshold was investigated. In the work of Ram *et al.*, the electrical conductivity in dependence of the filler loading for short carbon fibers (SCFs) with varying aspect ratio within in a PVDF matrix was studied.[91] They found that with an increase in aspect ratio (from 147 to 735), the percolation threshold reduced from 0.87 to 0.47 wt.%, respectively.[91]. This behavior was also found for other filler types, for example, in carbon nanotubes (CNTs) in an epoxy matrix[92] and was corroborated in simulations.[93] A higher aspect ratio is beneficial to create at least one continuous filler path, since the probability to get in contact with another filler particle is increased. Nassar *et al.* used this to create stable electrical interconnects by 3D printing a composite of high aspect ratio CNTs in a thermoplastic polyurethane matrix. The high aspect ratio increased the contact area between the individual CNTs, which lowered their susceptibility to deformation.[94]

The aspect ratio of a filler is also related to its shape, which has also been investigated regarding its impact on the electrical percolation threshold. In a simulation work of Xing *et al.*, the influence of roundness on the percolation threshold was studied.[95] Filler shape was changed incrementally from a tetrahedron to a sphere (see Figure 1.6A). They found an increase in percolation threshold from 0.1511 (tetrahedron) to 0.2896 (sphere) and attributed this to the larger excluded volume that fillers with sharp edges occupy.[95] Excluded volume here is referred to the volume that each filler particle occupies without allowing their overlapping.[95] Kwon *et al.* investigated the percolation threshold of spheres, rods, and plates with similar radius of gyration (R_g) via Langevin dynamics simulation.[96] They concluded a shape dependent increase in percolation threshold of the order rods < plates < spheres (see Figure 1.6B).[96]

Another factor that has an impact on the electrical properties is the size of the filler particles which is closely linked to the shape. Some simulation works concluded that if the size of the filler increases, the percolation threshold for spheres increases, but for rods and plates decreases.[96] Li *et al.* developed an analytical model to describe this observation for graphite plates that matched the experimentally obtained threshold values.[97] For spherical silver particles in epoxy resin, Wu *et al.* demonstrated an increase in percolation threshold (from 63 to 78 wt.%) with increasing particle size (50 to 1000 nm), fitting to the simulation data.[90] Although these studies describe well the observations for well-defined particles, for irregular shaped fillers, such as aggregates of carbon black (CB), different trends have been reported. The effect of the aggregate size of CB on the electrical percolation threshold was studied both experimentally, by breaking the original aggregates by ball-milling, and in simulations with both showing larger aggregates being beneficial for electrical percolation reduction (see Figure 1.6C).[52]

During the preparation of CPCs, the conductive filler must be incorporated into the polymer matrix, mainly done by shear mixing or ultrasonication. The quality of this step, i.e., how homogenously the filler is dispersed, affects the electrical percolation. For anisotropic fillers like CNTs, better dispersion leads to lower percolation thresholds and increased conductivity.[92] Due to the high aspect ratio of the individual CNT, agglomeration leads to a less efficient volume spanning (see Figure 1.6D). A common strategy to address the dispersion problem in CNTs is to functionalize their surface to achieve a more favorable chemical affinity towards the polymer matrix.[98] Although the functionalization results in a better dispersion of the nanotubes, the overall electrical conductivity of the composite is often reduced. This is because the functionalization process can create an insulating layer around the nanotubes that increases the contact resistance,[99] introduces defects in the nanotube structure,[100] or shortens the length of the nanotubes.[101] Wu *et al*. reported a percolation threshold of 2 vol% for pristine CNTs in a low density polyethylene (LDPE) composite, while after functionalization with carboxyl or hydroxyl groups, it increased to 4 or 4.3 vol.%, respectively.[102]

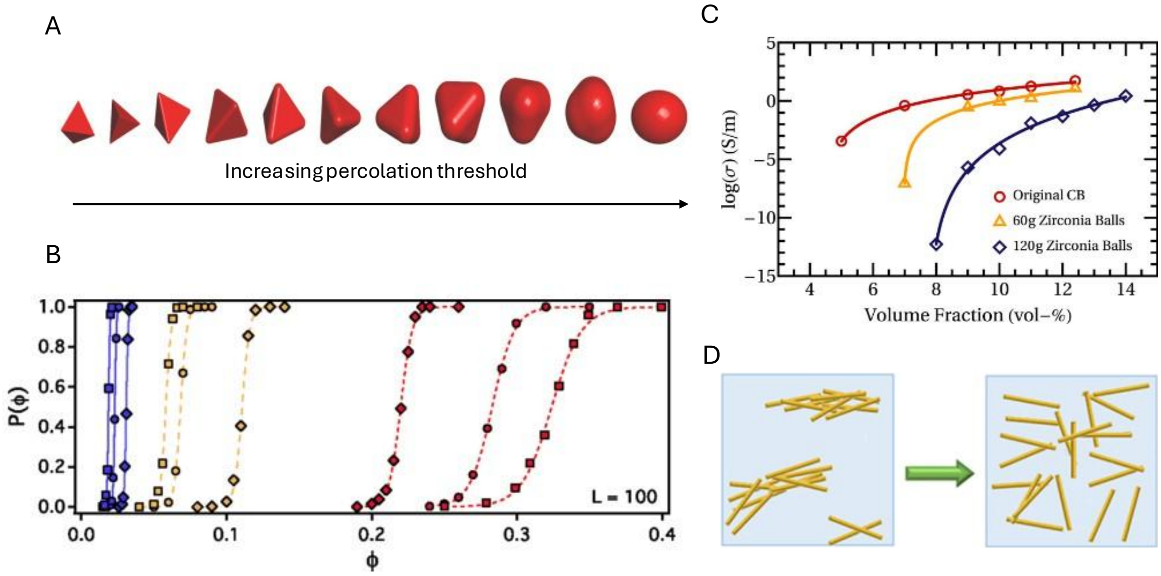

Figure 1.6. A: Change in filler shape from tetrahedral to spherical. Adapted with permission from reference.[95] B: Percolation probability as a function of filler volume fraction for rods (blue), plates (yellow), and spheres (red). Increasing filler size is indicated by the symbols in increasing order of diamond, circle, square. Adapted with permission from reference.[96] C: Logarithm of the electrical conductivity as a function of the volume fraction of carbon black in PDMS. The colors indicate the treatment of the carbon black as untreated (red), ball-milled with 60 g (yellow), and 120 g (blue) zirconia balls. A higher amount of zirconia balls implies a reduction in the carbon black aggregate size. Reproduced with permission under creative commons license CC BY from reference.[52] D: Different degree of dispersion for rod-like fillers in a matrix. In agglomerated form the fillers do span the volume efficiently. Once separated the covering is increased and more contacts between the rods are enabled. Adapted with permission under creative commons license CC BY from reference.[103]

Strategies to minimize percolation threshold

To reduce the percolation threshold, several strategies have been developed that aim to change the filler distribution from random to directed. One of them is the so-called double percolation. Here, two immiscible polymers form a blend, in which the conductive filler predominantly distributes in only one of them (see Figure 1.7A).[104] This concept was used, for example, by Li *et al*, who used an immiscible blend of polypropylene (PP) and epoxy in a 1:1 weight ratio with CB as the conductive filler. Compared to the neat epoxy matrix, they could lower the percolation threshold by approximately 50% from 14.5 wt.% to 7.4 wt.%.[105] Although the filler particles are directed into a specific phase, the percolation mechanism within this phase remains mainly random. A second strategy, segregated composites, addresses this point. Here, the conductive filler is directed to the interface of a) two different matrices or b) the grain boundaries of a crystallized matrix phase. In that way, the filler only distributes along the interface area and is entrapped in it (see Figure 1.7B).[106] Chen *et* *al*. reduced the percolation threshold of CNTs in a blend of polycarbonate (PC) and acrylonitrile-butadiene-styrene (ABS) from 0.24 wt.% (neat PC) to 0.05 wt.% in a segregated composite.[107] For both strategies, the correct choice of matrix and filler material, as well as the processing are key parameters to consider. A third strategy is based on the addition of a third phase in the form of insulating particles that takes out available volume from the system (see Figure 1.7C). The reduction in percolation threshold is here dependent on the amount of volume occupied by the third phase.[108] In a composite of multi-walled CNTs in PP, Bao *et al*. reduced the electrical percolation threshold from 0.90 to 0.63 vol.% by adding 30 wt.% of calcium carbonate particles.[109]

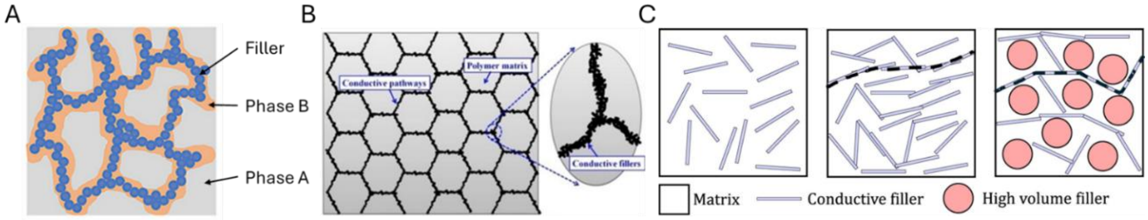

Figure 1.7. A: Schematic representation of a double percolation concept. Two immiscible phases (A and B) in which one phase (B) percolates through the other one (A). The conductive filler predominantly distributes in the percolating phase (B). Adapted with permission from reference.[110] B: Schematic representation of a segregated composite. The conductive filler is distributed at the interface of polymer particles. Reproduced with permission from reference.[106] C: Schematic representation of volume exclusion via the addition of a third component (here shown as red spheres). Reproduced with permission from reference.[108]

1.3.2. Particle contacts

For a CPC to be conductive, the created electrical filler network need to transfer electrons between the fillers throughout the whole volume of the composite. The limiting factor in this electron transport is the contact between the individual filler particles. The intrinsic resistance of the fillers is typically orders of magnitude lower than the contact resistance.[111] Understanding how the filler-filler contacts impact the electrical conduction between them, is crucial to predict and to design the conductivity of CPCs.

Role of contact points

As the filler is dispersed within the non-conductive matrix, the contact between two fillers often is hindered by a layer of matrix material in between them.[53] Therefore, true physical contact is rare and more often the particles only come in close contact with each other. Although not directly in contact, electrons can be transported from one particle to another by two different processes: electron tunneling and electron hopping. Tunneling describes the effect of electrons passing a small gap off insulating material between conductive media.[112] The conductivity σ_{DC} reached by electron tunneling can be expressed as:

$$\sigma_{DC} \propto e^{(-A \cdot D)} \tag{1.2}$$

where A is the tunnel parameter and D the tunneling distance.[53] The interparticle distance plays an important role, since the achievable conductivities decrease exponentially with increasing gap distance. Therefore, tunneling is dominating for small distances. Hopping describes electron transport via multiple intermediate steps. These steps are facilitated by a change in the redox state of the intermediate state. These small electron "hops" make this process more dominating for larger distance transport.

The type of interparticle contacts is for both cases important in determining the final conductivity of CPCs. As shown in Figure 1.8A-D, different filler types exhibit different types of contacts. As spherical fillers typically show point contacts, rod-like fillers can additionally align in parallel exhibiting linear contacts. Plates or flakes can overlap to a certain degree and create area contacts, while more complex fractal fillers show multiple contact points. In a recent work, Perius *et al*. investigated the impact of contact resistance on the electrical conductivity of spherical silver-PDMS composites.[23] They found that, when increasing the filler concentration (36 to 53 vol.%), the contact resistance drops by several orders of magnitude by increasing the contact spot diameter.[23]

Contact points under deformation

As interparticle contact spots are dominant for electrical conduction in CPCs, their behavior when deformed is determinant for the performance in flexible or stretchable electronics. Jin *et al*. used coarse-grained molecular statics simulations to investigate the change in CNT networks under strain deformation.[113] They found that during applied strain some CNT bundles break by individual CNTs sliding apart from each other.[113] Another type of network deformation was proposed by Lee *et al*. for metallic nanowire meshes.[114] Here, the network itself had a certain degree of stretchability resulting from the mesh structure of the nanowire connections (see Figure 1.8E). A less dense mesh, as obtained with higher aspect ratio wires, allowed for more intrinsic stretchability.[114] This deformation concept is similar to Kirigami structures that have been used on a macroscopic level to create stretchable conductors.[115, 116]

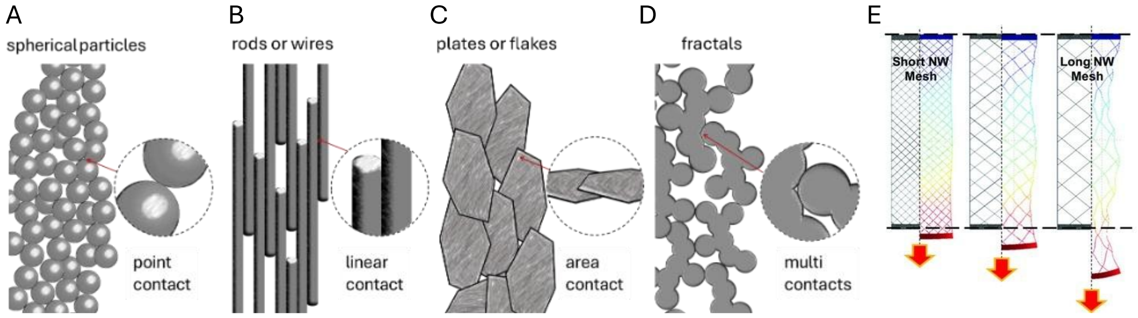

Figure 1.8. Contact situation of A: spherical particles B: rods or wires C: plates or flakes and D: fractal structures. E: COMSOL simulations of metallic nanowire meshes with increases length of the nanowires. Colored parts indicate the deformation under tensile load (indicated by the red arrow). Reproduced with permission from reference.[114]

One can imagine that point contacts under deformation switch between contact or no-contact configuration. Fillers that are rod or flake like, however, since they exhibit larger contact area per contact, deformation does not lead to an immediate disconnection of the contact. This may result in a sharp (point) or progressive (are) change in electrical conductivity among deformation.

1.4. Mechanical Properties

The inherent mechanical properties described above for the matrix materials are strongly affected by the presence of filler particles and the structure of the network that they form. This section focuses on how the mechanical properties are determined by the filler materials and their interactions with the matrix. The effect of fillers on the mechanical reinforcement of polymers, was already investigated early on for fiber enhanced polymers. The reinforcement mechanism was attributed to the synergistic effects of stiff fibers and surrounding polymer matrix.[117] There are two phenomena in composites that are observed under mechanical deformation, the Payne effect and the Mullins effect, both named after the main contributors of their understanding.[118, 119] The Payne effect describes non-linear behavior under increasing dynamic strain oscillation. This manifests as a decrease in storage modulus as the strain deformation is increased (see Figure 1.9A).[120] This behavior is independent of the degree of matrix crosslinking indicating that the main contributor is the filler-filler and the filler-matrix interactions but not the matrix itself.[121] This was confirmed by recent studies[122] and the Payne effect is often related to mechanism like deagglomeration of fillers,[123] reorganization of the filler network,[124] or matrix chain desorption from the filler surface.[125] If the Payne effects describes the decrease of modulus in dynamic oscillation, the Mullins effect describes the stress-softening under continuous cyclic strain deformation. In a nutshell, stress-softening refers to a reduced stress response after the first loading and unloading cycle in a uniaxial tensile test measurement.[126] Subsequent cycles create a hysteresis loop caused by partial destruction of the materials structure (see Figure 1.9B).[126] This is especially important to consider for strain sensors, since the mechanical signal would not be constant for the first cycles.[127] Stress-softening was reported for both filled and unfilled polymers, however, unfilled polymers only exhibit this effect if they can crystallize.[128] The mechanisms causing the stress-softening are not fully understand yet, but common hypotheses include the rupture of weak (physical) bonds,[129, 130] chain slippage,[131] or network rearrangements.[132]

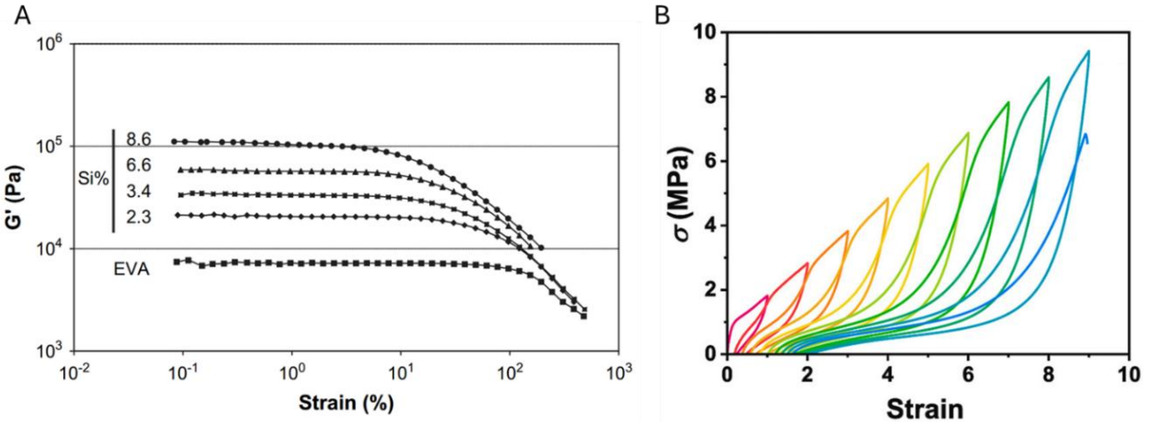

Figure 1.9. A: Strain dependence of the storage modulus for composites containing different amounts of fumed silica in an ethylene and vinyl acetate (EVA) copolymer. Adapted with permission from reference.[133] B: Stress-strain curves for a butadiene rubber vulcanizate containing 17 vol.% silica particles. Adapted with permission from reference.[134]

The mechanical properties of a composite are influenced by the incorporation of filler particles. Their size, aspect ratio, and dispersion state are important parameters that determine the extent of this property change.

Particle Size

Smaller particles, as they have a higher surface-to-volume ratio, typically increase the elastic modulus of a composite, since the larger surface allows for more interaction points with the matrix.[135] The important parameter in that case is the surface area of the filler. If the particles are too small, however, they tend to form agglomerates, which reduce the effective surface area exposed to the matrix, reducing the reinforcement effect. This is because larger structures within the composites are more prone to accumulate stresses and initiate cracks.[135] A decrease in modulus with decreasing particle size was shown for silica particles below 100 nm in a polyimide matrix.[136] For particles >1 µm it was reported that the elastic modulus remains independent of the particle size.[137]

Aspect ratio

The aspect ratio of the filler particles plays an important role in the load transfer of the composite. High aspect ratio fillers typically improve stress distribution due to their high surface area.[135] This results in composites with higher elastic modulus and reduced stretchability compared to composites made with lower aspect ratio fillers.[138] Such effect has been reported for MWCNTs in an epoxy matrix with a weight fraction of 0.5 wt.%.[139] An aspect ratio of 455 induced an elastic modulus of 3.4 GPa while an aspect ratio of 1000 increased the modulus to 3.6 GPa. At the same time the strain at break reduced from 300 to 270%, respectively.[139]

For fillers with high aspect ratio, their orientation within the composite alters the mechanical properties depending on the direction of applied deformation.[140] This leads to an increased elastic modulus parallel to the alignment and a reduced elastic modulus when deforming perpendicular to the direction of alignment. In general, a higher degree of orientation causes a higher degree of stiffness. For randomly oriented fibers, the composite exhibit isotropic properties and, therefore, reduced elastic modulus compared to aligned fibers, if elongated in direction of alignment.[141]

Filler Dispersion

A good dispersion of the filler within the matrix is a key factor for a strong mechanical reinforcement.[142] A uniform distribution of the fillers ensures a homogenous load transfer through the composite under mechanical stress. This means that every filler experiences the same stress and no stress concentration points are created. In bad dispersions, the fillers form agglomerates, which are often points of stress concentration, increasing the probability of crack formation and failure.[135] A good or bad dispersion depends strongly on the filler-matrix interactions. If they are high, the fillers tend to disperse better in the matrix, allowing for multiple interaction points. It was shown that if silica particles of a composite were functionalized to match the affinity with the matrix, the elastic modulus increased from 2.4 to 3.5 GPa for the same fixed volume fraction of 5 vol.%.[136] The case of weak filler-matrix interactions lead to filler detachments, defects, or reduced mechanical strength.[143]

1.5. Trade-off: Electrical conduction and mechanical flexibility

A CPC to be used in the field of stretchable and flexible electronics should provide a certain degree of conductivity and be stretchable and bendable. Adding a stiff filler particle into a flexible, polymeric matrix enhances certain mechanical properties, for example toughness, stiffness, or tensile strength. However, other mechanical properties deteriorate with the addition of filler particles, for example the elongation at break. Therefore, the filler content must be carefully optimized to preserve favorable mechanical performance. It has been reported that the elongation at break for MWCNTs and graphene platelets in an epoxy matrix decreases from 3.5% in neat epoxy resin to 2 and 1.5%, respectively, when adding 1 vol% of each filler.[144] This enhancement of mechanical properties with increasing filler loading has, however, a limit. At very high filler loadings, the tendency of the fillers to agglomerate increases and, therefore, the composite strength decreases.[145] Additionally, the packing density increases and the inter particle distance between the fillers decreases, leading to a higher number of defects or voids (see Figure 1.10A).[146] These defects are failure points in the composite, resulting in deteriorated mechanical properties. For instance, in CB/PP composites, it was reported that an increase of CB over 40 wt.% led to a decrease in tensile strength and elastic modulus.[147]

Conductivity is an important parameter for stretchable electronics, which typically increases with filler concentration in a composite. To obtain high conductivity, concentration needs to be high, which increases mechanical strength and reduces stretchability. This is the trade-off and the biggest weakness of composite materials, to adjust their mechanical properties by the concentration of the filler. Chodak *et al.* studied the effect of CB in PP. They found that an increase in electrical conductivity at the percolation threshold is concomitant with a decrease in the elongation at break. This highlights the interplay that an increased electrical conductivity usually goes along with reduced stretchability and increased stiffness (see Figure 1.10B).[148]

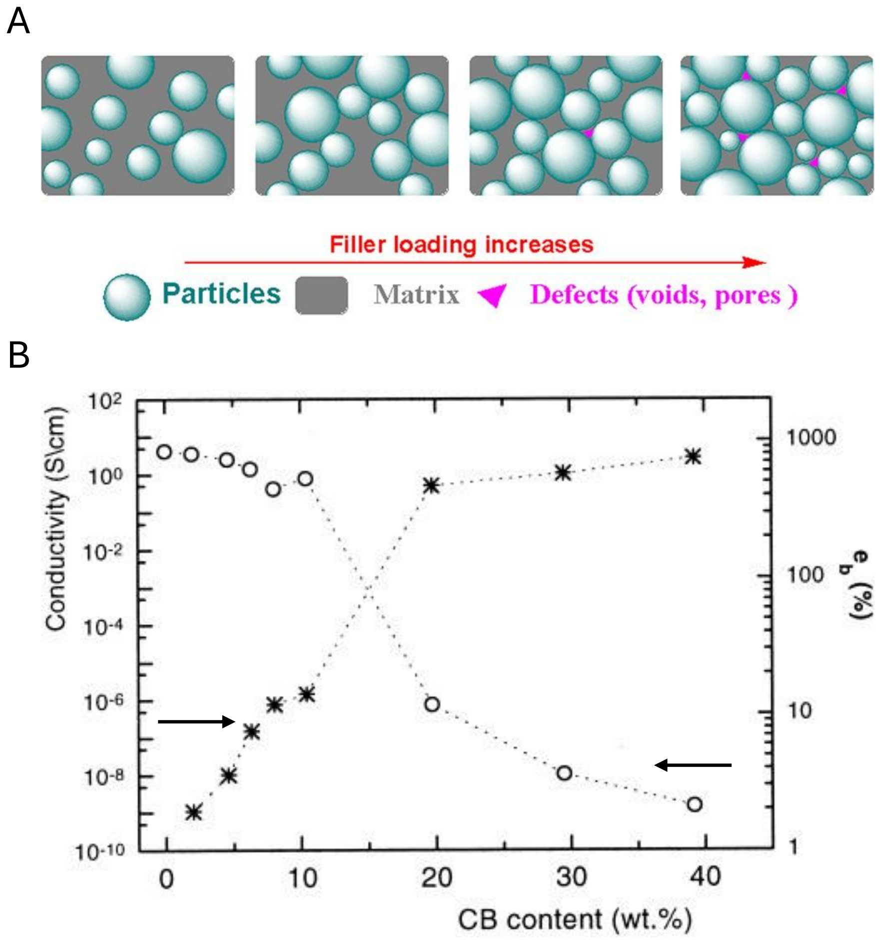

Figure 1.10. A: Schematic representation of void formation with increasing amount of filler particles. Reproduced with permission from reference.[146] B: Conductivity (stars) and elongation at break (open circles) as a function of CB concentration for a CB/PP composite. As concentration increases, conductivity increases, but, at the same time, the elongation at break decreases, showing the trade-off between electrical and mechanical properties. Adapted with permission from reference.[148]

Determining the conductivity under rest conditions and mechanical properties in elongation experiments are important to characterize conductive polymer composites (CPCs). However, their final performance as flexible and stretchable conductor depends on the combined electromechanical properties, i.e., the change in electrical properties among mechanical deformation. This includes the change in conductivity during cyclic strain deformation as well as time-dependent relaxation processes.

An important parameter, especially for stretchable sensors, is the so-called Gauge Factor (GF). It describes the change in resistance depending on an applied strain and is calculated according to Equation 1.3:[149]

$$GF = \frac{\Delta R}{R_0} \cdot \frac{1}{\varepsilon} = 1 + 2\nu + \frac{\Delta \varrho}{\varrho_0} \cdot \frac{1}{\varepsilon} \qquad (1.3)$$

Where ΔR is the change in resistance, R_0 is the initial resistance, ε is the applied strain, ν is Poisson’s ratio, $\Delta\varrho$ the change in resistivity, and ϱ_0 the initial resistivity. The Poisson’s ratio describes the ratio between the transverse (ε_t) and the longitudinal (ε_l) strain during uniaxial deformation according to Equation 1.4:[150]

$$\nu = \frac{\varepsilon_t}{\varepsilon_l} \qquad (1.4)$$

Adjusting the GF for CPCs is of relevance to realize either very sensitive sensors (high GF) or stable interconnects (low GF). Many studies focused on deriving universal correlation to the GF. In the work of Garcia *et al.*, two correlations were reported. First, a relationship between high conductivity values in the unstrained composite and low GF values. Second, the study found that the GF of graphene-loaded polysiloxane composites decreased with increasing filler concentration.[151] A similar trend was recently reported for composites of silver-coated copper particles and an acrylic emulsion. It was shown that the GF at particle loadings of 40 wt.% was one order of magnitude higher than the one at the highest measured particle concentration of 75 wt.% (272 vs. 22, respectively).[152] Higher values of GF are often observed for concentrations close to the electrical percolation threshold.[151] The electrical network at this concentration regime is only based on a few conductive paths, making it sensitive to any changes in the particle contacts. Another influencing factor was reported by Aviles *et al.* who observed a correlation between higher modulus of graphene and CNT composites and higher GFs.[153]

The change in resistance during uniaxial deformation has been reported for many different composite systems.[154] This resistance change is not always ideal, i.e., exactly following the applied strain deformation (see Figure 1.11A). Yang *et al.* investigated the electrical signal of uniaxial tensile tests of CNT/graphene fillers in silicone.[155] Cyclic tests always showed a shoulder peak after maximum strain deformation, regardless of the applied strain. They proposed the viscoelasticity of the matrix as reason for this behavior and performed relaxation tests to confirm this. As shown in Figure 1.11B, the relaxation times after strain deformation was increased with every cycle. While with the shortest relaxation times no secondary peak was observed, at longer relaxation times, the magnitude of the peak was increasing.[155] Mersch *et al.*, performed uniaxial tensile tests on commercially available carbon-filled silicone yarn and measured force and electrical resistance.[156] They observed a non-ideal resistance response for cyclic deformation and relaxation tests. Besides viscoelasticity of the matrix, they proposed that the combination of longitudinal extension and transversal contraction is an additional driving force to create these electromechanical features.[156]

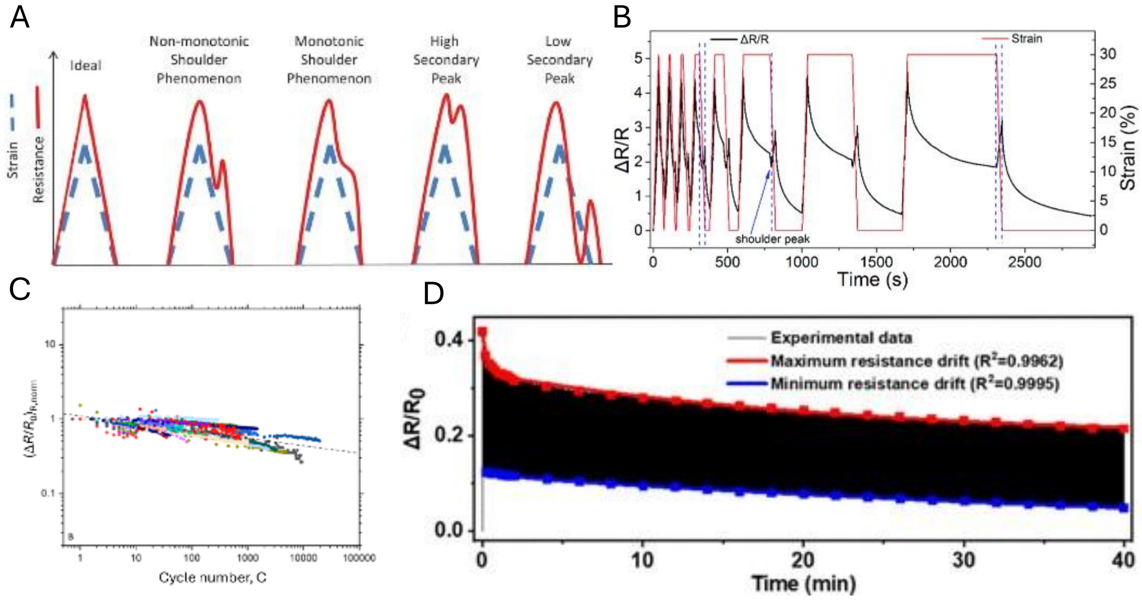

Figure 1.11. A: Different resistance responses observed in CPCs under uniaxial strain deformation. In the ideal case, the electrical signal is congruent to the applied strain profile. Any distortion of the signal is considered non-ideal and originates from several reconfiguration processes within the composite. Reproduced with permission under creative commons license CC BY from reference.[156] B: Change in resistance for CNT/graphene silicone rubber composite after an applied strain of 30% hold for a different amount of time. In shorter time scales the second peak is reduced compared to longer relaxation times. Reproduced with permission from reference.[155] C: Normalized fractional change in resistance as a function of the cycle number for multiple different CPC composites. The dotted line denotes a power law fit according to the relation $(\Delta R/R_0)_R \propto C^{-0.1}$. Adapted with permission from reference.[157] D: Change in resistance as a function of time for a CB/CNT/TPU composite during 2000 cycles between 0 and 5% strain. Red and blue lines are fits according to the Maxwell-Wiechert model. Reproduced with permission from reference.[158]

To create electronic devices, the electrical signal response upon mechanical deformation needs to be reliable and stable over many cycles of loading and unloading. Long-term cycle stability is, therefore, an important performance test for CPCs. In the comprehensive work of Boland, the global trend of resistance change with cycle numbers was investigated. It was found that CPCs in general decay over cycle number according to a power law with the exponent of -0.1 (see Figure 1.11C).[157] A similar was reported by Zhang et al., when a CB/CNT in TPU composite underwent

2000 cycles of 5% strain deformation.[158] They successfully applied the Maxwell-Wiechert model described for polymer relaxations to the resistance relaxation in the composite (see Figure 1.11D).[158] Although this model does not describe mechanistically the Mullins effect it indeed does capture the changes of the material due to stress-softening under repeated uniaxial deformation, visible as an exponential decay of the peak resistance values over time.

While many different CPCs have been designed that cover a broad range of electrical and mechanical properties, ranging from stable conductors to sensitive strain sensors, the main limitations of solid composites cannot be overcome. These include the reduced stretchability at higher filler loadings, requiring more complex and advanced fabrication methods to tackle it. The following section addresses concentrated suspensions and how their properties offer opportunities to create truly soft conductors.

1.6. Concentrated suspension

In the previous sections, solid composites alongside their electrical and mechanical properties were discussed. Those composites are limited by the trade-off between electrical and mechanical properties, especially at higher filler loadings, where the composites tend to become brittle. Brittleness typically leads to spontaneous failure under load, making the material non suitable for soft electronics. Our approach is the use of conductive particle suspensions. Using fluids as matrices allows the material to be put into any desired shape by encapsulating, making the maximum elongation solely dependent on the encapsulant material. Additionally, the ability to reconfigure allows the fluid to sustain deformation and return to its original shape, avoiding risks of breaking and reducing fatigue. As electrical conductivity is desired, the fillers need to come into sufficiently close contact to allow electron transport through the whole volume, i.e., they need to form an electrically percolating network as was the case in the CPCs. In that sense, concentrated, conductive suspensions can be seen as liquid composites.

As particles interact with each other and with the surrounding, the mechanical properties of the suspension change due to these interactions. One of these properties is the viscosity.[159] Depending on the concentration of the particles, different regimes of suspensions are distinguished. In the dilute suspension regime, typically at filler volume fractions $\phi < 0.01$, the concentration is so low that the particles are not interacting with each other.[160] The viscosity is described as a linear function of filler concentration, originally predicted by Einstein in the form of Equation 1.5.,[161]

$$\eta_R = 1 + 2.5\phi \tag{1.5}$$

where η_R is the relative viscosity (ratio of the suspension viscosity and solvent viscosity) and ϕ is the filler volume fraction. At higher filler concentrations, the semi-dilute regime starts ($0.01 < \phi < 0.1$). In that regime, particles start to interact with each other resulting in an exponential increase of viscosity with increasing filler concentration, which was described by the model of Krieger & Dougherty (see Equation 1.6),[162]

$$\eta_R = \left(1 + \frac{\phi}{\phi_{max}}\right)^{-2.5\phi_{max}} \tag{1.6}$$

with ϕ_{max} being the maximum packing fraction. The reason for this change in scaling is the increasing probability of collision between particles with increasing filler concentration.[160] Every collision of two particles creates friction, which acts against the flow field, increasing the resistance towards flow, i.e., the viscosity (see different models in Figure 1.12A).

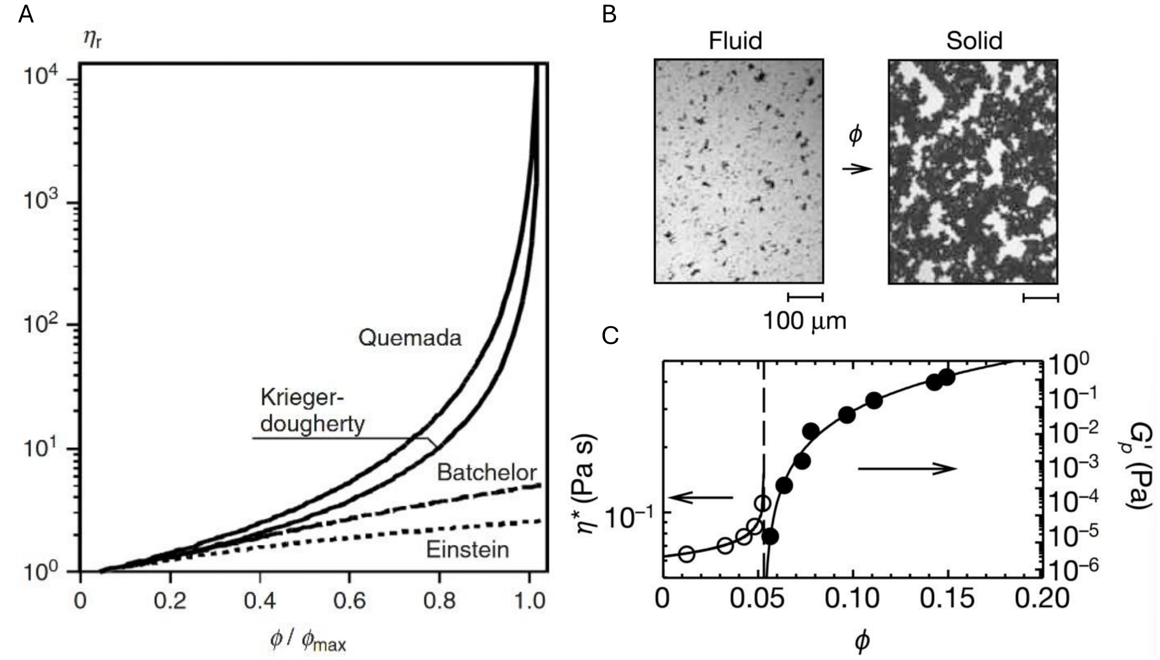

Figure 1.12. A: Relative viscosity (ratio of suspension viscosity and viscosity for $\phi = 0$) as a function of filler concentration according to different rheological models. Models by Einstein and Batchelor predict a linear relationship, while newer models of Krieger & Dougherty or Quemada predict an exponential increase due to the increasing inter particle interactions. Reproduced with permission from reference.[163] B: Light microscopy images of a CB-mineral oil suspension at low and higher filler concentration. C: Complex viscosity and storage modulus as a function of the filler concentration. The jamming transition is defined at the concentration where the viscosity diverges to high, and the storage modulus to low values. Both reproduced with permission from reference.[164]

At even higher concentrations ($\phi > 0.1$), the regime of concentrated suspensions is reached. At this point, particles are packed densely enough to induce a transition from viscous liquid behavior to viscoelastic solid behavior (see Figure 1.12B). This transition is often described as a jamming transition.[164] Trappe *et al.* proposed that this transition manifests at a concentration where the zero-shear viscosity diverges infinity and an onset of elasticity is observed (see Figure 1.12C).[164] This onset is quantified by the storage modulus, *G'*, which is a measure of the elastically stored energy in the material and, hence, only defined if the material is in a solid-like state. This is mediated by the formation of a stress-carrying particle network, creating a gel-like material. This gel is maintained by physical interactions instead of chemical ones, allowing a certain degree of reconfiguration under deformation. This regime, in which the particles are in close contact forming a 3D network, is the most promising scenario for creating conductive suspensions and is, therefore, discussed in detail below.

1.6.1. Formation of particle gels

Particle gels are based on physical network formation. This means that the bonds between the particles are created by van der Waals forces, which are reversible[165] and may change under external stimuli. The formation of a particle network is a function of agglomeration of dispersed particles, of the volume fraction of the particles, or a combination of both.[166] If the particle concentration is low, network formation is governed by agglomeration. To describe this agglomeration behavior, different mechanisms were proposed. Diffusion limited colloidal aggregation (DLCA) and reaction limited colloidal aggregation (RLCA) are both based on the particle-particle interaction and the collision probability. In DLCA, the attraction of the particles is assumed to be high, and a collision of two particles always leads to a bond with infinite bond strength. That means that the cluster formation is irreversible. The resulting clusters exhibit a fractal dimension of 1.85, meaning they are more open structured (see Figure 1.13A).[167] In RLCA, not every collision results in a permanent bond between particles. In fact, multiple collisions are necessary until a bond is formed, leading to a higher fractal dimension (2.1) and more compact clusters (see Figure 1.13B).[167] The aggregation process is slower compared to the DLCA mechanism. Although these mechanisms were already successfully used to explain aggregation phenomena in different colloidal systems (gold, silica, or polystyrene)[167] the assumption of infinite bond strength doesn't explain time dependent properties like relaxations.[168, 169] For a system of particles in a fluid matrix, in which the particles are able to reconfigure after mechanical deformation, non-finite bond strength is an important parameter to be considered.

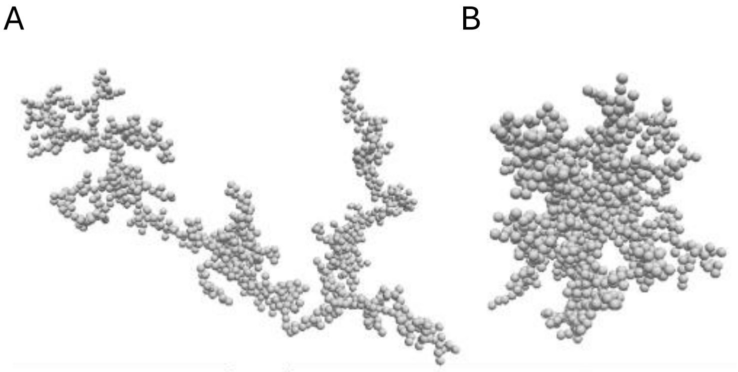

Figure 1.13. Schematic representation of aggregates formed by A: DLCA, and B: RLCA mechanism. Reproduced with permission from reference.[170]

The introduction of finite bond strength, meaning the formed bonds can again be broken, was considered with the reversible diffusion limited colloidal aggregation (RDLCA) model. With this, relaxation processes can be described due to cluster reconfiguration.[169] While these models are more affected by the aggregation kinetics, especially important in diluted systems, other concepts to describe the gel formation from a random percolation point of view (analogously to the electrical percolation) have been discussed. One of those is the elastic percolation model. Based on the site percolation model (as discussed in subsection **1.3.1 Network formation**, now each connection between two particles gets assigned an elastic contribution. This contribution is described either by only an elastic spring (central-force (CF) model)[171] or by an additional bending contribution, that allows the bonds to stretch and bend (bond-bending (BB) model).[172]

A particle gel with the particles being in contact with each other can be defined as a jammed state. These particle contacts create a solid-like material behavior that is characterized by a yield stress.[169] A yield stress is the minimum stress that needs to be applied to this material so it starts flowing, exhibiting liquid-like properties characterized by the loss modulus G''.[159] A conventional way of defining a particle gel is by its mechanical properties. If the storage modulus surpasses the loss modulus the material exhibits solid-like behavior pointing to a network of connected filler particles in the matrix.[173]

1.6.2. Rheology of particle gels

The addition of particles into a fluid has a significant impact on the flow properties related to the interactions of particles with each other and the surrounding liquid. Imagine a Newtonian fluid, which exhibits an independent viscosity of the applied shear rate, and add insoluble particles into it. Within the dilute concentration regime, the suspension still behaves as a Newtonian liquid, since the concentration of particles is so low, that they are not interacting with each other. The resistance against the flow is only on a single particle level. With increasing concentration, in the semi-dilute regime, the particles start to occasionally interact with each other, causing additional resistance against deformation. At this point, the flow behavior changes from Newtonian to shear-thinning: with increasing shear rate the viscosity decreases. Further addition of filler particles enhances the shear-thinning effect and, eventually, leads to the so-called yield stress fluid, which exhibits solid-like behavior and only flows if a stress larger than the yield stress is applied.[159] A very high particle concentration may lead to additional effects, like shear-thickening: at high shear rates the viscosity increases due to increasing contacts between the particles.[174]

Besides changes in the flow behavior, the addition of particles induces viscoelastic properties to suspensions. Viscoelasticity combines solid-like properties (elasticity), with liquid-like properties (viscosity). Elastic components are quantified by the storage modulus *G’*, as a measure of elastic energy stored within the material. Viscous contributions are quantified by the loss modulus *G”*, which describes dissipated energy. Upon deformation, these contributions are commonly modeled as either a Hookean spring (elastic, solid) or a Newtonian dashpot (viscous, liquid), respectively. As both only describe ideal elastic or viscous behavior, many materials are not solely described by these simple models. Especially, concentrated particle suspensions, due to their filler-filler and filler-matrix interactions, exhibit more complex, viscoelastic behavior. Different combinations of springs and dashpots have been used to model a more realistic response of such complex materials. Combining a spring and a dashpot in series (see Figure 1.14A) forms a Maxwell element which describes materials that behave like liquids flow continuously. In contrast, placing a spring and a dashpot in parallel (see Figure 1.14B) creates a Kelvin-Voigt element, which represents solid-like materials where viscous flow is limited by elastic contributions (spring).[175]

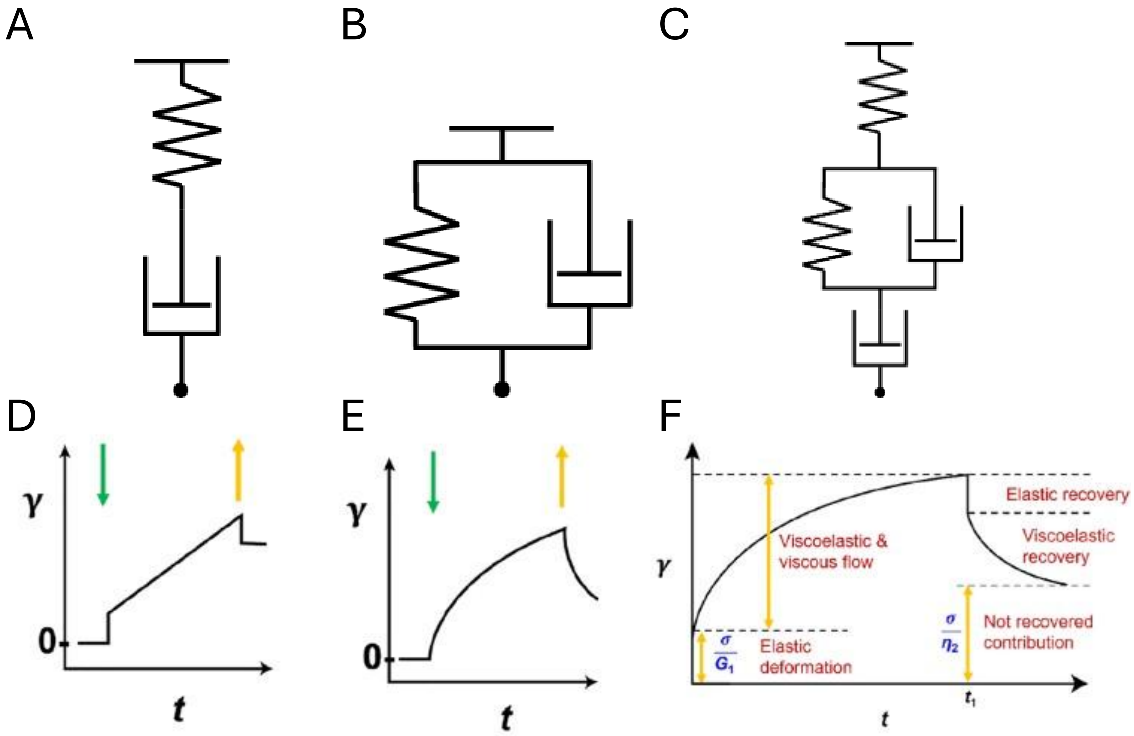

Figure 1.14. Spring-dashpot models to describe viscoelastic behavior. A: Maxwell-model. It consists of a spring and a dashpot in series and describes well viscoelastic liquid like behavior, since the dashpot deforms permanently without an option for recovery. B: Kelvin-Voigt model. It consists of a spring and a dashpot in parallel. This model describes well a viscoelastic solid material, since any deformation of the dashpot is gradually recovered by the spring that pushes back the dashpot. C: 4-element or Burgers model. Represents a combination of a Maxwell and a Kelvin-Voigt element allowing to describe instant elastic deformation (first spring), viscoelastic recovery phenomena (Kelvin-Voigt element), and permanent deformation (last dashpot). D: Strain response after applying (green arrow) and removing (yellow arrow) stress according to the Maxwell model. E: Strain response after applying and removing stress according to the Kelvin-Voigt model. F: Strain response after applying and removing according to the Burgers model. Panel D-F were adapted with permission under the creative common license BY-NC-ND 4.0 from reference.[175]

If a finite stress is applied, the Maxwell model describes well the immediate elastic strain response by the spring element, followed by a continuous linear response from the dashpot. The deformation of the dashpot after stress removal is irreversible in this model. As in the Kelvin-Voigt model the spring and dashpot elements are in parallel, no instantaneous elastic response can be described, however, non-linear viscoelastic response can be modeled. Upon stress release, the spring element forces the dashpot back into its initial position creating a reversible model. Since none of these models is ideal to describe the complete strain response, further combinations have been proposed. A versatile model used to describe viscoelastic behavior is the Burgers model (also called 4-element model, see Figure 1.14C). As it combines both, Maxwell and Kelvin-Voigt elements, the proper modeling of instantaneous deformation and viscoelastic retardation and relaxation can be done accurately, for example, from a creep recovery test, i.e., constant stress over time with subsequent stress removal.[175] This test is key to distinguish between viscoelastic solids and viscoelastic liquids. If the material recovers 100% of the imposed strain deformation, it means that the elastic components dominate and return back to their initial configuration. Contrary, an incomplete recovery of strain implies that some energy was losses in viscous deformation, typical for a viscoelastic liquid material.[174] This model has been successfully applied, for example, to describe the mechanical properties of PP, [176] or in double percolation systems of CB in a melt blend of polystyrene (PS) and polymethylmethacrylate (PMMA).[177]

1.6.3. Conductive Suspensions

In suspensions with conductive particles, their interactions create both electrical and mechanical networks, which are determinative for their electromechanical properties. These networks may, but not necessarily, form at the same filler concentration. Despite its relevance, studies on electrical and mechanical network interplay are limited. In the comprehensive work of Penu *et al.*, the authors distinct between the electrical percolation, rheological percolation, and rigidity percolation in polymer melts filled with MWCNTs.[178] Both rheological and rigidity percolation are based on mechanical properties. While rigidity percolation refers to the creation of a stress-carrying network, rheological percolation may occur at lower filler concentration due to interactions between the MWCNTs and the polymer coils.[178] Indeed, a lower rheological percolation than electrical percolation was found for several filler/polymer systems including CB-polyethylene (7.58 wt.% and 10.61 wt.%, respectively)[179] and reduced graphene oxide-polystyrene-co-acrylonitrile (0.1 vol.% and 0.17 vol.%).[180] As rheological percolation is mediated by polymers between the particles that create a soft connection between them, it can occur before electrical conduction. In the work of Richards *et al.*, the electrical and mechanical networks of a carbon black suspension in propylene carbonate (PC) was investigated.[181] They reported an electrical percolation threshold as low as 1 vol.% compared to a mechanical percolation threshold of 23 vol.% in a CB-PC suspension.[181] This discrepancy may be explained by the non-polymeric solvent that was used in their case, which prevents mechanical interactions of the polymers. They, additionally, observed that under shear flow, the electrical conductivity only decreased marginally, although the shear force was sufficient to overcome the particle attraction. A stress-carrying network is, therefore, not a requirement for electron conduction, which is dominated by non-contact mechanisms like electron tunneling or hopping.[181]

Although the understanding of particle networks in suspensions was topic in some studies, their application as soft electronic components is barely investigated. Flow batteries, which utilize liquid electrolytes as conductors, are currently an active area of research. Parant *et al.*, dispersed carbon black in a mixture of water, alginate, and arabic gum as stabilizers.[182] They measured the conductivity of the suspension while pumping it through a syringe to simulate flow conditions.[182] Independent of the applied flow rate, the suspensions remained conductive. Higher CB loadings (7.5 wt.%) showed constant conductivity while lower concentrations were affected by the flow and reduce conductivity with increasing flow rate.[182] The integration of conductive suspensions into flexible and stretchable electronics is barely exploited. In the work of Wang *et al.*, they used silver flakes in viscoelastic liquid-like polymer matrix based on polyethylene glycol.[183] Mechanical stability in the matrix is achieved by hydrogen bonds between the polymer chains, allowing for reconfiguration under mechanical deformation. Under continuous deformation, the silver flakes migrate towards the surface of the suspension, increasing the local filler concentration and conductivity. Printing onto an elastic substrate as well as encapsulating into an elastic tape were demonstrated to create electric circuits that can be implemented into wearables to monitor, for example, the movement of a human finger.[183] Nevertheless, this viscoelastic conductor achieved its best performance only after several cycles of deformation, when the silver flakes structurally assembled at the interface between encapsulant and material, creating an irreversible structure.

The electrofluids proposed in this thesis are composed of conductive, carbonaceous filler particles dispersed in a liquid matrix. After reaching the percolation threshold, the electrofluids exhibit electrical conductivity and maintain it due to transient particle contacts. These non-permanent interaction points allow the structure to adapt and reconfigure, creating reversible properties. The underlying mechanism of dynamic particle contacts maintaining electrical networks remains unexplored in existing literature.

2. Open questions

Despite significant progress in the field of soft electronic materials, the potential of highly concentrated particle suspensions as alternative soft conductors remains mostly unexplored. To address this gap, this thesis introduces *Electrofluids* as a novel class of liquid electronic components. Building on this concept, the following section outlines key questions concerning their electrical and mechanical properties, aiming to clarify the fundamental principles that govern their performance and assess their suitability for future applications in soft electronics.

Topic 1: Electrical and mechanical network formation and interplay in electrofluids.

A fundamental requirement for electrofluids is the creation of an electrical network through conductive filler contacts. In highly concentrated suspensions, achieving this level of connectivity might imply the development of a mechanical network in return. The choice of filler and solvent is, therefore, critical, as it governs the interactions of these networks. Moreover, their interplay is anticipated to be a dominant factor influencing the electromechanical properties of electrofluids. A comprehensive understanding of these network structures and their interactions has been lacking and is addressed in this thesis.

Topic 2: Requirements for electrofluids as strain sensors and stable conductors.

Electrofluids can only be considered viable materials for flexible and stretchable electronics if their properties can be tailored to satisfy the specific requirements of targeted applications. This thesis addressed the critical question of material selection and design strategies necessary to develop electrofluids that function effectively as strain sensors and stable conductors.

Topic 3: Strategies to reduce percolation thresholds in electrofluids

Minimizing the amount of conductive filler required to achieve electrical percolation is desirable not only for economic reasons but also for processing considerations, as higher filler loadings typically lead to increased material stiffness. This thesis explores the effectiveness of volume-exclusion strategies to optimize conductivity while preserving material flexibility.

3. Electrofluids with tailored rheoelectrical properties: liquid composites with tunable network structures as stretchable conductors

This chapter is based on the content of the article:

Schmidt, Dominik S., Tobias Kraus, and Lola González-García. "Electrofluids with Tailored Rheoelectrical Properties: Liquid Composites with Tunable Network Structures as Stretchable Conductors." ACS Applied Materials & Interfaces 16.33 (2024): 43942-43950.

https://doi.org/10.1021/acsami.4c07230

3.1. Abstract

Flexible and stretchable electronics require both sensing elements and stretching-insensitive electrical connections. Conductive polymer composites and liquid metals are highly deformable but change their conductivity upon elongation and/or contain rare metals. Solid conductive composites are limited in mechanoelectrical properties and are often combined with macroscopic Kirigami structures, but their use is limited by geometrical restraints. Here, we introduce “Electrofluids”, concentrated conductive particle suspensions with transient particle contacts that flow under shear that bridge the gap between classic solid composites and liquid metals. We show how carbon black forms large agglomerates when using incompatible solvents that reduce the electrical percolation threshold by one order of magnitude compared to more compatible solvents, where CB is well-dispersed. We analyse the correlation between stiffness and electrical conductivity to create a figure of merit of first electrofluids. Sealed elastomeric tubes containing different types of electrofluids were characterized under uniaxial tensile strain and their electrical resistance was monitored. We found a dependency of the piezoresistivity with the solvent compatibility. Electrofluids enable the rational design of sustainable soft electronics components by simple solvent choice and can be used both as sensor and electrode materials, as we demonstrate.

3.2. Introduction

Soft electronic materials are from the basis of stretchable sensors,[184, 185] human-machine interfaces,[186] wearables,[187, 188] and implants.[189] Some are ideal conductors that retain their electrical conductivity under mechanical deformation; others are suitable as sensors because their electrical resistance reacts sensitively to pressure,[190] tension,[190] or bending.[191] A common way to assess the sensitivity of a material towards deformation is the Gauge Factor (GF):

$$GF = \frac{\Delta R}{R_0} \cdot \frac{1}{\varepsilon} = 1 + 2\upsilon + \frac{\Delta \varrho}{\varrho_0} \cdot \frac{1}{\varepsilon} \tag{3.1}$$

in which ΔR is the change in resistance, R_0 the initial resistance, ε the strain, v the Poisson's ratio, $\Delta\varrho$ the change in resistivity, and ϱ_0 the initial resistivity. The change in resistance with strain can be divided into the contributions of geometrical changes (based on Poisson's ratio) and the change in intrinsic resistivity (piezoresistivity).

In sensor development, materials with large piezoresistivity are used to reach large GF. In classical semiconductor strain sensors, the contribution of the piezoresistivity exceeds the geometrical contribution by up to 70 times due to changes in their band structure,[192] but they are susceptible towards mechanical fracture at small strains.[193] Conductive polymer composites (CPCs) with conductive filler such as carbon black (CB),[194-197] Carbon Nanotubes (CNTs),[198, 199] graphene,[200] or metal particles[201, 202] in a non-conductive polymer matrix offer, in contrast, a large stretchability.[203] Their gauge factors are dominated by the increasing particle distances under strain and/or crack formations and can be tuned; for example, Zheng et al. reported GF of 15.75 for CB in PDMS[204] and Yang et al. up to 143 in graphene-silicone rubber nanocomposites.[205]

Connecting sensors while remaining overall stretchable requires low strain sensitivity conductors as electrodes. The yield strains of solid metals make it difficult to design such electrodes with them. Encapsulated liquid metals enable strains of up to 1000%[10] but are not exempt of resistance changes due to geometry and exhibit GF similar to solid metals.[206] Kirigami structures inspired by the traditional Japanese paper cutting technique have been used to create macroscopic structures that confer flexibility to rigid components[207] and maintain low GF[208] down to 0.25 as reported for Kirigami-structured graphene sheets at strains between 0 and 240%.[209] Their macroscopic geometry requires tailored designs for each targeted application, complicating integration.

The conductive polymer composite community has also addressed this challenge using different strategies. For example, composites can be patterned to create wavy surfaces[210] or serpentine circuits inspired in the abovementioned Kirigami-structure to achieve ultra-stretchable conductors that retain electrical properties at uniaxial strains over 300%.[211] Another approach, sometimes combined with the previous one, is to use highly anisotropic conductive fillers such as silver nanowires or carbon nanotubes, which reduce the strain sensitivity of the composite in comparison to the use of spherical particles.[103, 212, 213] Cai et al. combine single wall CNTs and a hydrogel matrix based on boric acid that utilizes self-healing properties to achieve gauge factors as low as 0.24 at 100% strain.[214]

A combined strategy uses liquid metal inclusions as conductive filler embedded in elastomeric matrices.[215, 216] Markvicka *et al*. and Tutika *et al*. demonstrated that the dispersion of liquid metal droplets into a PDMS matrix can yield stretchable connectors with minimal changes in resistance value upon deformation.[17, 217] Initially, the composite is electrically insulating since the liquid metal droplets are in contact through an oxide layer. Under local pressure, particles coalesce, forming a continuous conductive path. Upon mechanical deformation or severe damage, these composites have shown autonomous self-healing since the remaining discrete particles rupture and coalesce, reducing the change of the electrical resistance and achieving negligible GFs.

Silver flakes have been demonstrated to reduce the electrical sensitivity during strain since they can reconfigure and slide during the mechanical deformation, retaining the electrical conductivity of the filler network.[218, 219] Recently, Wang *et al*. reported an electronic interconnect based on silver flakes in a viscoelastic polymeric matrix.[183] The liquid mixture was encapsulated in a stretchable elastomer. During stretching, silver flakes migrated towards the surface, densifying conductive paths and, therefore, increasing conductivity. The structural and electrical changes produced in the composite are, therefore, irreversible. As far as we know, this is the only example of a “liquid” composite reported as soft alternative electronic component; other particle types and the effect of different polymeric matrices remain unexplored.

Here, we demonstrate that microscopic percolating 3D networks of conductive particles can be formed in highly concentrated dispersions that we call “Electrofluids”. Their transient structures were tailored to tune their mechanoelectrical properties for stable conductors or sensors. Carbon black particles were dispersed in solvents with different polarities and viscosities to create the electrofluids. The hierarchical CB with its aggregates of fused graphitic primary particles form weakly bonded agglomerates in the liquid.[213] The aggregates are stiff, but their contacts in the electrofluid agglomerates are transient, allowing electrical connections to constantly reform even when flowing. We show how the electrofluids’ hierarchical microstructure can be tuned by using solvents that lead to different particle-particle and particle-matrix interactions to design the electrofluids’ electromechanical properties. Their rheological and electrical responses under shear and uniaxial strain were investigated and the results were used to prepare conductors with tailored gauge factors. We demonstrate the use of electrofluids in soft robotics and wearables with a sensor-conductor prototype.

3.3. Results and Discussion

Carbon black (CB) is composed of primary particles that fuse into aggregates[220] during production that are visible in transmission electron microscopy (TEM) (Figure 3.1A, see Methods section for details). In dispersion or during drying, weaker van der Waals forces connect the aggregates to agglomerates that are visible in scanning electron microscopy (SEM) (Figure 3.1B)[220]. The overall hierarchical structure of the CB that we used in this work is depicted in Figure 3.1C. Raman spectroscopy showed only characteristic carbon peaks at 1341 cm-1 (D-band) and at 1580 cm-1 (G-band)[221, 222], indicating the graphitic nature of the CB and the absence of functional groups on its surface (see Figure S3.1 in the SI). Such carbon surfaces are hydrophobic,[223] suggesting that the powder will weakly interact with polar solvents and form stable dispersions in non-polar liquids. The polarity of the solvent as well as its viscosity will affect CB agglomeration.

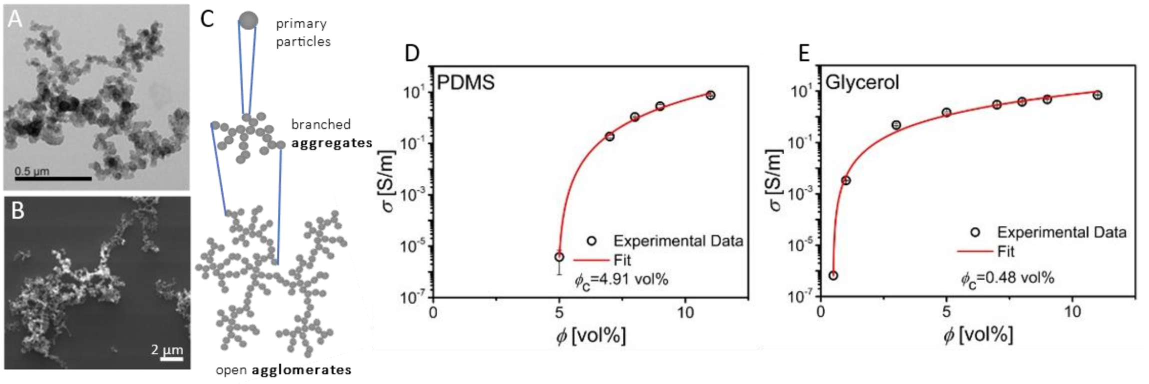

Figure 3.1: A: Transmission electron micrograph of Carbon black (CB) aggregates and its constituent primary particles. B: Scanning electron micrograph of agglomerates formed in ethanol by weakly connected CB aggregates. C: Hierarchical structure of the CB filler. D: Percolation of the mixture CB-PDMS and E: Percolation of the mixture CB-Glycerol. The red lines fit to a classical percolation relation described in Equation 3.2 (more information can be found in Figure S3.2 in the SI).

We prepared CB suspensions – "Electrofluids" – in liquid PDMS, hexadecane, glycerol, and ethylene glycol. Their electrical conductivities at different CB loadings were determined by measuring the electrical resistance in 4-point-probe configuration (details described in the Method section). The percolation threshold (ϕ_c) was then determined by fitting the electrical conductivity σ to

$$\sigma = A \cdot (\phi - \phi_c)^t \qquad (3.2)$$

from classical percolation theory[91], where A is a constant, *f* is volume fraction of the filler, and t is a critical exponent. The percolation thresholds strongly depended on the liquid matrix (Figure 3.1D-E and Figure S3.2 A-B in SI). Percolation in PDMS (Sylgard 184 base) occurred at nearly 5 vol% CB (Figure 3.1D). Silicone-CB mixtures have been extensively studied and are commonly used to create conductive solid composites by cross-linking the PDMS matrix.[224] Carbon-based composites such as our carbon black electrofluid are generally less conductive than metal-based composites due to the lower intrinsic conductivities of carbon.[225] The difference is amplified by the contact resistances between carbon particles (CB, CNTs, graphene flakes, etc.) that are generally higher than that of metal-metal contacts.[226] However, they are of great interest for certain applications, in which electrical conductivity values are less critical, since they are sustainable (metal-free) and cost-effective.[227] The percolation threshold and the conductivities that we found in suspension are in good agreement with the values reported in the literature for the solid composites.[228-230]

All other solvents required less CB for percolation. Hexadecane is non-polar like PDMS but has a lower viscosity ($\eta_{\mathrm{Hexadecane}}$ = 3.34 mPa·s versus η_{PDMS} = 4500 mPa·s) and caused a percolation threshold of 1.43 vol% CB, more than 3 times below that for PDMS (see Figure S3.2A). A reduced percolation threshold for less viscous liquids has already been reported by Rwei et al.[231] and attributed to a higher mobility of the CB that promotes filler reorganization and the formation of conductive pathways.[231] Similar findings were reported by Bauhofer et al. for carbon nanotubes.[232]

Glycerol is closer in viscosity to PDMS (η_{Glycerol} = 1480 mPa·s) but caused percolation at 0.48 vol. % CB, 10 times below PDMS (Figure 3.1E). Glycerol is a small molecule with 3 OH-groups and a high polar moment, while the PDMS Si-O backbone is shielded by methyl groups that confer a hydrophobic character. The CB apparently forms large agglomerates that fill space with a connected network and reduce the percolation threshold in polar solvents.

Synergic effects of viscosity and polarity lent CB in ethylene glycol ($\eta_{\mathrm{Ethylene\ glycol}}$ = 16 mPa·s) the lowest percolation threshold of all studied systems (0.17 vol. %, compare Figure S3.2B). Hexadecane has a similar viscosity but is non-polar, which increased the threshold in comparison to ethylene glycol. The strong role of polarity on CB percolation that we find here has not been reported before. In the following, we will test our hypothesis that large agglomerates of CB aggregates form and strongly promote percolation.

We compared the sizes of CB agglomerates in non-polar hexane and polar ethylene glycol using analytical centrifugation (AC) at relatively low CB concentrations of 0.002 wt. %. Note that the highly viscous liquids PDMS and glycerol make AC cumbersome and imprecise (see Method section for further details) and were not included. Figure 3.2A shows the size distributions with a mean hydrodynamic diameter in hexane of 840 nm. Ethylene glycol caused a bimodal distribution with maxima at 1942 and 6478 nm, indicating the formation of bigger agglomerates of CB. This result is in good agreement with Subramanian *et al.*, who investigated the effect of lignosulfonates on CB dispersibility in water and found that the most hydrophobic lignosulfonates were the best dispersing agents and decreased the mean particle diameter by reducing agglomeration.[233]

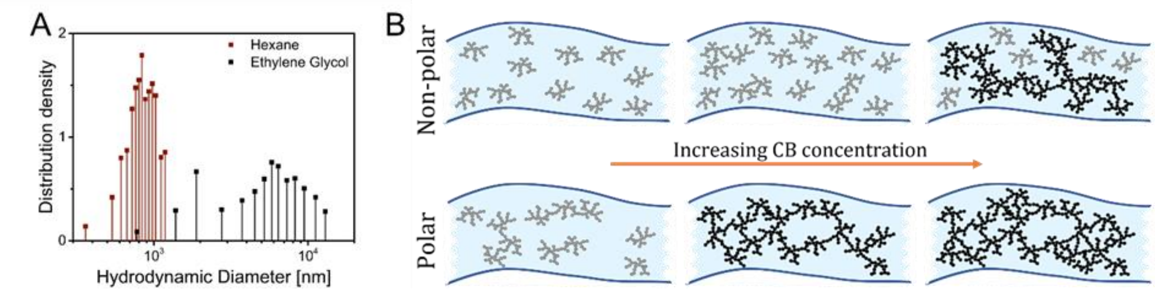

Figure 3.2: A: Size distribution densities of CB dispersed in ethylene glycol and in hexane. B: Proposed CB network formation in polar and non-polar solvents.

Figure 3.2B illustrates the model that we propose for CB network formation based on above results. Electrofluids with low CB concentrations in non-polar solvents contain CB aggregates and possibly small agglomerates with diameters of approximately 1 μm that disperse well in the matrix. The formation of networks at increasing CB concentrations in such solvents is dominated by the random percolation of CB units that collide.

Polar solvents cause stronger attractions between the CB, inducing the formation of larger agglomerates that are several μm in diameter. At very low concentrations, agglomerates cannot span the entire volume. As their concentration increases, they form a percolating network. Agglomeration facilitates percolation because larger agglomerates of CB are more efficient in filling space.

The percolation threshold in non-polar solvents was lower than in polar ones of the same viscosity (cf. hexadecane and ethylene glycol in the SI Figure S3.2A and B). Their percolation thresholds are smaller than those of more viscous solvents of the same polarities because their reduced viscosity facilitate the formation of agglomerates.[231]

Electrofluids combine electrical conductivity with mechanical adaptability. The electrical percolation study presented above confirms the formation of electrically conductive filler networks and the role of solvent polarity on its formation. These results do not provide, however, insight into the mechanical properties of the formed networks, and mechanical and electrical properties of networks do not necessarily overlap.[178] Therefore, we studied the viscoelastic behavior of the electrofluids and characterized the storage modulus *G'* that represents the elastic stored energy and accounts for the stiffness of the material and the loss modulus *G''* that represents the dissipated energy and, therefore, the damping of the material by means of oscillatory rheology. Electrodes were coupled to the rheometer (see Method Section for details) to concurrently measure the electrical resistance of the samples at each strain *in-situ*. The results for electrofluids containing 5 vol. % CB in PDMS and glycerol are shown in Figure 3.3A-B (cf. Figure S3.2A-B in the SI for hexadecane and ethylene glycol).

The storage modulus *G'* is, in all cases, larger than the loss modulus *G''*, indicating the presence of a mechanical network. The shape of the curves resembles the typical gel-like behavior, in which the *G'* remains constant and over the *G''* at low strains (linear viscoelastic (LVE)-region), followed by a decrease (yield point, γ_y or τ_y), and a cross-over between the storage and the loss moduli (*G'* = *G''*, flow point, γ_f or τ_f) at increasing strains, indicating the transition from a solid-like to a liquid-like behavior.[159]

We focus now on electrofluids containing 5 vol. % CB in PDMS and glycerol, i.e., Figure 3.3A-B. Their *G'* were found to be on the same order of magnitude (6390 Pa for CB-PDMS and 3760 Pa for CB-glycerol), inferring slightly higher stiffness of CB-PDMS, even when the proximity to the percolation threshold is one order of magnitude different (ratio ϕ/ϕ_c of 1.02 for CB-PDMS and 10.42 for CB-glycerol). The brittleness of the systems, however, differed considerably. A way of estimating it is the so-called flow transition index (FTI), which is defined as the ratio between the stress at the flow point and at the yield point τ_f/τ_y. The closer the ratio is to 1, the higher is the tendency of the sample to undergo brittle fracture. In this context, it means that the initial network structure is broken or unable to resist the deformation and, therefore, starts flowing. We found the CB-PDMS system to be more brittle (FTI = 5.3) than the CB-glycerol (FTI = 51.7) at 5 vol. % of CB. This is consistent with the model described above, CB aggregates are well-dispersed in PDMS and the CB network in PDMS at 5 vol. % contains only few CB-CB contacts. When they break at the yield point, the network cannot take up force anymore, and the electrofluid flows almost immediately. The CB network in glycerol at 5 vol. % is mechanically more stable because more CB-CB contacts exist (electrical percolation found at 0.41 vol. % CB), and CB-CB interactions are stronger. At the yield point, some CB-CB contacts in the network break, but the network is strong enough to sustain plastic deformations without flowing. The peak in *G''* at ~6% strain in Figure 3.3B indicates the breakup of the CB mechanical network; its area is known to be correlated with the energy dissipated in the process.[159]

Relations between mechanical and electrical networks can be investigated with *in-situ* resistance measurements during the rheological tests (see section Methods for details). Figures 3.3A and B also show the evolution of the electrical resistance (RDC) during the oscillatory test. The evolution of their resistances with strain were in line with the different rheological regions described above. At low strain, in the LVE-region, the signal remained almost constant since the mechanical network absorbed the deformation elastically. The overall resistances were 15300 Ω and 23 Ω for CB-PDMS and CB-glycerol, respectively, a large difference that is in good agreement with the values of electrical conductivity presented in the corresponding percolation curves shown in Figure 3.1D-E. At the strain where *G''* increased and plastic deformations ensued, electrical resistances increased, and the filler network was destroyed. The materials retained electrical conductivity even far beyond the flow point. We argue that this is due to transient contacts in a “steady state”, where network connections form and break at identical rates. This transient network is electrically conductive but mechanically weak.

Electrofluids based on 5 vol% of CB in hexadecane and ethylene glycol (Figure S3.3A and B in the SI) were sufficiently far above the electrical percolation threshold to exhibit low electrical resistance at rest and were rheologically similar. Both presented comparable evolutions of *G’* and *G’’* and the changes of their resistances with strain were in line with the different rheological regions described above. At low strains, resistance remained constant, because the mechanical network absorbed the deformation elastically. At the strain where *G’’* increased, the electrical resistance increased as well until reaching a plateau at strains larger than the flow point that we attribute to the transient CB network introduced above.

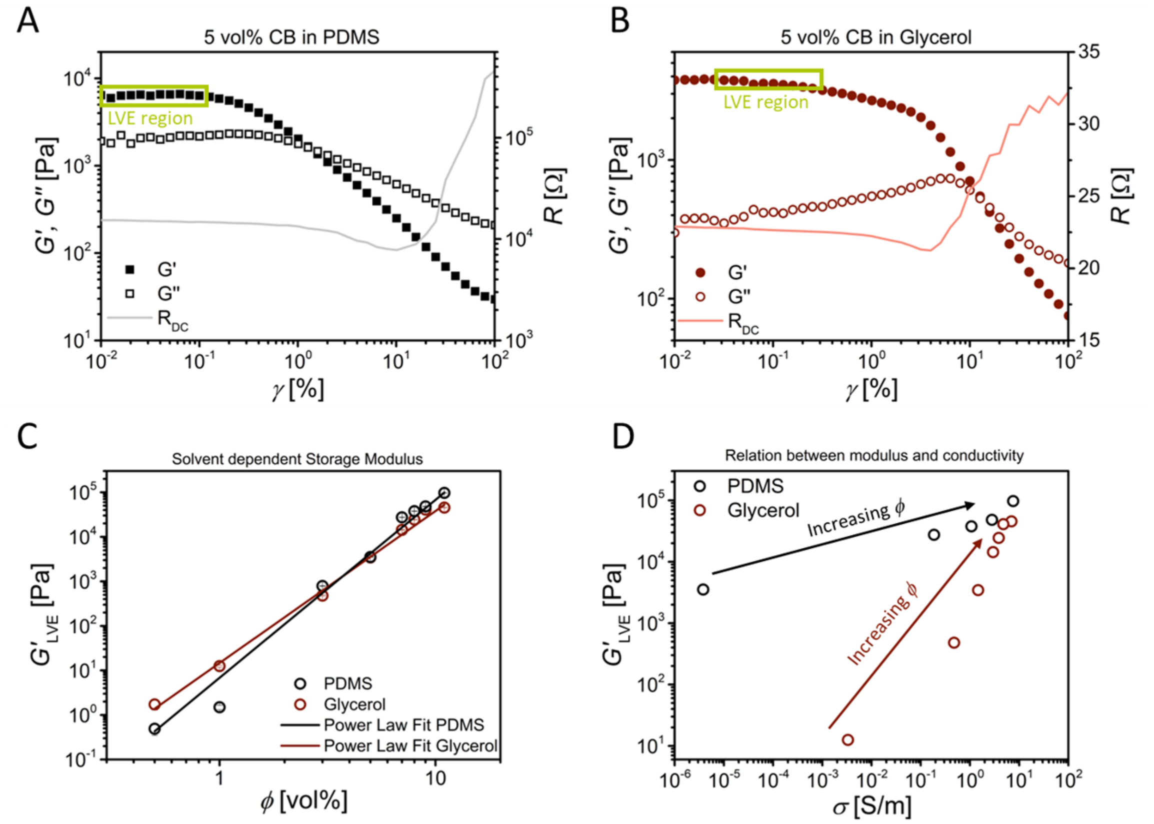

Figure 3.3: Oscillatory amplitude sweeps at ω=10 rads^{-1} in the range of 0.01-100% strain. Closed symbols: Storage Modulus. Open symbols: Loss Modulus. Light line: Resistance. A: 5 vol% CB in PDMS. B: 5 vol% CB in Glycerol. C: Storage Modulus as a function of filler volume fraction and used solvent. Experimental points were fitted with a power law $G' \sim \phi^n$. D: Storage Modulus’ plateaus as a function of conductivity. Volume fractions were 5, 7, 8, 9, and 11 vol% for PDMS and 1, 3, 5, 7, 8, 9, and 11 vol% for glycerol.

The overall stiffness of all electrofluids, represented by the *G’* value at the LVE-region, was dominated by the filler-filler and filler-matrix interactions. Figure 3.3C shows that the plateau values of the storage modulus (LVE-region) from amplitude sweeps scaled with CB volume fraction as $G' \sim \phi^n$, with n = 3.99 for the non-polar PDMS and n = 3.41 for the polar glycerol.

Glycerol interacts weakly with the non-polar CB that formed a mechanically strong network below 1 vol% CB. The storage modulus increases with CB loading because the network became mechanically stronger. The dispersed CB aggregates in PDMS-based electrofluids (Figure 3.2B) interact with the polymer chains and reduce their mobility, reinforcing the mixture even at CB loadings below percolation. This effect is weaker than that of agglomeration in glycerol-based electrofluids, which is reflected in the values of the storage moduli. Similar relations between filler dispersion and the stiffness of solid composites have been reported elsewhere.[234] At CB contents above percolation (5 vol%) in PDMS, a mechanically rigid network formed. The combined contributions of the filler-matrix interactions and the mechanical network formation explain the higher scaling exponent for PDMS than for glycerol.

A low elastic modulus at a high electrical conductivity is beneficial for soft conductors that can be formed by filling electrofluids in an elastic tube, for example. Figure 3.3D gives the relation between the plateau *G'* values and the electrical conductivity (*s*) of the resting electrofluid. The increase of conductivity with *G'* suggests a direct correlation with the stiffness, but the exact relation depends on the polarity of the solvent. The scaling of *G'* in glycerol-based electrofluids follows a power law, while that in PDMS only for volume fractions above 7 vol% CB. In consequence, glycerol-based electrofluids provide higher conductivity at comparable stiffness. These results highlight the close interplay between the electrical and the mechanical networks and thus, the macroscopic material properties. The non-linear relations enable rational tuning of the rheoelectrical properties of electrofluids.

Consider the use of electrofluids in soft robotics. Some components of soft robots require stable electrical conductivity upon mechanical deformations, others (sensors) must have a high sensitivity to detect small pressures, compressions, strains, bending, etc. We tested the suitability of electrofluids for both cases and loaded different types in silicone tubes that were electrically connected at their ends (see details in the Method section). We quantitatively evaluated the electrical response of encapsulated electrofluids under uniaxial strain and refer to their "piezoresistivity" in the following, extending the term that is well-established in conductive composites analogously for electrofluids. Uniaxial tensile tests were performed on electrofluids with 9 vol% CB in PDMS and in glycerol, and the electrical resistance changes were measured *in-situ*. The CB concentrations ensured percolation and good electrical conductivity in both solvents. We subjected the sample to cyclical loads resulting in 0-10% strain at a constant strain rate of 10% per second (Figure 3.4A). Electrical resistance was recorded during the entire experiment. All details on the setup can be found in the Method section and in Figure S3.4 in the SI.

Figure 3.4A shows the relative changes in electrical resistances during 1000 cycles. The electrical resistance change for the PDMS-based electrofluid was much higher than that for the glycerol-based one. A common parameter that is suitable to evaluate this difference is the gauge factor (GF, see Equation 3.1 in the introduction). The gauge factor of the 9 vol% CB-glycerol was 1.02±0.01, that of 9 vol% CB-PDMS was 2.55±0.2, i.e., more than double, indicating a higher sensitivity. This difference is in good agreement with the corresponding rheoelectrical measurement (Figure 3.4B), where the increase of electrical resistance beyond the LVE-region was larger for PDMS than for glycerol. Rheoelectrical measurements thus qualitatively predicted the uniaxial tensile test results for electrofluid-based devices and enabled a rational fluid design for specific applications.

When a solid conductive composite sample is stretched, its overall resistance tends to increase. This increase can have a geometrical and a piezoresistive component. A material with a Poisson's ratio of 0.5 (incompressible material, e.g., rubbers and their composites) with a GF = 2 does not exhibit piezoresistivity, i.e., the resistivity of the material remains constant and the change in resistance is purely due to its geometrical deformation. A GF > 2 indicates positive piezoresistivity, i.e., an increase of the material's resistivity upon strain. Our electrofluids based on CB-PDMS had GF > 2, and their response can be compared to that of liquid metals in tubes, which typically have gauge factors around 2.[206] A GF < 2 indicates negative piezoresistivity; such materials are poor sensors but stable conductors. Our glycerol-based electrofluid falls in this category, indicating a change in the CB network that decreases the intrinsic electrical resistivity of the electrofluid. Even small changes in the particle contact, i.e., closer contact or increased contact area, are sufficient to improve the electrical conductivity of the overall network and compensate for the geometrical changes.

The difference between the electrofluids' GF can be explained when considering CB-solvent interactions. PDMS is a non-polar polymer that interacts strongly with CB aggregates. In solid composites, positive piezoresistivity is typically attributed to the particles losing contact forced by the alignment of the polymer chains during stretching[218] and the formation of cracks;[149] being this last cause not applicable in the case of electrofluids. In the electrofluids, CB aggregates interact with the PDMS polymer chains as was concluded from the rheological measurements (see section above). The strongly adsorbed polymers reduce CB-CB interactions and make the joints weaker. Upon stretching, the polymer chains align, and the CB network gets disrupted, losing some of the connections.

Glycerol is, however, a small polar molecule that poorly interacts with the CB aggregates. Upon stretching, the large agglomerates are pulled apart, but due to the poor solvent affinity they will reconfigure to maximize CB-CB contacts. A large part of the geometrical changes is thus compensated, leading to a GF smaller than 2.

We exploited the solvent-dependent differences in the electrofluids properties to design electromechanical components. Figure 3.4C-E shows elastomer tubes filled with 9 vol% CB in PDMS and 9 vol% CB in glycerol, respectively (see Video1 as electronic SI). We connected them in series and attached them to the finger of a glove. At rest, the electrical signal was constant, and the blue LED was on. Bending the finger increased the resistance of the CB-PDMS electrofluid, triggering the red LED. Bending the wrist deformed the CB-Glycerol electrofluid, but its resistance increase was small, and the red LED remained off. A combination of the two electrofluids thus enabled the design of robotic structures, in which one part serves as a deformation sensor while the other faithfully transmits the signal.

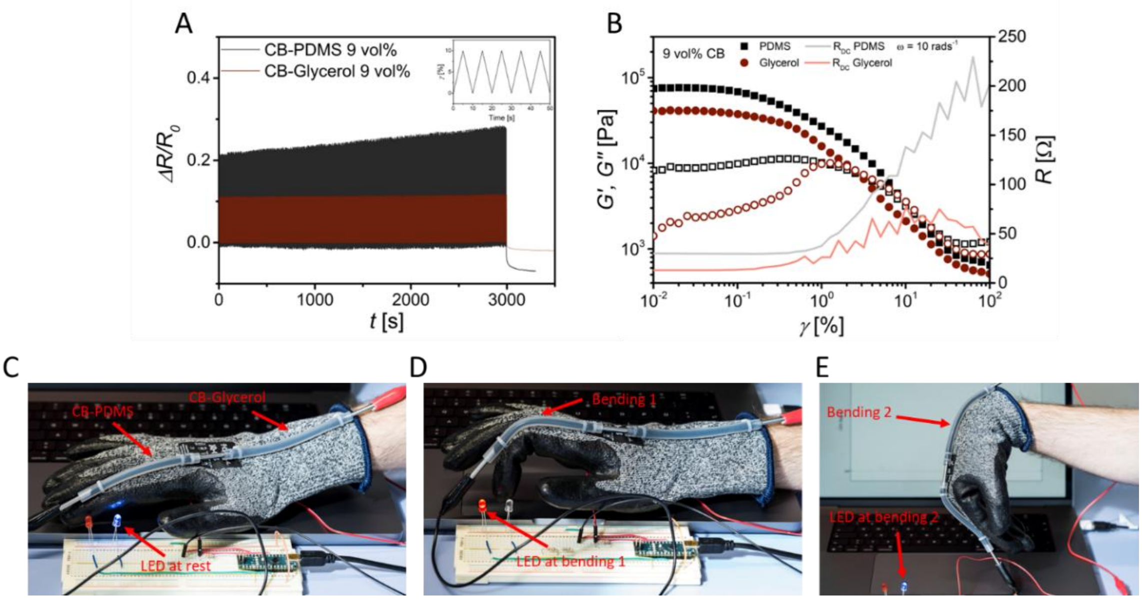

Figure 3.4: A: Change in resistances measured during cyclical loading between 0% and 10% strain (1000 cycles) for 9 vol% CB in glycerol and PDMS. The inset shows the strain profile. B: Rheoelectrical characterization of 9 vol% CB in PDMS and glycerol. C-E: Electrofluid-filled tubes attached to a glove. A sensing electrofluid senses the motion of the finger region; it is connected to a permanently conductive electrofluid lead at the wrist. A blue LED lights at low resistance of the connected tubes, a red LED indicates high resistance. C: Sensing glove at rest. D: Bending the finger triggers the red LED. E: Bending the wrist does not change resistance. A video of the demonstrator operation can be found as SI.

To assess the limits of the electrofluid containing 9 vol% CB in glycerol as stable signal transmitter, we investigated the relation between uniaxial deformation and electrical response at larger uniaxial strains. A silicone tube containing the electrofluid underwent 100 cycles at increasing and decreasing strain (10%-100%-10%) at a constant rate, while monitoring the electrical resistance changes (see Methods section for details). The results are summarized in Figure 3.5. At increasing strain, the changes in electrical resistance also increase; however, when calculating the GF, which considers the geometrical changes and the strain, we observed that all the values are below 2, indicating a decrease in resistivity that opposes the mechanical deformation. Interestingly, when the electrofluid underwent lower strain cycles (75%-10%) after the maximum strain (100%), the changes in resistance were larger compared to the initials, particularly marked at low strains, resulting in a GF larger than 2 at 10% strain. This could be an indication of strain memory of the material. For example, if this electrofluid undergoes small strains during application, a GF = 1 at 10% strain is to be expected; if, however, undergoes large deformations, the GF at 10% strain afterwards is expected to be much larger, 2.5 (Figure 3.5C).

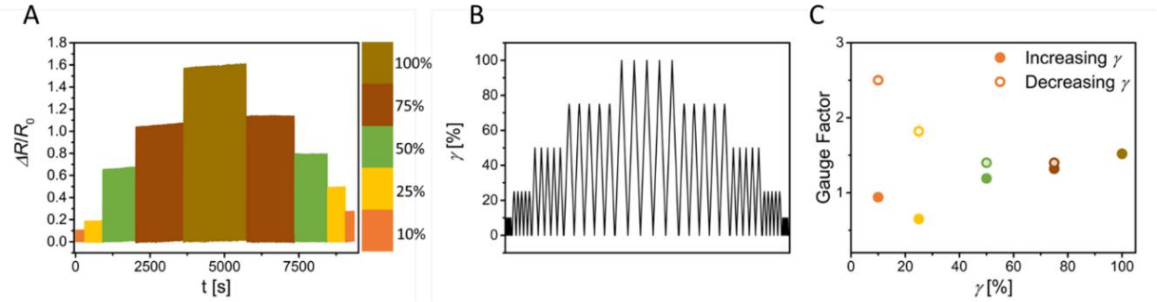

Figure 3.5: A: Change in resistance of a 9 vol% CB in Glycerol sample stretched to different strain amplitudes. From orange to brown 100%, 75%, 50%, 25% and 10%. Each strain value was cycled for 100 cycles. B: Used Strain profile for the electromechanical test. C: Gauge factors of 9 vol% CB-Glycerol electrofluid at the different strain values. Filled symbols indicate increasing strain amplitude and open symbols decreasing strain amplitude.

3.4. Conclusion

In this work, we introduced “Electrofluids” as electrically conductive liquid composites and demonstrated their tunability as flexible, stretchable conductors and as strain sensing materials. Carbon black (CB) was used as an electrically conductive filler. Suspensions with increasing CB concentration in polar and non-polar solvents exhibited large differences in mechanical network strength and electrical conductivity. We explain the differences using a model based on the affinity of the conductive filler towards the liquid matrix. High affinity towards non-polar liquids led to smaller agglomerates and increased both the percolation threshold and the stiffness at higher volume fractions. Low filler-solvent affinities in polar liquids led to larger agglomerates even at low concentrations, reducing the percolation threshold. *In-situ* rheoelectrical measurements showed a close connection between the mechanical and the electrical network in the systems, giving a direct correlation between the stiffness and electrical conductivity. Polar solvents deliver an improved figure of merit, *i.e.*, higher conductivity at comparable stiffness.

We tested the sensitivity of different electrofluids’ conductivity to uniaxial strain and found that electrofluids with non-polar liquids present slight piezoresistivity and higher electrical sensitivity towards uniaxial strains. Surprisingly, electrofluids based on polar liquids retain better the electrical conductivity even at high strains (100%) since the CB network reconfigures and compensate the geometrical changes imposed by the strain. Both exhibited good reproducibility of their responses over cycles. We used a demonstrator to show that electrofluids with the same filler work as strain sensor and a stable conductor. This single-component strategy reduces production costs and enables more sustainable materials simplifying the recyclability processes.

We envision the use of fillers and liquids that expand the electrofluid portfolio to achieve a wide range of electromechanical properties. Metal particles, flakes, and wires, or their mixtures, with liquids should lead to a broad range of electromechanical responses. For example, 1D objects such as carbon nanotubes reduce the percolation threshold and can align under suitable flow conditions, imparting memory to the electrofluids.

3.5. Experimental Section

Electrofluid preparation

Used chemicals were acetylene black, 100% compressed (Alfa Aesar, Germany), PDMS Sylgard 184 (Dow Corning, USA), glycerol ReagentPlus ≥99% (SigmaAldrich, Germany), hexadecane ReagentPlus 99% (SigmaAldrich, Germany), hexane ReagentPlus 99% (SigmaAldrich, Germany), and ethylene glycol ReagentPlus ≥99% (SigmaAldrich, Germany). All chemicals were used as purchased without further purification. To prepare electrofluids, the desired amount of acetylene black powder was weighed in a vessel and covered with the liquid matrix. The mixing was done with a DAC 150.3 SP VAC-P speedmixer (Hauschild, Germany) at 2350 rpm for 3 min to obtain an electrofluid paste.

Electron Microscopy

Scanning electron microscopy (SEM) images were recorded using a FEI Versa 3D DualBeam FIB-SEM system (FEI, USA) at 10 kV. Transmission electron microscopy (TEM) images were carried out with a JEM 2010 (JEOL, Germany) at 200 kV. To prepare the samples, the CB was dispersed in ethanol and treated in an ultrasonic bath. A droplet of the dispersion was placed on a silicon wafer (for SEM) or on a TEM grid and dried before the imaging.

Raman Spectroscopy

The Raman measurements were performed with a Renishaw inVia Raman spectrometer at a wavelength of 532 nm. A small amount of sample was put onto a glass slide and put into focus. Wavelengths from 800 to 2200 cm-1 were tested.

Electrical Conductivity

The measurement of conductivity was done with a 4P-probe measurement to eliminate the wire and contact resistances. For that, the paste was filled in a custom-made, Teflon® mold (1.5x1.5 cm2 with a thickness of 0.5 cm), which ensures applicability of the 4P-probe measurement model. The measurement was done using a Keithley Tectronix 2350 Sourcemeter (Tectronix, USA). A current-voltage Curve was recorded, and the resistance was extracted from the slope of the linear function.

Particle Size Characterization

The particle size distribution was analyzed using a LUMiSizer (LUM, Germany). The analysis of glycerol and PDMS samples was not possible due to the high viscosity of these solvents. Therefore, suspensions of 0.002 wt% CB in hexane and ethylene glycol were prepared and treated 20 min in an ultrasonic bath. Suspensions were then transferred into rectangular polyamide (PA) cuvettes. The centrifuge procedure used speeds between 2000 and 4000 rpm accumulating a total measurement time of 5 h. The analysis was done using StepView 6 software. The particle size distribution was determined using volume weighted analysis.

Rheological characterization

All rheological tests were performed with an Anton-Paar MCR302e rheometer. The measurements were done at 25 °C with a stainless-steel 25 mm parallel plate geometry with a gap height of 500 µm. Oscillatory rheology was performed in terms of an amplitude sweep with a strain from 0.01% to 100% with a fixed angular frequency of 10 rad/s. The LVE range was determined from the region of constant storage modulus. The yield point was determined as the strain, at which the storage modulus deviates 3% from the LVE region.

Rheoelectric measurements were done with coupling a Keysight E4980A dielectric spectrometer (Keysight, USA) to the rheometer. The temperature and geometrical conditions were the same as described above. The lower plate and the upper geometry served as electrodes for the electronic measurements. In oscillation mode, the same settings as described previously have been used. For each rheological measurement point, the electrical resistance was measured.

Uniaxial electroemechanical tests

All uniaxial electromechanical tests were performed on a ZwickRoell tensiometer (ZwickRoell, Germany). The test specimens were attached to the tensiometer and connected via copper wires to a Keithley Sourcemeter (see Figure S3.3 in the SI). For the cycling test, strain cycles of 10% were applied with a speed of 10%/s for a total of 2000 cycles. The first 1000 cycles were taken as initial equilibrium cycling until a constant signal was achieved. All further processed data was taken after this initial cycling. No waiting time was applied between the maximum and minimum strain load. For the different maximum strain values the sample was mounted the same way and was precycled for 1000 cycles at 10% strain. Afterwards, different strain values from 10 to 100% were applied for 100 cycles at each strain amplitude. All strains were tested subsequently on the same sample, starting with the smallest deformation. After reaching 100% the strain was lowered from 75% to 10%. The change in resistance was recorded with a Keithley DAQ6510 Sourcemeter (Tectronix, USA).

Demonstrator

Electrofluids were filled into silicone elastomer tubes and connected electrically via metal pins, before sealed. One tube was filled with CB-PDMS 9 vol% and the other one with CB-Glycerol 9 vol%. Both tubes were attached to a glove and connected in series with a simple circuit containing a red and a blue LED that were controlled with an Arduino device. Illumination of the LEDs was triggered at different resistance values: blue for initial resistance and red for high resistance.

Acknowledgements

We acknowledge funding by the European Research Council (ERC) under the European Union's Horizon 2020 research and innovation program (Grant Agreement No. 949785 ELECTROFLUID). We acknowledge Dominik Perius and Marcus Koch for SEM and TEM images. We thank Albenc Nexha for performing the Raman measurements. Additionally, we thank Niclas Hautz and Petra Herbeck-Engel for helping with the demonstrator and creating the videos and photos. We also thank Eduard Arzt for his continuing support of the project. There are no conflicts to declare.

3.6. Supporting information

Raman spectrum of Carbon black

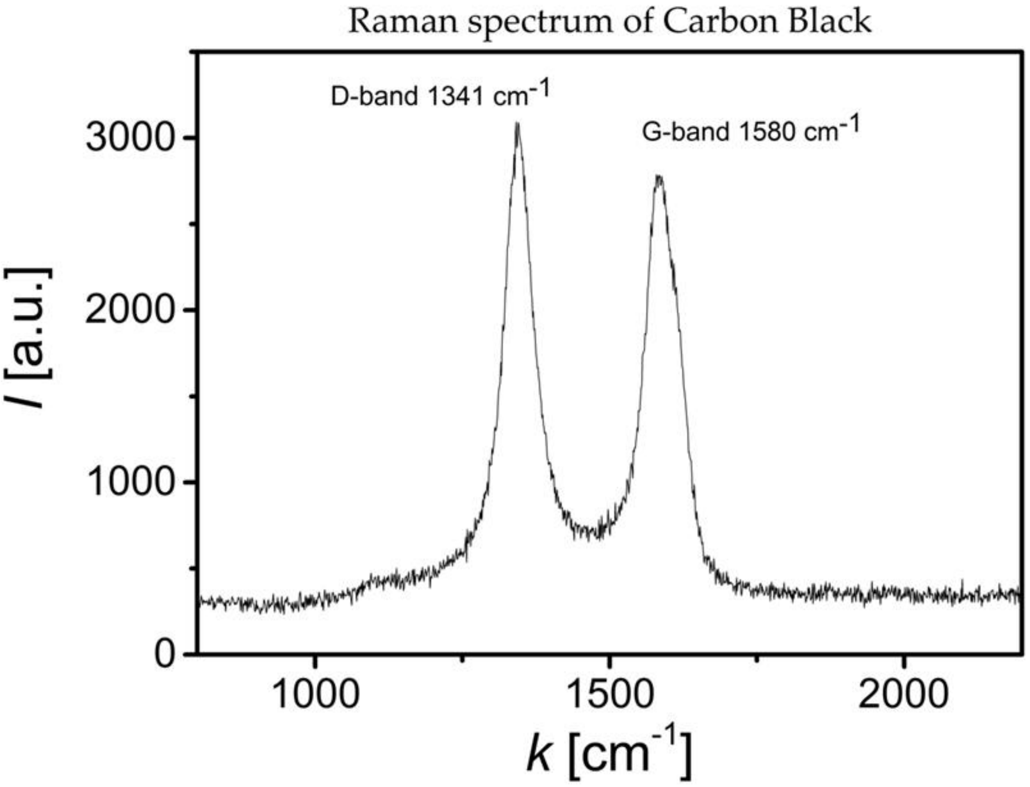

Figure S3.1: Raman spectrum of Carbon black powder.

Electrical percolation data

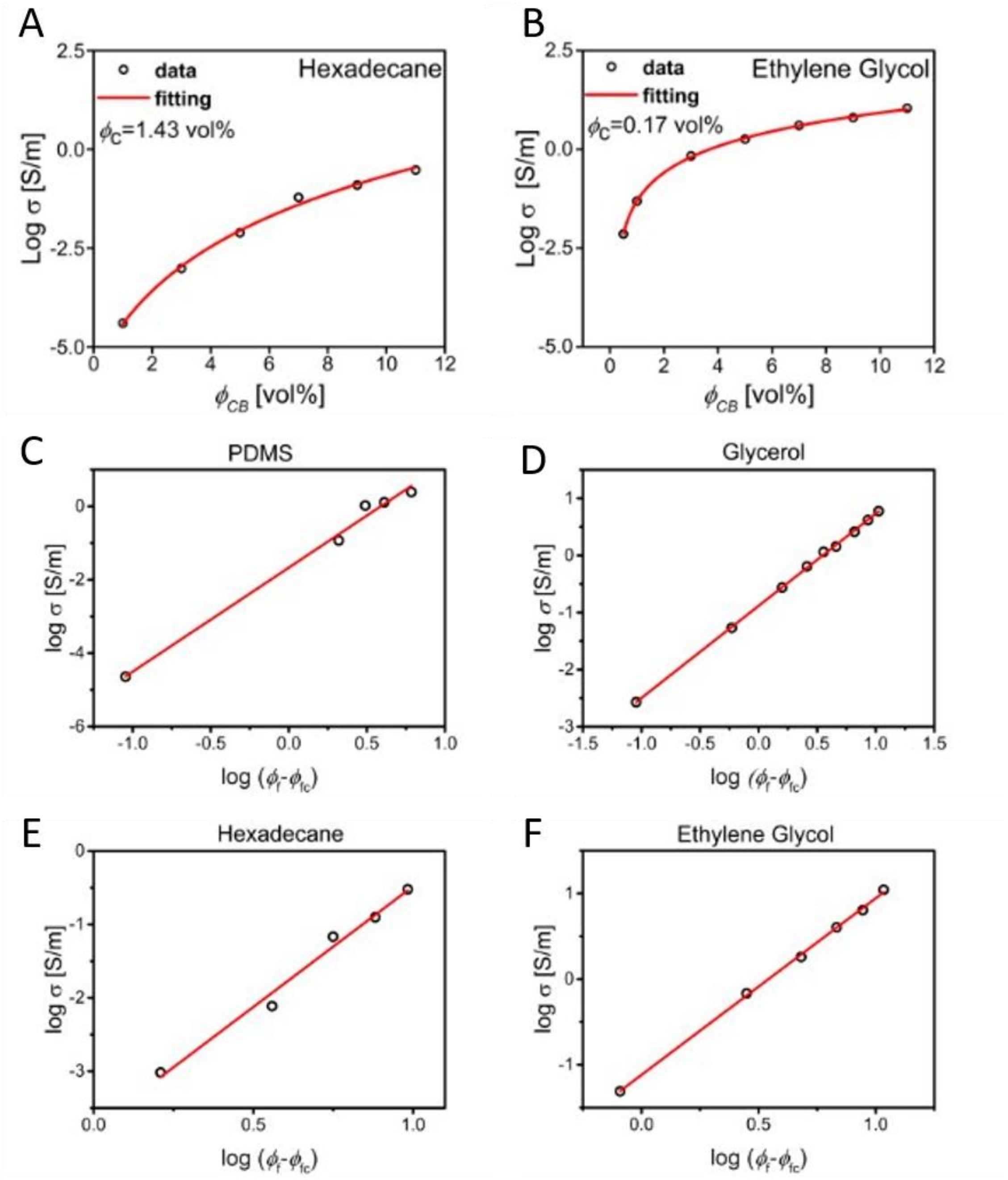

Figure S3.2: Percolation threshold for CB in hexadecane (A) and ethylene glycol (B). Linear fitting curves of the percolation threshold determination for the CB mixtures in PDMS (C), in glycerol (D), in hexadecane (E), and in ethylene glycol (F).

Rheoelectrical measurements

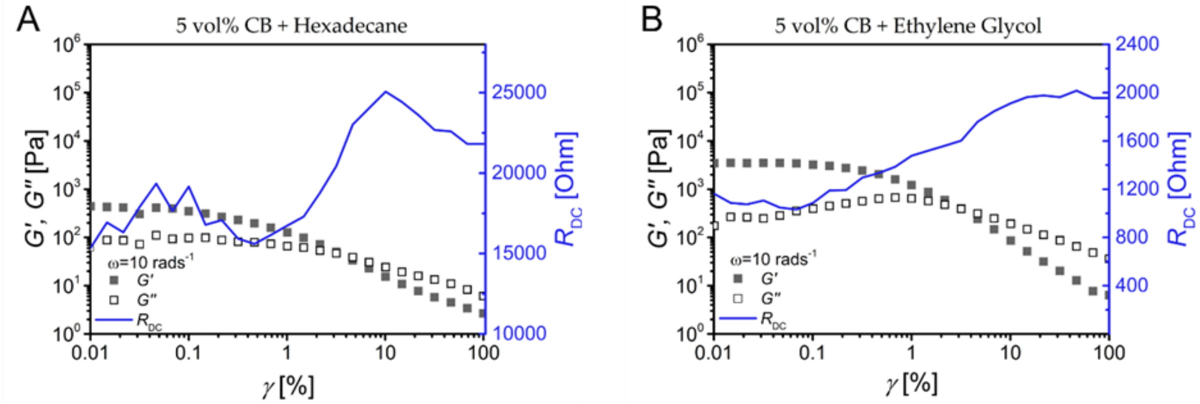

Figure S3.3: Rheoelectrical measurements of 5 vol% CB in A) hexadecane and B) ethylene glycol.

Uniaxial tensile tests

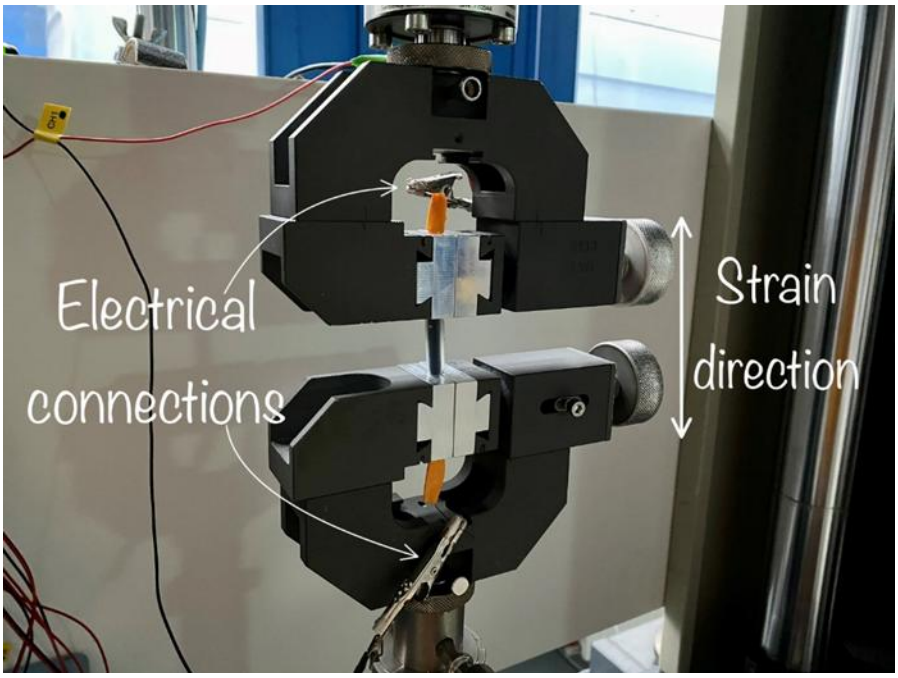

Figure S3.4: Image of the uniaxial tensile test set-up. The electrofluid was encapsulated in an EcoFlex® tube, clamped into the tensile machine, and electrically connected to the Keithley DAQ6510 Sourcemeter.

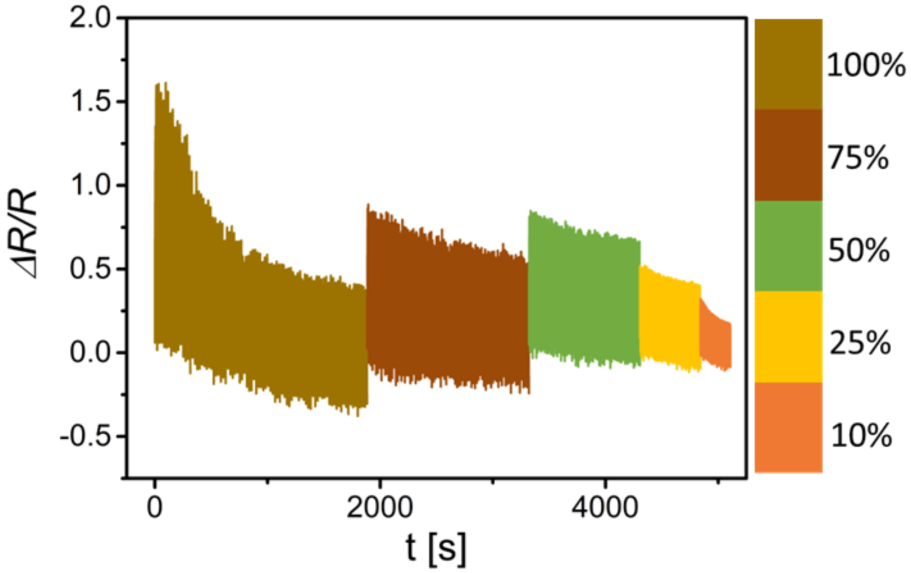

Figure S3.5: Change in resistance of a 9 vol% CB in PDMS sample, stretched to different strain amplitudes. From brown to orange 100%, 75%, 50%, 25%, and 10%. Each strain value was cycled for 100 cycles.

Videos of the demonstrators can be found as electronic supporting information: Video1 and Video2.

4. Conductive emulsions with selective filler distribution as volume exclusion strategy in electrofluids

This chapter is based on the content of the published article:

Schmidt, Dominik S., Dominik Perius, and Lola González-García. "Conductive emulsions with selective filler distribution as volume exclusion strategy in electrofluids." Journal of Physics: Materials 9.1 (2026): 015019

DOI: 10.1088/2515-7639/ae3e18

4.1. Abstract

A classical approach to reduce the percolation threshold in conductive polymer composites is the so-called volume exclusion. While this method proved to lower filler concentration required to achieve electrical conductivity in solid composites, it remains unexplored for liquid conductive composites such as electrofluids (EFs). We propose the combination of emulsions and conductive particles to create EFs with reduced filler content. Conductive emulsions were prepared based on two immiscible liquids, glycerol and polydimethylsiloxane (PDMS), and carbon black (CB) as the conductive filler. The structural characterization of stable emulsions revealed a selective distribution of CB in the PDMS phase (continuous phase), around glycerol droplets (dispersed phase). This configuration led to a decrease in percolation threshold proving the viability of volume exclusion as strategy in EFs. The combination of the CB network and the glycerol droplets resulted in unpredictable mechanoelectrical properties such as a reduced stiffness scaling compared to CB-electrofluids in the pure solvents and the reduction of a strain thickening behavior with increased filler concentration. We evaluated the role of the CB in the emulsion formation, and its impact on the droplet size and size distribution and concluded that this effect must be synergetic with the creation of a stress-carrying filler network that absorbs the elastic energy from the droplet deformation at large strains.

4.2. Introduction

Soft electronic components are of great interest for applications demanding stretchable sensors[235] or stable conductors,[17] like wearables[236] or implants.[237] Conductive polymer composites (CPCs) are a common type of material to create electrical conductors with relatively low Young's modulus.[238] They consist of conductive filler particles dispersed in a non-conductive polymeric matrix, often elastomers. The high variety of conductive fillers and matrices confers on them a high versatility and a broad degree of tunability in their properties. For example, fillers can be found with different shapes and of different nature such as silver[239], copper,[240] or gold[241] spherical particles, silver wires[239] or flakes;[242] carbon materials such as fractal carbon black (CB),[243] carbon nanotubes (CNTs),[244] and graphene flakes;[245] or 2D materials such as MoS_2[246] or MXenes.[247] Depending on the filler and the matrix, the minimum amount of filler required to create at least one conductive path throughout the composite volume, the so-called percolation threshold, might vary significantly.[248] Besides the economic considerations, reduced percolation thresholds are desired to minimize the reinforcement effects of increased filler loadings, which lead to stiffer composites[249] with reduced elongation at break.[144] Typical approaches for reduced percolation are the selection of high aspect ratio fillers like rods or wires[92, 250, 251] or inducing agglomeration by selecting low affinity matrices,[252] restricting the possible combinations.

Another strategy to reduce the percolation threshold, independently of the filler shape and nature, is the so-called "volume exclusion" using a third phase in the composite. The idea is to restrict the available volume for the filler, forcing the conductive network formation at lower concentrations. Three main approaches can be distinguished in conductive composites. First, double percolation systems rely on the preferential dispersion of the conductive filler in one polymer of an immiscible polymer blend. As both polymers form a percolative system, like found in heterojunctions, if the filler in turn forms a percolative network in its preferential phase, the overall composite turns conductive. Sumita *et al*. employed such strategy by blending polypropylene (PP) with polymethylmethacrylate (PMMA) and adding CB as the conductive filler, which preferentially distributed in the PMMA phase.[104] Similarly, Li *et al*., prepared solid composites based on an immiscible blend of PP and epoxy with CB as conductive filler. They found a percolation threshold of 7.4 wt.% in a 50:50 weight ratio of PP and epoxy. This was approximately half compared to the percolation threshold using only epoxy as the matrix (14.5 wt.% CB).[105] Recently, Topcu *et al*. reported a reduction of the percolation threshold of ca. 50% (from 0.46 vol.% to 0.19 vol.%) of multi-walled CNTs (MWCNTs) using a double percolation strategy with a mixture of polystyrene (PS) and ethylhexyl acrylate (EHA) compared to the use of pure homopolymer of PS as a matrix.[253] Second, some types of segregated composites also make use of immiscible polymers but, in this approach, the filler locates at the polymer-polymer interface, reducing further the volume available for it.[106] Chen *et al.* studied the electrical conductivity of CNTs in a blend of polycarbonate (PC) and acrylonitrile-butadiene-styrene (ABS).[107] The selective localization of CNTs at the interface between these polymers led to a reduced percolation threshold of 0.05 wt.% for the segregated composite compared to the 0.24 wt.% CNT in the pure PC phase.[107] Lastly, a relatively simpler approach uses a filling third phase, for example, non-conductive fillers, that are distributed in the composite matrix taking away available volume of the continuous phase for the conductive filler. Bao *et al*. used solid particles of calcium carbonate ($CaCO_3$) as the third phase in a composite containing MWCNTs and PP.[109] They found that by adding 30 wt.% of $CaCO_3$ the electrical percolation threshold was lowered from 0.90 to 0.63 vol.% MWCNTs attributed to the volume exclusion effect, that increased the effective MWCNT concentration in the polymer phase.[109] To alleviate the impact that such solid fillers might have on the macroscopic stiffness of the final composite, softer materials can be used.[254]

All the abovementioned approaches have been successfully applied in solid conductive composites to reduce the electrical percolation threshold. A new type of truly soft conductor are electrofluids (EFs), liquid composites containing conductive filler particles in a liquid matrix.[255] To the best of our knowledge, none of the volume exclusion approaches has been investigated in EFs so far. Due to the liquid nature of EFs, we propose the use of emulsions filled with conductive particles as a volume exclusion approach. An emulsion consists of two immiscible liquids, where the dispersed phase forms droplets to minimize the contact area with the so-called continuous phase.[256] By introducing the conductive filler in the continuous phase, the dispersed phase would act as volume exclusion component, leading to a reduced percolation threshold. The addition of particles to an emulsion has an impact on its stability. Koos reported a ternary phase diagram of a solid-liquid-liquid emulsion, indicating stable emulsions depending on the volume fractions of the constituents.[257] It was shown that an increase of the volume fraction of the filler's preferential phase transforms the emulsion from a pendular state to a capillary state.[257] In the work of Kandy *et al*., the effect of MWCNTs on the rheological properties of highly concentrated emulsions was studied.[258] They formed an emulsion based on an aqueous dispersed phase (based on water with ammonium salts) and a continuous oil phase (based on canola and paraffinic oil). Cryogenic scanning electron microscopy images revealed the selective assembly and formation of a 3D network of MWCNTs in the continuous oil phase of the emulsion. The presence of the filler impacted the droplet size and size distribution during the manufacturing process, leading to an increased shear viscosity and increased stiffness.[258] Although their rheological properties have been investigated, the conductive properties of such particle filled emulsions remain unexplored. Especially, the interplay between mechanical and electrical networks, which is determinant for the mechanoelectrical properties.

In this work, we report conductive emulsions as a volume exclusion strategy to lower the electrical percolation threshold in electrofluids. We investigated the stability of emulsions composed of polydimethylsiloxane (PDMS) and glycerol at different ratios and successfully created stable conductive emulsions by adding increasing amounts of CB. Electrical characterization revealed a reduction in the percolation threshold, consistent with the preferential dispersion of CB within the non-polar PDMS phase. This model was supported by optical microscopy images of CB-containing emulsions. Rheological characterization coupled with *in-situ* electrical measurements of the emulsions was performed to determine their mechanoelectrical properties and understand the interplay between the mechanical and the electrical networks. We observed that increasing CB concentration led to a) increased stiffness of the emulsions and b) the suppression of the strain thickening at large amplitudes observed in pure emulsions. Two hypotheses are discussed to explain these effects: droplet size reduction and CB-network interaction with the droplets. Further analysis revealed that, although CB influences droplet size and size distribution, the dominant contribution to the mechanoelectrical response arises from the percolating network formed above its percolation threshold in the continuous phase, which affects the coherent mechanical properties of the droplets.

4.3. Results and Discussion

The emulsions were prepared mixing glycerol (polar) and polydimethylsiloxane (PDMS, non-polar), as immiscible liquids.[259] After mixing, the emulsions span homogeneously the whole sample volume (see Figure S4.1A in the Supporting Information). To determine the optimum ratio of the liquids and maximize the emulsion stability, different mixtures were prepared at increasing PDMS concentration (see Methods Section for details), and their stability was assessed by means of analytical centrifugation (AC). Figure 4.1A shows the cuvettes with PDMS/glycerol emulsions after the AC protocol and Figure 4.1C shows the percentage of the emulsion phase that remained stable after the test (open circles).

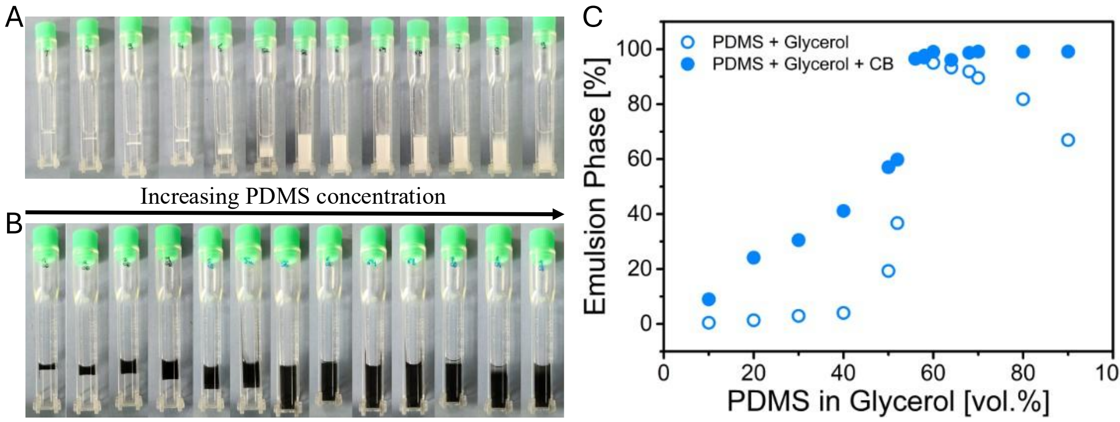

Figure 4.1: Polyamide AC cuvettes filled with PDMS/glycerol emulsions with different concentrations of PDMS in glycerol A) without and B) with CB after analytical centrifugation. C) Percentage of the emulsion phase of the total volume, that remained stable after the AC test, for different concentrations of PDMS in glycerol. Open symbols refer to pure emulsions and closed symbols refer to CB-containing emulsions.

During centrifugation, the excess of the pure liquids separated due to their different densities (0.97 and 1.26 g·cm^{-3} for PDMS and glycerol, respectively) revealing the stable emulsion fraction, clearly distinguished as turbid fraction (see Figure 4.1A). The layer at the top of the cuvette corresponds to PDMS and the one at the bottom to glycerol. Optical microscopy images revealed that the emulsion is formed by glycerol droplets that are dispersed within the PDMS phase (see Figure S4.1B of the Supporting Information). Since the emulsion contains both liquids, the effective density lays between the one of PDMS and glycerol, therefore, it laid in the middle, separating the pure solvent phases. At increasing PDMS concentration, the emulsion phase shifted downwards (due to the increasing amount of low-density phase) until a critical concentration was reached, at which the emulsion was sufficiently stable to sustain the AC test. These stable emulsions were observed for a certain ratio range, while higher concentrations of PDMS led to phase separation after the AC test. To determine the critical composition range for stable emulsions, we quantified the percentage of the emulsion phase present in the cuvettes after the AC test at increasing PDMS concentration (see open circles in Figure 4.1C). Note that the AC test was performed at a relative centrifugation force (rcf) of 2350 *g* during 20 h, which is equivalent to a long-term stability test of ca. 5 years in storage conditions (1 *g*). The transmission threshold between the phases in the AC test was set to 20% (see Methods section and Figure S4.2 in the Supporting Information for details). As expected from the photographs, the percentage of emulsion phase increased gradually with rising PDMS concentration up to a 50:50 ratio, beyond which a pronounced increase in the phase growth was observed. Stable emulsions (over 95% of emulsion phase) were found in the range of 56 vol.% to 60 vol.% of PDMS in glycerol, with the maximum (~97% of emulsion phase present) found for 58 vol.% of PDMS. We calculated the instability index for this emulsion and found a value of 0.033, indicating marginal changes in its stability during the test. Moreover, the sedimentation velocity was also estimated based on the transmission changes during the AC test, resulting on 2.1 μm/s, which corresponds to ~$0.9 \cdot 10^{-3}$ μm/s at 1 *g*. Further addition of PDMS reduced the emulsion proportion and induced the separation of the excess of PDMS, visible at the top of the cuvette. A similar trend was observed in oil-in-water emulsions composed of corn oil and oleic acid (oil phase) and sodium carboxymethylcellulose, triethanolamine, and water (aqueous phase). The authors reported that the stability of the emulsion increased with increasing dispersed phase (oil phase) content.[260]

Carbon black (CB) was selected as the conductive filler to create a percolating network and confer the material of electrical conductivity. Previous reports showed that the addition of solid fillers to an emulsion may change the stability of the emulsion depending on the type of filler.[261, 262] To exclude that, the same AC test was performed with the PDMS/glycerol mixtures adding a small amount of CB. After mixing, the CB was evenly distributed over the entire volume (see Figure S4.1C of the Supporting Information). Photographs of the cuvettes after the AC protocol are shown in Figure 4.1B. With the addition of CB, below the critical concentration (low PDMS ratios) only two different phases can be distinguished: a black phase on top and a clear phase at the bottom. Due to the hydrophobic nature of its surface, CB has a higher affinity towards the PDMS phase.[255] Carbon black was, therefore, present in both, the pure PDMS phase (top) and the emulsion phase (within the PDMS), making undistinguishable among them both while the glycerol remained clear. When reaching the critical concentration for stable emulsions, a homogeneous black phase was observed. The AC analysis (filled circles in Figure 4.1C) revealed a similar trend compared to the samples without CB (open circles in Figure 4.1C). However, one must notice that, with CB, the pure PDMS phase and the emulsion phase are indistinguishable, provoking an overestimation of the second one in the graph, particularly at high PDMS contents. At low PDMS ratios, a more gradual increase was observed also due to this overestimation, while at high PDMS volume ratios, the graph reached a plateau. Mazurek *et al*. found a similar behavior when they studied PDMS/glycerol mixtures.[259] They investigated the viscosity of the emulsions of different ratios and found an increase with increasing glycerol concentration. The maximum in viscosity was found at approximately 48 vol.% of glycerol in the mixture (52 vol.% of PDMS), close to our stable emulsion composition: 58 vol.% PDMS. One must notice that the small discrepancy can be caused due to the emulsion preparation or the stability evaluation method, they followed the evolution of the viscosity while we focus here on their stability by AC. The instability index and the sedimentation velocity for this combination were also calculated from the AC test, leading to 0.048 and $1.2 \cdot 10^{-3}$ μm/s at 1 *g*, respectively, close to the values obtained for the corresponding pure emulsion. From this point onward, all further experiments were conducted using the emulsion with 58 vol.% PDMS in glycerol.

The addition of a conductive filler to a liquid matrix only leads to a conductive network if the concentration of filler is high enough to ensure the creation of a continuous path that spans the entire volume. This minimum concentration is defined as the percolation threshold (ϕ_c) and is related to the electrical conductivity (σ) by the formula: $\sigma = A(\phi - \phi_c)^t$, where A is a constant, ϕ is the filler fraction, and t is a critical exponent.[248] To determine the percolation threshold of the CB in the emulsion, we measured the electrical conductivity of emulsions at increasing CB concentration using a 4-point-probe set up (see Methods section for details). Figure 4.2A shows the percolation curve of CB in the emulsion system (blue circles) compared to those of CB-electrofluids in pure PDMS (grey circles) and pure glycerol (black circles) extracted from reference.[255]

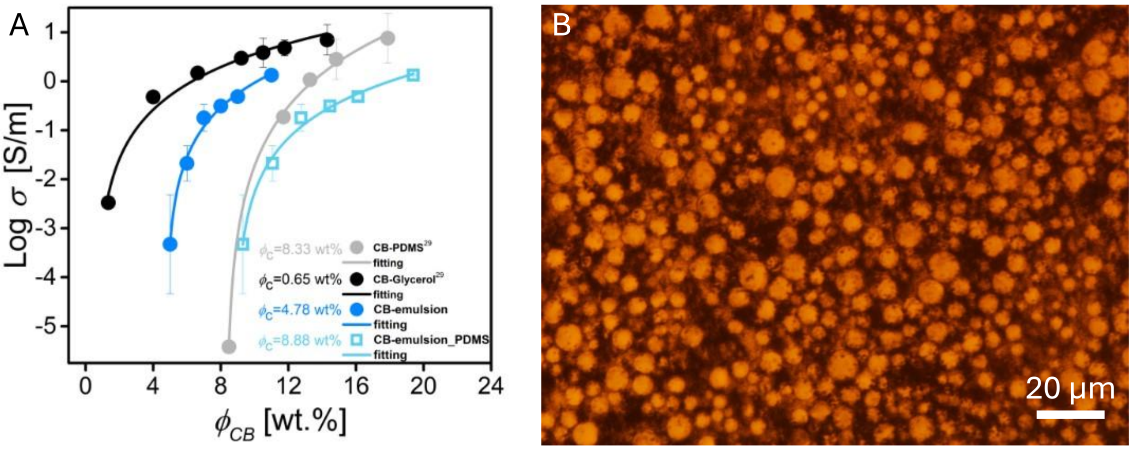

Figure 4.6: A) Electrical percolation curves of CB in different liquids. Grey, closed circles: PDMS [255], black, closed circles: glycerol [255], blue, closed circles: PDMS/glycerol emulsion, cyan, open squares: emulsion PDMS/glycerol normalized to the weight of PDMS in the emulsion. Solid lines are fit functions according to classical percolation theory $\sigma = A(\phi - \phi_c)^t$.[248] The concentration of the percolation threshold derived from the fit function corresponding to each system are noted in the graph. B) Optical microscopy image of a PDMS/glycerol emulsion filled with 3 wt.% CB with a 50x magnification.

The percolation threshold of CB in the emulsion was found at 4.78 wt.% CB, which laid between that reported for the two pure solvents 0.65 wt.% CB and 8.33 wt.% CB for glycerol and PDMS, respectively.[255] If we assume that the CB is solely dispersed in the PDMS phase, the normalization of CB content in the emulsion to the amount of PDMS must fit to this second value. The normalized percolation curve is displayed as cyan, open square symbols in Figure 4.2A, and the fitting delivered a critical concentration for percolation of 8.88 wt.% CB, which deviates less than 6% from previous reported value for CB in pure PDMS.[255]

To confirm that CB distributes preferentially in the PDMS phase around the glycerol droplets, we recorded optical microscopy images of a 3 wt.% CB-emulsion (see Figure 4.2B and Figure S4.3). Clear droplets were distinguishable in the micrographs while the CB was surrounding them, dispersed in the continuous phase. Imagine CB in pure PDMS at a concentration of 5 wt.% (below the percolation threshold), the fillers are then well-dispersed, and the connectivity is not sufficient to create a percolating path (see Figure 4.3A). Imagine now the same amount of CB in the emulsion; glycerol droplets take out part of the volume, that is no longer available for CB particles. They are, therefore, forced into a restricted volume around the droplets. As a result, the agglomerates become larger, inducing the formation of a percolated pathway at lower concentrations than in the pure PDMS matrix (see Figure 4.3B). This explains the reduced percolation threshold by volume exclusion for electrofluids (EFs).

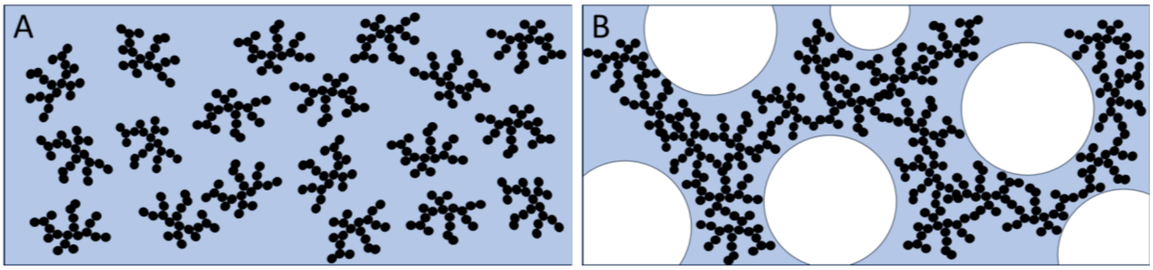

Figure 4.7: A) CB dispersed in pure PDMS at a concentration below the percolation threshold (<8.33 wt.%). B) Volume exclusion concept for CB-emulsions. CB dispersed in PDMS at the same concentration with glycerol droplets taking out 39.7% of the space (under the assumption of additive volumes).

The addition of conductive solid particles to simple liquid matrices in concentrations above the percolation threshold renders the suspension electrically conductive but increases the stiffness and the viscosity concomitantly. This behavior was observed, for example, in EFs based on CB suspensions in pure glycerol and PDMS.[255] The case of emulsions as matrices is, however, more complex: the presence of a high concentration of droplets typically leads to an enormous increase of the viscosity compared to the constituent liquids. This increase is due to the elasticity of the droplets caused by the surface energy and depends on the droplet concentration and size.[263] When adding particles to this system, multiple interactions between the droplets, the filler, and the continuous phase influence the final mechanoelectrical properties. Therefore, the trade-off between conductivity and elasticity for conductive emulsions might differ compared to simple conductive suspensions. To evaluate the flow behavior and viscosity of emulsions at different filler concentrations, rotational rheology was performed. The electrical resistance was monitored *in-situ* giving access to the electrical network during the mechanical deformation. Figure 4.4A shows the flow curves (and electrical resistance for conductive systems) of the pure solvents (PDMS and glycerol), the pure emulsion (58 vol.% PDMS in glycerol), and CB-emulsions at different concentrations.

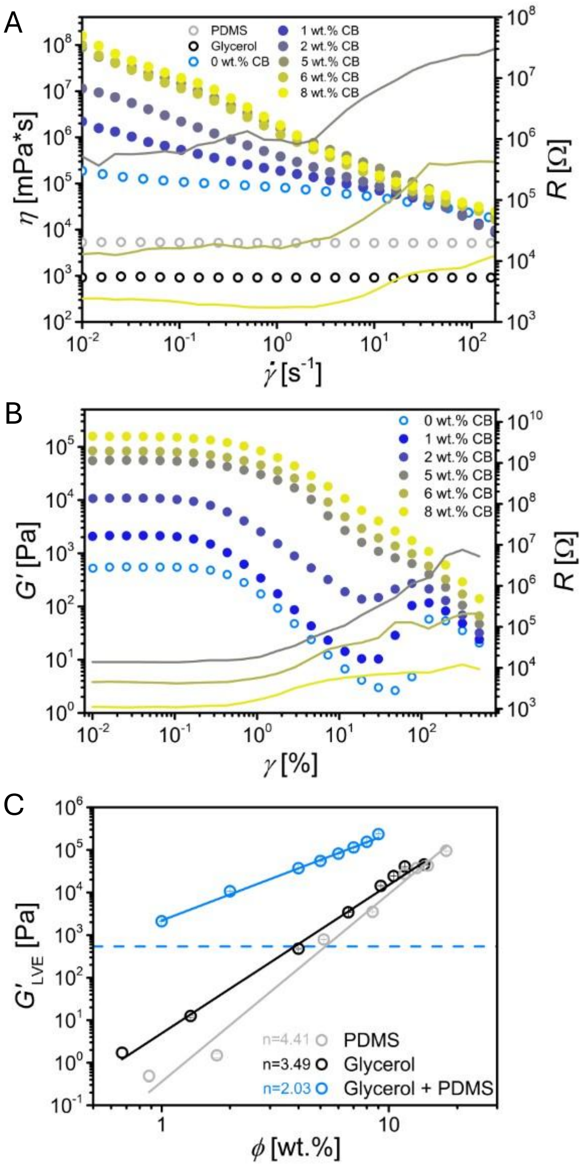

Figure 4.8: A) Flow curves of the pure solvents (grey, open circles: PDMS, black, open circles: glycerol), PDMS/glycerol emulsion (cyan, open circles), and CB-emulsions at increasing CB concentration (closed circles from dark blue to bright yellow at increasing CB concentration). Solid lines with the same color code represent the electrical resistance values measured during the flow curve for electrically conductive CB-emulsions (weight percentages below 4 wt.% were not electrically conductive, thus are not shown). B) Amplitude sweeps of PDMS/glycerol emulsions and CB-emulsions at increasing CB concentration. The symbol and color code are the same as in the previous panel. Solid lines represent the resistance measured during the test at each strain value. C) Storage modulus (*G'*) at the LVE-region *vs.* CB weight percentage for grey: CB in PDMS, black: CB in glycerol, and cyan: CB in PDMS/glycerol emulsion. Dashed line denotes the *G'* value of the unfilled emulsion. Solid lines are fit functions based on power law scaling $G' \propto \phi^n$.

Compared to the pure solvents, all emulsions showed increased viscosity at low shear rates. Only the presence of glycerol droplets (without CB) increased 35 times the viscosity compared to pure PDMS. We observed that the addition of CB filler increased further the low shear viscosity even at concentrations below the electrical percolation. This phenomena is attributed to the internal resistance against deformation that builds up by the fillers.[264] Additionally, all emulsions (with and without CB) presented a shear thinning flow behavior (viscosity decreases with increasing shear rate) in contrast to the pure solvents that presented a Newtonian flow behavior (independent viscosity value). At higher shear rates, the droplets deform and align in the flow direction reducing the resistance to flow (viscosity) and promoting a shear thinning behavior. Similar observations are reported in literature for oil-in-water and water-in-oil emulsions.[265, 266] The addition of CB also increased the degree of shear thinning, defined by a steeper slope in the flow curve.[174] At low shear rates, the viscosity increased with the CB concentration in the emulsions since the particles oppose to the flow. When filler particles are aligned under shear deformation (higher shear rates), the denser filler network loses more interparticle connections, which results in a stronger shear thinning. At very high shear rates, the influence of the CB in the viscosity is basically negligible and all the emulsions reach approximately the same viscosity value.

The electrical resistance, which only depends on the CB network, remained constant at low shear rates (small changes are attributed to the scattering of the measurements). Under this deformation, the breaking rate of the transient contacts between the particles is then equivalent to the forming connection rate, retaining the electrical properties. When the critical shear rate $\dot{\gamma}_{crit} \approx 2\ s^{-1}$ was reached, the resistance started to increase due to the increase of the breaking connection rate that was no longer compensated with the formation of new connections. This critical shear rate was independent of the CB concentration in this study. A similar behavior was recently reported for EFs based on multi-walled carbon nanotubes (MWCNTs) in pure glycerol.[267] Under shear flow, EFs kept their electrical conductivity constant until a critical shear rate, which was also independent of the MWCNT concentration. In contrast to our work, the MWCNT-based EFs lost their electrical conductivity completely at shear rates above 50 s^{-1},[267] while CB-emulsion EFs showed different increments of the resistance but preserved electrical conductivity in all studied cases. The different behaviors found in these two types of EFs can be attributed to a) the constrained volume in the CB-emulsions that restricts the mobility of the filler under shear flow and increases the probability of filler-filler contacts and b) the poor alignment of CB due to their fractal morphology. MWCNTs exhibit a high aspect ratio and remain unconfined within the EFs, which promotes their alignment along the shear direction while disrupting connectivity in the perpendicular direction to the flow field (direction of electrical measurement).

To further understand the interplay between the glycerol droplets and the CB network in conferring the mechanical properties of the emulsions, we analyzed their elastic and viscous responses by means of oscillatory amplitude sweeps at 10 rad/s (see details in the Methods section). Additionally, we measured the electrical resistance, to track the impact of deformation on the conductive CB network. The storage modulus (*G'*) in relation to the applied shear strain is depicted in Figure 4.4B while the corresponding loss modulus (*G''*) is shown in Figure S4.4 of the Supporting Information. Three different regimes can be distinguished in the mechanical response of all emulsions. The small amplitude oscillatory shear (SAOS) assesses the elastic behavior of the material. This region of small deformations is defined by the so-called linear viscoelastic (LVE) region, where *G'* is independent of the applied shear strain. The *G*' value in this region is a measure of the stiffness of the material.[268] With increasing CB concentration, the *G'* value increased from an initial value of 550 Pa (for the pure emulsion) to almost 158 MPa (at 8 wt.% CB), which means an increase of three orders of magnitude in stiffness. Analogous to the invariant *G*', at this low strain deformation, the electrical resistance also showed a plateau value. The initial resistance in this case decreased the higher the CB concentration was as expected from the percolation curve. At larger deformations, when the *G*' deviates more than 3% from the plateau value (typically by a decrease), the medium amplitude oscillatory shear (MAOS) region, or yield zone, starts.[174] This initial point, known as yield point, quantifies the maximum stress that the material stores as elastic energy (τ_{yield}). From this point on, the mechanical network undergoes plastic deformations. This region extends up to the flow point—the stress, at which the material transitions from a solid-like to a liquid-like behavior (τ_{flow})—and it is visible in the amplitude sweep as the crossover between *G*' and *G*''. Within the MAOS region, an increase in the electrical resistance of the conductive samples was observed (see Figure S4.4 in the Supporting Information). Similarly to the yield stress, we define an electrical yield stress ($\tau_{\text{el. yield}}$) as the stress needed to increase the initial resistance by 10%. The comparison between these three parameters (yield point, flow point, and electrical yield) as functions of the CB content is shown in Figure S4.5 in the Supporting Information. All three showed a power law scaling with CB concentration. A similar scaling law of the yield stress of different particle suspensions was previously reported[269, 270] and attributed to a transition from disordered particle interactions to ordered structures.[270] No previous reports were found for the flow point and the electrical yield stress. The electrical yield stress appeared at approximately 1/3 of the flow stress for all studied samples, indicating that large distortions in the mechanical CB network must occur prior, affecting the electrical network.

Strains beyond the flow point are considered to be in the large amplitude oscillatory shear (LAOS) region. Here, the network strength is not sufficient to sustain the stress, and the material behaves as a liquid. In this region, a continuous decay of the moduli is expected as often observed in complex fluids, i.e. polymer melts, particle suspensions, or emulsions.[271] We, however, observed an increase in *G*' and *G*'' for the pure emulsion and those with CB content below the electrical percolation threshold (1 and 2 wt.%). This phenomenon, called strain thickening, has been reported in some highly concentrated particle suspensions.[272-274] Although still under discussion, the last studies point particle jamming due to frictional contacts that generate a frictional network as the cause of the increased elastic modulus.[275] In emulsions, such behavior has so far only been reported in particle-stabilized systems;[276, 277] however, the underlying mechanism remains unclear. We observed that, with increasing CB concentration, the intensity of the strain thickening decreased, turning to a small shoulder at 5 wt.% CB, which coincided with the transition to the electrical network formation (percolation threshold of 4.78 wt.% CB). At this point, two hypotheses could explain how the presence of CB inhibits the strain thickening effect: a) the CB filler induces a change in mean droplet size during the mixing process, influencing the strain thickening effect and b) the CB filler network hinders the droplet-droplet contact and absorbs the elastic energy originated from droplet deformation. These two hypotheses are revised below in this text.

Figure 4.4C shows the relation of the storage modulus at the LVE-region, as a measure of the stiffness of a material, with the CB concentration for the selected emulsion and the CB-electrofluids using pure solvents extracted from ref [255]. The value of *G'* for the unfilled emulsion is shown by a light blue dashed line. This value (544 Pa) is similar to the one found for 4 wt.% filler loading in a glycerol CB-electrofluid (479 Pa). The CB-emulsions exhibit *G*' values above the CB-electrofluids in both glycerol and PDMS, due to the high elastic deformation that the glycerol droplets uptake. The *G*' of all EFs scaled with a power law to the type $G' \propto \phi^n$, giving different scaling exponents that depend on the filler network and the filler-matrix interactions. Previous reports show that in combinations where the filler-solvent interactions dominate (high affinity between them as in the case of CB-PDMS), the resulting exponent is larger due to the additional reinforcement contribution compared to those, in which the stiffness is solely a result of the filler-filler interactions (low affinity as in the case of CB-glycerol).[255] In the emulsion, the continuous phase is PDMS, where the CB is localized. A similar scaling exponent than that for CB-PDMS (n = 4.41) with an offset from the initial *G'* of the pure emulsion was, therefore, expected. The obtained exponent from the fitting is, on the contrary, lower than that for CB-Glycerol (n = 2.03 and n = 3.49, respectively). This result is compatible with both of our previous hypotheses. On one hand, if the CB influences the glycerol droplet size during the mixing, smaller droplets may interfere with the CB-CB interactions, reducing their contribution to stiffness. On the other hand, the elastic scaling exponent would also be reduced if the CB network absorbs the elastic energy from the droplets' deformation.

To test the first hypothesis, we investigated the influence of the CB on the glycerol droplet size using optical microscopy image analysis of emulsions at different filler concentrations. Exemplary micrographs are shown in Figure 4.5A-C for CB-emulsions with filler loadings of 3, 5, and 7 wt.% CB. Additional micrographs used for image analysis are displayed in Figure S4.6 of the Supporting Information.

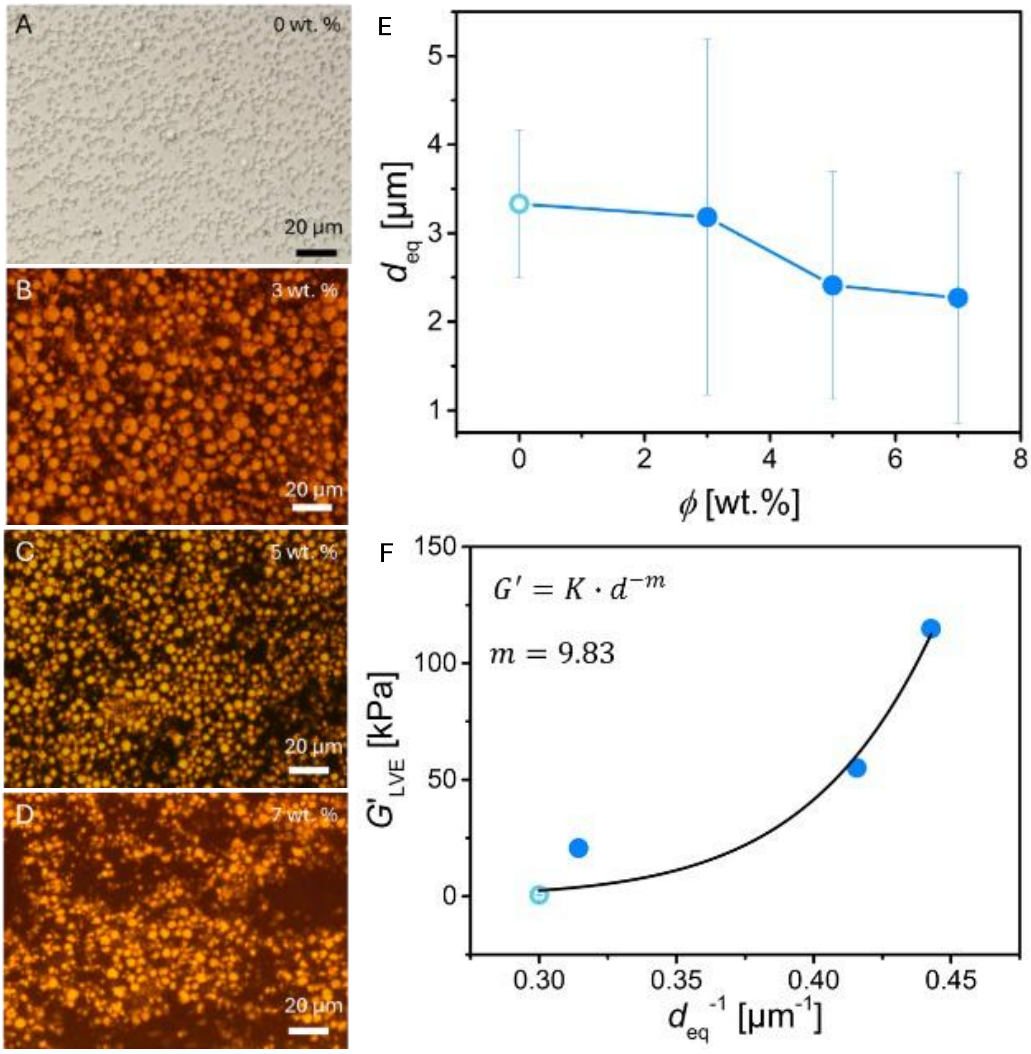

Figure 4.9: Optical microscopy images of PDMS/glycerol emulsions filled with A) 0, B) 3, C) 5, and D) 7 wt.% CB. E) Mean equivalent diameter of glycerol droplets depending on the weight percentage of CB. Cyan, open circle indicates the pure emulsion values and blue, closed circles the values for the CB-emulsion; lines are a guide to the eye. F) Plateau storage modulus of the pure emulsion (cyan, open circle) and CB-containing emulsions (blue, closed circles) depending on the inverse droplet diameter squared. The black line is a power law fit according to Ref [278].

To quantify the droplet size, the images were processed using a commercial analysis software (see Methods section and Figure S4.7 of the Supporting Information for details) and the mean equivalent diameter was calculated. We observed a decrease in the average droplet size with increasing CB concentration, up to a 32.2% for 7 wt.% CB (Figure 4.5D). This effect is in good agreement with previous reports, in which a decrease of droplet size in a water-in-oil emulsion was observed as a consequence of the presence of a stiff filler, such as CNTs, that disrupts the droplets during the mixing process.[258, 279] To analyze the impact of this reduction in size on the mechanical properties, Mudeme *et al*. used a modified power law of the form $G' = \mathrm{K} \cdot d^{-m}$ (where

K is a constant, d is the droplet diameter, and m a fitting exponent)[278] based on the Princen-Kiss model ($G' \propto d^{-1}$)[280] and the Malkin model ($G' \propto d^{-2}$).[281] These models, developed in particular for highly concentrated emulsions (HCEs), attribute the increase of elastic modulus with decreasing droplet size to the interfacial energy stored caused by a compression of droplets at emulsion concentrations above packing density.[282] The original models proposed universal exponents of 1 and 2; however, Mudeme *et al*. reported exponents between 1.67 and 2.25 for different emulsions. Variations in the experimental exponent have been attributed to the concentration of the dispersed phase,[281, 283] the droplet polydispersity,[281] and the use of surfactants that change the droplet interactions.[284] The emulsion in this work contains less dispersed phase fraction than required to be classified as HCE (ϕ=0.42 compared to ϕ=0.64 for random close packing). Nevertheless, we tested the unfilled 58 vol.% PDMS in glycerol emulsion with different droplet sizes, achieved by varying the rpm during the mixing process (see Methods section for details) for their elastic scaling to be compared with literature values. The scaling exponent of the elastic modulus with d^{-1} was found to be m=1.09 (see Figure S4.8 in the Supporting Information). This value, very close to 1, suggested a good correlation with the theoretical Princen-Kiss model. We used the same equation to evaluate the scaling of *G*’ of CB-containing emulsions since increasing filler content led to a reduction of the average droplet size. The fitting depicted in Figure 4.5E shows an exponent of m=9.83, far from any values reported of unfilled emulsions. The reduction of the droplet size by its own cannot explain this scaling the variations of *G*’ found in this study. Another factor to be considered is the impact that smaller droplets have on the strain thickening effect. As described above, we found a decrease of the strain thickening at increasing CB concentration in the emulsions. We performed amplitude sweeps of the unfilled emulsions with different droplet sizes (see Figure S4.9A in the Supporting Information) and calculated the strain thickening ratio, *i.e.* the ratio between the highest *G*’ value in the thickening regime and the *G*’ value before the increase (see Figure S4.9B in the Supporting Information). The reduction in droplet size caused an increase of the strain thickening effect in the pure emulsion. This is the opposite result of what we observed in the CB-containing emulsions. Therefore, the changes described in this study cannot be attributed to the reduced droplet size of the glycerol droplets by the presence of CB. We believe that both effects, reduced stiffness scaling and suppressed strain thickening, are related to the difference in elastic modulus between CB network and glycerol droplets. The presence of glycerol droplets causes a weaker scaling of stiffness of the CB network due to their lower elastic modulus. At high deformations (LAOS region), the CB network around the droplets acts as a stress-carrying network, transporting and distributing the elastic energy, which leads to the suppression of the strain thickening effect.

4.4. Conclusion

In this study, we present stable, electrically conductive emulsions, based on selective distribution of CB filler in polydimethylsiloxane (PDMS) and glycerol mixtures. Analytical centrifugation revealed an optimum ratio of 58 vol.% PDMS in glycerol for emulsion stability. The addition of CB rendered the emulsion conductive at half of the concentration for the electrical percolation threshold of CB-PDMS electrofluids. This is consistent with the proposed model, in which the CB particles (hydrophobic) tend to disperse better in PDMS (non-polar, continuous phase) than in glycerol (polar, dispersed phase). The glycerol droplets act, therefore, as volume exclusion component proving the feasibility of this strategy in liquid composites. The normalization of the CB concentration to the PDMS amount in the emulsion deviated less than 6% to that reported for CB-PDMS electrofluid. Unique mechanical properties of the CB-emulsions were found, such as a strain thickening behavior at low CB contents and a reduced scaling exponent of the storage modulus with increased filler concentration. The impact of the presence of CB in the emulsion preparation was evaluated by image analysis of optical micrographs. A reduction of glycerol droplet size was observed, laying the foundations of one of the hypotheses to explain the mechanical behavior of the CB-emulsions. Further analysis using pure emulsions with variable droplet size revealed this to not be the only effect governing the mechanical properties found in CB-emulsions. We believe that the presence of filler particles, particularly above the percolation threshold, creates a stress-carrying network around the glycerol droplets, that acts as a damping material and absorbs the elastic energy formed droplet deformation. Concomitantly, the contribution of CB to the scaling of storage modulus of the emulsions at increasing filler content is significantly reduced due to the presence of glycerol droplets compared to CB-electrofluids based on pure solvents. We envision the rational design of emulsion-based electrofluids through the selective combination of solvents and fillers, enabling a broad range of tunable mechanoelectrical properties. The predictability of these properties, however, remains limited due to the current lack of comprehensive research.

Carbon-based electrofluids have demonstrated utility as strain sensors,[60] stable conductors,[29] and conductive greases.[42] The emulsion-based electrofluids introduced here add a further dimension of tunability to their mechanoelectrical properties, thereby broadening their applicability range. Moreover, these emulsions deliver electrical performance comparable to single-solvent electrofluids while exhibiting substantially higher viscosities. Elevated viscosities mitigate sedimentation, enabling the use of dense metal fillers—such as silver particles or flakes—to yield electrofluids with markedly higher electrical conductivity, approaching that of liquid metals. Collectively, these advances position emulsion-based electrofluids as a versatile platform for soft, reconfigurable, and high-conductivity devices.

4.5. Methods

Sample preparation

Sylgard 184 (Dow Corning, USA) and glycerol ReagentPlus ≥99% (SigmaAldrich, Germany) were used as immiscible phases to prepare the emulsions and the carbon black (CB) used as filler was acetylene black, 100% compressed (Alfa Aesar, Germany). All chemicals were used as received. To create the emulsions, Sylgard 184 and glycerol were weighed into a cup and mixed with a DAC150.3 SP speedmixer (Hauschild, Germany) at 3500 rpm for 5 min. For the CB-emulsions, CB was weighed and subsequently, the two liquids added to the same cup. The mixing protocol was the same as for pure emulsions. Inspired by previous reports,[259, 285, 286] pure emulsions with varying droplet sizes were prepared using the same PDMS/glycerol ratio (58:42) but using different rpm values (1000, 1500, and 2000 rpm) for 5 min.

Analytical Centrifugation

The prepared emulsions were filled with a syringe into 2 mm rectangular polyamide cuvettes. The cuvettes were put into a LUMiSizer 6510 (LUM, Germany) and centrifuged at 2350 rcf for 20 h. Transmission profiles were recorded during this time. A transmission threshold of 20% was chosen to distinguish the turbid emulsion phase from the transparent PDMS and glycerol phase (see Figure S4.2 of the Supporting Information). The percentage of emulsion in the cuvette was calculated by measuring the length of the emulsion phase in the cuvette and dividing by the total length of the filled cuvette.

Optical Microscopy

Emulsions were placed on a glass slide (Carl Roth, Germany) and covered with a cover glass (VWR, USA). The cover glass was firmly pressed and slid onto the sample to achieve a thin layer by shear. A Nikon Eclipse LV100ND (Nikon, Japan) microscope was used to record the images. The images were taken in transmission mode.

Electrical conductivity measurements

The CB-emulsions were transferred into a Teflon® mold with the dimensions 1.5x1.5x0.5 cm. A 4-point probe setup connected to a Keithley 2350 sourcemeter (Tectronix, USA) was used to apply a current sweep and measure the resulting voltage. The fit of the I-V-curve was a linear regression, and the resistance was calculated from the slope value. The conductivity was derived by applying the following equation $\sigma=1/(2\cdot\pi\cdot s\cdot R)$, where σ is the conductivity, s is the distance between the electrodes (1 mm), and R is the measured resistance.

Rheoelectrical characterization

Rheology of the unfilled emulsions was performed using a MCR302e rheometer (Anton-Paar, Austria), with a concentric cylinder geometry (CC17) at a temperature of 25 °C. The bob was immersed slowly into the cup. A preshear of 175 s^{-1} for 30 s was applied followed by 15 min resting prior to the flow curves and the amplitude sweeps. Former ones were conducted at shear rates between 0.01 and 150 s^{-1} and the latter ones at strain values from 0.01 to 500%.

The characterization of the CB-emulsions was done in a MCR702e MultiDrive rheometer (Anton-Paar, Austria), in a 25 mm plate-plate configuration at 25 °C. The geometry was lowered slowly onto the sample and was let rest for 20 min to release initial stresses. Flow curves and amplitude sweeps were recorded at the same conditions as described above for the unfilled emulsions. For the electrical characterization, the upper and the lower geometries were connected to a Keysight E4980A LCR-meter (Keysight, USA). The LCR-meter was controlled with a python script to measure the resistance at each rheological measurement point.

The plateau value of the storage modulus (*G*') was calculated by taking the average *G*' of all points within the LVE region. The yield point was defined as the point where *G*' deviates 3% compared to the plateau values.

Image Analysis

The image for unfilled emulsions were segmented using the ImageJ Plugin WEKA.[287] Due to the poor contrast between glycerol droplets and PDMS, we marked several areas by hand and ran the WEKA algorithm to match the desired segmentation into two phases; PDMS and CB and glycerol droplets. For all other images, the commercial image analysis software Avizo (Avizo for EM-Systems, Thermo Fisher Scientific, USA) was used to determine droplet sizes. The optical micrographs were imported as 8-bit RGBA ".jpg" images of a size 2560×1920 pixels. Their physical pixel size was 68 nm due to the magnification in the optical microscope of 50x. The images were converted to 8-bit grayscale images (see Figure S4.7A of the Supporting Information). Non-local means filtering (10 px search window, 3 px local neighborhood) was employed to denoise the images prior to segmentation (see Figure S4.7B of the Supporting Information). Manual grayscale histogram thresholding was used to segment the droplet phase of the images. The threshold was set approximately at the minimum between the two peaks (see insert in Figure S4.7B in the Supporting Information). The result was a binary image consisting of pixels corresponding to the droplet phase and the "background" phase, i.e., PDMS+CB (see Figure S4.7C of the Supporting Information). Additional filtering artifacts were removed using the functions "Despeckle" (7 px Kernel Size in x/y), which removes single pixels that did not correspond to droplets, and "Remove Small holes", which closes gaps in segmented droplets (see Figure S4.7D of the Supporting Information). The final binary image was converted to a label image (see Figure S4.7E of the Supporting Information), where groups of connected pixels were identified as single droplets. In the label image, different droplets have different "labels" (numbers) assigned to them. Avizo provides functions to convert binary images to label ones: first, neighboring but apparently connected droplets need to be separated using the "Separate Objects" function, which employs a watershed-segmentation on a distance-transformed binary input image to split the droplets. Afterwards, the split objects are labelled (function "Labeling" with a 26-neighborhood) to obtain the label image. Droplets on the image border were removed from the label image using the "Border Kill" function (see Figure S4.7F of the Supporting Information). Finally, every unique label, i.e., droplet in the border-killed label image was analyzed using the "Label Analysis" module. Label areas A_i for every label i were computed by counting the number of pixels of the label and multiplying it by the physical size. The area-equivalent diameter $d_\mathrm{eq,i}$ was computed as

$$d_{eq,i} = 2\sqrt{\frac{A_i}{\pi}} \qquad (4.1)$$

Additionally, the circularity for every label y_i was calculated as

$$\psi_i = \frac{4\pi A_i}{{P_i}^2} \qquad (4.2)$$

where P is the perimeter of the label. Perfect circular droplets have $\psi = 1$, less-circular ones have $\psi \in (0,1)$. To exclude droplets that appeared visibly damaged we filtered our label analysis by allowing only labels with $\psi > 0.3$. Average area-equivalent diameters $\overline{d}_{eq}$ were obtained by

$$\overline{d}_{eq} = \frac{1}{N}\sum_i^N d_{eq,i} \qquad (4.3)$$

Acknowledgements

The authors acknowledge funding by the European Research Council (ERC) under the European Union's Horizon 2020 research and innovation program (Grant Agreement No. 949785 ELECTROFLUID). The authors thank Miguel Baños Maestro for his help acquiring optical microscopy images, Minh Quan Bui and Simon Blum for technical support, and Sergio Lago-Garrido, Niclas Hautz, and Gun Woo Park for fruitful discussions.

4.6. Supporting Information

Emulsion preparation and phase identification

Figure S4.1A shows a filled cuvette of 58 vol.% PDMS in glycerol emulsion before the analytical centrifugation (AC) test. The whole volume of the cuvette is filled with opaque emulsion and no phase separation was observed. Figure S4.1B shows an optical microscopy image of the same emulsion. Here, a polar ink was added that preferentially dissolves in glycerol to distinguish the emulsion phases. Blue, glycerol droplets can be observed in the image while the non-colored continuous phase corresponds to the PDMS.

A filled cuvette of the emulsion with carbon black (CB) before the AC procedure is shown in Figure S4.1C. Noticeably, the CB colored the emulsion homogeneously black. Only after the AC test, the phase separation can be observed for some mixtures.

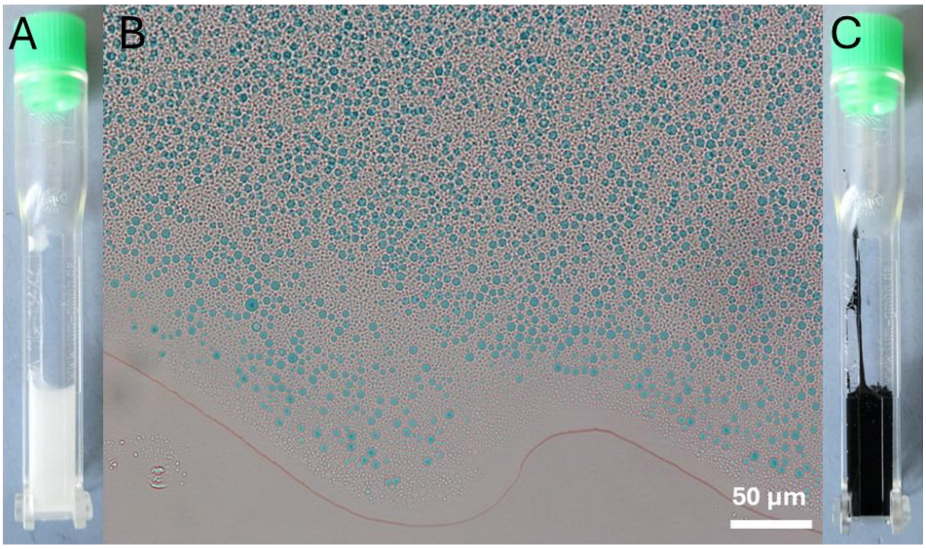

Figure S4.1: A: Cuvette filled with an emulsion of 58 vol.% PDMS in glycerol before AC test. B: Microscope image of the same emulsion with the glycerol phase in blue. C: cuvette filled with an emulsion of 58 vol.% PDMS in glycerol containing CB before AC test.

Analytical centrifugation test

To determine the percentage of stable emulsion phase at different PDMS/glycerol ratios, the transmission profiles of the emulsions among the length of the cuvette were recorded during an AC test. Figure S4.2 shows those transmission profiles. The x-axis denotes the distance from the center of rotation of the analytical centrifuge.

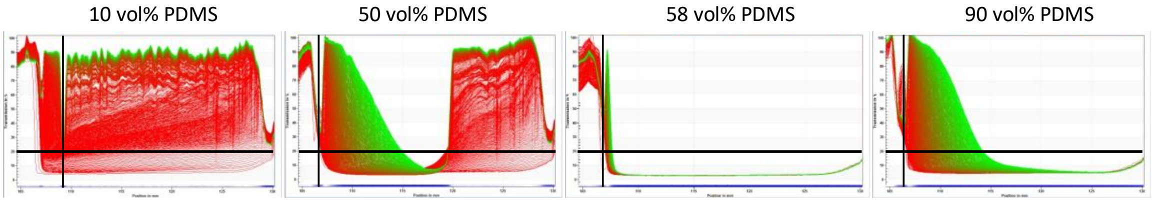

Figure S4.2: Transmission profiles for PDMS/glycerol emulsions with different concentrations of PDMS. Solid line marks 20% transmission.

To derive the percentage of emulsion phase we defined the appearance of an emulsion by a transmission value of ≤ 20 % (indicated by the horizontal black line). The used length of the cuvette was limited by the cell bottom and the meniscus (indicated by the vertical black line). The percentage of emulsion phase was calculated by the division of the length with transmission below 20% and the total length.

Optical microscopy images of 3 wt.% CB in PDMS/glycerol emulsion

Figure S4.3 shows optical microscopy images of 3 wt.% CB mixed into the PDMS/glycerol emulsion at different magnifications.

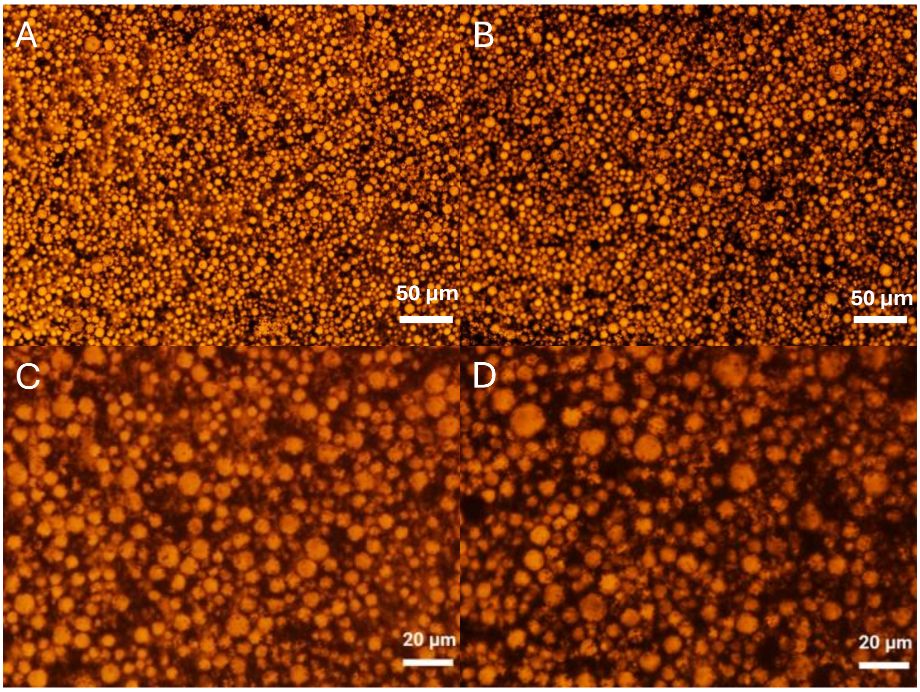

Figure S4.3: Optical microscopy images of 3 wt.% CB in PDMS/glycerol emulsion with a magnification of A-B: 20x and C-D: 50x.

Oscillatory rheology

Figure S4.4 shows amplitude sweeps of PDMS/glycerol pure emulsion and at increasing CB concentration.

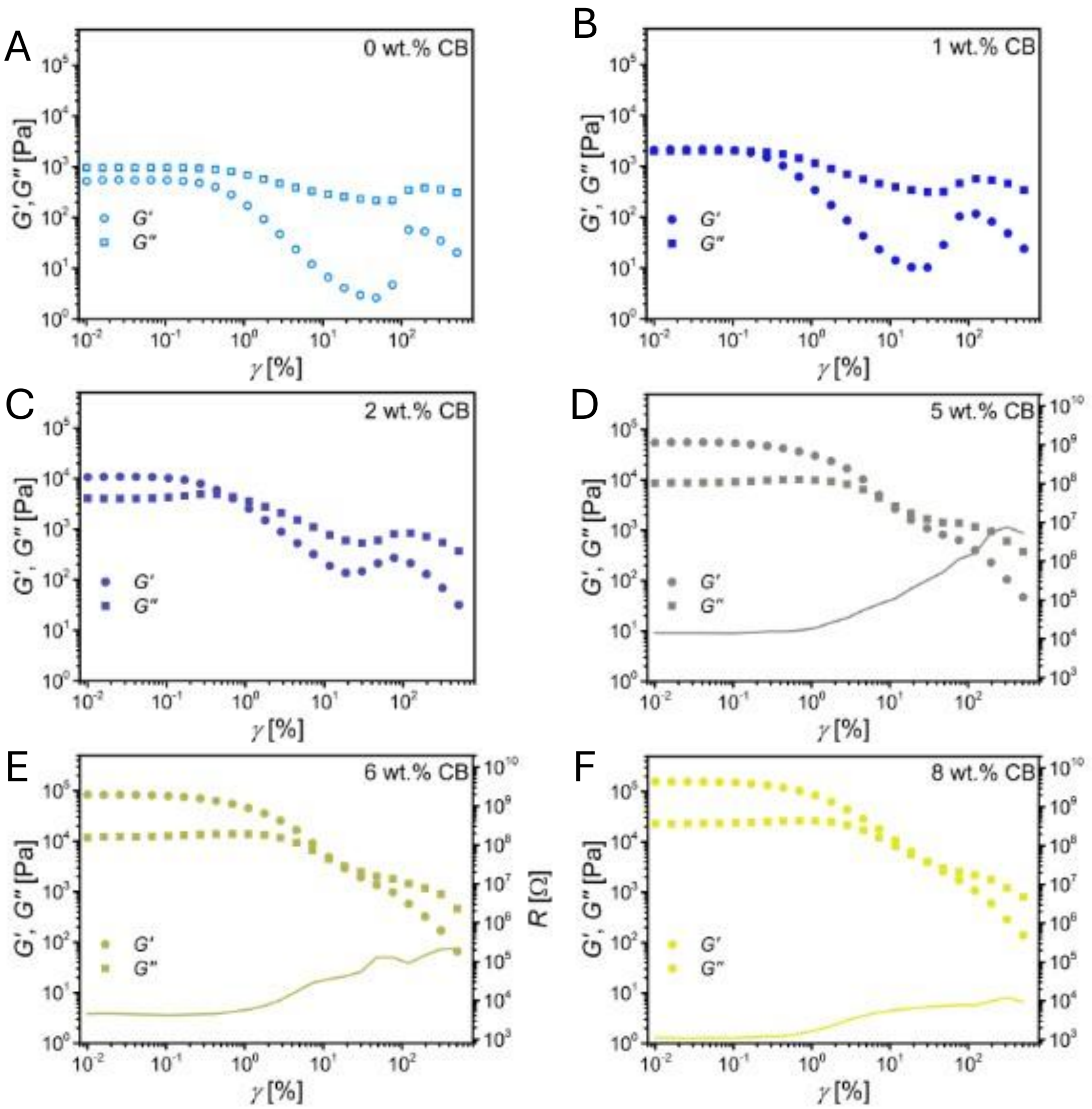

Figure S4.4: Storage (*G*') and loss (*G*'') modulus as a function of strain for PDMS/glycerol emulsions with different amounts of CB filler. A: 0 wt.%, B: 1 wt.% C: 2 wt.%, D: 5 wt.%, E: 6 wt.%, and F: 8 wt.%.

Figure S4.5 shows the evolution of the yield and the flow stresses, as well as the electrical yield stress in dependence of the filler weight percentage of the emulsion. With increasing filler concentration, all stress values increase. The electrical yield stress always appears at slightly higher values than the mechanical yield stress, but at considerably lower values than the flow stress.

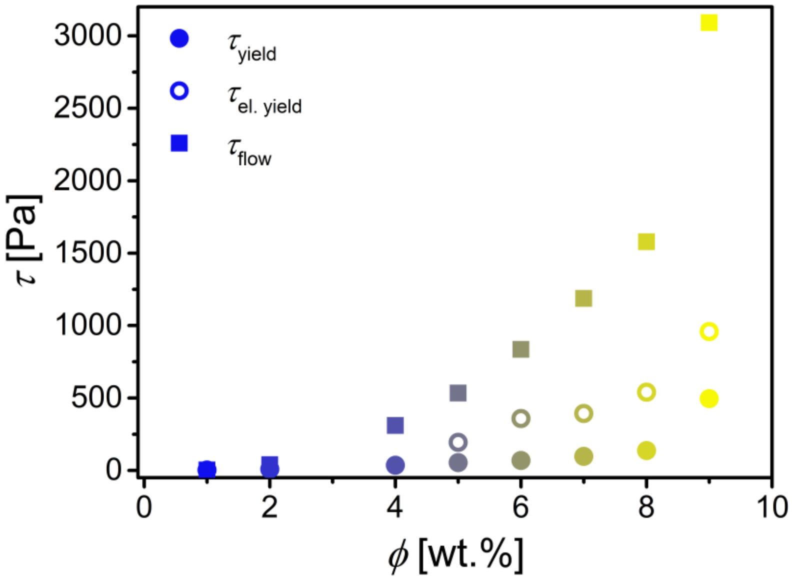

Figure S4.5: Shear stress vs CB weight percentage for mechanical yield stress (closed circles), electrical yield stress (open circles), and mechanical flow stress (closed squares). Colors from blue to yellow indicate increasing CB concentration.

Optical microscopy and image analysis

Figure S4.6 shows the micrographs used for image analysis and particle characterization. For the case of the pure emulsion (without CB), the image displayed in Figure 4.5A of the main text was used.

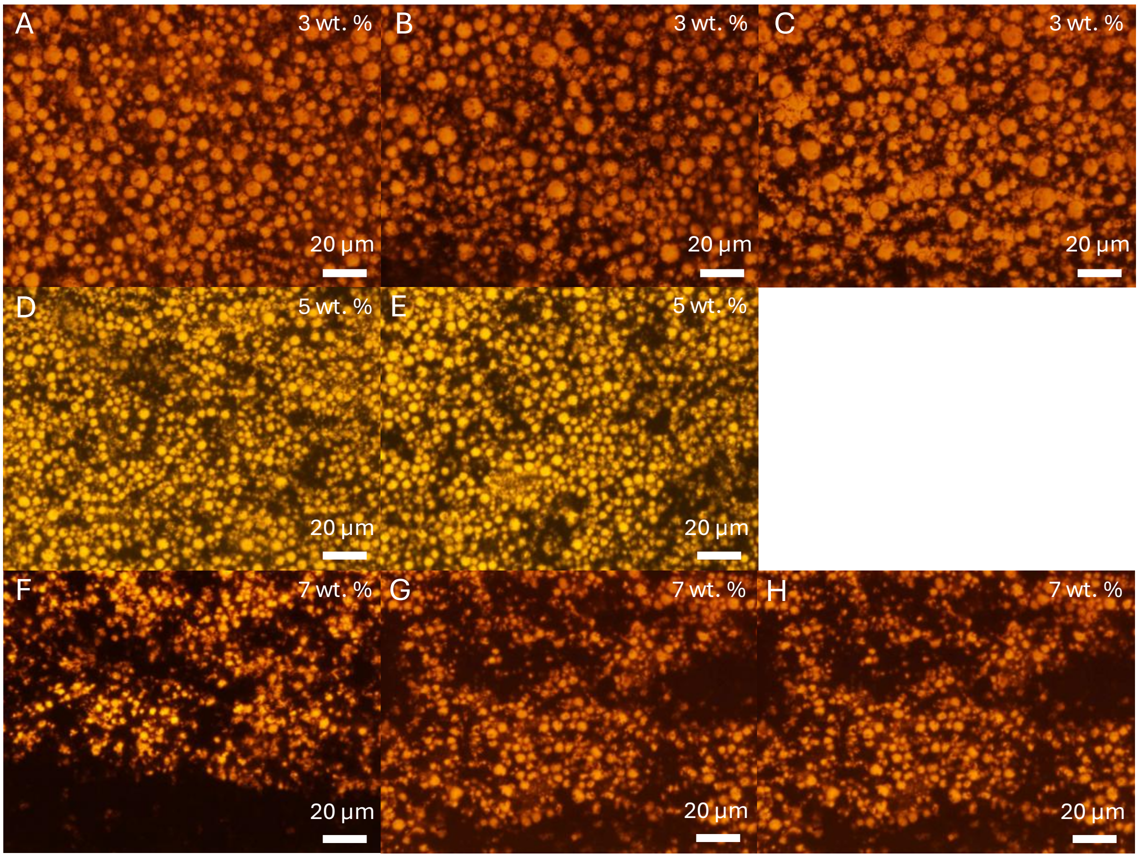

Figure S4.6: Optical microscopy images used for image analysis of 3 wt. % (A-C), 5 wt. % (D-E), and 7 wt. % (F-H).

Figure S4.7 shows the image processing procedure using the commercial software Avizo. The optical micrographs (Figure S4.7A) were filtered (Figure S4.7B) and segmented into binary images (Figure S4.7C). Small features that result from noise in the raw images were subsequently removed (Figure S4.7D) and individual droplets labelled (Figure S4.7E). Before analyzing their individual sizes, droplets ranging through the boundaries were removed (Figure S4.7F). For an in-depth description of the individual image processing operations, see the Methods section in the main text.

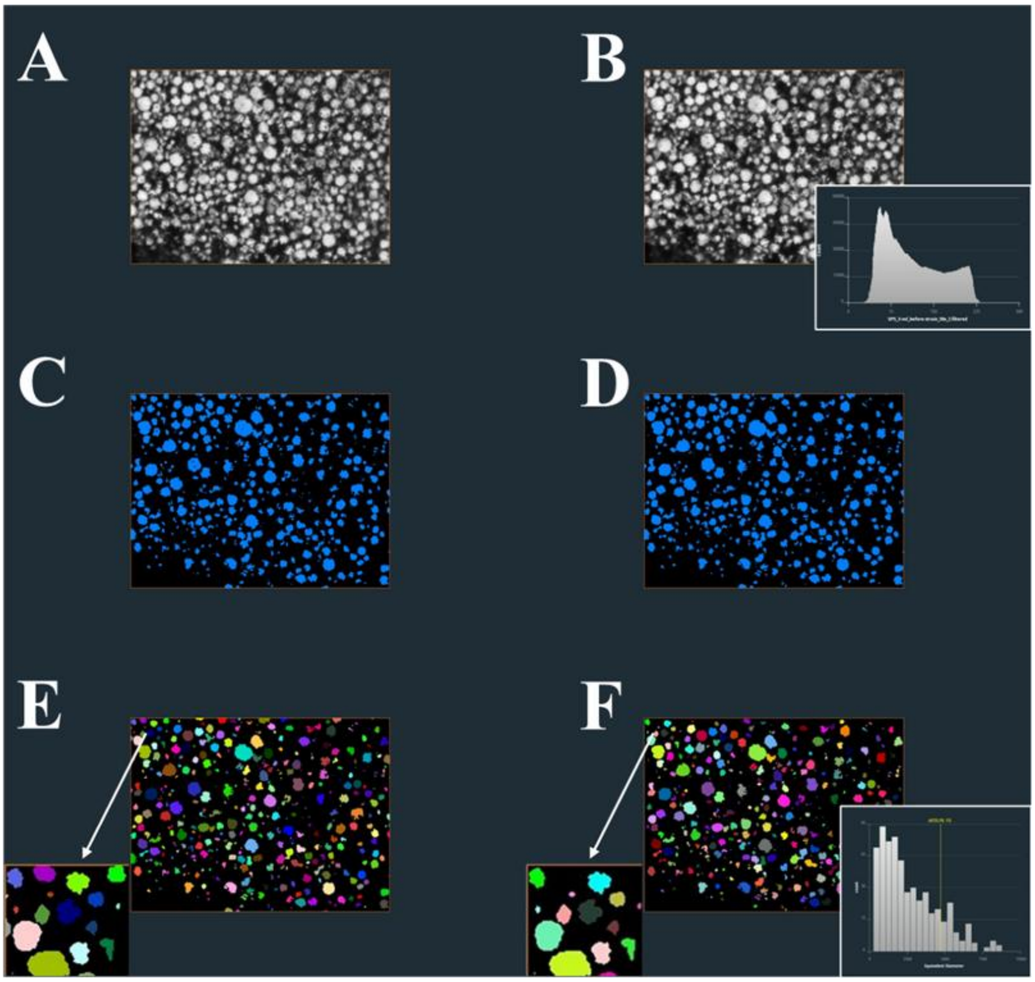

Figure S4.7: A: Greyscale, raw optical micrograph of the emulsions. B: Non-local means filtered image of A with the greyscale histogram in the lower right. C: Segmented droplet phase from simple histogram thresholding of B. D: Feature-cleaned version of C. E: Label-image of D where individual, non-touching droplets were assigned unique identifiers, shown as different-colored droplets. F: Border-killed label image where droplets piercing through the image border were removed.

Influence of the droplet size on the mechanical properties of unfilled emulsions

Figure S4.8 shows the plateau storage modulus *G'* as a function of inverse droplet diameter in unfilled PDMS/glycerol emulsions. Different droplet sizes are generated by mixing the unfilled emulsion at different rotational speeds. The points were fitted according to the empirical model: $G' = K \cdot d^{-m}$, where *K* is a fitting parameter and *n* is the scaling exponent. We obtained a value of *m*=1.09.

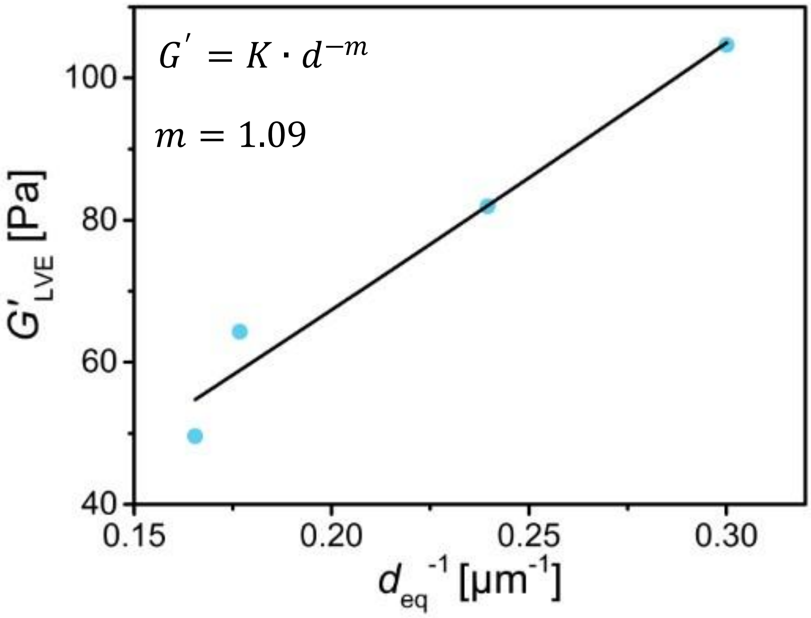

Figure S4.8: Plateau storage modulus vs d^{-1} of the unfilled emulsion. X-axis values from low to high are related to increased mixing speed (1000, 1500, 2000, and 3500 rpm) corresponding to smaller droplet sizes. The black line is the fit function according to the power law model $G' = K \cdot d^{-m}$.

Figure S4.9A shows the storage modulus *G'* during an amplitude sweep of emulsions, mixed with different mixing speeds. We correlate a reduction in mixing speed with larger droplet sizes (as has been demonstrated already multiple times in literature). It can be seen that the tendency of strain thickening is increased the higher the mixing speed and, therefore, the smaller the droplet size. Figure S4.9B shows the influence of the droplet size on the strain thickening ratio: D*G'*/*G'*$_0$, where D*G* is the difference in *G'* value at the peak and the lowest point before the thickening starts (*G'*$_0$). It can be seen that with decreasing droplet size (increasing inverse diameter) the strain thickening ratio increases for the unfilled emulsion.

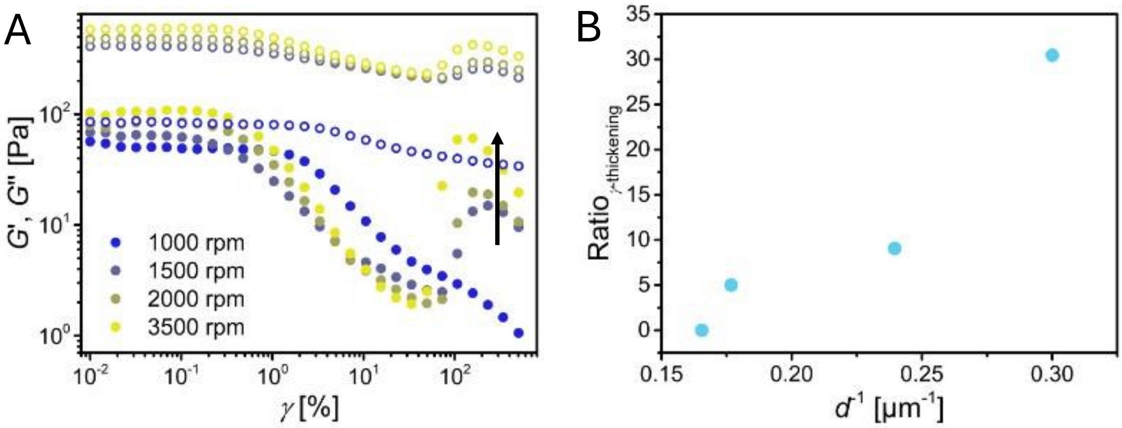

Figure S4.9: A: Amplitude sweep of 58 vol.% PDMS in glycerol emulsions prepared with different rpm for 5 min in a speedmixer. The black arrow indicates the increasing strain thickening with increasing mixing speed. B: Strain thickening ratio as a function of the inverse droplet size for the unfilled emulsion

5. Morphology-driven electromechanical performance of graphene-based electrofluids for emerging soft electronic systems

This chapter is based on the content of the article under review:

Schmidt, Dominik S.; Fortugno, Paolo; López-Cámara, Claudia-F.; Wiggers, Hartmut; and González-García, Lola. " Morphology-Driven Electromechanical Performance of Graphene-Based Electrofluids for Emerging Soft Electronic Systems." Submitted to the journal Advanced Materials Technologies.

5.1. Abstract

Electrofluids, concentrated suspensions of electrically conductive particles, have recently attracted attention for their potential as soft conductors. In this study, we investigated the influence of morphological differences in two-dimensional (2D) filler materials (graphene-like) on the electromechanical properties of glycerol-based electrofluids. Plasma synthesized few-layered graphene (FLG), chemically exfoliated multi-layered graphene (MLG), and bulk graphite were used as 2D fillers, which differed in specific surface area, aspect ratio, and intrinsic stiffness. Results showed that both electrical and mechanical percolation thresholds decreased with increasing filler aspect ratio. The high aspect ratio of the FLG promotes network formation at low filler concentrations, conferring its electrofluids with the lowest electrical (0.16 wt.%) and mechanical (0.63 wt.%) percolation threshold. Rheological amplitude sweeps revealed a larger linear viscoelastic region for electrofluids containing few-layered graphene, caused by their reduced internal stiffness and higher aspect ratio. This large capacity for storing elastic energy of FLG-electrofluids makes them almost insensitive to uniaxial tensile strain when encapsulated in elastomers, leading to gauge factors below 1, ideal for soft electrical resistors. In contrast, MLG-electrofluids exhibited good sensing properties as strain gauges. The presented study on structure-property relationships helps for rational design of electrofluids with tailored electromechanical properties that can be tuned for different use cases.

5.2. Introduction

Liquid conductors are a proven alternative for stretchable and flexible electronics.[288] Due to their liquid nature, they overcome limitations of classical materials such as brittleness and fatigue. Commonly, liquid metals[11] and ionic liquids are employed.[289] A recently presented type of liquid conductors is electrofluids (EFs),[255, 267, 290] suspensions of conductive filler particles that form transient, percolating networks within a liquid matrix. To some extent, EFs can be described as liquid composites, in which the filler particles reconfigure under mechanical deformation and maintain conductive pathways through transient contacts. There are already studies focused on their utilization, for example, as stretchable batteries[61] or as strain sensors with different designs processed via direct ink writing.[290] The affinity between filler and matrix plays a major role in the formation of the filler network. It has been shown that when replacing a non-polar polymer (polydimethylsiloxane) with a polar molecule (glycerol) in EFs using carbon black as the conductive filler, the electrical percolation threshold decreases by an order of magnitude due to the formation of larger carbon black agglomerates.[255] Besides the importance of the filler-matrix affinity, the type of filler has been reported to have an effect in the network formation. Multi-walled carbon nanotubes (MWCNTs) were investigated as conductive fillers in EFs with glycerol as a matrix leading to conductive networks at very low filler loading that can flow while retaining electrical conductivity. They have been proposed as fluid interconnects.[267]

Filler particles can be classified by their morphology: 0D (spheres), 1D (wires, rods, tubes), or 2D (flakes, sheets). To create a conductive network, fillers must come in contact to each other. The morphology not only affects the creation of the network, but also the interparticle geometrical contacts. For example, spherical particles can only form point contacts, wires can form linear contacts, and flakes can form planar contacts, which leads to different contact resistances in the conductive network. For instance, solid composites using anisotropic fillers (1D and 2D fillers) have shown superior conductivity compared to those using spherical fillers with comparable filler concentration.[96] Additionally, those fillers, characterized by high aspect ratio, have been proven to reduce the amount of filler required to make the composite conductive, i.e., the percolation threshold. [92, 93]

Different types of 2D fillers have been explored in the recent years to fabricate soft conductor solid composites, e.g., sheets of semiconducting MoS_2,[246] MXenes,[291] silver flakes,[292] or graphene flakes.[293] MoS_2 is mostly used due to its semiconducting properties in electronics and optoelectronics[294] and has been recently studied as conductive filler in polymer composites to create materials with negative piezoresistivity.[246] MXenes are transition metal carbides or nitrides that are used in electrode materials due to their high conductivity and beneficial electrochemical properties.[295] Silver flakes are typically introduced into composites to make use of their high intrinsic conductivity. Since silver is a costly material, carbonaceous materials are proposed as alternatives due to their reduced costs, low density, and, for certain types like graphene, comparable electrical conductivity.[225] Therefore, ultracapacitors,[296] strain sensors,[297] electrodes[298], and actuators[299] have been prepared using graphene as filler material.

A monolayer of graphene provides an exceptional high value of intrinsic conductivity of 10^8 S/m,[66] similar to metallic conductivity. This conductivity, however, is reduced when the layers stack, forming a multilayer graphene flake. Ultimately, when the number of layers is great enough, the particles exhibit bulk properties, i.e., graphite.[300] Moreover, the properties of different graphene-like particles change depending on their preparation method. The commonly used syntheses are top-down procedures, such as electrochemical exfoliation of bulk graphite. In this process, ions are intercalated between the individual layers of the graphite by applying a voltage that causes a partial oxidation and, thus, an increase in the interlayer distance. Subsequently, the intercalated ionic species are reduced under formation of gaseous reaction products, which cause the exfoliation of the graphite layers.[301] In a recent work, Mardlin *et al*. developed an alternative procedure based on thermomechanical exfoliation, avoiding the use of additional solvents.[69] The authors mechanically stirred graphite flakes with a maximum torque of 35 N·m at 250 °C and created exfoliated sheets with less than 5 layers and a surface area up to 433 m^2/g.[69] The common factor of these exfoliation procedures is the relative high oxidation that the particles undergo. Therefore, in many cases, a reduction step must be applied. An alternative approach for the synthesis of graphene sheets is the bottom-up microwave plasma synthesis. Using this method, a hydrocarbon reactant is typically injected into a plasma reactor, where it is decomposed into its atomic constituents. Further downstream, these atoms and molecules recombine into different chemical products, leading to the gas-phase formation of solid carbonaceous structures. Depending on the reaction conditions, the nucleation and growth of the final carbon product can be tailored to produce, e.g., few-layer graphene particles.[68, 302, 303]

In this work, we discuss morphological differences of three different 2D-structured carbonaceous species and their respective impact on electromechanical properties in conductive suspensions, EFs. Plasma-synthesized few-layered graphene (FLG), commercial multi-layered graphene flakes (MLG), and graphite powder (GrP) are used to create EFs with glycerol as the matrix material. The electrical and mechanical percolation for these systems was determined by 4-point-probe conductivity measurements and oscillatory rheology, respectively. A figure of merit of stiffness versus electrical conductivity is presented and the relationship between the specific surface area and both the electrical and the mechanical networks formation in the EFs is here discussed. Rheoelectrical characterization was employed to assess the electromechanical response of EFs under mechanical deformation. Finally, selected EFs were encapsulated and underwent uniaxial mechanical deformations while the changes in electrical resistance were monitored to determine their piezoresistivity. FLG-EFs show a remarkably low sensitivity (Gauge Factor of 1) at different strains, making this material a promising candidate as stretchable conductive resistors, whereas the other two EFs exhibited potential as stretchable strain sensors with relatively large piezoresistivity. We discuss the interplay between filler morphology and electromechanical properties of EFs, serving as general guidance for a rational design of 2D-based EFs.

5.3. Results and Discussion

Two different graphene fillers were used to fabricate glycerol-based electrofluids: commercial multi-layered graphene powder (MLGs) and self-synthesized, plasma-made few-layered graphene flakes (FLGs). Commercial graphite powder (GrP) was also investigated as reference material. The FLGs were produced following the procedure described in previous publications.[70, 302] Briefly, FLG sheets were synthesized by injecting approx. 190 sccm of ethanol vapor into a microwave plasma reactor operated at atmospheric pressure. The generated carbon particles produced via this method were collected in a fiber filter positioned downstream of the plasma region. Commercial MLGs were sourced from Enerage Inc. (Taiwan), which prepares the flakes via chemical exfoliation.[304] Commercial GrP was purchased from Sigma Aldrich and consists of a fine powder of graphite particles. Scanning electron microscopy (SEM) images (Figure 5.1A-C) show the morphology of the studied species after dispersing them in ethanol and drop casting on a silicon wafer. FLGs showed relatively large, crumbled fractal structures. A closer look using transmission electron microscopy (TEM) revealed small building blocks of graphene flakes (lateral sizes up to 300 nm)[302] that form larger agglomerates (see Figure S5.1 of the Supporting Information). Contrarily, MLGs and GrPs consist of relatively smooth, larger individual particles, appearing the MLG flakes to have a more pronounced 2D morphology (higher aspect ratio). Despite these differences, analytical centrifugation (AC) of the particles dispersed in ethanol revealed similar size distributions (1.5 - 4.5 µm range) for all three particle types (see Figure 5.1D). This size range, although in good agreement with the particle characteristics described above for MLGs and GrPs, contrasts with the observations made for FLGs. This, however, can be attributed to a strong agglomeration of FLGs in ethanol forming larger structures.

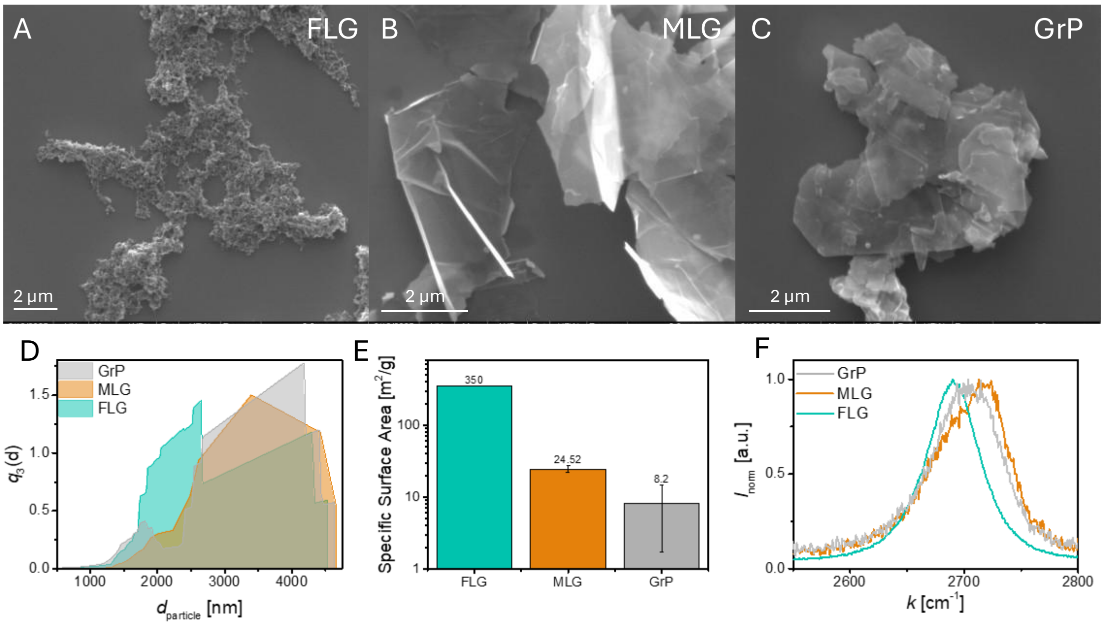

Figure 5.1. A-C: SEM images of FLG, MLG, and GrP, respectively, on a silicon wafer. D: Volume weighted size distribution of the different graphene fillers in ethanol done with analytical centrifugation E: Specific surface area determined by BET for FLG, MLG, and GrP particles. F: Raman spectra for wavenumbers between 2550 and 2800 cm^{-1}.

Brunauer-Emmett-Teller (BET) measurements were performed to evaluate the impact of the geometrical characteristics of the different particles on their specific surface area (SSA). The results depicted in Figure 5.1E show that FLG exhibited the largest SSA (350 m^2/g), followed by MLG (25 m^2/g), and GrP (8 m^2/g). We attribute these differences primarily to the different aspect ratio of the particles. In 2D structures, the influence of the particle lateral size in the SSA is minimized due to their high anisotropy, however, the degree of delamination plays a major role.[305] Imagine a disk of diameter 1 a.u. and thickness 0.001 a.u., thus its surface area is 1.574 a.u.^{2}. A transversal cut in the middle of the disk would lead to a minimal increase of the surface area to 1.576 a.u.^{2}, while a longitudinal cut (exfoliation) would lead to an increase to 3.145 a.u.^{2}. Considering the thickness of a single graphene layer to be 0.34 nm and its SSA 2630 m^2/g,[306] the estimated number of layers based on the BET results would be in average 7.5 layers for FLGs, 105.2 layers for MLGs, and 328.8 for GrPs, equivalent to thicknesses of 2.6, 35.8, and 111.8 nm, respectively. This calculation is, however, based on the SSA of powders, and aggregation/agglomeration effects are not considered. These effects could lead to an underestimation of the SSA and, therefore, overestimation of the number of layers.

As alternative method to determine the average number of layers of graphene particles, Raman measurements were also performed (see Figure 5.1F). Previous reports demonstrated the correlation between the shape of the 2D Raman band at wavenumbers of approximately 2700 cm^{-1} with the number of AB-stacked graphene layers in the range of 1 to 5.[307] Yet, it is challenging to distinguish between the spectra of graphene with more than 5 layers from that of bulk graphite.[307] Raman spectra of MLG and GrP showed a broad, asymmetric peak (FWHM > 60 cm^{-1}) shifted to larger wavenumbers, indicating 5 or more layers.[307] The spectrum of the FLG, however, showed a symmetric and relatively narrow peak (FWHM ≈ 55 cm^{-1}) that has been reported as characteristic for monolayer graphene sheets. This is based on AB-stacked layers and, therefore, might underestimate the number of layers when the particles present turbostratic stacking.[308-311] Despite the degree of uncertainty, we estimate the average number of FLG layers to be 2–7.

EFs were prepared by mixing the different graphene species with glycerol at different filler concentrations. Their electrical conductivity was measured using a 4-point-probe set-up (see Methods section for details). Figure 5.2 shows the so-called electrical percolation curves for the three filler types using glycerol as liquid matrix.

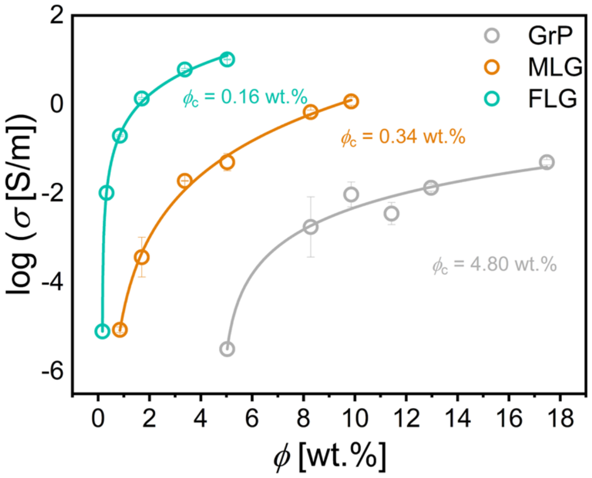

Figure 5.2. Electrical percolation curves for glycerol-based EFs using different 2D-structured carbonaceous fillers at increasing concentrations. Data points were fitted according to classical percolation theory as shown in Equation 1. Numbers in the graph indicate the critical concentration for percolation. Each datapoint represents the mean value of n=3 measurements.

The curves were fitted according to the classical percolation theory,

$$\sigma = A \cdot (\phi - \phi_c)^t, with\ \phi > \phi_c \tag{5.1}$$

where σ is the electrical conductivity, A is a fitting parameter, ϕ is the filler concentration, ϕ_c is the critical filler concentration, and t is the critical exponent.[248] The electrical percolation threshold is defined as the critical filler concentration from which on at least one conductive path in the volume is formed, inducing a transition from an insulator to a conductor material. This critical filler concentration is influenced by factors such as filler size,[52] aspect ratio,[251] surface area,[312] and their interactions with the matrix.[313] These parameters determine how efficiently the filler is on creating connections, thus forming a volume spanning network. We found that the FLG-EFs had a slightly lower percolation threshold (0.17 wt.%) compared to MLG-EFs (0.35 wt.%), and far below with respect to the one for GrP-EFs (4.80 wt.%). The observed critical percolation concentrations exhibited an inverse relationship with the surface area of these carbonaceous species, in good agreement with previously reported findings in the literature. For instance, Haridas *et al.* demonstrated that the percolation threshold decreased from 10.4 vol.% to 8.2 vol.% upon replacing graphite (SSA 6.8 m^2/g) with graphene nanoplatelets exhibiting a specific surface area >300 m^2/g.[69, 272] As discussed above, the SSA is related to the thickness of the 2D-structured carbonaceous species and, therefore, with their aspect ratio.

For 2D materials, the aspect ratio is calculated from the quotient of lateral size and thickness. The broad size distribution obtained from AC results (1.5 - 4.5 μm) hinders the calculation of an exact lateral size; for the following discussion, we assume that MLG and GrP particles have a lateral size of 3 μm. For the FLG, the lateral size of the individual sheets obtained from TEM images and previous reports was approximately 300 nm.[302] Using these lateral sizes and the estimated number of layers of each particle described above, the corresponding aspect ratios were calculated as 176.5 (FLG), 83.3 (MLG), and 26.8 (GrP). For anisotropic fillers, the percolation threshold was reported to scale inversely proportional to the aspect ratio as $\phi_c \sim$ aspect ratio^{-1}, i.e., a higher aspect ratio causes a lower percolation threshold.[314, 315] Using this simplified relation, the percolation thresholds are predicted as 0.97 wt.% (FLG), 2.03 wt.% (MLG), and 6.18 wt.% (GrP), respectively (see Methods section for the calculation details). The numbers obtained, although overestimated, fit the order found for the EFs. Nevertheless, this approximation assumes perfectly distributed, monomodal particles, and neglects any agglomeration effects.

Carbonaceous particles tend to present hydrophobic surfaces, making the polar glycerol a relatively bad solvent for particle dispersion. As the oxygen content can vary depending on the fabrication method, we measured it for each filler and normalized it by the SSA (see Table S5.1 in the Supporting Information) in order to evaluate the filler-matrix affinity. Low oxygen contents were found, indicating weak filler-matrix and stronger filler-filler interactions. In FLGs, the oxygen content per m^2 SSA was particularly low (0.022 mg/m^2), one order of magnitude less when compared to the one measured for MLG (0.875 mg/m^2) and GrP (0.156 mg/m^2). Agglomeration effects due to poor filler-matrix interactions have been reported to reduce the percolation threshold of EFs. If the filler and the solvent have a strong affinity, filler-matrix interactions have an increasing contribution over filler-filler interactions, promoting a good dispersion. On the other hand, a mismatch in polarity shifts the contribution towards filler-filler interactions, promoting agglomeration.[255] Since all EFs in this study were prepared using glycerol (i.e., a polar matrix) and all fillers show a relatively low concentration of polar groups on their surface, all tested fillers tended to agglomerate to reduce contact with the matrix. Particularly strong tendency is expected for FLGs due to their low oxygen content, explaining the lower percolation threshold observed in FLG-EFs relative to those containing MLG and GrP.

Figure 5.2 also shows that the maximum conductivity achieved in the three EFs differed. FLG-EFs exhibited the highest maximum conductivity (10.26 S/m), followed by MLG-EFs (1.45 S/m), and GrP-EFs (0.05 S/m). In a theoretical work, Zare *et al*. developed a model to determine the influence of different filler and matrix properties on the electrical conductivity of solid graphene composites.[316] They found a correlation between the maximum conductivity and the number of layers of the graphene filler. Single or few layered graphene showed the highest conductivities, while an increased number of layers decreased the maximum conductivity.[316] The order of fillers in terms of increasing maximum conductivity obtained in this study aligns with the expected behavior associated with a reduced number of layers. Additionally, the oxygen content in the filler materials must be considered, assuming that it represents defects present on the graphene lattices, i.e., electron scattering points[317, 318] or causes an increase in the interlayer distance.[319] We investigated this effect by comparing the electrical conductivity of EFs using MLGs with low and high oxygen content and found increased conductivity for EFs with MLGs with low oxygen content at all concentrations above electrical percolation (see Figure S5.2 in the Supporting Information). Therefore, the higher oxygen content found in both MLG and GrP particles (compared to FLG) would also lead to a reduction in the maximum electrical conductivity of these EFs.

The evolution of the mechanical and electrical networks under shear deformation was studied by means of oscillatory amplitude sweeps coupled with *in-situ* electrical resistance measurements (see Methods section for details). These measurements provide insight into the stored elastic energy (storage modulus, *G*') and the dissipated energy (loss modulus, *G*''). The coupling with *in-situ* electrical resistance measurements allows for tracking changes in the electrical network properties during applied deformation. Results for selected filler concentrations are depicted in Figure 5.3A. The concentrations were chosen based on their position on the percolation curve to ensure sufficient electrical conductivity in all samples (i.e., 5 wt.% FLG, 8 wt.% MLG, and 13 wt.% GrP). Results corresponding to other concentrations can be found in Figure S5.3 in the Supporting Information.

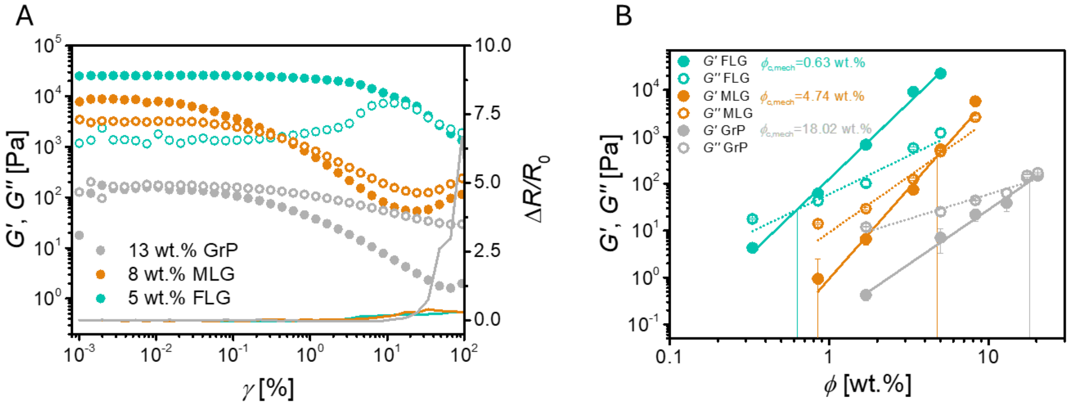

Figure 5.3. A: Rheoelectric amplitude sweep for different carbon-based EFs. Closed symbols refer to *G*' and open symbols to *G*''. Solid lines are the relative change in electrical resistance. B: *G*' (closed circles) and *G*'' (open circles) values within the linear viscoelastic region (LVE) at different filler concentrations. All data points were fit with a power law following $G=A*\phi^n$, solid lines for *G*=*G*' and dotted lines for *G*=*G*''. The solid vertical lines denote the corresponding mechanical percolation concentrations, also indicated as numbers in the graph, which were determined by the intersection of the fit functions of *G*' and *G*''.

In the mechanical response, three main regions can be identified in the graphs. First, the linear viscoelastic (LVE) region at low strains, which is defined by a constant *G'* value, where the deformations are elastically absorbed by the EF. The value of *G'* within this region reflects the stiffness of the material. The three examined EFs exhibited markedly different stiffness values; surprisingly, in the inversed order of the employed filler concentrations. Additionally, for both FLG and MLG-based EFs, a well-defined mechanical network was observed, as indicated by *G' > G''* in the LVE-region. This mechanical network conferred a solid-like (gel-like) behavior to the EFs. This means that the FLG- and MLG-EFs retained their shape at rest, while GrP-EF exhibit fluid-like behavior and flows without the need of external forces. The end of the LVE is defined by the yield point, corresponding to a 3% deviation from linearity of *G'*. Beyond this point, plastic deformations occur, leading to irreversible structural changes. The yield point for the FLG-EF was determined at significantly higher strains compared to MLG -and GrP-EFs, also at other concentrations (see Figure S5.4 in the Supporting Information), indicating higher elasticity of the FLG filler network.[320, 321] At even larger strains, *G'* and *G''* intersect at the so-called flow point, denoting a transition from solid-like to liquid-like behavior. The strain (stress) required to induce complete plastic deformation of the EFs (and, therefore, make them flow) was found at ~48% strain (1306.62 Pa) for the FLG-EF and at ~0.07% (2.49 Pa) for the MLG-EF. No flow point was observed for the GrP-EF since it exhibited liquid-like behavior even at the smallest strain deformation, giving it the weakest network of all three tested EFs. A remarkable difference between FLG and MLG-EFs is the pronounced increase in *G''* observed for the former and not for the latter right before the flow point, indicative of network breakup processes.[321] Since *G''* represents the dissipated energy via internal friction—an effect amplified by the presence of numerous filler-filler contacts[321]—

these results suggest a more interconnected filler network in the FLG-EF than in the MLG- and GrP-based EFs.

The change in electrical resistance ($\Delta R/R_0$) was monitored during the test in order to investigate the electrical network during deformation. At the LVE-region, the electrical resistance remained constant for all EFs. At higher strains, both FLG-EF and MLG-EF showed a small, gradual increase of 30% and 40%, respectively. In contrast, a strong response was found for GrP-EF, which showed an increase in resistance of >800%, starting at ca. 20% strain. The higher aspect ratio of both FLGs and MLGs led to networks in which the particles tend to form planar contacts. Under mechanical deformation, the particles slide on each other retaining electrical conductivity. Although the distortion of the electrical network is similar, a large difference was found in the mechanical response. As described above, both the LVE-region and the flow point of the MLG-EF were remarkably smaller than those for FLG-EF, meaning that the mechanical network of FLG-EF withstands larger strains before breaking. As the electrical behavior (dominated by the particle contacts)[322] is comparable, we attribute this difference in the EFs' mechanical properties to the intrinsic properties of the fillers. Multi-layer graphene particles are stiffer than FLGs due to their significantly higher number of layers,[323] leading to more brittle networks than the FLGs, which can absorb mechanical energy by stretching and bending.[324] The largest electrical response to applied strain was found for the GrP-EF. Graphite powder presents the lowest SSA and the largest number of layers, making them more bulky and relatively stiff, decreasing the number of contact points in the network per weight unit. The contact between particles in this case seemed to be very labile—even considering that GrPs-EFs are studied at larger concentration of fillers, the filler network was not sufficiently strong to achieve clear gel-like behavior—, resulting in easy breakage upon mechanical deformation, and leading to great increase in the electrical resistance.

The mechanical network is linked to stress-carrying particle contacts. We studied its formation at increasing filler content by means of the evolution of *G'* (elastic component, solid behavior) and *G''* (viscous component, liquid behavior) in the LVE-region of the EFs (see Figure 5.3B). We define the mechanical percolation threshold as the critical concentration, at which G' > G'',[325, 326] i.e., the EF no longer flows at rest but presents a gel-like behavior (see Methods section for details). This critical concentration increased from 0.63 wt.% for FLG-EFs to 4.73 wt.% for MLG-EFs, and 18.02 wt.% for GrP-EFs. Haridas *et al*. reported a similar trend for exfoliated graphene sheets in polyethylene oxide (PEO), where the mechanical percolation threshold decreased with increasing SSA of the sheets.[272] Regardless of the type of carbonaceous species used, electrical percolation occurred at lower filler concentrations than the mechanical percolation. Similar behavior was previously reported by Penu *et al.* for carbon nanotube (CNT)-polymer composites.[178] They concluded that a single volume spanning cluster was sufficient to achieve electrical conductivity, yet insufficient to provide a rigid mechanical network.[178] In a more recent work on EFs containing multi-walled CNTs, the same trend was reported and used to create flowable conductive joints.[327] In addition, *G*' values are a measure of the material stiffness. The trend of *G*' matches the one observed for the SSA values, i.e., the larger the SSA, the higher the storage modulus value at a given filler concentration. This trend, although also found in solid polymer composites,[312, 328] relies on a different mechanism in the EF case. In polymers, reinforcement occurs when polymeric chains bond (chemically or physically) to the filler surface, restricting their movement. In the studied EFs, however, the molecular nature of glycerol and the relatively hydrophobic character of the 2D-structured carbonaceous species hinder the reinforcement effects. As a result, their mechanical properties are primarily governed by the filler-filler contacts,[329] that increase in number and area with higher SSA, as well as by the intrinsic stiffness of the fillers themselves.[330, 331]

An increase in filler concentration results in a simultaneous rise in both electrical conductivity and stiffness. This causes a trade-off between these two parameters, which are of relevance for EFs performance and processing.[290] The resulting Figure of Merit (FoM) is displayed in Figure 5.4 and describes the relation between electrical and mechanical network properties. The data was fitted with a simple power law according to $G' \sim A \cdot \sigma^m$, with *A* being a constant and *m* the scaling exponent.

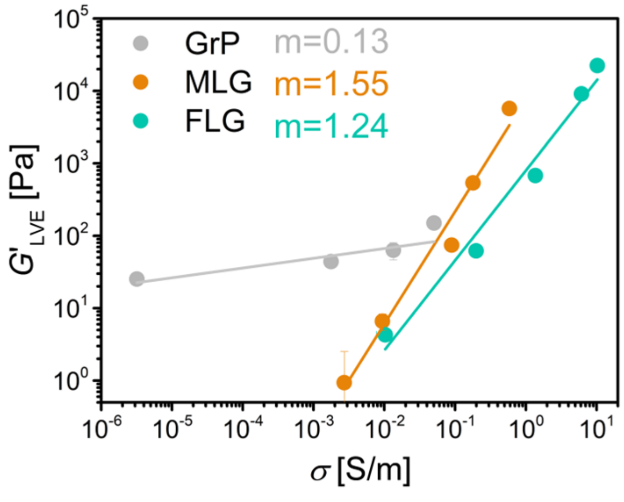

Figure 5.4. Figure of Merit for *G*' against conductivity. Concentrations increase from left to right as 0.17, 0.33, 0.85, 1.7, 3.37, and 5 wt.% FLG, 0.85, 1.7, 3.37, 5, 8.27, and 9.87 wt.% MLG, and 5, 8.27, 13, and 17.47 wt.% GrP. Solid lines represent a power law fit function of the form $G' = A * \sigma^m$, with *m* indicating the corresponding exponent.

FLG- and MLG-EFs showed a similar *m* exponent (1.24 and 1.55, respectively) with an offset of one order of magnitude towards higher conductivities for the FLG-EFs. GrP-EFs exhibited a significantly smaller *m* exponent (0.13). These scaling exponents describe the preferential reinforcement of the electrical or the mechanical network with the increase of filler concentration. When deriving the individual scaling exponents for conductivity and storage modulus (see Figures S5.5A and S5.5B in the Supporting Information), it was found that the conductivity scales with the exponent of 2.55 for both FLG- and MLG-EFs, meaning that the electrical network develops comparably. In terms of stiffness, MLG-EFs exhibited a slightly larger value of 3.85 compared to 3.25 for the FLG-EFs. Therefore, the observed difference in the FoM is originated from the mechanical network development. The GrP-EFs represent a special case. Here, the scaling exponent of conductivity (4.65) exceeds that of stiffness (2.33), contrary to the behavior observed for FLG- and MLG-based EFs, despite the higher intrinsic stiffness of the GrP particles. This suggests that overall stiffness is primarily governed by the effectiveness of filler-filler contacts, which do not contribute as strongly and result in the reduced scaling exponent.

To test the performance of EFs as stretchable conductors or sensors, we designed uniaxial tensile test measurements. For this purpose, EFs were encapsulated in elastomeric tubes, attached to a uniaxial tensile tester, subjected to cyclic loads of 10%, 20%, and 40% strain while the electrical resistance was recorded (see Methods section for details). Figure 5.5A shows the change of resistance over time for the different EFs over cycles of 40% strain with a strain rate of 10%/s.

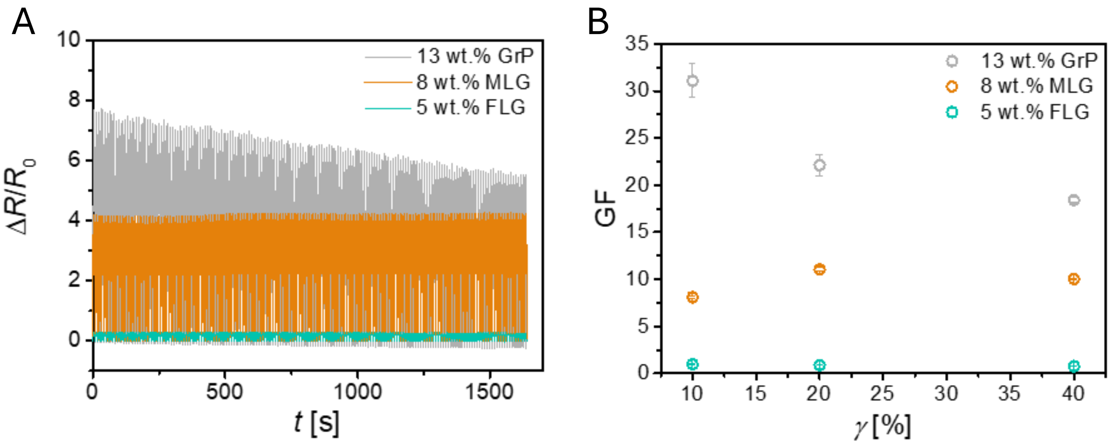

Figure 5.5. A: Change in resistance of cyclic tensile test measurements at a strain of 40% for 13 wt.% GrP (grey), 8 wt.% MLG (orange), and 5 wt.% FLG (turquoise) electrofluids. B: Gauge Factor values for different electrofluids at different strain values calculated from the respective cyclic test. Each data point represents the mean GF determined for n=5 different cycles.

A constant cyclic behavior was found after an initial equilibration time for all EFs, except for the 13 wt.% GrP-EF that reduced amplitude over the cycles. Remarkably, the FLG-EF showed a minimal change in resistance compared to the other two filler types. To facilitate a quantitative comparison of the sensitivity of the electrical response with the uniaxial deformation, the Gauge Factor (GF) was calculated using the first part of Equation 5.2:

$$\mathrm{GF} = \frac{\Delta R}{R_0} \cdot \frac{1}{\varepsilon} = 1 + 2\upsilon + \frac{\Delta \rho}{\rho_0} \cdot \frac{1}{\varepsilon} \tag{5.2}$$

where R_0 is the initial resistance, ΔR is the difference of initial resistance and measured resistance, ε is the applied strain, υ is the Poison's ratio, ρ_0 is the initial resistivity, and $\Delta\rho$ the difference of initial and measured resistivity. Derived from Equation 2, a GF=2 indicates the absence of piezoresistivity, assuming a Poison's ratio of 0.5 for ideal incompressible materials. Figure 5.5B shows the GF at different strains for the three studied EFs. The lowest GF was found for the FLG-EF, which was strain independent with a value of approximately 1. A GF = 1 is a rare case since it is characteristic of materials with negative piezoresistivity, i.e., the resistivity decreases with applied strain.[255] On the opposite side, GrP-EF exhibited the largest GF of 31 at 10% strain and 18 at 40% strain. Intermediate values were found for MLG-EF with a GF between 8 and 11 depending on the applied strain.

In solid composites based on graphene fillers, values of GF comparable to those presented in this study for MLG-EFs and GrP-EFs have been reported. For example, Liu *et al*. found a GF of 17.7 when using commercial graphene flakes in a TPU matrix.[332] Solid composites with such low GF, as observed for FLG-EFs, are rare, pointing to a potentially distinct material behavior when FLGs are combined with the electrofluid concept. In the work of Zheng *et al*., PDMS composites based on either CB or CNTs were fabricated and subjected to 10% uniaxial tensile strain.[204] They found GF values of 15.75 and 4.36, respectively, discussing that lower aspect ratio fillers are more prone to lose contact under strain than higher aspect ratio fillers.[204] This observation is in good agreement with our results for 2D carbonaceous fillers.

Despite the differences in deformation modes, shear *versus* elongation, the observed small changes in resistance for FLG-EF, intermediate for MLG-EF, and large for GrP-EF are in good agreement with the results of the amplitude sweeps and the structural model described for the different graphene-based EFs, allowing predictions on the electromechanical behavior in uniaxial deformation based on the rheoelectrical behavior. The network created by FLGs is more elastic and the connections stronger, which retains electrical conductivity. Unlike the FLG, in MLG-EF and GrP-EF, the elastic network was weaker. Upon mechanical deformation, their network is destroyed, and the relaxation depends solely on the reconfiguration of the particles in the liquid matrix (re-agglomeration). Stress relaxation tests performed in shear deformation support this hypothesis (see Figure S5.6 in the Supporting Information). The residual modulus found for FLG-EF (and not in MLG- or GrP-EFs) is indicative of remaining elastic contributions in the material, i.e., FLG-EF is a viscoelastic solid. This means that even after the flow point, the breakage of the network is not complete and some elastic network remains, retaining the electrical connectivity and, therefore, explaining the minimal change in electrical resistance.

Summing up, the performance of electrofluids with 2D-carbonaceous materials as fillers is controlled by structural and surface design levels that influence network formation and functional properties:

1. High specific surface area (SSA) and aspect ratio lower percolation thresholds (both electrical and mechanical) that lead to higher electrical conductivity. Few-layer graphene (FLG) exhibits the largest SSA and aspect ratio of all the fillers studied, enabling dense contact networks and superior electrical performance.
2. A mismatch between the polarity surface of the filler and the liquid carrier fosters agglomeration, promoting the network formation at lower filler contents. The interparticle interactions are stronger compared to the particle-solvent interactions, leading to stronger networks. We used glycerol (a polar solvent) as liquid carrier; FLG with very low oxygen content (high hydrophobicity) forms stronger networks than MLG and GrP.
3. High oxygen content not only changes the hydrophilicity of the particles (see previous point), also it is a measure of number of lattice defects on the surface of 2D-carbonaceous particles. MLG and GrP with higher oxygen levels showed reduced maximum conductivity due to increased interparticle spacing and number of defects.
4. Filler particles with low intrinsic bending stiffness generate networks that adsorb more elastic energy. This is reflected in longer range of elastic deformation and low electrical resistance sensitivity. FLG-EFs exhibited the largest LVE-region and flow stress whereas the smallest Gauge Factor.

Studies on the influence of the aspect ratio of one-dimensional (1D) fillers on the electromechanical properties of conductive polymer composites have been reported.[333] In contrast, systematic investigations of the effects of layer stacking in two-dimensional (2D) fillers remain scarce. We anticipate that our findings extend beyond electrofluids and are broadly applicable to other classes of composite materials. Therefore, we conclude that the structural investigation of graphene fillers allows for rational predictions on the electromechanical behavior of electrofluids. Stretchable sensors, as well as stretchable resistors, can be created by choosing the type of graphene filler, enabling further tunability of electrofluids as soft electronic components. For example, to fabricate stable, stretchable electrical resistors (low GF), the ideal electrofluid contains sheet-like particles that present the combination of high aspect ratio (large contact areas), poor compatibility with the solvent (strong contacts), high level of purity (high intrinsic conductivity), and low intrinsic bending stiffness (elastic energy absorption).

5.4. Conclusion

In this study, we examined the electrical and mechanical properties of electrofluids (EFs) formulated with three different types of 2D carbonaceous fillers: few-layered graphene (FLG), multi-layered graphene (MLG), and bulk graphite (GrP). These fillers differ in oxygen content, intrinsic stiffness, number of layers, and aspect ratio. Plasma synthesized FLG combined the highest aspect ratio, lowest oxygen content, strongest agglomeration behavior in polar solvents, and lowest bending stiffness among the studied materials. Consequently, FLG-EFs form networks in glycerol at the lowest filler loadings compared to those with MLG or GrP. In contrast, the higher oxygen content of MLG and GrP introduced lattice defects, limiting their EFs maximum conductivity. Rheological measurements revealed a significantly larger linear viscoelastic region for FLG-EFs, enabling greater elastic energy storage. We attributed this finding to the reduced bending stiffness of few-layered graphene species, which allows bending and crumpling resulting in a more elastic network rather than brittle. Uniaxial tensile tests confirmed strain-insensitive electrical behavior with a gauge factor of 1, indicating negative piezoresistivity for FLG-EFs in contrast to the large positive piezoresistivity exhibited for MLG- and GrP-EFs. These findings demonstrate that rational selection of 2D fillers with certain morphology enables tunability of electromechanical properties in electrofluids.

5.5. Methods

Sample preparation

The used chemicals were: self-made few-layered graphene prepared following the procedure described in a previous work,70 graphene powder P-ML20 (Enerage Inc., Taiwan), graphite powder, <20 µm, synthetic (Sigma-Aldrich, Germany), and glycerol ReagentPlus ≥99 % (Sigma-Aldrich, Germany). All chemicals were used as received. To prepare the electrofluids, the desired amount of filler was weight into a cup, and, subsequently, the glycerol was added. The mixing was performed with a 2-step mixing in a DAC 150.3 SP VAC-P speedmixer (Hauschild, Germany) at a speed of 1000 rpm for 5 min and 2500 rpm for 7 min. Images of the samples are shown in Figure S5.8 in the Supporting Information. Test specimens for uniaxial tensile testing were prepared by filling the electrofluids into a tube made from Ecoflex silicon polymer. After injection of the electrofluid, two copper cables were introduced and the tube sealed again with Ecoflex.

Electron microscopy

Scanning transmission microscopy (SEM) was done using a FEI Versa 3D DualBeam FIB-SEM system (FEI, USA) at 10 kV. For transmission electron microscopy (TEM), a JEOL JEM-2200FS microscope (JEOL, Japan) was used at an acceleration voltage of 200 kV. Sample preparation included well-dispersing the nanoparticles in ethanol for

20 minutes via sonication. Afterwards, few droplets were drop-casted on a silicon wafer (SEM imaging) or on a lacey carbon support on a copper TEM grid.

BET measurements

The Brunauer-Emmett-Teller (BET) specific surface area analysis (SSA) was done with a Nova 800 (Anton-Paar, Austria) using nitrogen adsorption. The samples were degassed under vacuum at 250 °C for 960 min.

Elemental analysis

The fillers were analyzed for elemental oxygen presence using an ELTRA® ELEMENTRAC ONH-p 2.

Raman measurements

For Raman spectroscopy, a small amount of sample powder was transferred onto a glass slide and compacted with a spatula. The measurements were done at room temperature and under ambient atmosphere, at wavenumbers between 100 and 3200 cm^{-1}. The device used was a Renishaw inVia Raman spectrometer that was operated at a laser wavelength of 532 nm.

Analytical centrifugation

The particle size distribution was analyzed using a LUMiSizer analytical centrifuge (LUM, Germany). Suspensions of 0.002 wt.% of filler in ethanol were prepared and mixed at the same conditions as the final samples. Suspensions were then transferred into rectangular polyamide (PA) cuvettes. The centrifuge procedure used speeds between 2000 and 4000 rpm accumulating a total measurement time of approximately 2 h. The analysis was performed using StepView 6 software. The particle size distribution was determined using volume weighted analysis.

Electrical conductivity measurement

The conductivity measurements were performed in a 4-Point-probe configuration to neglect the wire and contact resistances. For that, each electrofluid was filled in a custom-made, Teflon® mold (1.5x1.5 cm^2 with a thickness of 0.5 cm), a geometry that ensures the applicability of the 4P-probe measurement model. Current-Voltage curves were recorded using a Keithley 2350 Sourcemeter (Tectronix, USA). The resistance was extracted from the slope of the linear function.

Predictions on the electrical percolation threshold were done following the approximation of $\phi_c \sim \text{aspect ratio}^{-1}$. The extracted percolation thresholds are in vol.%, since this relation describes percolation from a volume occupation point of view. Values of 0.57 vol.% (FLG), 1.2 vol.% (MLG), and 3.7 vol.% (GrP) were obtained. The transformation to wt.% was done according to Equation 5.3:

$$\phi_w(wt.\%) = \frac{\phi_v \cdot \rho_f}{\phi_v \cdot \rho_f + (1 - \phi_v) \cdot \rho_m} \cdot 100 \qquad (5.3)$$

with ϕ_v being the volume fraction of the filler, ρ_f the density of the filler, and ρ_m the density of the matrix. For all fillers, a density of 2.16 g/cm^3 was used.

Rheological measurements

All rheological measurements were performed with a MCR702e TwinDrive rheometer (Anton-Paar, Austria). If not declared differently, all measurements were done at 25 °C using a parallel plate geometry with a diameter of 25 mm (PP25) with a gap of 0.5 mm. Oscillatory amplitude sweeps were performed at a strain ranging from 0.001 to 100 % at a frequency of 10 rad/s. Resistance data were recorded using a Keysight E4980A LCR-meter (Keysight, USA). LCR-meter and rheometer were coupled in a way that the electrical signal was recorded at every rheological data point.

We determined the concentration for mechanical percolation by first fitting the data of *G'* and *G''* to a power law of the form displayed in Equation 5.4:

$$G' = \mathrm{A} \cdot \phi^n \qquad (5.4)$$

where A is a constant, ϕ is the filler concentration and *n* is the scaling exponent. The intersection between the fit functions for *G'* and *G''* values is defined as the critical concentration for mechanical percolation. This procedure has been reported for the determination of mechanical network formation in particle filled suspensions.[325, 326]

Stress Relaxation measurements were performed by applying a step strain with a subsequent holding for 30 min, during which the stress was monitored. The relaxation modulus *G*(*t*) was calculated according to Equation 5.5:

$$G(t) = \frac{\tau(t)}{\gamma} \qquad (5.5)$$

where $\tau(t)$ is the stress over time and γ is the applied step strain.

Uniaxial tensile tests

All uniaxial electromechanical tests were performed with a Hegewald & Peschke Inspect 5 tensiometer (Hegewald & Peschke, Germany). The test specimens were attached to the tensiometer and connected via copper wires to a Keithley DMM6500 Digit Multimeter (Tectronix, USA) (see Figure S5.7 in the Supporting Information). The samples were mounted at a length of 30 mm and then pre-stretched to a length of 39 mm. For the cycling test, strain cycles of 40 % to 10 % were applied with a speed of 10 %/s. The samples were pre-cycled for a total of 1000 cycles to equilibrate the sample and the subsequent 300 cycles were used for representation.

Statistical Analysis

For the electrical conductivity, samples were prepared, and their conductivity was acquired three times (number of measurements n=3). The storage modulus values within the LVE represented in Figure 5.4 are the mean value of all data points within this LVE region (the number of points vary from sample to sample). Gauge factor values were calculated from n=5 randomly selected cycles within the whole measurement. The presented data points are the mean values from these 5 cycles, and the error bars show their standard deviation.

Acknowledgements

L.G-G and D.S.S. acknowledge funding by the European Research Council (ERC) under the European Union's Horizon 2020 research and innovation program (Grant Agreement No. 949785 ELECTROFLUID). We thank Dominik Perius for acquiring SEM images and Albenc Nexha for performing the Raman measurements L.G-G and D.S.S. acknowledge Sergio Lago-Garrido, Niclas Hautz, and Gunwoo Park for fruitful discussions. P.F. acknowledges support from the International Max Planck Research School SurMat and funding by the German Research Foundation (DFG) within priority program 2289 (project number: 462473659).

5.6. Supporting Information

Morphology and surface chemistry

Figure S5.1 shows TEM images of the FLG particles at three different magnifications. At higher magnifications, the individual sheets can be distinguished from the ones forming larger aggregates.

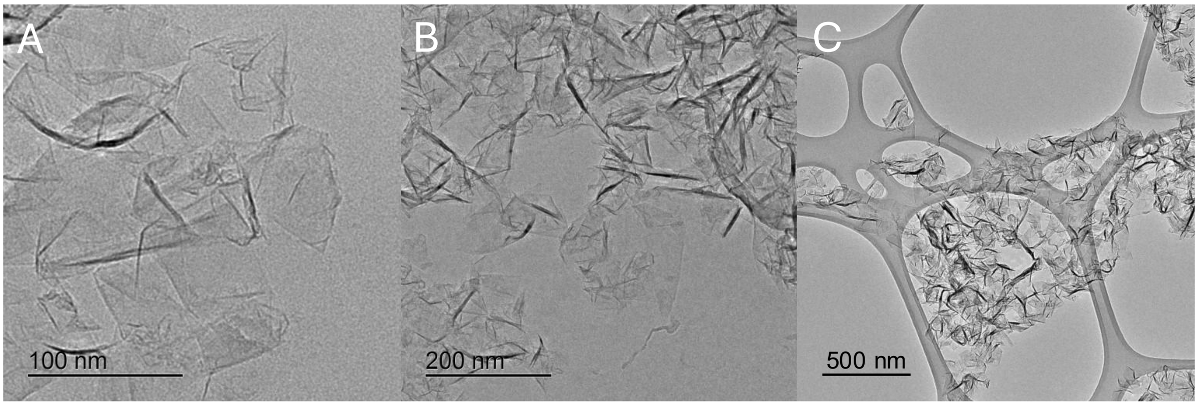

Figure S5.1: TEM images of FLG at different magnifications.

Table S5.1 summarizes the oxygen content of each filler by means of the weight percentage. Additionally, the mass of oxygen was normalized by the surface area of each filler type to get a more accurate comparison of the actual surface coverage.

Table S5.1: Results of the oxygen content analysis and normalization to the exposed surface area for the three different graphene fillers.

Filler	FLG	MLG	GrP
Oxygen content [wt.%]	0.768	2.146	0.128
Oxygen content per surface area [mg/m^2]	0.022	0.875	0.156

Maximum conductivity of MLG-EFs

Figure S5.2 shows the difference in electrical conductivity for MLG flakes with different oxygen content. The one with high oxygen content (2.15 wt.%) is the filler that was used the present study. The sample with lower oxygen content (1.76 wt.%) showed higher absolute numbers of conductivity, aligning with the discussed influence of defects that are induced with increasing oxygen content

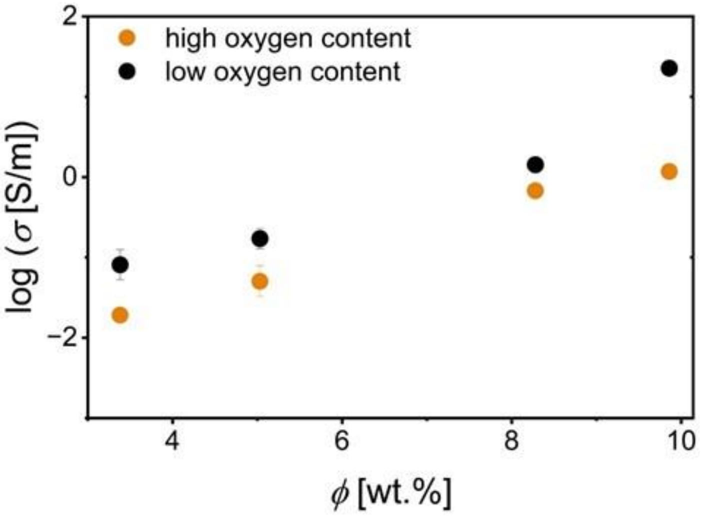

Figure S5.2: Electrical conductivity as a function of filler concentration for MLG flakes with high oxygen content (orange) and low oxygen content (black).

Oscillation rheology

Figure S5.3 shows the amplitude sweeps for different filler concentrations for different filler types with coupled *in-situ* electrical measurements, showing the change in resistance.

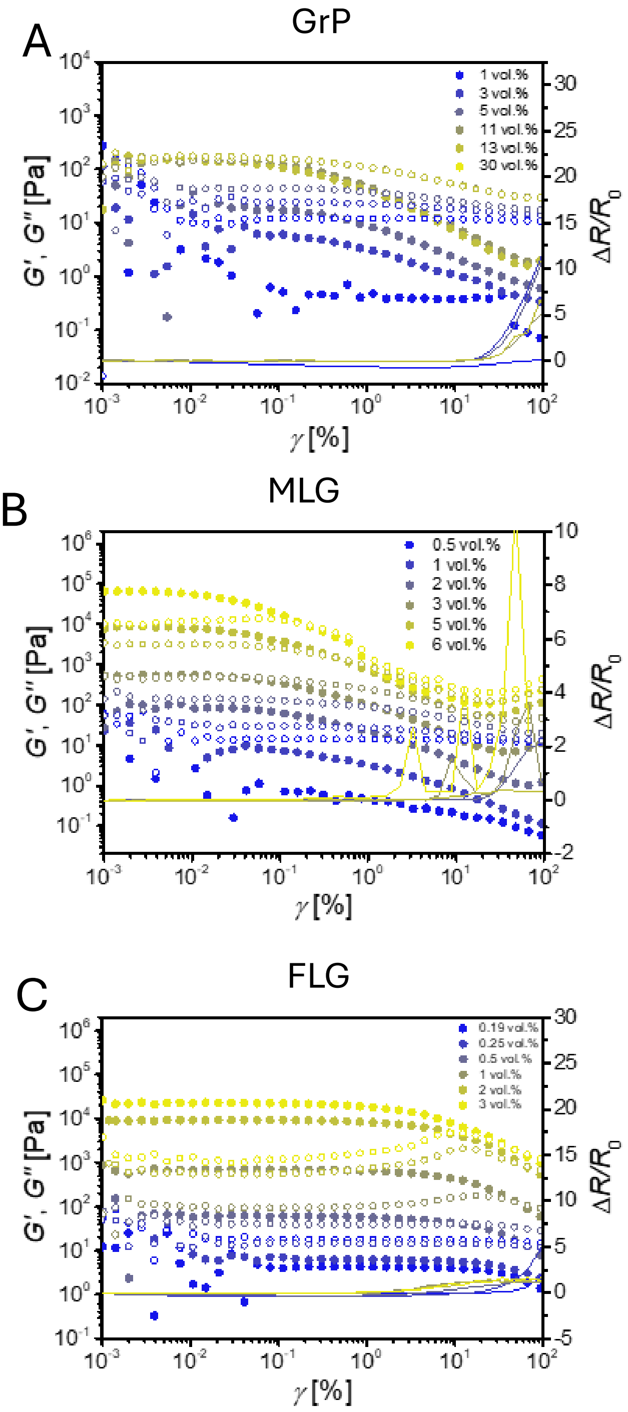

Figure S5.3: Amplitude sweeps with *in-situ* monitored change in resistance for A: GrP-EFs, B: MLG-EFs, and C: FLG-EFs. Concentration increases from blue to yellow with *G'* being denoted with closed symbols and *G''* with open symbols.

Conductivity, modulus scaling, and yield strain scaling

Figure S5.4 shows the yield strain γ_{yield} for different filler concentrations in the different electrofluids. The yield strain was determined by the point of a 3% deviation of the G' value from the LVE value. It was observed that the yield strain of FLG-EFs is significantly higher compared to MLG and GrP-EFs. We relate this observation to the intrinsic elasticity of the FLG filler itself, allowing them to bend and deform, adding additional elasticity to the materials and extending the breaking point of the network.

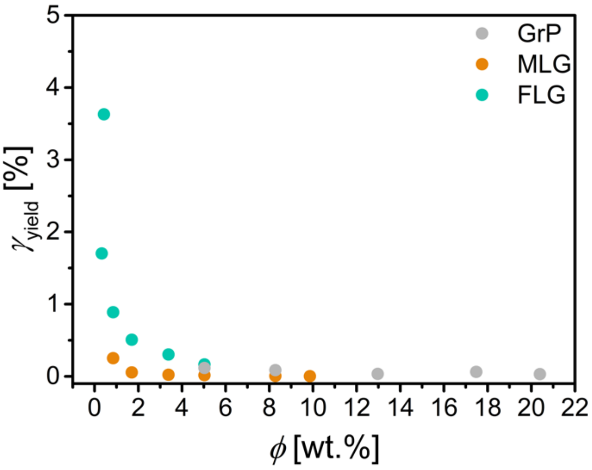

Figure S5.4: Yield strain values as a function of filler concentration for GrP (grey), MLG (orange), and FLG (turquoise) electrofluids.

Figure S5.5A shows the power law scaling behavior of electrical conductivity in dependence of the filler concentration. Figure S5.4B shows the same power law scaling but for the storage modulus.

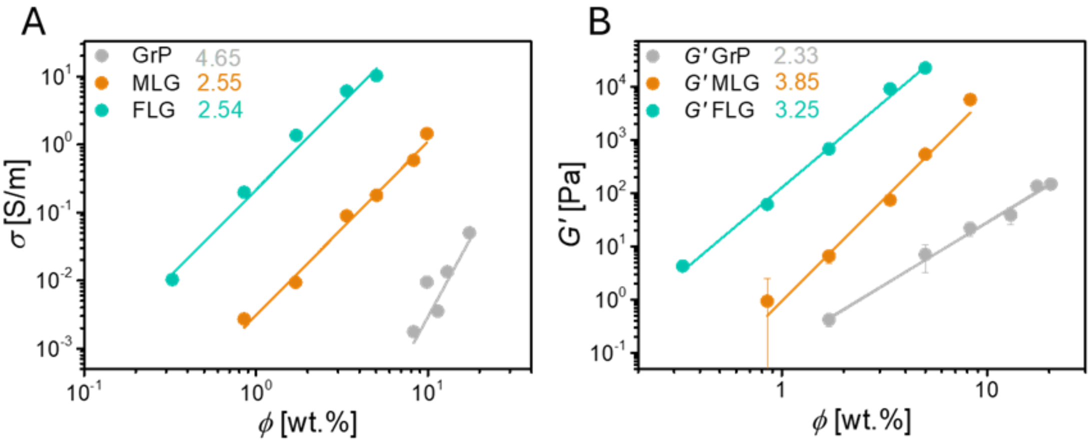

Figure S5.5: A: Conductivity and B: Storage modulus as a function of filler concentration on a double log plot. Solid lines are a power law fit of the type $\sigma/G' \sim \phi^t$. Corresponding scaling exponents are displayed within the graphs.

Stress relaxation measurements

Figure S5.6 shows the results of a stress relaxation measurement for the three studied EFs. The evolution of the relaxation modulus *G*(*t*), normalized by the initial modulus G_0, after applying a step strain (instantaneous deformation to the desired strain and keeping it constant) gives information on the elastic network properties. The main difference found was between FLG-EF versus MLG- and GrP-EF. For FLG-EF a residual relaxation modulus of 29.5% was found, indicative for elastic contributions that remained after deformation. Also at higher applied strain (80%) some elasticity was kept. For MLG and GrP-EFs, however, *G*(*t*) decayed to zero meaning that the network was destroyed completely and no driving force to elastically restore parts of the initial structure exist.

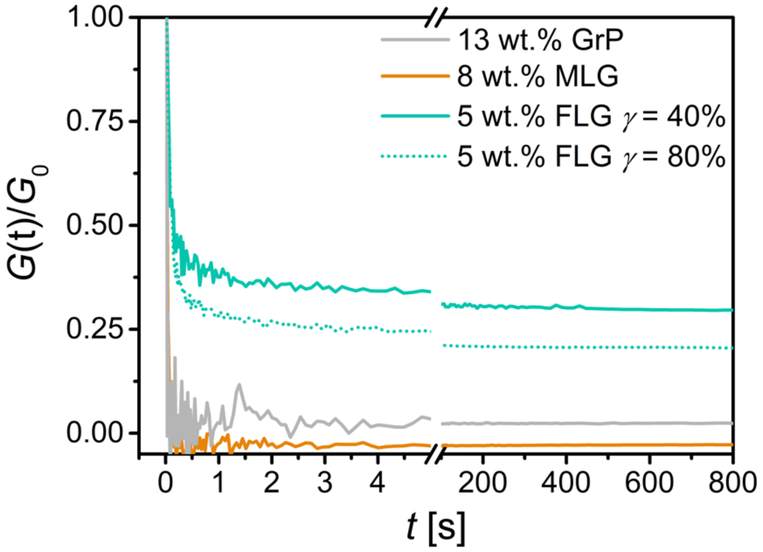

Figure S5.6: Normalized relaxation modulus from the stress relaxation experiments of 13 wt.% GrP (grey), 8 wt.% MLG (orange), and 5 wt.% FLG (turquoise) in glycerol with an applied step deformation of 40%.

Tensile test setup

Figure S5.7 shows an exemplary electrofluid encapsulated with an EcoFlex tube mounted into a tensile testing machine. Two coppers cables were inserted at both sides and connected to the Keithley sourcemeter. In Figure S6A the sample is shown in the pre-stretched state before the measurement and in Figure S6B it is shown at a strain of 40%.

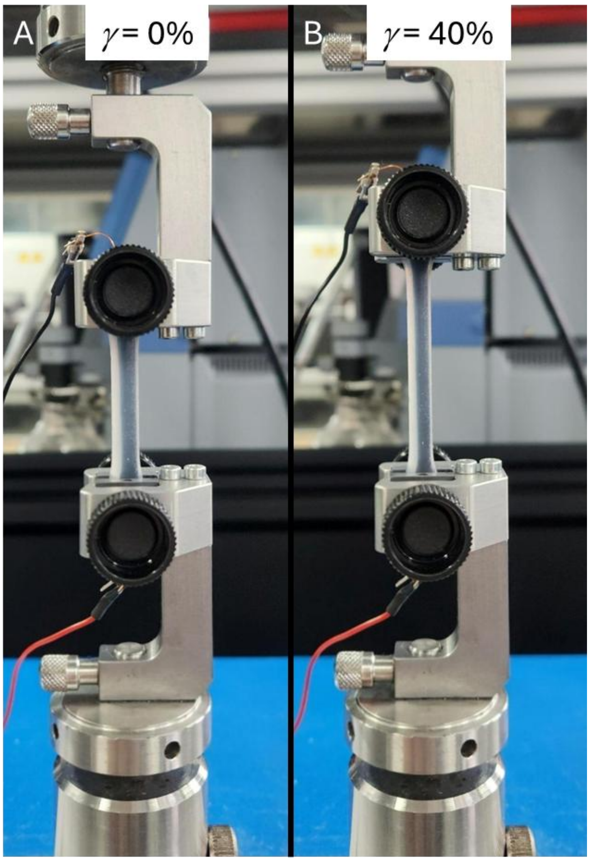

Figure S5.7: Encapsulated electrofluid mounted into a tensile testing machine. Both ends of the tube contain copper wires to connect to a Keithley. A: Sample in pre-stretched condition B: Sample at 40% strain.

Sample images

Figure S5.8 shows images of electrofluids, each prepared with a different 2D carbonaceous filler.

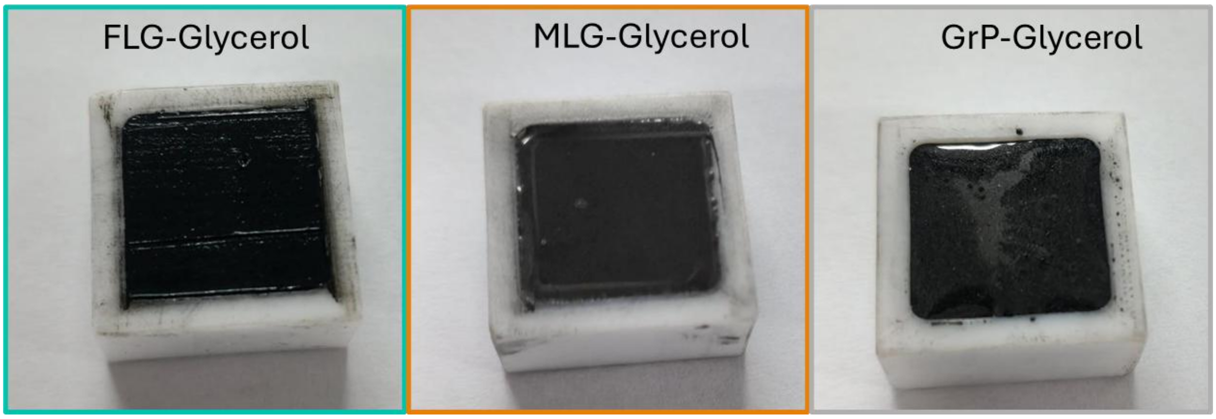

Figure S5.8: Electrofluids prepared with different 2D carbonaceous fillers in glycerol. From left to right FLG, MLG, and GrP as filler particles.

6. General discussion

In the preceding chapters (**3–5**), individual electrofluid systems were examined in detail, each highlighting distinct electromechanical behaviors and material properties. This chapter brings these findings together, integrating previously reported results with new, unpublished data to provide a broader perspective on electrofluid performance. The discussion aims to establish a comprehensive understanding of their underlying mechanisms and evaluate how these materials align with the current state of the art of soft electronic materials.

6.1. Electrical and mechanical networks

As electrofluids (EFs) are designed to conduct electricity while being able to flow, both electrical and mechanical networks play a crucial role in their performance for targeted applications. To see the impact of the filler shape, the electrical percolation threshold of electrofluids using different carbonaceous fillers dispersed in both a polar matrix (glycerol) and a non-polar matrix (polydimethylsiloxane, PDMS) is discussed. Figure 6.1A shows a graph of percolation curves for EFs based on glycerol as a matrix. Among all carbon-based EFs, those containing multi-walled carbon nanotubes (MWCNTs) yield the lowest percolation threshold of 0.05 wt.% in glycerol,[267] followed by few-layered (FLG) and multi-layered (MLG) graphene flakes, which created conductive networks at slightly higher filler concentrations, 0.16 and 0.34 wt.%, respectively. This trend is consistent with the literature that reports a similar order of ϕ_c (rods) < ϕ_c (plates) < ϕ_c (spheres).[96] The next filler to reach percolation was carbon black (CB) at ϕ_c = 0.59 wt.%. The fractal nature of the CB aggregates is known to help to reach percolation at smaller filler concentrations compared to their spherical counterparts, but the comparison to rods and plates depends on other variables, such as aspect ratio or size. Therefore, its position in the filler order of concentration to create electrical networks in EFs was unpredictable. Surprisingly, CBs' specific surface area (SSA) is larger than that of MLGs (75 m^2/g compared to 25 m^2/g), revealing that the SSA value of the fillers is useful to predict percolation trends when comparing only particles with the same shape.

The EF based on graphite flakes (GrP) exhibited a percolation threshold of 4.80 wt.%, one order of magnitude above the other filler types. This might be attributed to the large, compact clusters (surface area of < 10 m^2/g) with a smaller aspect ratio and limited contact points, resulting in properties closer to spherical particles.

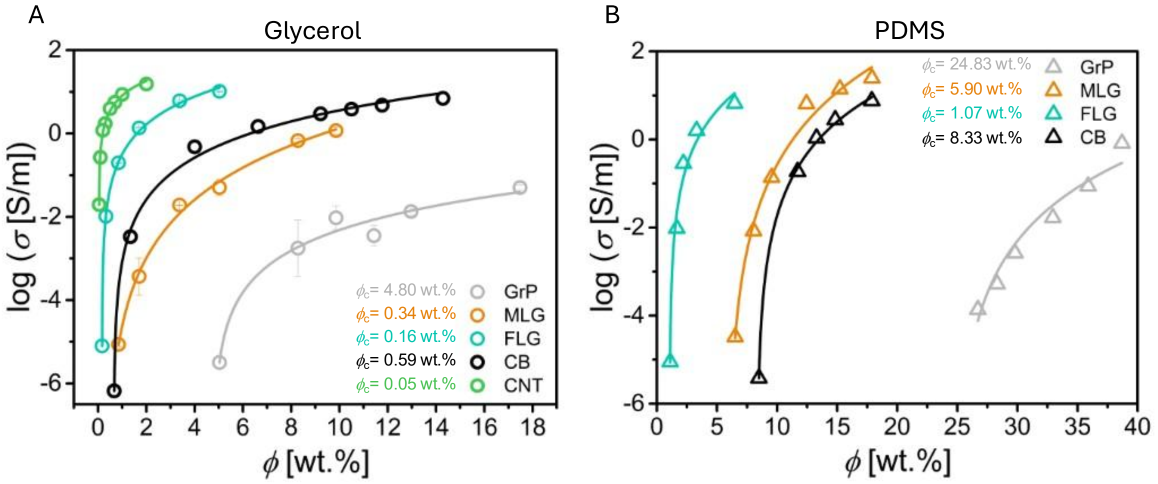

Figure 6.1. A: Electrical percolation curves of electrofluids based on glycerol as matrix. B: Electrical percolation curves of electrofluids based on PDMS. Percolation data of MWCNTs in glycerol were extracted from reference.[267] Electrofluids with MWCNTs could not be created in PDMS as a matrix and are, therefore, not shown. For both panels, the solid lines are the fits, done according to classical percolation theory described in Equation 1.1.

As discussed in **Chapter 3** for CB-based EFs, a major determinative factor that affects the percolation threshold is the affinity of the conductive filler to the surrounding matrix. Figure 6.1B shows the percolation threshold for EFs based on PDMS. Note that it was not possible to create EFs based on MWCNT dispersed in PDMS, and, therefore, no data for this is shown. Compared to the glycerol-based EFs, the use of PDMS as matrix material increased the percolation threshold in all cases by approximately one order of magnitude. The affinity of a filler towards a matrix is governed by the surface chemistry of the filler and the chemical composition of the matrix. All studied carbon-based fillers exhibited a predominantly non-polar surface with a low amount of oxygen groups. Dispersed in glycerol, a small polar molecule, the fillers tend to minimize contact with the matrix, leading to a high driving force for agglomeration. Larger agglomerates form, which span the available volume efficiently and create a conductive path at low filler loading. In PDMS, a non-polar polymer, the affinity with the filler is high, creating a better dispersion of smaller agglomerates. The position of the fillers in the order of concentration for percolation was the same as for glycerol-based EFs, demonstrating that the effect of solvent affinity is independent of the filler type.

The creation of a conductive network is required to confer the material with electrical conductivity. This, however, must not necessarily be concomitant with the creation of a mechanical network, i.e., electrical and mechanical networks are not necessarily formed at the same filler loading.[178] Actually, there are several definitions proposed for the onset of the mechanical percolation, such as rigidity percolation or rheological percolation.[178] Here, the mechanical percolation threshold is defined as the filler concentration that causes the storage modulus *G’* to exceed the loss modulus *G’’*, creating a solid-like (or gel-like) material. This means that the filler network can transmit stress through the entire sample volume. In Figure 6.2, the evolution of *G’* and *G’’* with respect to the filler concentration for selected EFs is shown. The order of increasing mechanical percolation thresholds followed the same trend as observed for the electrical one. Among all glycerol-based EFs (Figure 6.2A), the mechanical percolation was reached at a larger filler loading than the electrical percolation. This phenomenon has been explained in literature for the case of MWCNTs by the electron tunneling mechanism, which does not require direct physical contact but occurs already at filler-filler distances of 1 nm and below.[178] This conduction mechanism can be found in all the studied fillers and explains the presence of electrical networks at lower concentrations than those for mechanical networks. A mechanical network, however, requires the particles to be in contact and transmit stress through the network. This implies that a less dense filler network is sufficient for electron conduction but not enough for stress transfer. Moreover, there are other variables to be considered beyond this study; for example, when the particles get into contact, the type of interaction, whether particles slide or create frictional contacts, also influences the creation of a mechanical network at a given filler loading.

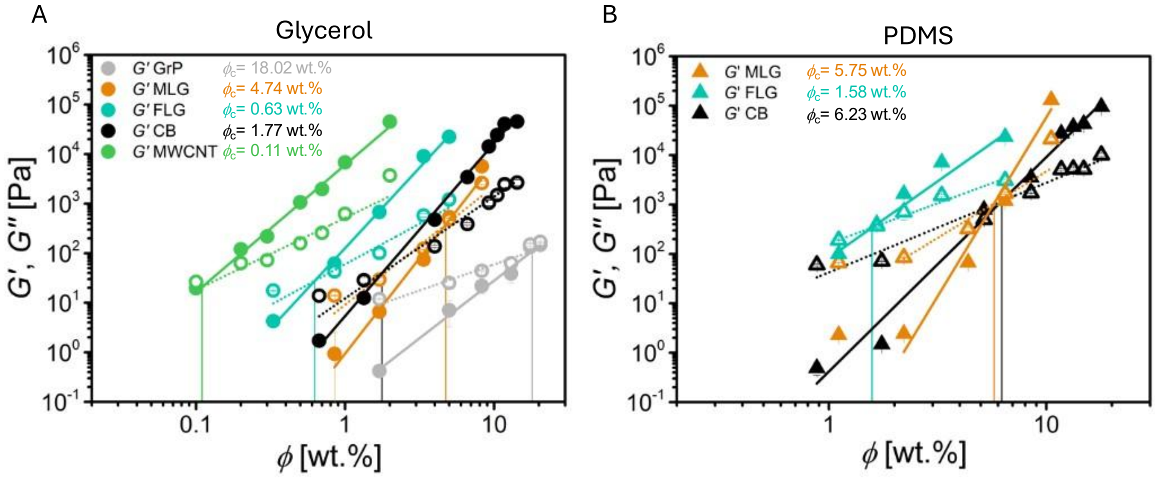

Figure 6.2. Plots of *G’* (filled symbols) and *G’’* (open symbols) as a function of filler weight fraction for A: Glycerol-based electrofluids containing GrP (grey), MLG (orange), FLG (turquoise), CB (black), and MWCNT (green) B: PDMS-based electrofluids containing MLG (orange), FLG (turquoise), and CB (black). Data of MWCNT electrofluids was extracted from reference.[267] Solid and dotted lines represent fit curves of *G’* and *G’’* data, respectively, with a power law of the form $G' = A*\phi^t$. Vertical solid lines mark the intersection of the fit curves, which serve as an indicator of the condition $G' = G''$ and, therefore, the mechanical percolation threshold.

In the case of the PDMS-based electrofluids (Figure 6.2B), the same shape-dependent trend for increasing mechanical percolation threshold was observed. Moreover, the critical concentrations were higher than for the glycerol-based EFs for the same filler. This may be related to the strong filler-matrix interactions in a non-polar matrix. The carbonaceous fillers are attached to the polymer chains, restricting their movement (reinforcement effect). Therefore, even at concentrations at which the fillers are not in physical contact with each other, the reinforcement effect results in the stiffening via the polymer matrix. Similar trends of $\phi_{c,mech} < \phi_{c,elec}$ have been seen for oxidized MWCNTs in polyethylene terephthalate (PET),[334] or CB in high density polyethylene (HDPE).[179] All these composite systems have in common that the affinity of filler and matrix is high.

Table 6.1 summarizes the electrical and mechanical percolation thresholds for different fillers in both glycerol and PDMS matrices. The ratio between these thresholds ($\phi_{c,\ elec}$ / $\phi_{c,\ mech}$) was calculated to indicate to which extent the two percolation thresholds differ from each other. For glycerol-based EFs, the ratio was low, all of them below 0.5. This reflects that the electrical network formation occurred at significantly lower filler concentrations, probably due to the strong tendency of the fillers to agglomerate and create filler-filler contacts and the absence of reinforcement effects due to the molecular nature of glycerol. When using PDMS as a matrix, the ratio increases and narrows the gap between both thresholds. For MLG and CB, the ratio was even above 1, indicating that the mechanical percolation was reached at lower filler concentrations than electrical percolation. This effect is then attributed to the polymer chains of PDMS. Different PDMS molecular weights, i.e., different chain lengths, could change the value of this ratio; however, this study was beyond the scope of this thesis.

Table 6.1: Overview of the electrical and mechanical percolation thresholds for different carbonaceous fillers dispersed in glycerol or PDMS.

Matrix	**Filler**	$\phi_{c,\ elec}$ **[wt.%]**	$\phi_{c,\ mech}$ **[wt.%]**	$\phi_{c,\ elec}$ / $\phi_{c,\ mech}$
Glycerol	GrP	4.80	18.02	0.27
	MLG	0.34	4.74	0.07
	FLG	0.16	0.63	0.25
	CB	0.59	1.77	0.33
	MWCNT	0.05	0.11	0.45
PDMS	MLG	5.90	5.75	1.03
	FLG	1.07	1.58	0.68
	CB	8.33	6.23	1.33

According to what was discussed above, the filler morphology seems to be the main driving force to establish the concentration order at which the percolation (both mechanical and electrical) takes place. However, the underlying mechanisms to create electrical conduction or enable stress transfer are different. It is, therefore, interesting to analyze whether there is a universal scaling that describes the relation between these two parameters. Figure 6.3A shows such a plot: mechanical percolation threshold versus electrical percolation threshold for glycerol- and PDMS-based EFs using different carbonaceous fillers. The percolation thresholds showed a power law scaling with a slope of ~1, indicating the exponent. This is interesting because it implies that the transition from a conducting to a stress-transferring network happens in the same way, regardless of the type of filler or matrix that was used. Even when using EFs that showed mechanical before electrical percolation (MLG and CB in PDMS), they still follow an exponent of 1.

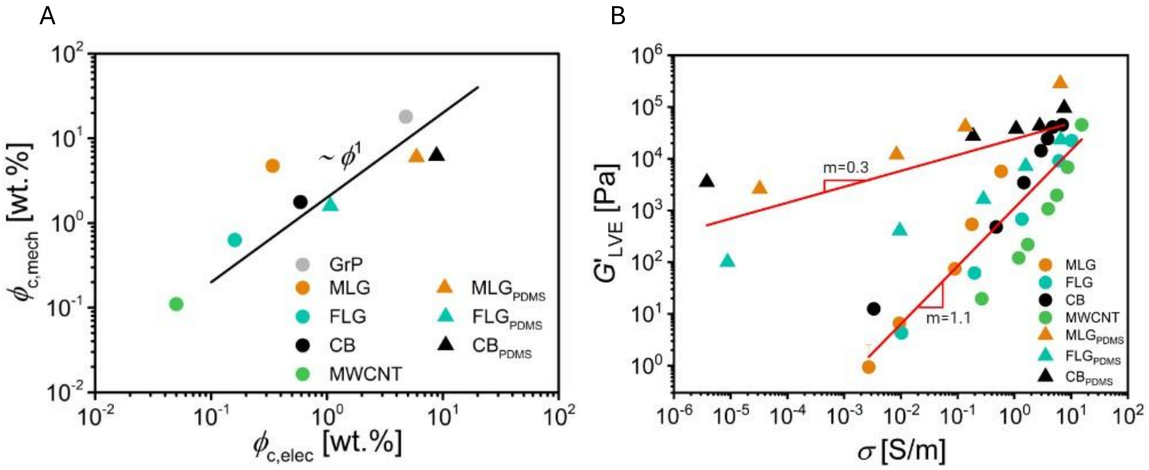

Figure 6.3. A: Electrical percolation threshold as a function of the mechanical percolation threshold of different electrofluids. The solid line shows a linear scaling with a slope of 1. B: Figure of Merit of selected electrofluids showing the parameters storage modulus at the LVE and conductivity. The filler concentration in each electrofluid increases from left to right. Points in the legend without an index refer to electrofluids based on glycerol.

As a general rule, the conductivity of EFs increases with increasing filler loading, as well as increases the storage modulus. This trend resembles the trade-off between electrical conductivity and brittleness in conductive polymer composites (CPCs) discussed in section **1.5. Trade-off: Electrical conduction and mechanical flexibility in Chapter 1**. The advantage of EFs is that the breakage of the mechanical network does not entail the breakage of the material itself, but that it flows, adapting to the new shape, and neither does it entail the loss of electrical conductivity. A common way of comparing the performance of materials, particularly when this kind of trade-off exists, is to represent their main properties in a Figure of Merit (FoM). Figure 6.3B compares these two properties: conductivity $\sigma$and storage modulus G' in the linear viscoelastic region (LVE), which represents the stiffness of the material, for selected electrofluids. This plot does not contain information about absolute filler loadings, but within the same electrofluid, the concentration increases from left to right in the plot. It is universal that an increase in conductivity entails an increase in modulus and, therefore, stiffness. Glycerol and PDMS-based electrofluids show different scaling exponents. While the former one scaled with an exponent of 1.1, the latter one scaled with 0.3. This implies a stronger scaling of G' with increasing conductivity, i.e., filler loading, in the case of Glycerol-based electrofluids.

Based on the data discussed above, the following conclusions are drawn regarding electrical and mechanical network formation. First, for a given matrix, the type of filler strongly affects both the electrical and mechanical percolation threshold. In general, 1D fillers showed the lowest thresholds, followed by 2D fillers and fractals. For a given filler, changing the matrix from polar to non-polar increased the percolation threshold but did not change the general trend. Second, a universal scaling law for the values of electrical and mechanical percolation thresholds was found. Regardless of the type of filler or matrix used, both thresholds determined for different electrofluids followed a linear proportionality. And third, the type of matrix determines the type of scaling behavior of the FoM (storage modulus vs. conductivity). A matrix with non-matching affinity (glycerol) caused a stronger power law scaling than a matching matrix (PDMS) system. This is attributed to the increasing influence of filler-matrix interactions in electrofluids with a high affinity between filler and matrix. Additionally, the molecular and polymeric nature of the matrix may play a role in the offset of stiffness at low filler loadings.

6.2. Electrofluids as strain sensors or stable conductors

An essential performance parameter for stretchable conductors is the Gauge Factor (GF), which was introduced with **Equation 1.3 in Chapter 1**. This parameter quantifies the sensitivity of a material, in terms of change in electrical resistance, at a given applied strain. The larger the value, the higher the sensitivity and *vice versa*. When a uniaxial strain is applied, for example, the changes in resistance might originate from two sources: geometric changes applied to the sample (elongation in the strain direction and contraction in the perpendicular direction) and piezoresistive effect (a change in the volumetric resistivity of the material, for example, due to structural distortions). According to Equation 1.3, a GF of 2 (assuming the typical Poisson's ratio of 0.5 for elastomers), indicates that the changes in resistance are only governed by geometric changes caused by the deformation. Typical examples of materials with a GF = 2 are metals that do not undergo internal structural changes during deformation.[335] For materials that exhibit a GF < 2, a negative piezoresistive effect is observed, i.e., an increase of intrinsic conductivity; while the positive piezoresistivity (increase in resistivity) leads to GF > 2, which is the most common case of CPCs.

Among electrofluids, both negative and positive piezoresistivity were observed. In **Chapter 3**, the role of the solvent type in the formation of the CB network and its impact on the electrofluids' sensitivity to mechanical deformation were discussed. Briefly, CB in glycerol tends to create larger agglomerates, while CB in PDMS is predominantly dispersed and attached to the polymer chains. Mechanical deformation caused in both cases a breakup of filler contacts, but, in CB-glycerol electrofluids, a reconfiguration that favors filler-filler contacts took place that compensated for the geometrical changes, leading to a GF = 0.97 (negative piezoresistivity) while CB-PDMS delivered an almost perfect geometrical change

(GF = 2.68). Figure 6.4 summarizes the GF of selected electrofluids at a deformation of 10% strain. All selected electrofluids contained a filler loading sufficiently above the electrical percolation threshold (indicated in the figure caption) to ensure electrical conductivity and a proper comparison.

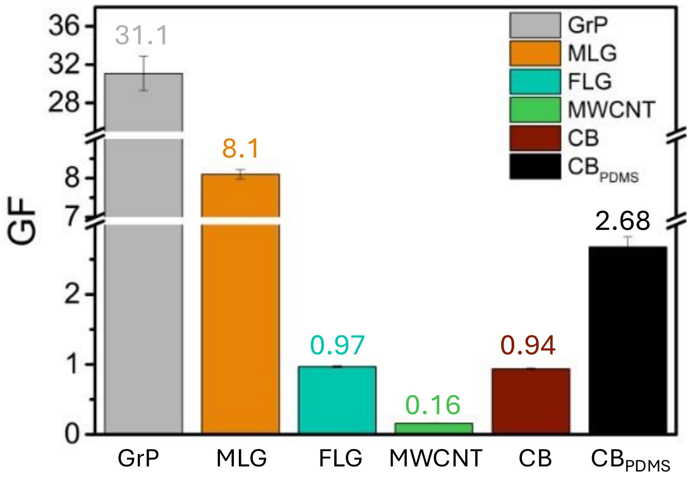

Figure 6.4. Gauge Factors for different electrofluids at an applied strain of 10%. Values were calculated according to Equation 1.3 after an initial equilibration time in the form of precycling. Filler weight fractions in the different electrofluids were as follows: 13 wt.% GrP, 8 wt.% MLG, 5 wt.% FLG, 1 wt.% MWCNT, 14.3 wt.% CB, 17.9 wt.% CB in PDMS. If not said differently, fillers without an index were dispersed in glycerol.

When comparing the results obtained for CB-, FLG-, and MWCNT-glycerol electrofluids, i.e., fractal, 2D, and 1D fillers, it was observed that all of them present a negative type of piezoresistivity with GF < 2. These three fillers have shown a strong agglomeration tendency in polar solvents, leading to open networks. The strong interaction between the fillers, together with their open structure, confers the network elastic properties. Upon mechanical deformation, these networks react in the micro-scale as Kirigami structures, absorbing the mechanical energy and even reconfiguring, increasing their electrical conductivity. The largest difference was shown by the MWCNT-glycerol electrofluid, which exhibited almost no change with the applied strain (GF = 0.16). Composites based on MWCNTs have been reported to be less sensitive to strain deformation than, for example, CB.[28, 336, 337] This has been attributed to their larger aspect ratio.[337] Therefore, MWCNTs may overlap and entangle, decreasing the probability of losing conductive paths due to strain deformation.[337] Networks of low aspect ratio particles (e.g., CB) rely on many contacts between individual aggregates or agglomerates and are, therefore, more prone to undergo changes when deformed.[337] Furthermore, it may be considered that MWCNTs are not stiff but, in fact, have a certain degree of internal flexibility and can bend and buckle under applied strain,[338] which additionally increases their capability of creating favorable configurations.

Significantly higher GF values were found for electrofluids based on MLG and GrP in glycerol, and, contrary to the other fillers, they showed positive piezoresistivity. Since both fillers contain a significantly higher number of layers than the FLG, their bending stiffness is also increased. This makes them less flexible and prevents a stable elastic network during mechanical deformation. The measured oxygen content for these two filler types was also increased compared to, for example, the FLG flakes. Slightly reduced filler-filler interactions contribute further to an easier breakup of the network structure, which causes a higher GF. Additionally, the difference in absolute conductivity plays a role as well. It has been reported that the GF for many composites scales inversely with the zero-strain conductivity of the composite, i.e., higher conductivity yields a smaller GF.[151] As discussed in **Chapter 5**, the maximum conductivity of graphene-filled electrofluids depends on the thickness of the filler and the oxygen content. Thinner fillers, like the FLG, achieved higher electrical conductivity than fillers with a higher number of layers, like MLG or GrP.

Electrofluids can be designed to act as strain sensors or as stable conductors. Based on the discussion above, a strain sensor requires either a) a matching affinity between filler and matrix, b) a low aspect ratio, or c) a combination of both. Consequently, a stable conductor is achieved if fillers with high aspect ratio and intrinsic flexibility are chosen that are dispersed in a non-matching affinity matrix, which fosters agglomeration.

6.3. Strain dependent properties

Materials that are designed for the use in flexible and stretchable electronics must endure strain deformation that goes beyond the limits of the LVE region. As described in section **1.4 Mechanical Properties in Chapter 1**, the Payne and the Mullins effects are two commonly observed phenomena for CPCs under strain deformation. The former one describes the decrease in storage modulus with increasing applied strain, i.e., strain-softening. The latter one describes stress hysteresis during continuous loading and unloading, often called stress-softening. Both effects are discussed in more detail in the framework of electrofluids.

Strain-softening

If an oscillating deformation is applied to a solid composite, its storage modulus typically decreases, commonly known as the Payne effect.[118, 122] This behavior was found for several elastomers filled with different particles, such as silica[123] or carbon black.[122, 339] The origin and mechanism of this Payne effect in CPCs are still under discussion. Some studies relate it to the polymer matrix and its interactions with the filler,[339, 340] while others put the focus on the filler-filler interactions.[122] In concentrated suspensions, although typically not referred to as Payne effect, a decrease in *G'* with increasing strain (strain-softening) is a common phenomenon. Following the analogy of electrofluids as liquid composites, it is worth discussing this effect. Figure 6.5A-C shows the evolution of *G'* during several oscillatory amplitude sweeps for glycerol-based EFs with three different filler particles: CB, MLG, and MWCNT (see Methods section in the Appendix for details). As discussed previously in **Chapters 3 and 5** for the case of CB- and MLG-EFs, respectively, an increase in strain caused a reduction in *G'* due to the destruction of the filler network, independent of the filler type that was used. This is visible in the first sweep of increasing strain for all EFs. As a result of the strain-softening effect, a reduction of at least one order of magnitude in the value of *G'* was observed. The presence of "Payne effect" and the absence of polymer chains in the selected EFs, which use glycerol as the matrix, makes it reasonable to think that the conductive filler network is responsible for the strain-softening in electrofluids.

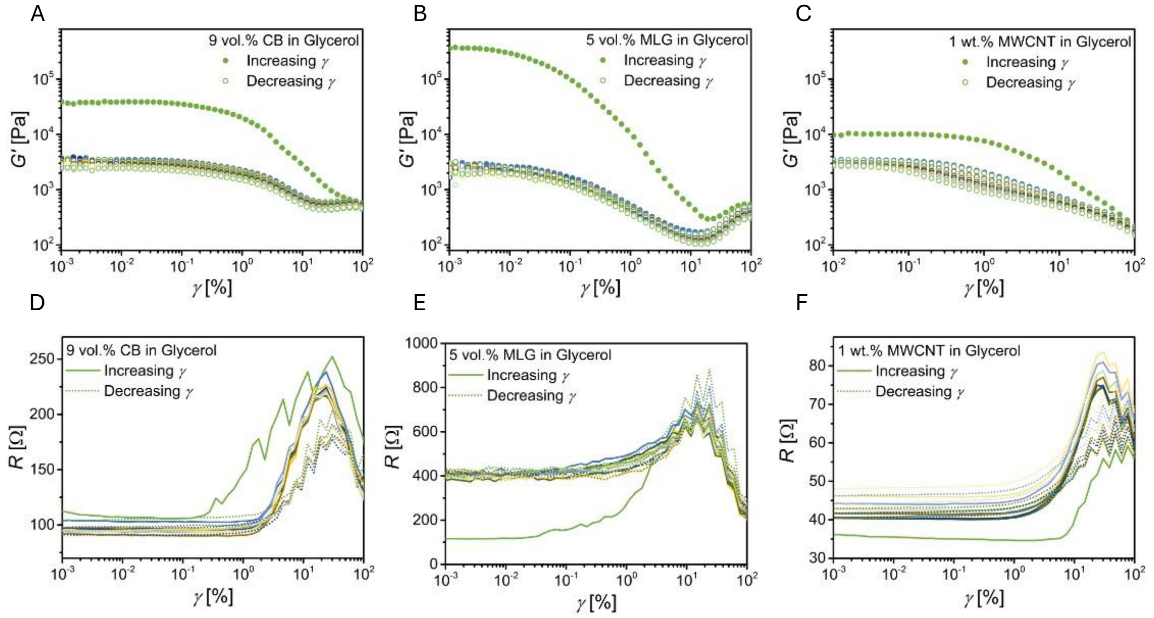

Figure 6.5. Strain sweep curves for A: 9 vol.% CB in glycerol, B: 5 vol.% MLG in glycerol, and C: 1 wt.% MWCNT in glycerol measured in oscillation rheology at a constant frequency of 10 rad/s. Filled symbols indicate *G'* at increasing strains and open symbols *G'* at decreasing strains. Resistance-strain curves for D: 9 vol.% CB in glycerol, E: 5 vol.% MLG in glycerol, and F: 1 wt.% MWCNT in glycerol measured *in-situ* during strain sweeps in oscillation rheology. Solid lines indicate increasing strains and dotted lines indicate decreasing strains.

In solid composites, the Payne effect can be recovered or induce permanent softening in the material. To study the reversibility of the strain-softening in EFs, the strain was swept in the opposite way, from the highest strain to the lowest. It can be observed that *G'* values are below the original ones, ending the cycle at lower *G'* (even by one or two orders of magnitude for some cases). After this first cycle, the values obtained for *G'* in the subsequent ones matched with only marginal changes for each following sweep. It is remarkable, however, that at high strains, the *G'* reached in all sweeps the same value, an indication of a similar network destruction. This behavior was also reported for ESBR polymer filled with CB, which showed reduced modulus at low strain and similar modulus at high strain compared to the initial amplitude sweep.[341]

In order to follow the filler network evolution, the electrical resistance signal was monitored *in-situ* (see Figure 6.5D-F). In all the cycles, the electrical signal remained constant until the break of the mechanical network (yield point), from which it increased (at strains of 0.14% for CB, 0.03% for MLG, and 2.29% for MWCNT) due to the breakage of the electrical network. One could define this strain-dependent resistivity as an electrical Payne effect. Similar to the unrecovered softening of the mechanical network, the subsequent cycles led to a mismatch of the electrical signals at the same strain values, with larger resistances for the case of MLG- and MWCNT-glycerol EFs but, surprisingly, slightly lower for the CB-glycerol EF. In a recent work by Zhao *et al.*, CB/SBR composites underwent loading and unloading cycles, showing a small hysteresis of the mechanical response (lowering *G'*) and a large hysteresis of the electrical response with an increase in electrical resistance.[342] Due to the unmatching recovery responses, the authors attributed the Payne effect to the matrix properties. Warasitthinon *et al.*, however, reported independent strain-softening for CB in paraffinic oil and SBR polymer and, therefore, attributed the cause of the Payne effect to the CB network.[122] In this thesis, a correlation between electrical and mechanical response was observed. Since the electrical response is only related to the filler particles and due to the molecular nature of the selected matrix (glycerol), it is postulated that the origin of the Payne effect within EFs is mainly due to the filler network. The changes observed by the three different filler types are, therefore, attributed to the structure of the created network and the particle contact geometry in each case.

Stress-softening

The reduction in stress during continuous strain deformation cycles of CPCs is called stress-softening.[119, 128] Following their analogy as liquid composites, the hysteresis effect on electrofluids that undergo cyclic uniaxial tensile strain was investigated (see Methods section in the Appendix for details). Since they must be encapsulated for this test, the mechanical properties are dominated by the encapsulant material and, therefore, only the measured resistance was taken as an indicator for structural changes during continuous deformation. The results are displayed in Figure 6.6A-C for the selected electrofluids: CB-, MLG-, and MWCNT-glycerol.

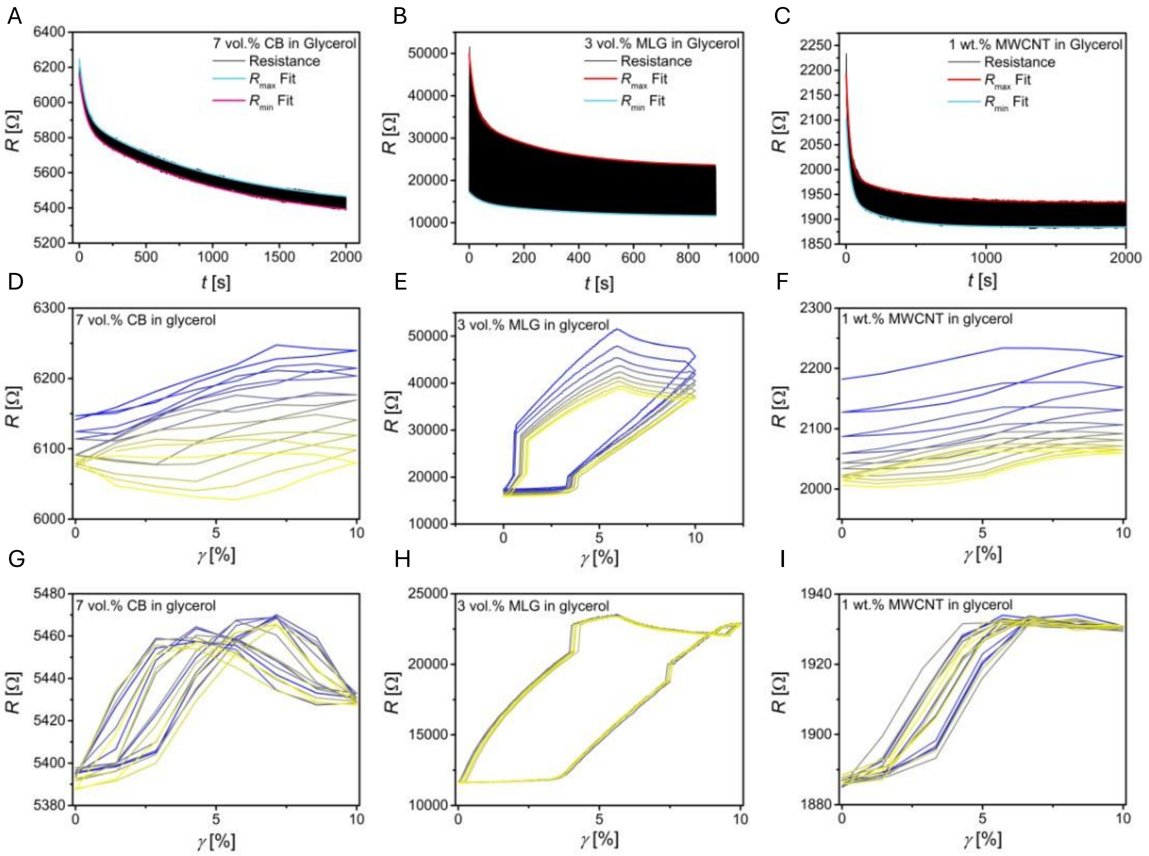

Figure 6.6. Resistance over time plots during uniaxial tensile tests of 10% strain and a strain rate of 10 %/s for A: 7 vol.% CB in glycerol, B: 3 vol.% MLG in glycerol, and C: 1 wt.% MWCNT in glycerol. The maximum and minimum resistance values of each cycle were determined and fitted according to the Maxwell-Wiechert model in Equation 6.1. Resistance vs strain representation of the first 9 cycles of the tensile test (D: 7 vol.% CB in glycerol, E: 3 vol.% MLG in glycerol, and F: 1 wt.% MWCNT in glycerol) and for the last 9 cycles of the tensile test for G: 7 vol.% CB in glycerol, H: 3 vol.% MLG in glycerol, and I: 1 wt.% MWCNT in glycerol.

An overall decreasing resistance signal over time was observed for the three types of electrofluids. During the first few cycles, a strong decrease was visible, indicating most of the structural changes. After several hundred cycles, the signal stabilized. To describe the resistance relaxation, some studies tried to link stress and electrical relaxation, applying the same equations derived for mechanical relaxation.[158] One approach applied to CPCs is the use of the Maxwell-Wiechert model, consisting of a spring in parallel to *n* Maxwell elements.[158] For the electrical analogy, the spring corresponds to a resistor, and the dashpot accounts for a relaxation time element. The corresponding electrical model is defined according to the following equation:

$$R = R_0 + \sum_{i=1}^{n}\left(R_i * e^{-\frac{t}{\tau_i}}\right) \tag{6.1}$$

with R_0 being the resistance offset, *n* the number of parallel Maxwell-element equivalents, R_i the resistance of the spring equivalent in each Maxwell element, and τ_i the relaxation time constant for the Maxwell-element equivalents.[158] In order to fit the model to our experimental data, the maximum and the minimum resistance values per cycle were extracted, and the resulting curves were subsequently fitted to a two-element Maxwell-Wiechert Model according to Equation 6.1 (solid red lines for the maximum and solid blue lines for the minimum resistance values). The good quality of the fittings indicates that the electrical response is strongly correlated to the underlying changes in the mechanical network proposed by the model. It is surprising, however, that all three electrofluids followed a relaxation mechanism developed for viscoelastic polymers, although the used matrix, glycerol, is a molecular solvent. To explain this, the following possible hypotheses are discussed:

1. The strong hydrogen bonds between glycerol molecules create a 3D network that is comparable to the one that formed in entangled polymer melts.
2. The filler-filler network has a stronger contribution to relaxation than expected from the results of solid composites that are dominated by the cured polymer matrix.
3. The encapsulant material, in this case a silicone polymer, influences the response of the electrofluid due to its own relaxation.

The first hypothesis can be discarded due to the negligible elastic contribution exhibited for pure glycerol in an amplitude sweep. The measured torque values were too small to resolve any network, and, therefore, it is unlikely that the H-bonds confer sufficient strength to cause any of the observed effects. To distinguish between hypotheses two and three, the fitted relaxation time constants among different samples were compared (see Table 6.2). If the encapsulant is the main driving force (third hypothesis), these constants should be similar for the three systems since the encapsulant material employed was the same.

Table 6.2. Time constants of the different electrofluids extracted from the fit function of the Maxwell-Wiechert model. Here, only the time constants for the maximum in resistance are shown.

Electrofluid	τ_1 [s]	τ_2 [s]
7 vol.% CB in glycerol	45.730	1047.4
3 vol.% MLG in glycerol	21.581	271.06
1 wt.% MWCNT in glycerol	26.746	393.72

Although smaller differences were found in the first-order time constant than in the second one, the increase in the order MLG < MWCNT < CB was the same for both. This leads to the conclusion that the encapsulant material is not the dominant factor of the resistance relaxation; it is more likely that the inherent viscoelasticity of the electrofluid causes this decay (hypothesis 2). The qualitative nature of these results, however, does not exclude certain contributions from the mechanisms described in hypothesis 3. For example, all electrofluids investigated here contained filler concentrations significantly above the percolation threshold. Their high stiffness may limit the contribution of the encapsulant, which might be larger electrofluids with lower concentrations.

While the Maxwell-Wiechert model is valuable to monitor the overall decrease in resistance, it lacks information about the intracycle hysteresis. Figure 6.6D-F shows the resistance vs strain plots of the first 9 cycles for the three different electrofluids. Similar to the stress hysteresis described for solid composites, the resistance signal in the case of electrofluids also showed a strong hysteresis behavior. Continuing with the analogy, one can refer to it as an electrical Mullins effect. As the electrical response depends on the conductive filler network, it is suggested that changes in filler-filler contacts are the main responsible for this behavior in electrofluids. In contrast, in the last 9 cycles of the tensile test (see Figure 6.6G-I), the hysteresis almost vanished, showing only slight changes between the cycles. The material dissipated most energy at this level of deformation and reached an equilibrium state where no further non-recoverable changes occurred.[343] While the hysteresis behavior decreased, non-linearities arose in the last cycles, i.e., the resistance curves at increasing and decreasing strains showed a crossover. These non-linear features are discussed in detail in the following section.

6.4. Non-linear, intracycle resistance response

In the previous section, the stress-softening effect and its impact on the electrical response, particularly in the initial cycles during repetitive tensile deformation was discussed. Therefore, precycling is needed prior to material application to ensure stable responses. Here, the focus is on the intracycle response to deformation after the stabilization cycles of electrofluids encapsulated in elastomers. As discussed in section **1.5 Trade-off: Electrical conduction and mechanical flexibility in Chapter 1** in the electrical response intracycle of solid CPCs, often a double peak is observed, which is often referred to in literature as a “shoulder peak”. These shoulders have been experimentally observed in many different solid composites based, for example, on graphene flakes,[332] CNTs,[28, 344] or silver flakes.[218] Although very often reported, only few studies discussed the origin of this effect. Yang *et al.* concluded that the viscoelasticity of the matrix is the main reason for the appearance of the shoulder peaks.[155] In their study on CNT/graphene silicone rubber composites, changing the time the composite was under load (holding time) influenced the degree of the non-linear response. As the matrix is delaying the reconfiguration of the conductive filler, longer loading times caused a larger magnitude of the secondary peak, as the network had time to fully relax.[155] Mersch *et al.* proposed that, although viscoelasticity may play a role, geometrical changes due to the change in cross-sectional area during tensile deformation are the driving force to create secondary peaks.[156] The impact of the applied strain was studied by Zhang *et al.* in a composite of MWCNT in a TPU matrix. They observed shoulder peaks more prominently at strains of 30% than of 10%, confirming that the degree of deformation impacts the signal response.[345]

Selected electrofluids were encapsulated in elastomeric tubes and underwent continuous uniaxial deformation (see Methods section in the Appendix for details). Figure 6.7A-B shows a zoom into few tensile cycles of this experiment. The response within one deformation cycle did not follow the expected linear increase and decrease of the input strain. Although the non-linear responses were different for the different studied electrofluids, they followed the same shape. The change in resistance showed two peaks within one cycle of loading and unloading, one prior to the maximum strain deformation and one afterwards. Based on the understanding of electrofluids, the following hypothesis for this behavior is proposed: During stretching, the mechanical network ruptures (strain beyond the LVE-region), causing the partial breaking of the conductive network and, therefore, the increase in electrical resistance. Before the stretching is completed, the particles, which are mobile, start relaxing, generating the subsequent decrease of resistance and, with it, the first peak. This effect is enhanced due to the inertia of the tensile machine when changing from loading to unloading, leading to the lowest resistance at the end of the loading phase. With the start of the unloading phase, the relaxed state of the networks is again perturbed, causing the breakage of the new filler-filler contacts, which results in a sudden increase in resistance. However, immediately after that, the strain is released, returning the network to its original state. Here, the decrease in resistance prior to the strain release is concomitant with the relaxation process, leading to the second peak. The effect of the electrofluid matrix material is shown in Figure 6.7A for CB-based electrofluids in glycerol and PDMS that underwent a deformation of 10% at a strain rate of 10 %/s. We can observe that this effect is more pronounced for the electrofluid based on PDMS than for the glycerol one. This is a combination of a) larger sensitivity, which caused the resistance to increase more upon mechanical deformation, and b) faster relaxation dynamics, which causes the peak to be more pronounced (lower relative minimum). Both effects can be attributed to the weaker filler-filler interactions between the CB particles in the non-polar PDMS matrix; they are easy to break, and preliminary X-ray Photon Correlation Spectroscopy (XPCS) measurements (results not shown here) suggest that they break in smaller pieces that can reform faster than that of CB in glycerol, which may lead to different relaxation times; although this requires further investigations.

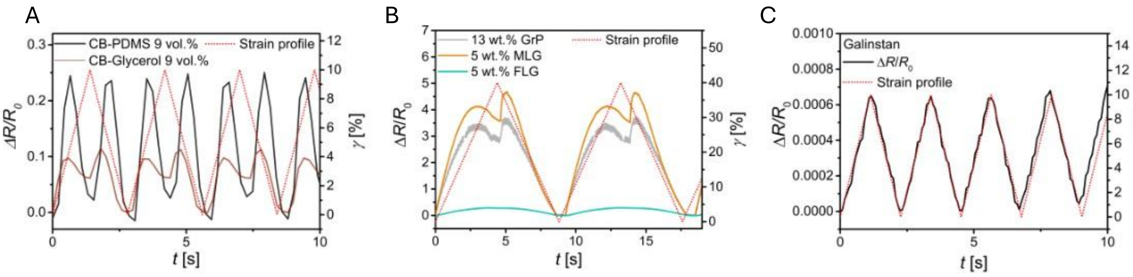

Figure 6.7. Uniaxial tensile tests at a strain rate of 10 %/s for A: 9 vol.% CB in PDMS (black) and glycerol (red) at a strain of 10%, and B: 13 wt.% GrP (grey), 5 wt.% MLG (orange), and 5 wt.% FLG (turquoise) in glycerol at 40% strain. C: Uniaxial tensile test of Galinstan filled in a silicone polymer tube and tested with 10% strain and 10 %/s strain rate. Red dotted lines indicate the applied strain profile

The influence of the filler type was tested using GrP, MLG, and FLG particles in glycerol matrix with a uniaxial deformation of 40% at a strain rate of 10 %/s. The results, displayed in Figure 6.7B, show the presence of secondary peaks. Depending on the type of 2D carbonaceous filler used, the magnitude of the secondary peak was different. While the signal for GrP and MLG-based electrofluids is very similar, showing a prominent secondary peak, it was almost neglectable for the FLG-electrofluid. This might be attributed to the different network structures that these fillers form in glycerol, as discussed in **Chapter 5**. The strong connections between FLG particles in glycerol lead to very small changes in the electrical resistance upon deformation, and the high elasticity of the FLG network, caused by the low bending stiffness of the FLG particles, reduces the effect of viscoelastic relaxation processes.

To determine the influence of the encapsulant and the geometrical changes (proposed as an explanation in literature) in the “double peak” response of electrofluids, an encapsulated liquid metal (Galinstan) was tested under the same conditions (10% strain at a strain rate of 10 %/s). An almost perfect linear response of resistance change with the applied strain was observed (see Figure 6.7C). This suggests that materials without intrinsic network structure do not show secondary peaks, pointing to an effect originating from the filler network restructuring.

However, although the geometrical changes cannot explain the presence of non-linearities, it has been proposed for CPCs that the change in transversal dimension during uniaxial deformation might densify the internal filler network structure, leading to the reduction of electrical resistance. To exclude this factor, shear experiments were performed using a plate-plate geometry in the rheometer, in which, by definition, the geometry of the sample is constant. This configuration allows for applying strain, avoiding the contribution of the encapsulant material and macroscopic geometrical changes. A CB-based electrofluid in PDMS was chosen, as it showed the strongest secondary peak in uniaxial deformation. A constant strain deformation, either in the small amplitude oscillatory shear (SAOS) or in the large amplitude oscillatory shear (LAOS), was used at a fixed angular frequency of 0.1 rad/s. Figure 6.8 shows the results of these tests. Under SAOS conditions (Figure 6.8A), the electrical resistance signal was basically unaffected by the deformation, showing only a small deviation with no cyclic characteristics. This is consistent with the fact that in the LVE, the deformations are purely elastic, so the network retains its filler contacts. Under LAOS conditions (Figure 6.8B), however, very pronounced shoulder peaks were observed. Here, the mechanical network is broken, which has an impact on the electrical network as well. These results indicate that the applied strain must be high enough to induce plastic deformations in the filler network to create a) a cyclic response and b) secondary or shoulder peaks. Additionally, as there is no geometrical change during a rheological test, assuming perfect measurement conditions, this experiment showed that the change in cross-sectional area is not the driving force in the underlying mechanism of the "double peak" response but, probably, a factor that leads to filler rearrangement.

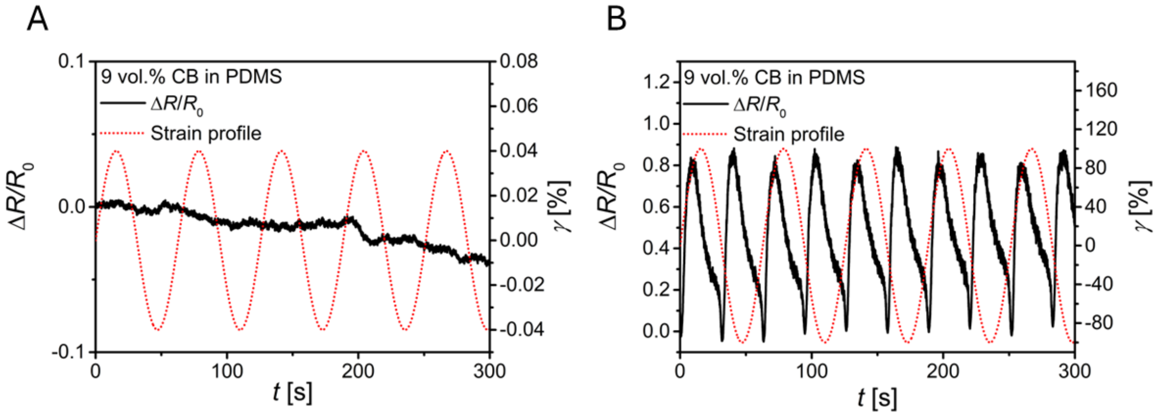

Figure 6.8. Change in resistance vs time for a constant amplitude test of 9 vol.% CB in PDMS in a rheometer with a fixed frequency of 0.1 rad/s under A: SAOS conditions (0.04% strain), and B: LAOS conditions (100% strain).

Electrofluids show non-linear intracycle resistance responses in both uniaxial and shear deformation. Geometrical changes and contributions from the encapsulant material are not applicable explanations for the effect of secondary or shoulder peaks in electrofluids. The hypothesis is that the requirements for their appearance are a) the existence of a network structure and b) a sufficient strain that causes breakage of network connections to induce changes in the electrical resistance and particle mobility (relaxation). The magnitude of this effect is related to the filler network, i.e., it depends on the filler-matrix interactions and the filler type, which allows for tunability of this response.

6.5. Time dependent properties

Up to this point, electrical and mechanical networks and their formation have been discussed, but the time dependency of these materials has not yet been addressed. In the previous section, the presence of a double peak or shoulder peak in the electrical response of strain intracycle and the possible relation to the network rearrangement due to relaxation processes was discussed. Therefore, here, the time dependent properties of electrofluids are discussed. This topic is of particular interest to understand the dynamics of the filler network and its implications in their use in sensing applications.

Thixotropy

One of the common types of fluid behavior in concentrated suspensions is thixotropy, defined as a decrease in viscosity over time under applied constant shear flow.[346] As discussed by Wang *et al.*, the evolution of stress after reducing the shear rate from a high to a low rate gives insights into the thixotropic nature of a material.[347] Thixotropic materials present a stress increase after an initial drop attributed to structural reconfiguration.[347] After a certain time, the stress reaches an equilibrium value, indicating a complete rebuild of the network. Here, EFs based on 6 vol.% CB suspended in PDMS and glycerol are compared (see Figure 6.9) regarding their thixotropic recovery after a step-down shear test (see Methods section in the Appendix for details). The CB-PDMS EF showed the described increase in stress over time, after reducing the shear rate, which indicates thixotropic behavior. The CB-glycerol EF also showed an increase in stress, pointing towards thixotropic behavior, however, at longer time scales, the stress values started to gradually decrease. This is different from the expected response of thixotropic materials. In fact, it can be described as antithixotropy, characterized by a decrease of stress over time, to differentiate it from thixotropy, which is typically related to an increase in stress upon step-down shear.[347] However, one must notice that antithixotropic behavior observed in this kind of test can also be wrongly assigned to viscoelasticity (stress relaxation) because both deliver the same stress response in a step-down shear rate test. To be able to distinguish them, these tests must be performed using a complementary measurement by means of orthogonal superposition (i.e., imposing a small oscillatory deformation during the transient step-down experiments, to extract the evolution of *G*' and *G*'' simultaneously, which are determinative for viscoelastic relaxation processes).[347] Antithixotropy has been linked to aggregation of attractive particles[348] or a shear-induced densification.[347] For CB suspensions with antithixotropic properties, Wang *et al.* argued that the initial stress increase is related to the formation of agglomerates and their connection that increases the resistance against shear flow. The decrease in stress at longer measurement times is attributed to a shear-induced densification of these agglomerates, forming more closed structures, which decrease the effective volume thereof.[347]

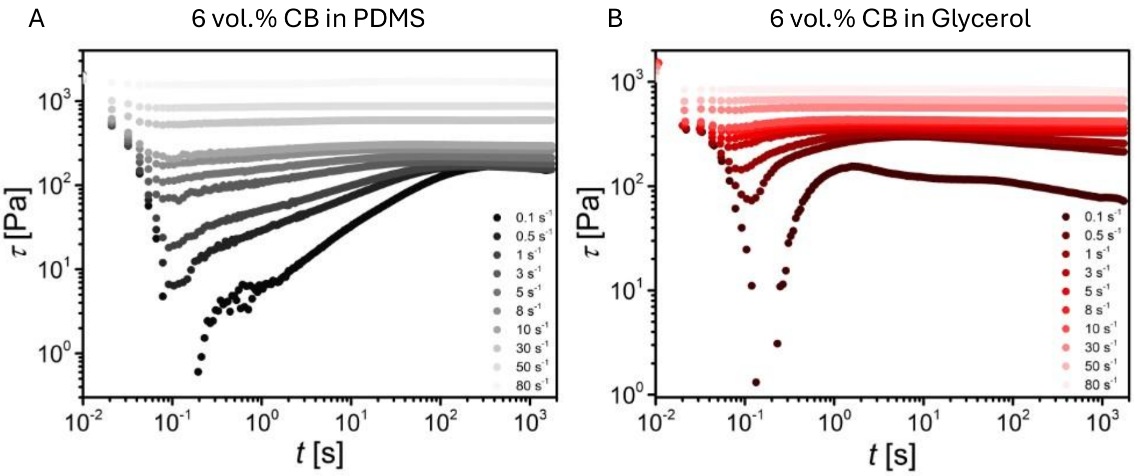

Figure 6.9. Stress as a function of time for a step-down shear rate test for A: 6 vol.% CB in PDMS and B: 6 vol.% CB in glycerol. Colors from bright to dark indicate decreasing shear rates from 80 to 0.1 s^{-1}. Before each shear rate step, the sample was sheared at 100 s^{-1} for 2 minutes.

The absence or presence of antithixotropy is not the only difference found for both EFs. In the thixotropic region, a faster recovery for CB-glycerol EF (before the stress starts decreasing) than that for CB-PDMS EF was observed, which also slows down before reaching equilibrium. This is reflected in the thixotropic recovery time, defined as the time needed to reach the maximum stress response, which was 1 to 2 orders of magnitude higher for the PDMS-based EF (see Table 6.3).

Table 6.3. Characteristic thixotropic recovery times $t_{\text{thixotropy}}$ based on step-down shear rate tests on 6 vol.% CB in PDMS and glycerol.

Step-down shear rate [s^{-1}]	$t_{\text{thixotropy}}$(CB-PDMS) [s]	$t_{\text{thixotropy}}$(CB-Glycerol) [s]
0.1	612.4	1.576
0.5	293.9	6.966
1	186.5	3.721
3	114.2	2.520
5	83.35	2.089
8	58.69	1.930
10	44.31	1.709

The influence of the liquid matrix nature on the CB network formation has been discussed in **Chapter 2** and in previous sections of this chapter. The large differences found in the thixotropic behavior and recovery times between CB suspended in PDMS and in glycerol indicate that the filler-matrix affinity also plays a role in the time-dependent properties of EFs. The faster recovery observed for CB networks in glycerol can be attributed to the strong agglomeration tendency of CB due to the poor affinity with glycerol, in contrast to the case of CB in PDMS. According to the hypothesis of Wang *et al.* described above, the long-term stress evolution can also be explained by the difference in affinity. Shear-induced densification of agglomerates causes a decrease in effective volume, which manifests as a decrease in stress at longer time scales. Denser agglomerates imply a reduction in surface area that is in contact with the matrix. In glycerol, CB avoids this matrix contact, explaining the observed stress reduction. Since the filler-matrix interactions in the CB-PDMS EFs are higher, overall smaller and dispersed agglomerates are formed. For higher shear rates, this is not observed because the applied shear is too high to allow reagglomeration.

Creep

In a creep test, the material undergoes a constant stress load over time, and the monitored response in strain or compliance, called retardation, is monitored.[349] After a certain time, the stress is removed, and the strain or compliance relaxation is recorded. Depending on the applied stress and the viscoelastic properties of the material, it reacts with a certain degree of strain deformation. The induced strain deformation γ is transformed into creep compliance $J(t)$ by normalizing with the applied stress σ_0 according to Equation 6.2:

$$J(t) = \frac{\gamma(t)}{\sigma_0}. \qquad (6.2)$$

As discussed in section **1.5.2. Rheology of gels in Chapter 1**, the Burgers model can describe the different parts of a creep curve within the viscoelastic region. This test is predominantly performed to distinguish between viscoelastic solid and viscoelastic liquid behavior. When coupled with an electrical measurement device, not only the mechanical relaxation, but also the electrical relaxation processes can be monitored.

Figure 6.10 shows the results of these rheoelectrical creep tests at two different stresses for 6 vol.% CB in glycerol (Figure 6.10A and C) and in PDMS (Figure 6.10B and D) (see Methods section in the Appendix for details). The stresses were chosen to deform the material within the viscoelastic regime (Figure 6.10A and B) or in the viscous flow regime (Figure 6.10C and D). The solid vertical line indicates the point of stress removal. After applying stress, within the viscoelastic region, both EFs responded with an immediate increase in creep compliance, related to the elastic (spring-like) components with no time delay. This first increase showed a higher magnitude in the CB-glycerol EF compared to the CB-PDMS EF, indicating a more elastic, or stiffer, filler network. This finding is in good agreement with the network model based on CB-matrix affinity discussed in this thesis. The subsequent, non-linear increase in compliance is related to time dependent retardation caused by the viscoelastic components. Here, the CB-PDMS EF showed stronger viscoelastic behavior than the CB-glycerol EF. After stress removal, the opposite compliance behavior was observed, i.e., an immediate reduction due to the restoration of elastic components of the network and a gradual recovery of viscoelastic components afterwards. Since neither of the two EFs reached 0 creep compliance after relaxation, we conclude that a permanent deformation was induced, a characteristic of viscoelastic liquid materials.[174] The *in-situ* recorded electrical resistance signal helped to track the electrical network during the deformation. Apparently, there were no major changes observed during retardation or recovery. This indicates that, although the mechanical network was deformed, the electrical connections (electrical network) were sufficient to ensure the conduction of electrons. This aligns well with the percolation thresholds in EFs that indicate electrical conduction does not necessarily require a strong mechanical network.

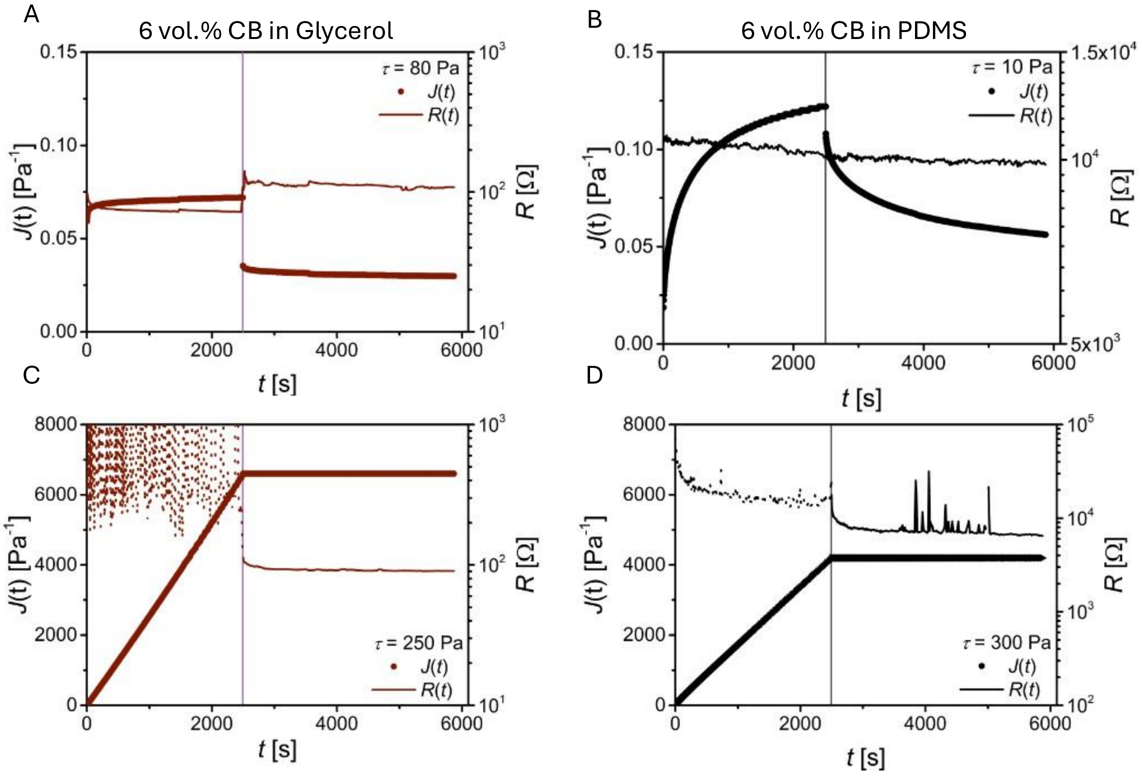

Figure 6.10. Creep tests with coupled electrical resistance measurements. A: 6 vol.% CB in glycerol at 80 Pa, B: 6 vol.% CB in PDMS at 10 Pa, C: 6 vol.% CB in glycerol at 250 Pa, and D: 6 vol.% CB in PDMS at 300 Pa. Closed symbols show the creep compliance and solid lines the electrical signal. Solid vertical lines indicate the point of stress removal within the test. Stress values were chosen to match creep compliance values between the different electrofluids.

At higher stress (Figure 6.10C-D), both EFs transitioned from viscoelastic liquid behavior to viscous fluids. Once the stress was applied, the compliance increased linearly over time, meaning that there is no further resistance against flow. The internal network cannot withstand that high stress and breaks (absence of elastic contributions). When the stress was removed, no relaxation occurred since the initial network structure was destroyed entirely, leaving no further information about the development of the mechanical network. An interesting point that evidences the potential of the rheoelectrical setup is that, in this region, the network reforming can be followed through the electrical signal. Under high stress, the electrical signal of the CB-glycerol EF scattered at high resistance values due to the constant destruction of CB agglomerate contacts. Among stress removal, a constant creep compliance was measured as expected, but the electrical resistance showed a fast relaxation, reaching a constant value around 100 Ω, as an equilibrium value. A similar behavior was also observed for the CB-PDMS EF with slight differences. Here, the scattering at increasing creep compliance was reduced compared to the CB-glycerol EF, and the recovery of the electrical signal was slightly slower to reach the final electrical resistance that was larger (10 kΩ), as expected for CB-PDMS EF. In both cases, the recovery was indicative of a build-up of a new filler network after the destruction of the initial one. The matching value of the electrical resistance before and after the test suggests that the new electrical network has the same equivalent circuit as the initial one, i.e., it fully recovers. From a methodological point of view, it can be concluded that the integration of electrical measurements into rheological tests is a powerful tool to track recovery phenomena that otherwise would remain undetected.

Stress Relaxation

If creep describes the material's response under a constant stress, stress relaxation describes it at a constant strain.[174] In this test, a step strain deformation is applied, held, and the relaxation of stress is monitored. Analogously to creep tests, here, the stress $\sigma(t)$ is transformed to the relaxation modulus $G(t)$ by normalizing to the applied strain γ_0 as described in Equation 6.3.

$$G(t) = \frac{\sigma(t)}{\gamma_0}. \qquad (6.3)$$

For a better comparison, the relaxation modulus is often normalized further by the initial modulus G_0, which is defined as the first value after the applied step strain deformation; therefore, the curves typically start at $G(t)/G_0 = 1$. The distinction between viscoelastic solid and viscoelastic liquid can be made by the degree of modulus relaxation. If the modulus relaxes gradually to zero after applied deformation, the material behaves like a viscoelastic liquid. The closer the value of residual modulus is to the initial one, the more it behaves like a viscoelastic solid. This is due to the reconfiguration and movement of particles that cause dissipation of energy, which is no longer stored in the network, causing a reduction in stress. Figure 6.11A-B shows the results for EFs containing 5 vol.% CB in glycerol and PDMS, respectively (see Methods section in the Appendix for details). The CB-glycerol EF showed viscoelastic solid behavior at both strains. Higher strains typically cause more network distortions and, therefore, lower equilibrium values of the relaxation modulus because less elastic energy remains in the material. On the contrary, the relaxation modulus of the CB-PDMS EF approached 0 at both strains, revealing its viscoelastic liquid behavior. One may notice that the definition of a viscoelastic liquid or solid differs from the creep measurements. The reason for that is the different degree of deformation. While in creep tests, the stress was chosen to be within the linear viscoelastic region, here, the applied strain was beyond the yield point (larger strains). Therefore, the observed material behavior is not directly comparable but complementary.

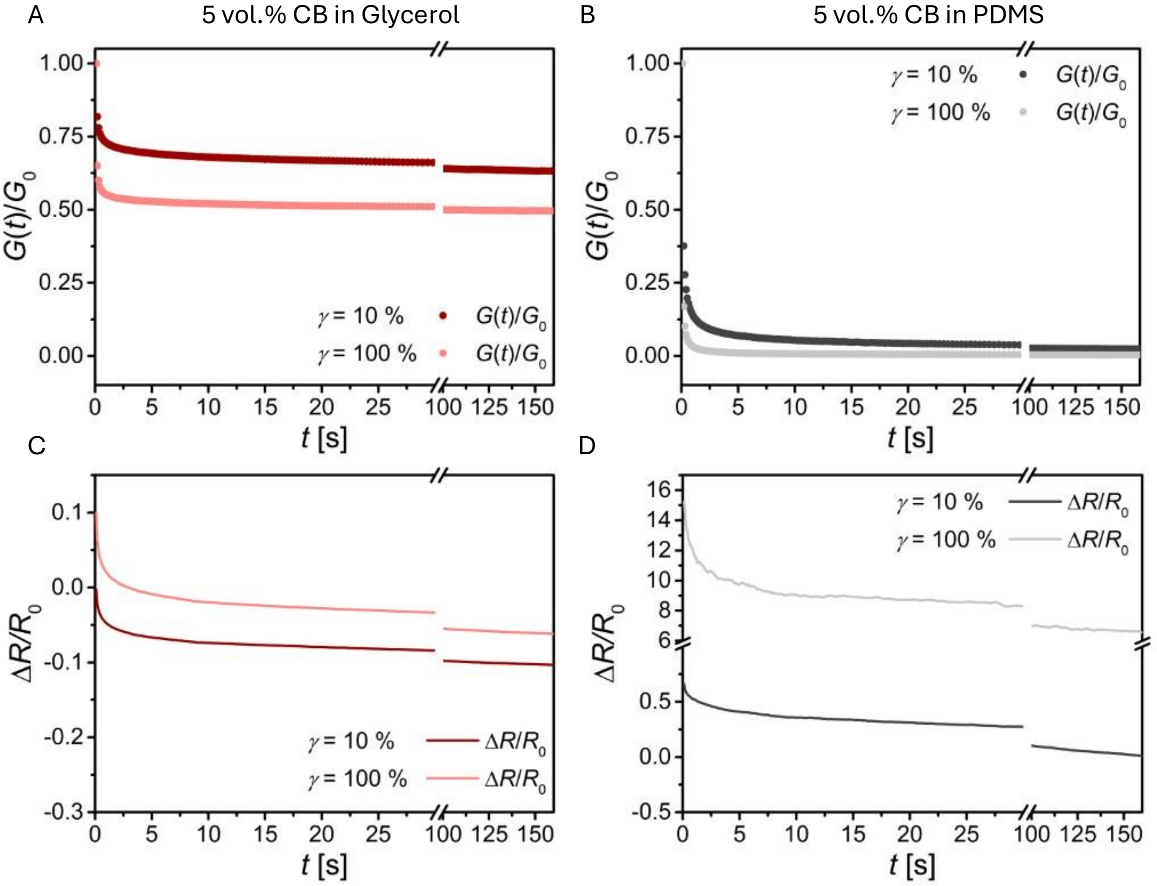

Figure 6.11. Normalized relaxation modulus as a function of time for a stress relaxation experiment for A: 5 vol.% CB in glycerol, and B: 5 vol.% CB in PDMS. Change in resistance as a function of time for the same stress relaxation experiment for C: 5 vol.% CB in glycerol, and D: 5 vol.% CB in PDMS. Each sample was tested at three different strains; dark and bright color distinguishes between 10% and 100% strain.

The electrical resistance signal was monitored simultaneously (see Figure 6.11C-D). In the case of the CB-glycerol EF, the electrical resistance was only slightly affected by the deformation. This is consistent with previous measurements on such EFs, showing only small changes in electrical resistance due to the favorable agglomerate network. CB-PDMS EFs, however, showed a larger change in resistance after deformation, which increased with the applied strain. Here, the affinity of the CB to the matrix is higher, and, therefore, the filler contacts in the network are easier to break, leading to larger electrical responses. Although not directly comparable, the differences in the change in resistance observed for stress relaxation tests in shear deformation are consistent with the calculated GF values reported above in section **6.2. Electrofluids as strain sensors or stable conductors**. Applying a step strain out of the LVE value may be used as a tool to test the material's response under application-specific conditions, to predict their behavior as strain sensor or stable conductor.

Differences seen in stress relaxation tests may also be related to the observed effect of secondary and shoulder peaks under cyclic deformation. The major relaxation for both EFs took place within the first few seconds after an applied step strain, sufficiently fast to cause a decrease in resistance between the loading and unloading phases. The CB-PDMS EF relaxed to a greater extent in shorter time scales, consistent with the preliminary results on XPCS mentioned above.

Electrofluids based on CB have shown interesting time dependent properties. Although the main focus here has fallen on the filler-matrix interactions and their impact on the filler network behavior, the above-described tests enable a more holistic understanding of electrofluids as liquid conductors and, therefore, should be applied to other systems. In particular, due to their potential to predict the sensitivity of electrofluids in their electrical responses to applied strain, for their application as soft electronic components.

7. Conclusions

This thesis introduces *Electrofluids* for the first time as a novel class of material envisioned as alternatives for soft electronic components. Electrofluids consist of concentrated suspensions of conductive particles dispersed in non-conductive liquid matrices. Throughout this work, their fabrication has been demonstrated and their electromechanical properties systematically investigated. The primary objectives were: a) to elucidate the interplay between electrical and mechanical networks within these systems and b) to demonstrate the potential of electrofluids with tailored properties for targeted applications. Based on the results discussed in the preceding chapters, the following conclusions can be drawn:

- Electrical percolation can be reached by adding a sufficient amount of conductive particles into a liquid matrix, resulting in Electrofluids- stable suspensions that conduct electricity while flowing.
- The affinity between filler particles and solvents affects the agglomeration behavior and, therefore, the electrical percolation threshold. A mismatch between the polarity of the solvent matrix and the filler surface results in reduced electrical percolation thresholds.
- The onset of the electrical and mechanical network formation (percolation thresholds) often differs due to the distinct mechanisms. In the case of the studied electrofluids, electrical percolation was often achieved at lower filler loadings due to the non-contact conduction mechanism of carbon materials.
- Preferential filler distribution enables exploitation of volume exclusion effects to create conductive emulsions with reduced electrical percolation threshold.
- Electrical and mechanical percolation thresholds are not necessarily identical, with the electrical one often being achieved at lower filler loadings due to the non-contact conduction mechanism of carbon materials.
- The filler type plays a role in network formation. In good agreement with the literature of solid composites, the percolation thresholds, both electrical and mechanical, for different filler types in electrofluids were found to follow the incremental order: nanowires < flakes < fractals.
- Moreover, the filler type and, therefore, the formed network has an impact on the electrical response of electrofluids under different deformation modes. More elastic networks of high aspect ratio fillers deliver lower electrical responses at larger strains, being promising stable interconnects.
- On the contrary, the design of electrofluids as strain sensors requires low aspect ratio fillers with large matrix affinity that form weak filler networks.

- Coupling *in-situ* electrical resistance measurements with rheological analysis allows the real-time tracking of particle rearrangement during and after mechanical deformation.
- Strain- and stress-softening effects in electrofluids are observed in both mechanical and electrical signals, attributing these effects to the filler network, not the matrix.
- The intracycle secondary and shoulder peaks in cyclic, uniaxial deformation are attributed to the destruction of the filler network and its subsequent relaxation.
- Preferential filler distribution enables exploitation of volume exclusion effects to create conductive emulsions with reduced electrical percolation threshold and tuned mechanical properties.

8. Outlook

This thesis provides a comprehensive understanding of the structure-property relationships of highly concentrated, conductive suspensions (Electrofluids). Although the fundamentals of this approach were discussed and evaluated, this thesis opens new research lines on this topic that are of interest to resolve more pieces to the puzzle.

Although this thesis focuses on carbon-based fillers, certain applications demand higher conductivity. For this, metal-based conductive fillers like silver, copper, or silver coated copper particles may be of interest in electrofluids. To address the problem of fast sedimentation of metal particles (densities are typically larger than 5 g/cm^3), one could consider using yield stress fluids as matrix materials that prevent sedimentation by trapping the particles. Another possible approach is the use of surfactants to stabilize the particles in the matrix. In this case, special care needs to be taken on the insulating effect of most surfactants.

Here, I used pristine materials with no further purification, which is a simple strategy to reduce preparation steps. However, to match certain affinities of fillers and matrix, pristine materials may not always meet the desired requirements. Further insights in surface modifications by means of chemical or physicochemical treatments could increase the number of specialized formulations with tailored properties.

Ultra small angle X-ray scattering (USAXS) is a powerful technique used to resolve structure of soft matter in the nano and micrometer range. The different hierarchical levels of carbon black span a vast amount of length scales. Primary particles are in the range of tens of nanometers while agglomerates can reach sizes of several micrometers, depending on the filler-matrix interactions. By using this technique in combination with tensile testing or rheology, the structure and the mechanical properties can be assessed simultaneously (i.e., network breakage and reconstruction). If also electrical measurements are coupled to this setup, three different layers of information can be monitored: structure, mechanical network, and electrical network, allowing a deeper analysis of the underlying deformation mechanisms and their impact on the macroscopic properties. While data acquisition has already been successfully done during the course of this thesis, the in-depth analysis of the three layers of data remains complex and should be addressed in future work to develop a comprehensive structural model of electrofluids.

Apart from the understanding of structure-property relationships, a further step is the integration of electrofluids into functional devices. Among others, this includes sensors, interconnects, or conductive lubricants. Finding promising use cases and targeting the design of electrofluids to fit their demands, is a crucial milestone to expand electrofluids applicability. In this thesis, proofs of concept have been shown and discussed, but further research, particularly in the electrofluid processing, for example via additive manufacturing, should be addressed to reach realistic, end-product prototypes.

This thesis presents for the first time Electrofluids, provides a solid comprehension of their fundamental properties, and will hopefully guide future work to excel their potential in both academic and industrial relevance.

References

1. Shirakawa, H.; Louis, E. J.; MacDiarmid, A. G.; Chiang, C. K.; Heeger, A. J., Synthesis of electrically conducting organic polymers: halogen derivatives of polyacetylene,(CH) x. *Journal of the Chemical Society, Chemical Communications* **1977,** (16), 578-580.

2. Poddar, A. K.; Patel, S. S.; Patel, H. D., Synthesis, characterization and applications of conductive polymers: A brief review. *Polymers for Advanced Technologies* **2021,** *32* (12), 4616-4641.

3. Potember, R. S.; Hoffman, R. C.; Hu, H. S.; Cocchiaro, J. E.; Viands, C. A.; Murphy, R. A.; Poehler, T. O., Conducting organics and polymers for electronic and optical devices. *Polymer* **1987,** *28* (4), 574-580.

4. Oh, J. Y.; Kim, S.; Baik, H.-K.; Jeong, U., Conducting polymer dough for deformable electronics. *Advanced materials (Deerfield Beach, Fla.)* **2016,** *28* (22), 4455-4461.

5. Dang, F.; Cai, Y.; Yang, P., Electrodeposition of graphene/polypyrrole electrode for flexible supercapacitor with large areal capacitance. *ACS Applied Energy Materials* **2024,** *7* (14), 5832-5838.

6. Kang, H. S.; Kim, D. H.; Kim, T. W., Organic light-emitting devices based on conducting polymer treated with benzoic acid. *Scientific Reports* **2021,** *11* (1), 3885.

7. He, H.; Zhang, L.; Yue, S.; Yu, S.; Wei, J.; Ouyang, J., Enhancement in the mechanical stretchability of PEDOT: PSS films by compounds of multiple hydroxyl groups for their application as transparent stretchable conductors. *Macromolecules* **2021,** *54* (3), 1234-1242.

8. Raman, S.; Ravi Sankar, A., Intrinsically conducting polymers in flexible and stretchable resistive strain sensors: a review. *Journal of Materials Science* **2022,** *57* (28), 13152-13178.

9. Ladd, C.; So, J.-H.; Muth, J.; Dickey, M. D., 3D printing of free standing liquid metal microstructures. *Adv. Mater* **2013,** *25* (36), 5081-5085.

10. Zhu, S.; So, J. H.; Mays, R.; Desai, S.; Barnes, W. R.; Pourdeyhimi, B.; Dickey, M. D., Ultrastretchable fibers with metallic conductivity using a liquid metal alloy core. *Advanced Functional Materials* **2013,** *23* (18), 2308-2314.

11. Dickey, M. D., Stretchable and soft electronics using liquid metals. *Advanced materials* **2017,** *29* (27), 1606425.

12. Rustagi, N.; Singh, R., Mercury and health care. *Indian journal of occupational and environmental medicine* **2010,** *14* (2), 45-48.

13. Dickey, M. D.; Chiechi, R. C.; Larsen, R. J.; Weiss, E. A.; Weitz, D. A.; Whitesides, G. M., Eutectic gallium-indium (EGaIn): a liquid metal alloy for the formation of stable structures in microchannels at room temperature. *Advanced functional materials* **2008,** *18* (7), 1097-1104.

14. Liu, T.; Sen, P.; Kim, C.-J., Characterization of nontoxic liquid-metal alloy galinstan for applications in microdevices. *Journal of Microelectromechanical Systems* **2011,** *21* (2), 443-450.

15. Chen, S.; Zhao, R.; Sun, X.; Wang, H.; Li, L.; Liu, J., Toxicity and biocompatibility of liquid metals. *Advanced Healthcare Materials* **2023,** *12* (3), 2201924.

16. Palleau, E.; Reece, S.; Desai, S. C.; Smith, M. E.; Dickey, M. D., Self-healing stretchable wires for reconfigurable circuit wiring and 3D microfluidics. *Advanced Materials (Deerfield Beach, Fla.)* **2013,** *25* (11), 1589-1592.

17. Markvicka, E. J.; Bartlett, M. D.; Huang, X.; Majidi, C., An autonomously electrically self-healing liquid metal–elastomer composite for robust soft-matter robotics and electronics. *Nature materials* **2018,** *17* (7), 618-624.

18. Yang, J.; Tang, D.; Ao, J.; Ghosh, T.; Neumann, T. V.; Zhang, D.; Piskarev, Y.; Yu, T.; Truong, V. K.; Xie, K., Ultrasoft liquid metal elastomer foams with positive and negative piezopermittivity for tactile sensing. *Advanced Functional Materials* **2020,** *30* (36), 2002611.

19. Bartlett, M. D.; Fassler, A.; Kazem, N.; Markvicka, E. J.; Mandal, P.; Majidi, C., Stretchable, high-k dielectric elastomers through liquid-metal inclusions. *Advanced Materials* **2016,** *28* (19), 3726-3731.

20. Thongruang, W.; Spontak, R. J.; Balik, C. M., Bridged double percolation in conductive polymer composites: an electrical conductivity, morphology and mechanical property study. *Polymer* **2002,** *43* (13), 3717-3725.

21. Choi, S.; Han, S. I.; Jung, D.; Hwang, H. J.; Lim, C.; Bae, S.; Park, O. K.; Tschabrunn, C. M.; Lee, M.; Bae, S. Y., Highly conductive, stretchable and biocompatible Ag–Au core–sheath nanowire composite for wearable and implantable bioelectronics. *Nature nanotechnology* **2018,** *13* (11), 1048-1056.

22. Lu, N.; Lu, C.; Yang, S.; Rogers, J., Highly sensitive skin-mountable strain gauges based entirely on elastomers. *Advanced Functional Materials* **2012,** *22* (19), 4044-4050.

23. Perius, D.; Engstler, M.; Blum, S.; González-García, L.; Kraus, T., Reconstruction of 3D Conductive Networks in Metal-Filled Elastomer Composites Indicates Dominance of Contact Resistances. *Small Structures* **2025**, 2500234.

24. Groover, M. P., *Fundamentals of modern manufacturing: materials, processes, and systems*. John Wiley & Sons: 2010.

25. Bashir, S.; Hina, M.; Iqbal, J.; Rajpar, A.; Mujtaba, M.; Alghamdi, N.; Wageh, S.; Ramesh, K.; Ramesh, S., Fundamental concepts of hydrogels: Synthesis, properties, and their applications. *Polymers* **2020,** *12* (11), 2702.

26. Maleki, B.; Kargar, P. G.; Ashrafi, S. S.; Ghani, M., Perspective Chapter: Introduction to Hydrogels–Definition, Classifications, Applications and Methods of Preparation. **2024**.

27. Deshpande, P.; Dornbrand-Lo, M.; Phondge, V.; Kelly, P.; Wong, A. K., Tissue engineering approaches for lymphedema: biomaterial innovations and clinical potential. *Frontiers in Cell and Developmental Biology* **2025,** *13*, 1537050.

28. Zheng, Y.; Li, Y.; Dai, K.; Liu, M.; Zhou, K.; Zheng, G.; Liu, C.; Shen, C., Conductive thermoplastic polyurethane composites with tunable piezoresistivity by modulating the filler dimensionality for flexible strain sensors. *Composites Part A: Applied Science and Manufacturing* **2017,** *101*, 41-49.

29. Huang, J.; Cao, L.; Xue, C.-Y.; Zhou, Y.-Z.; Cai, Y.-C.; Zhao, H.-Y.; Xing, Y.-H.; Yu, S.-H., Extremely soft, stretchable, and self-adhesive silicone conductive elastomer composites enabled by a molecular lubricating effect. *Nano Letters* **2022,** *22* (22), 8966-8974.

30. Han, L.; Liu, K.; Wang, M.; Wang, K.; Fang, L.; Chen, H.; Zhou, J.; Lu, X., Mussel-inspired adhesive and conductive hydrogel with long-lasting moisture and extreme temperature tolerance. *Advanced Functional Materials* **2018,** *28* (3), 1704195.

31. Das, S.; Irin, F.; Ma, L.; Bhattacharia, S. K.; Hedden, R. C.; Green, M. J., Rheology and morphology of pristine graphene/polyacrylamide gels. *ACS applied materials & interfaces* **2013,** *5* (17), 8633-8640.

32. Hsissou, R.; Seghiri, R.; Benzekri, Z.; Hilali, M.; Rafik, M.; Elharfi, A., Polymer composite materials: A comprehensive review. *Composite structures* **2021,** *262*, 113640.

33. Zardetto, V.; Brown, T. M.; Reale, A.; Di Carlo, A., Substrates for flexible electronics: A practical investigation on the electrical, film flexibility, optical, temperature, and solvent resistance properties. *Journal of Polymer Science Part B: Polymer Physics* **2011,** *49* (9), 638-648.

34. Xin, Y.; Cheng, Y.; Zhou, B.; Ren, H.; Yang, B.; Lou, Y.; Zhou, J.; Tao, C., Rheological Tunable Solid–Liquid Two-Phased Binary Metals Enable Thermoplastic and Electronic Conductive Composites for Conductive Adhesives and Conductive Wires. *Advanced Materials Technologies* **2025,** *10* (10), 2401902.

35. Tzounis, L.; Petousis, M.; Grammatikos, S.; Vidakis, N., 3D printed thermoelectric polyurethane/multiwalled carbon nanotube nanocomposites: A novel approach towards the fabrication of flexible and stretchable organic thermoelectrics. *Materials* **2020,** *13* (12), 2879.

36. Zhai, Y.; Yu, Y.; Zhou, K.; Yun, Z.; Huang, W.; Liu, H.; Xia, Q.; Dai, K.; Zheng, G.; Liu, C., Flexible and wearable carbon black/thermoplastic polyurethane foam with a pinnate-veined aligned porous structure for multifunctional piezoresistive sensors. *Chemical Engineering Journal* **2020,** *382*, 122985.

37. Kim, D. C.; Shim, H. J.; Lee, W.; Koo, J. H.; Kim, D. H., Material-based approaches for the fabrication of stretchable electronics. *Advanced Materials* **2020,** *32* (15), 1902743.

38. Park, S.; Mondal, K.; Treadway III, R. M.; Kumar, V.; Ma, S.; Holbery, J. D.; Dickey, M. D., Silicones for stretchable and durable soft devices: Beyond Sylgard-184. *ACS applied materials & interfaces* **2018,** *10* (13), 11261-11268.

39. Majidi, C., Soft-matter engineering for soft robotics. *Advanced Materials Technologies* **2019,** *4* (2), 1800477.

40. Choi, S.; Park, J.; Hyun, W.; Kim, J.; Kim, J.; Lee, Y. B.; Song, C.; Hwang, H. J.; Kim, J. H.; Hyeon, T., Stretchable heater using ligand-exchanged silver nanowire nanocomposite for wearable articular thermotherapy. *ACS nano* **2015,** *9* (6), 6626-6633.

41. Mujtaba, A.; Keller, M.; Ilisch, S.; Radusch, H.-J.; Thurn-Albrecht, T.; Saalwachter, K.; Beiner, M., Mechanical properties and cross-link density of styrene–butadiene model composites containing fillers with bimodal particle size distribution. *Macromolecules* **2012,** *45* (16), 6504-6515.

42. Peppas, N. A.; Hilt, J. Z.; Khademhosseini, A.; Langer, R., Hydrogels in biology and medicine: from molecular principles to bionanotechnology. *Advanced materials* **2006,** *18* (11), 1345-1360.

43. Utech, S.; Boccaccini, A. R., A review of hydrogel-based composites for biomedical applications: enhancement of hydrogel properties by addition of rigid inorganic fillers. *Journal of materials science* **2016,** *51*, 271-310.

44. Zhang, Y.; Tan, Y.; Lao, J.; Gao, H.; Yu, J., Hydrogels for flexible electronics. *ACS nano* **2023,** *17* (11), 9681-9693.

45. Buwalda, S. J.; Boere, K. W.; Dijkstra, P. J.; Feijen, J.; Vermonden, T.; Hennink, W. E., Hydrogels in a historical perspective: From simple networks to smart materials. *Journal of controlled release* **2014,** *190*, 254-273.

46. Kougkolos, G.; Golzio, M.; Laudebat, L.; Valdez-Nava, Z.; Flahaut, E., Hydrogels with electrically conductive nanomaterials for biomedical applications. *Journal of Materials Chemistry B* **2023,** *11* (10), 2036-2062.

47. Kamyshny, A.; Magdassi, S., Conductive nanomaterials for 2D and 3D printed flexible electronics. *Chemical Society Reviews* **2019,** *48* (6), 1712-1740.

48. Sharma, N.; Nair, N. M.; Nagasarvari, G.; Ray, D.; Swaminathan, P., A review of silver nanowire-based composites for flexible electronic applications. *Flexible and Printed Electronics* **2022,** *7* (1), 014009.

49. Lee, C.-J.; Park, K. H.; Han, C. J.; Oh, M. S.; You, B.; Kim, Y.-S.; Kim, J.-W., Crack-induced Ag nanowire networks for transparent, stretchable, and highly sensitive strain sensors. *Scientific reports* **2017,** *7* (1), 7959.

50. Zou, Z.; Zhu, C.; Li, Y.; Lei, X.; Zhang, W.; Xiao, J., Rehealable, fully recyclable, and malleable electronic skin enabled by dynamic covalent thermoset nanocomposite. *Science advances* **2018,** *4* (2), eaaq0508.

51. Zheng, Y.; Huang, X.; Chen, J.; Wu, K.; Wang, J.; Zhang, X., A review of conductive carbon materials for 3D printing: Materials, technologies, properties, and applications. *Materials* **2021,** *14* (14), 3911.

52. Coupette, F.; Zhang, L.; Kuttich, B.; Chumakov, A.; Roth, S. V.; González-García, L.; Kraus, T.; Schilling, T., Percolation of rigid fractal carbon black aggregates. *The Journal of Chemical Physics* **2021,** *155* (12).

53. Mondal, R. K.; Dubey, K. A.; Bhardwaj, Y. K., Role of the interface on electron transport in electro-conductive polymer-matrix composite: a review. *Polymer Composites* **2021,** *42* (6), 2614-2628.

54. Tiwari, S.; Purabgola, A.; Kandasubramanian, B., Functionalised graphene as flexible electrodes for polymer photovoltaics. *Journal of Alloys and Compounds* **2020,** *825*, 153954.

55. Reports, M. G. Carbon Black Feedstock (CBFS) Market Overview. https://www.marketgrowthreports.com/market-reports/carbon-black-feedstock-cbfs-market-112923 (accessed 06.11.2025).

56. Fan, Y.; Fowler, G. D.; Zhao, M., The past, present and future of carbon black as a rubber reinforcing filler–A review. *Journal of cleaner production* **2020,** *247*, 119115.

57. Watson, A. Y.; Valberg, P. A., Carbon black and soot: two different substances. *AIHAJ-American Industrial Hygiene Association* **2001,** *62* (2), 218-228.

58. Huang, J. C., Carbon black filled conducting polymers and polymer blends. *Advances in Polymer Technology: Journal of the Polymer Processing Institute* **2002,** *21* (4), 299-313.

59. Rahaman, M.; Aldalbahi, A.; Nayak, L.; Giri, R., Electrical conductivity of polymer–carbon composites: Effects of different factors. *Carbon-Containing Polymer Composites* **2019**, 159-210.

60. Donnet, J.-B., *Carbon black: science and technology*. CRC Press: 1993.

61. Mohammadi, M.; Mardi, S.; Phopase, J.; Wentz, F.; Samuel, J. J.; Ail, U.; Berggren, M.; Crispin, R.; Tybrandt, K.; Rahmanudin, A., Make it flow from solid to liquid: Redox-active electrofluids for intrinsically stretchable batteries. *Science Advances* **2025,** *11* (15), eadr9010.

62. Gong, T.; Jia, J.; Sun, X.-R.; Li, W.-D.; Ke, K.; Bao, R.-Y.; Yang, W., Design strategy for hierarchical structure of carbon black on microporous elastomer surface toward stretchable and compressive strain sensors. *Carbon* **2023,** *206*, 53-61.

63. Yong, S.; Aw, K., Modeling electrical resistance behavior of soft and flexible piezoresistive sensors based on carbon-black/silicone elastomer composites. *Sensing and Imaging* **2022,** *23* (1), 22.

64. Novoselov, K. S.; Geim, A. K.; Morozov, S. V.; Jiang, D.-e.; Zhang, Y.; Dubonos, S. V.; Grigorieva, I. V.; Firsov, A. A., Electric field effect in atomically thin carbon films. *science* **2004,** *306* (5696), 666-669.

65. Kuilla, T.; Bhadra, S.; Yao, D.; Kim, N. H.; Bose, S.; Lee, J. H., Recent advances in graphene based polymer composites. *Progress in polymer science* **2010,** *35* (11), 1350-1375.

66. Wang, Y.; Weng, G. J., Electrical conductivity of carbon nanotube-and graphene-based nanocomposites. In *Micromechanics and nanomechanics of composite solids*, Springer: 2017; pp 123-156.

67. Khanam, P. N.; Ponnamma, D.; Al-Madeed, M., Electrical properties of graphene polymer nanocomposites. In *Graphene-based polymer nanocomposites in electronics*, Springer: 2015; pp 25-47.

68. Johnson, R.; Zafar, M. A.; Thomas, S.; Jacob, M. V., A critical review on vacuum and atmospheric microwave plasma-based graphene synthesis. *FlatChem* **2025**, 100812.

69. Mardlin, K.; Osazuwa, O.; Kontopoulou, M., Solvent-free thermomechanical exfoliation of graphite into graphene nanoplatelet flakes: implications for conductive composites. *ACS Applied Nano Materials* **2022,** *5* (4), 4938-4947.

70. Fortugno, P.; Musikhin, S.; Shi, X.; Wang, H.; Wiggers, H.; Schulz, C., Synthesis of freestanding few-layer graphene in microwave plasma: The role of oxygen. *Carbon* **2022,** *186*, 560-573.

71. Al Faruque, M. A.; Syduzzaman, M.; Sarkar, J.; Bilisik, K.; Naebe, M., A review on the production methods and applications of graphene-based materials. *Nanomaterials* **2021,** *11* (9), 2414.

72. Lee, K. S.; Jeong, H. T., Optimization of electrochemical performance for activated carbon and functionalized graphene composite-based supercapacitor. *Journal of Materials Engineering and Performance* **2022,** *31* (6), 4679-4686.

73. Lu, S.; Wang, S.; Wang, G.; Ma, J.; Wang, X.; Tang, H.; Yang, X., Wearable graphene film strain sensors encapsulated with nylon fabric for human motion monitoring. *Sensors and Actuators A: Physical* **2019,** *295*, 200-209.

74. Journet, C.; Bernier, P., Production of carbon nanotubes. *Applied physics A: Materials science & processing* **1998,** *67* (1).

75. Paradise, M.; Goswami, T., Carbon nanotubes–production and industrial applications. *Materials & design* **2007,** *28* (5), 1477-1489.

76. Fan, Z.; Advani, S. G., Rheology of multiwall carbon nanotube suspensions. *Journal of Rheology* **2007,** *51* (4), 585-604.

77. Sandler, J.; Kirk, J.; Kinloch, I.; Shaffer, M.; Windle, A., Ultra-low electrical percolation threshold in carbon-nanotube-epoxy composites. *Polymer* **2003,** *44* (19), 5893-5899.

78. Wang, L.; Dang, Z.-M., Carbon nanotube composites with high dielectric constant at low percolation threshold. *Applied physics letters* **2005,** *87* (4).

79. Oseli, A.; Tomković, T.; Hatzikiriakos, S. G.; Vesel, A.; Arzenšek, M.; Rojac, T.; Mihelčič, M.; Perše, L. S., Carbon nanotube network formation and configuration/morphology on reinforcing and conductive performance of polymer-based nanocomposites. *Composites Science and Technology* **2023,** *237*, 110010.

80. Ma, P.-C.; Siddiqui, N. A.; Marom, G.; Kim, J.-K., Dispersion and functionalization of carbon nanotubes for polymer-based nanocomposites: A review. *Composites Part A: Applied Science and Manufacturing* **2010,** *41* (10), 1345-1367.

81. Lourie, O.; Wagner, H., Evaluation of Young's modulus of carbon nanotubes by micro-Raman spectroscopy. *Journal of Materials Research* **1998,** *13* (9), 2418-2422.

82. Lu, K.; Lago, R.; Chen, Y.; Green, M.; Harris, P.; Tsang, S., Mechanical damage of carbon nanotubes by ultrasound. *Carbon* **1996,** *34* (6).

83. Ruan, B.; Jacobi, A. M., Ultrasonication effects on thermal and rheological properties of carbon nanotube suspensions. *Nanoscale research letters* **2012,** *7* (1), 127.

84. Broadbent, S. R.; Hammersley, J. M. In *Percolation processes: I. Crystals and mazes*, Mathematical proceedings of the Cambridge philosophical society, Cambridge University Press: 1957; pp 629-641.

85. Kirkpatrick, S., Percolation and conduction. *Reviews of modern physics* **1973,** *45* (4), 574.

86. Berkowitz, B.; Ewing, R. P., Percolation theory and network modeling applications in soil physics. *Surveys in Geophysics* **1998,** *19* (1), 23-72.

87. Lux, F., Models proposed to explain the electrical conductivity of mixtures made of conductive and insulating materials. *Journal of materials science* **1993,** *28* (2), 285-301.

88. Wang, J.; Zhou, Z.; Zhang, W.; Garoni, T. M.; Deng, Y., Bond and site percolation in three dimensions. *Physical Review E—Statistical, Nonlinear, and Soft Matter Physics* **2013,** *87* (5), 052107.

89. Moisala, A.; Li, Q.; Kinloch, I.; Windle, A., Thermal and electrical conductivity of single-and multi-walled carbon nanotube-epoxy composites. *Composites science and technology* **2006,** *66* (10), 1285-1288.

90. Wu, H.; Wu, X.; Ge, M.; Zhang, G.; Wang, Y.; Jiang, J., Effect analysis of filler sizes on percolation threshold of isotropical conductive adhesives. *Composites Science and Technology* **2007,** *67* (6), 1116-1120.

91. Ram, R.; Rahaman, M.; Aldalbahi, A.; Khastgir, D., Determination of percolation threshold and electrical conductivity of polyvinylidene fluoride (PVDF)/short carbon fiber (SCF) composites: effect of SCF aspect ratio. *Polymer International* **2017,** *66* (4), 573-582.

92. Li, J.; Ma, P. C.; Chow, W. S.; To, C. K.; Tang, B. Z.; Kim, J. K., Correlations between percolation threshold, dispersion state, and aspect ratio of carbon nanotubes. *Advanced Functional Materials* **2007,** *17* (16), 3207-3215.

93. Schilling, T.; Jungblut, S.; Miller, M. A., Depletion-induced percolation in networks of nanorods. *Physical review letters* **2007,** *98* (10), 108303.

94. Nassar, H.; Dahiya, A. S.; Dahiya, R., Tunable Conductive Composite for Printed Sensors and Embedded Circuits. *Advanced Intelligent Systems* **2023,** *5* (10), 2300075.

95. Xing, Y.; Wang, W.; Hu, D.; Xu, W., Percolation threshold and excluded volume of overlapping spherotetrahedral particle systems: Shape evolution from tetrahedron to sphere. *Powder Technology* **2022,** *408*, 117713.

96. Kwon, S.; Cho, H. W.; Gwon, G.; Kim, H.; Sung, B. J., Effects of shape and flexibility of conductive fillers in nanocomposites on percolating network formation and electrical conductivity. *Physical Review E* **2016,** *93* (3), 032501.

97. Li, J.; Kim, J.-K., Percolation threshold of conducting polymer composites containing 3D randomly distributed graphite nanoplatelets. *Composites science and technology* **2007,** *67* (10), 2114-2120.

98. Avilés, F.; Cauich-Rodríguez, J. V.; Toro-Estay, P.; Yazdani-Pedram, M.; Aguilar-Bolados, H., Improving carbon nanotube/polymer interactions in nanocomposites. In *Carbon nanotube-reinforced polymers*, Elsevier: 2018; pp 83-115.

99. Jomaa, M.; Masenelli-Varlot, K.; Seveyrat, L.; Lebrun, L.; Jawhar, M. D.; Beyou, E.; Cavaillé, J.-Y., Investigation of elastic, electrical and electromechanical properties of polyurethane/grafted carbon nanotubes nanocomposites. *Composites Science and Technology* **2015,** *121*, 1-8.

100. Bai, L.; Bai, Y.; Zheng, J., Improving the filler dispersion and performance of silicone rubber/multi-walled carbon nanotube composites by noncovalent functionalization of polymethylphenylsiloxane. *Journal of Materials Science* **2017,** *52*, 7516-7529.

101. Smoleń, P.; Czujko, T.; Komorek, Z.; Grochala, D.; Rutkowska, A.; Osiewicz-Powęzka, M., Mechanical and electrical properties of epoxy composites modified by functionalized multiwalled carbon nanotubes. *Materials* **2021,** *14* (12), 3325.

102. Wu, X.; Yin, T.; Yang, Y.; Liu, W.; Wang, D.; Wan, L.; Liao, Y., The Influence of the Dispersion and Covalent Functionalization of CNTs on Electrical Conduction Under an Electric Field in LDPE/CNT Composites. *Polymers* **2025,** *17* (14), 1940.

103. Yun, G.; Tang, S.-Y.; Lu, H.; Zhang, S.; Dickey, M. D.; Li, W., Hybrid-filler stretchable conductive composites: from fabrication to application. *Small Science* **2021,** *1* (6), 2000080.

104. Sumita, M.; Sakata, K.; Asai, S.; Miyasaka, K.; Nakagawa, H., Dispersion of fillers and the electrical conductivity of polymer blends filled with carbon black. *Polymer bulletin* **1991,** *25*, 265-271.

105. Li, Y.; Wang, S.; Zhang, Y.; Zhang, Y., Carbon black-filled immiscible polypropylene/epoxy blends. *Journal of applied polymer science* **2006,** *99* (2), 461-471.

106. Pang, H.; Xu, L.; Yan, D.-X.; Li, Z.-M., Conductive polymer composites with segregated structures. *Progress in Polymer Science* **2014,** *39* (11), 1908-1933.

107. Chen, J.; Shi, Y.-y.; Yang, J.-h.; Zhang, N.; Huang, T.; Chen, C.; Wang, Y.; Zhou, Z.-w., A simple strategy to achieve very low percolation threshold via the selective distribution of carbon nanotubes at the interface of polymer blends. *Journal of Materials Chemistry* **2012,** *22* (42), 22398-22404.

108. Koronio, E.; Shachar-Michaely, G.; Regev, O.; Ziskind, G., A Study on Thermal Conductivity Enhancement in Composites Utilizing Excluded Volume Effects. *Langmuir* **2025**.

109. Bao, H.-D.; Guo, Z.-X.; Yu, J., Effect of electrically inert particulate filler on electrical resistivity of polymer/multi-walled carbon nanotube composites. *Polymer* **2008,** *49* (17), 3826-3831.

110. Lin, S.; You, W.; Yu, W.; Wang, X., Key factors in mechanical reinforcement by double percolation network: particle migration and shear stability of filler network. *Polymer* **2019,** *182*, 121820.

111. Yu, Y.; Song, G.; Sun, L., Determinant role of tunneling resistance in electrical conductivity of polymer composites reinforced by well dispersed carbon nanotubes. *Journal of Applied Physics* **2010,** *108* (8).

112. Jing, X.; Zhao, W.; Lan, L., The effect of particle size on electric conducting percolation threshold in polymer/conducting particle composites. *Journal of materials science letters* **2000,** *19* (5), 377-379.

113. Jin, L.; Chortos, A.; Lian, F.; Pop, E.; Linder, C.; Bao, Z.; Cai, W., Microstructural origin of resistance–strain hysteresis in carbon nanotube thin film conductors. *Proceedings of the National Academy of Sciences* **2018,** *115* (9), 1986-1991.

114. Lee, P.; Lee, J.; Lee, H.; Yeo, J.; Hong, S.; Nam, K. H.; Lee, D.; Lee, S. S.; Ko, S. H., Highly stretchable and highly conductive metal electrode by very long metal nanowire percolation network. *Advanced materials* **2012,** *24* (25), 3326-3332.

115. Won, P.; Park, J. J.; Lee, T.; Ha, I.; Han, S.; Choi, M.; Lee, J.; Hong, S.; Cho, K.-J.; Ko, S. H., Stretchable and transparent kirigami conductor of nanowire percolation network for electronic skin applications. *Nano letters* **2019,** *19* (9), 6087-6096.

116. Ning, X.; Wang, X.; Zhang, Y.; Yu, X.; Choi, D.; Zheng, N.; Kim, D. S.; Huang, Y.; Zhang, Y.; Rogers, J. A., Assembly of advanced materials into 3D functional structures by methods inspired by origami and kirigami: a review. *Advanced Materials Interfaces* **2018,** *5* (13), 1800284.

117. Cooper, G., The structure and mechanical properties of composite materials. *Review of Physics in Technology* **1971,** *2* (2), 49.

118. Payne, A. R., The dynamic properties of carbon black-loaded natural rubber vulcanizates. Part I. *Journal of applied polymer science* **1962,** *6* (19), 57-63.

119. Mullins, L., Effect of stretching on the properties of rubber. *Rubber chemistry and technology* **1948,** *21* (2), 281-300.

120. Hentschke, R., The Payne effect revisited. *Express Polymer Letters* **2017,** *11* (4).

121. Payne, A.; Whittaker, R.; Smith, J., Effect of vulcanization on the low-strain dynamic properties of filled rubbers. *Journal of Applied polymer science* **1972,** *16* (5), 1191-1212.

122. Warasitthinon, N.; Genix, A.-C.; Sztucki, M.; Oberdisse, J.; Robertson, C. G., The Payne effect: Primarily polymer-related or filler-related phenomenon? *Rubber Chemistry and Technology* **2019,** *92* (4), 599-611.

123. Meera, A.; Said, S.; Grohens, Y.; Thomas, S., Nonlinear viscoelastic behavior of silica-filled natural rubber nanocomposites. *The Journal of Physical Chemistry C* **2009,** *113* (42), 17997-18002.

124. Rharbi, Y.; Cabane, B.; Vacher, A.; Joanicot, M.; Boue, F., Modes of deformation in a soft/hardnanocomposite: A SANS study. *Europhysics letters* **1999,** *46* (4), 472.

125. Sternstein, S.; Zhu, A.-J., Reinforcement mechanism of nanofilled polymer melts as elucidated by nonlinear viscoelastic behavior. *Macromolecules* **2002,** *35* (19), 7262-7273.

126. Zhan, L.; Qu, S.; Xiao, R., A review on the mullins effect in tough elastomers and gels. *Acta Mechanica Solida Sinica* **2024,** *37* (2), 181-214.

127. Kondratov, A. P.; Lozitskaya, A. V.; Samokhin, V. N.; Volinsky, A. A., Mullins effect in polymer large deformation strain gauges. *Journal of Polymer Research* **2023,** *30* (1), 36.

128. Diani, J.; Fayolle, B.; Gilormini, P., A review on the Mullins effect. *European Polymer Journal* **2009,** *45* (3), 601-612.

129. Blanchard, A.; Parkinson, D., Breakage of carbon-rubber networks by applied stress. *Rubber Chemistry and Technology* **1952,** *25* (4), 808-842.

130. Suzuki, N.; Ito, M.; Yatsuyanagi, F., Effects of rubber/filler interactions on deformation behavior of silica filled SBR systems. *Polymer* **2005,** *46* (1), 193-201.

131. Houwink, R., Slipping of molecules during the deformation of reinforced rubber. *Rubber Chemistry and Technology* **1956,** *29* (3), 888-893.

132. Harwood, J.; Mullins, L.; Payne, A. R., Stress softening in natural rubber vulcanizates. Part II. Stress softening effects in pure gum and filler loaded rubbers. *Journal of Applied Polymer Science* **1965,** *9* (9), 3011-3021.

133. Cassagnau, P., Melt rheology of organoclay and fumed silica nanocomposites. *Polymer* **2008,** *49* (9), 2183-2196.

134. Zhong, X.; Song, Y.; Zheng, Q., Payne effect and Mullins effect of silica filled butadiene rubber nanocomposites vulcanizates and their unextractable gels. *Polymer* **2023,** *267*, 125634.

135. Arora, N.; Dua, S.; Singh, V. K.; Singh, S. K.; Senthilkumar, T., A comprehensive review on fillers and mechanical properties of 3D printed polymer composites. *Materials Today Communications* **2024**, 109617.

136. Odegard, G.; Clancy, T.; Gates, T., Modeling of the mechanical properties of nanoparticle/polymer composites. In *Characterization of Nanocomposites*, Jenny Stanford Publishing: 2017; pp 319-342.

137. Cho, J.; Joshi, M.; Sun, C., Effect of inclusion size on mechanical properties of polymeric composites with micro and nano particles. *Composites Science and Technology* **2006,** *66* (13), 1941-1952.

138. Guo, J.; Liu, Y.; Prada-Silvy, R.; Tan, Y.; Azad, S.; Krause, B.; Pötschke, P.; Grady, B. P., Aspect ratio effects of multi-walled carbon nanotubes on electrical, mechanical, and thermal properties of polycarbonate/MWCNT composites. *Journal of Polymer Science Part B: Polymer Physics* **2014,** *52* (1), 73-83.

139. Ayatollahi, M.; Shadlou, S.; Shokrieh, M.; Chitsazzadeh, M., Effect of multi-walled carbon nanotube aspect ratio on mechanical and electrical properties of epoxy-based nanocomposites. *Polymer Testing* **2011,** *30* (5), 548-556.

140. Aït Hocine, N.; Miranda, C.; Nauman, S.; Langlet, A., Electrical properties of elastomer-based composites reinforced with carbon nanotubes—A review. *Polymers for Advanced Technologies* **2024,** *35* (2), e6299.

141. Chou, T.; Kelly, A., Mechanical properties of composites. *Annual Review of Materials Science* **1980,** *10* (1), 229-259.

142. Ke, K.; Sang, Z.; Manas-Zloczower, I., Stretchable elastomer composites with segregated filler networks: effect of carbon nanofiller dimensionality. *Nanoscale Advances* **2019,** *1* (6), 2337-2347.

143. Guohua, L.; Zhiyong, Z.; Yangang, W., Research progress on highly conductive polymer composites based on carbon-based nanofillers. *Polymer Composites* **2025**.

144. Ervina, J.; Mariatti, M.; Hamdan, S., Effect of filler loading on the tensile properties of multi-walled carbon nanotube and graphene nanopowder filled epoxy composites. *Procedia Chemistry* **2016,** *19*, 897-905.

145. Fu, S.-Y.; Feng, X.-Q.; Lauke, B.; Mai, Y.-W., Effects of particle size, particle/matrix interface adhesion and particle loading on mechanical properties of particulate–polymer composites. *Composites Part B: Engineering* **2008,** *39* (6), 933-961.

146. Huang, X.; Iizuka, T.; Jiang, P.; Ohki, Y.; Tanaka, T., Role of interface on the thermal conductivity of highly filled dielectric epoxy/AlN composites. *The Journal of Physical Chemistry C* **2012,** *116* (25), 13629-13639.

147. Naik, P.; Pradhan, S.; Sahoo, P.; Acharya, S., Effect of filler loading on mechanical properties of natural carbon black reinforced polymer composites. *Materials Today: Proceedings* **2020,** *26*, 1892-1896.

148. Chodak, I.; Omastova, M.; Pionteck, J., Relation between electrical and mechanical properties of conducting polymer composites. *Journal of applied polymer science* **2001,** *82* (8), 1903-1906.

149. Chung, D., A critical review of piezoresistivity and its application in electrical-resistance-based strain sensing. *Journal of Materials Science* **2020,** *55* (32), 15367-15396.

150. Greaves, G. N.; Greer, A. L.; Lakes, R. S.; Rouxel, T., Poisson's ratio and modern materials. *Nature materials* **2011,** *10* (11), 823-837.

151. Garcia, J. R.; O'Suilleabhain, D.; Kaur, H.; Coleman, J. N., A simple model relating gauge factor to filler loading in nanocomposite strain sensors. *ACS applied nano materials* **2021,** *4* (3), 2876-2886.

152. Chen, J.; Cui, C.; Zhang, Q.-h., Impact of conductive-filler content on the static sensing performance of spray-coated flexible strain sensors for steel-bridge strain monitoring. *Smart Materials and Structures* **2025,** *34* (3), 035010.

153. Avilés, F.; May-Pat, A.; López-Manchado, M. A.; Verdejo, R.; Bachmatiuk, A.; Rümmeli, M. H., A comparative study on the mechanical, electrical and piezoresistive properties of polymer composites using carbon nanostructures of different topology. *European Polymer Journal* **2018,** *99*, 394-402.

154. Vo, T. S.; Kim, K., Recent Trends of functional composites and structures for electromechanical sensors: A review. *Advanced Intelligent Systems* **2024,** *6* (5), 2300730.

155. Yang, H.; Yao, X.; Yuan, L.; Gong, L.; Liu, Y., Strain-sensitive electrical conductivity of carbon nanotube-graphene-filled rubber composites under cyclic loading. *Nanoscale* **2019,** *11* (2), 578-586.

156. Mersch, J.; Winger, H.; Nocke, A.; Cherif, C.; Gerlach, G., Experimental investigation and modeling of the dynamic resistance response of carbon particle-filled polymers. *Macromolecular Materials and Engineering* **2020,** *305* (10), 2000361.

157. Boland, C. S., Quantifying the contributing factors toward signal fatigue in nanocomposite strain sensors. *ACS Applied Polymer Materials* **2020,** *2* (8), 3474-3480.

158. Zhang, Z.; Innocent, M. T.; Tang, N.; Li, R.; Hu, Z.; Zhai, M.; Yang, L.; Ma, W.; Xiang, H.; Zhu, M., Electromechanical performance of strain sensors based on viscoelastic conductive composite polymer fibers. *ACS Applied Materials & Interfaces* **2022,** *14* (39), 44832-44840.

159. Mezger, T. G., *Das Rheologie Handbuch*. Vincentz Network: 2016.

160. Selvakumar, R. D.; Dhinakaran, S., Effective viscosity of nanofluids—A modified Krieger–Dougherty model based on particle size distribution (PSD) analysis. *Journal of molecular liquids* **2017,** *225*, 20-27.

161. Einstein, A. Eine neue bestimmung der moleküldimensionen. ETH Zurich, 1905.

162. Krieger, I. M.; Dougherty, T. J., A mechanism for non-Newtonian flow in suspensions of rigid spheres. *Trans. Soc. Rheol* **1959,** *3* (1), 137-152.

163. Willenbacher, N.; Georgieva, K., Rheology of disperse systems. *Product design and engineering: Formulation of gels and pastes* **2013**, 7-49.

164. Trappe, V.; Prasad, V.; Cipelletti, L.; Segre, P.; Weitz, D. A., Jamming phase diagram for attractive particles. *Nature* **2001,** *411* (6839), 772-775.

165. Zaccarelli, E., Colloidal gels: equilibrium and non-equilibrium routes. *Journal of Physics: Condensed Matter* **2007,** *19* (32), 323101.

166. Trappe, V.; Sandkühler, P., Colloidal gels—low-density disordered solid-like states. *Current opinion in colloid & interface science* **2004,** *8* (6), 494-500.

167. Lin, M.; Lindsay, H. M.; Weitz, D.; Ball, R.; Klein, R.; Meakin, P., Universality in colloid aggregation. *Nature* **1989,** *339* (6223), 360-362.

168. Shih, W. Y.; Liu, J.; Shih, W.-H.; Aksay, I. A., Aggregation of colloidal particles with a finite interparticle attraction energy. *Journal of statistical physics* **1991,** *62* (5), 961-984.

169. Martinoty, P.; Sánchez-Ferrer, A., Viscoelastic properties of colloidal systems with attractive solid particles at low concentration: A review, new results and interpretations. *Advances in Colloid and Interface Science* **2025,** *335*, 103335.

170. Du, Y.; Liu, M.; Guo, L., Scattering phase function of fractal aggregates of TiO2 particulate photocatalyst simulated with discrete dipole approximation. *International Journal of Hydrogen Energy* **2020,** *45* (52), 28034-28043.

171. Feng, S.; Sen, P. N., Percolation on elastic networks: new exponent and threshold. *Physical review letters* **1984,** *52* (3), 216.

172. Kantor, Y.; Webman, I., Elastic properties of random percolating systems. *Physical Review Letters* **1984,** *52* (21), 1891.

173. Dickinson, E., Structure and rheology of colloidal particle gels: Insight from computer simulation. *Advances in colloid and interface science* **2013,** *199*, 114-127.

174. Mezger, T. G., *The rheology handbook*. Vincentz Network Hannover, Germany: 2012; Vol. 10.

175. Ramli, H.; Zainal, N. F. A.; Hess, M.; Chan, C. H., Basic principle and good practices of rheology for polymers for teachers and beginners. *Chemistry Teacher International* **2022,** *4* (4), 307-326.

176. Jia, Y.; Peng, K.; Gong, X.-l.; Zhang, Z., Creep and recovery of polypropylene/carbon nanotube composites. *International Journal of Plasticity* **2011,** *27* (8), 1239-1251.

177. Pan, Y.; Liu, X.; Hao, X.; Schubert, D. W., Conductivity and phase morphology of carbon black-filled immiscible polymer blends under creep: An experimental and theoretical study. *Physical Chemistry Chemical Physics* **2016,** *18* (47), 32125-32131.

178. Penu, C.; Hu, G. H.; Fernandez, A.; Marchal, P.; Choplin, L., Rheological and electrical percolation thresholds of carbon nanotube/polymer nanocomposites. *Polymer Engineering & Science* **2012,** *52* (10), 2173-2181.

179. da Silva, M. P.; Cavalcanti, S. N.; Alves, A. M.; Freitas, D. M.; Agrawal, P.; Vilar, E. O.; de Mélo, T. J., Evaluation of the rheological and electrical percolation of high-density polyethylene/carbon black composites using mathematical models. *Polymer Engineering & Science* **2021,** *61* (7), 2105-2116.

180. Gao, C.; Liu, P.; Ding, Y.; Li, T.; Wang, F.; Chen, J.; Zhang, S.; Li, Z.; Yang, M., Non-contact percolation of unstable graphene networks in poly (styrene-co-acrylonitrile) nanocomposites: Electrical and rheological properties. *Composites Science and Technology* **2018,** *155*, 41-49.

181. Richards, J. J.; Hipp, J. B.; Riley, J. K.; Wagner, N. J.; Butler, P. D., Clustering and percolation in suspensions of carbon black. *Langmuir* **2017,** *33* (43), 12260-12266.

182. Parant, H.; Muller, G.; Le Mercier, T.; Tarascon, J.; Poulin, P.; Colin, A., Flowing suspensions of carbon black with high electronic conductivity for flow applications: Comparison between carbons black and exhibition of specific aggregation of carbon particles. *Carbon* **2017,** *119*, 10-20.

183. Wang, T.; Liu, Q.; Liu, H.; Xu, B.; Xu, H., Printable and highly stretchable viscoelastic conductors with kinematically reconstructed conductive pathways. *Advanced Materials* **2022,** *34* (28), 2202418.

184. Ma, L.; Shuai, X.; Hu, Y.; Liang, X.; Zhu, P.; Sun, R.; Wong, C.-p., A highly sensitive and flexible capacitive pressure sensor based on a micro-arrayed polydimethylsiloxane dielectric layer. *Journal of Materials Chemistry C* **2018,** *6* (48), 13232-13240.

185. Wang, Z.; Gao, W.; Zhang, Q.; Zheng, K.; Xu, J.; Xu, W.; Shang, E.; Jiang, J.; Zhang, J.; Liu, Y., 3D-printed graphene/polydimethylsiloxane composites for stretchable and strain-insensitive temperature sensors. *ACS applied materials & interfaces* **2018,** *11* (1), 1344-1352.

186. Chen, T.; Shi, Q.; Zhu, M.; He, T.; Sun, L.; Yang, L.; Lee, C., Triboelectric Self-Powered Wearable Flexible Patch as 3D Motion Control Interface for Robotic Manipulator. *ACS Nano* **2018,** *12* (11), 11561-11571.

187. Hwang, B.-U.; Lee, J.-H.; Trung, T. Q.; Roh, E.; Kim, D.-I.; Kim, S.-W.; Lee, N.-E., Transparent stretchable self-powered patchable sensor platform with ultrasensitive recognition of human activities. *ACS nano* **2015,** *9* (9), 8801-8810.

188. Meng, K.; Wu, Y.; He, Q.; Zhou, Z.; Wang, X.; Zhang, G.; Fan, W.; Liu, J.; Yang, J., Ultrasensitive Fingertip-Contacted Pressure Sensors To Enable Continuous Measurement of Epidermal Pulse Waves on Ubiquitous Object Surfaces. *ACS Appl Mater Interfaces* **2019,** *11* (50), 46399-46407.

189. Melzer, M.; Makarov, D.; Schmidt, O., A review on stretchable magnetic field sensorics. *Journal of Physics D: Applied Physics* **2019,** *53* (8), 083002.

190. Chen, J.; Zhu, Y.; Chang, X.; Pan, D.; Song, G.; Guo, Z.; Naik, N., Recent Progress in Essential Functions of Soft Electronic Skin. *Advanced Functional Materials* **2021,** *31* (42).

191. Rao, Z.; Ershad, F.; Almasri, A.; Gonzalez, L.; Wu, X.; Yu, C., Soft electronics for the skin: from health monitors to human–machine interfaces. *Advanced Materials Technologies* **2020,** *5* (9), 2000233.

192. Barlian, A. A.; Park, W.-T.; Mallon, J. R.; Rastegar, A. J.; Pruitt, B. L., Semiconductor piezoresistance for microsystems. *Proceedings of the IEEE* **2009,** *97* (3), 513-552.

193. Zhang, S.; Cai, L.; Li, W.; Miao, J.; Wang, T.; Yeom, J.; Sepúlveda, N.; Wang, C., Fully Printed Silver-Nanoparticle-Based Strain Gauges with Record High Sensitivity. *Advanced Electronic Materials* **2017,** *3* (7).

194. Karuthedath, C. B.; Fikri, U.; Ruf, F.; Schwesinger, N., Characterization of Carbon Black Filled PDMS-Composite Membranes for Sensor Applications. *Key Engineering Materials* **2017,** *753*, 18-27.

195. Shintake, J.; Piskarev, E.; Jeong, S. H.; Floreano, D., Ultrastretchable Strain Sensors Using Carbon Black-Filled Elastomer Composites and Comparison of Capacitive Versus Resistive Sensors. *Advanced Materials Technologies* **2018,** *3* (3), 1700284.

196. Zhai, W.; Xia, Q.; Zhou, K.; Yue, X.; Ren, M.; Zheng, G.; Dai, K.; Liu, C.; Shen, C., Multifunctional flexible carbon black/polydimethylsiloxane piezoresistive sensor with ultrahigh linear range, excellent durability and oil/water separation capability. *Chemical Engineering Journal* **2019,** *372*, 373-382.

197. Fu, Y.-F.; Yi, F.-L.; Liu, J.-R.; Li, Y.-Q.; Wang, Z.-Y.; Yang, G.; Huang, P.; Hu, N.; Fu, S.-Y., Super soft but strong E-Skin based on carbon fiber/carbon black/silicone composite: Truly mimicking tactile sensing and mechanical behavior of human skin. *Composites Science and Technology* **2020,** *186*, 107910.

198. Ata, S.; Kobashi, K.; Yumura, M.; Hata, K., Mechanically Durable and Highly Conductive Elastomeric Composites from Long Single-Walled Carbon Nanotubes Mimicking the Chain Structure of Polymers. *Nano Letters* **2012,** *12* (6), 2710-2716.

199. Zuruzi, A. S.; Haffiz, T. M.; Affidah, D.; Amirul, A.; Norfatriah, A.; Nurmawati, M. H., Towards wearable pressure sensors using multiwall carbon nanotube/polydimethylsiloxane nanocomposite foams. *Materials & Design* **2017,** *132*, 449-458.

200. Shi, G.; Zhao, Z.; Pai, J.-H.; Lee, I.; Zhang, L.; Stevenson, C.; Ishara, K.; Zhang, R.; Zhu, H.; Ma, J., Highly Sensitive, Wearable, Durable Strain Sensors and Stretchable Conductors Using Graphene/Silicon Rubber Composites. *Advanced Functional Materials* **2016,** *26* (42), 7614-7625.

201. Chen, Z.; Xi, J.; Huang, W.; Yuen, M. M. F., Stretchable conductive elastomer for wireless wearable communication applications. *Scientific Reports* **2017,** *7* (1), 10958.

202. Larmagnac, A.; Eggenberger, S.; Janossy, H.; Vörös, J., Stretchable electronics based on Ag-PDMS composites. *Scientific Reports* **2014,** *4*, 7254.

203. Chen, J.; Yu, Q.; Cui, X.; Dong, M.; Zhang, J.; Wang, C.; Fan, J.; Zhu, Y.; Guo, Z., An overview of stretchable strain sensors from conductive polymer nanocomposites. *Journal of Materials Chemistry C* **2019,** *7* (38), 11710-11730.

204. Zheng, Y.; Li, Y.; Li, Z.; Wang, Y.; Dai, K.; Zheng, G.; Liu, C.; Shen, C., The effect of filler dimensionality on the electromechanical performance of polydimethylsiloxane based conductive nanocomposites for flexible strain sensors. *Composites Science and Technology* **2017,** *139*, 64-73.

205. Yang, H.; Yao, X.; Zheng, Z.; Gong, L.; Yuan, L.; Yuan, Y.; Liu, Y., Highly sensitive and stretchable graphene-silicone rubber composites for strain sensing. *Composites Science and Technology* **2018,** *167*, 371-378.

206. Park, J.; You, I.; Shin, S.; Jeong, U., Material approaches to stretchable strain sensors. *Chemphyschem* **2015,** *16* (6), 1155-63.

207. Wang, L.; Chiang, W. H.; Loh, K. J., Topological design of strain sensing nanocomposites. *Sci Rep* **2022,** *12* (1), 9179.

208. Huang, H.; Cai, C. J.; Yeow, B. S.; Ouyang, J.; Ren, H., Highly Stretchable and Kirigami-Structured Strain Sensors with Long Silver Nanowires of High Aspect Ratio. *Machines* **2021,** *9* (9).

209. Yong, K.; De, S.; Hsieh, E. Y.; Leem, J.; Aluru, N. R.; Nam, S., Kirigami-inspired strain-insensitive sensors based on atomically-thin materials. *Materials Today* **2020,** *34*, 58-65.

210. Xu, F.; Zhu, Y., Highly conductive and stretchable silver nanowire conductors. *Advanced materials* **2012,** *24* (37), 5117-5122.

211. Catenacci, M. J.; Reyes, C.; Cruz, M. A.; Wiley, B. J., Stretchable conductive composites from Cu–Ag nanowire felt. *ACS nano* **2018,** *12* (4), 3689-3698.

212. Yao, S.; Zhu, Y., Nanomaterial-enabled stretchable conductors: strategies, materials and devices. *Advanced materials* **2015,** *27* (9), 1480-1511.

213. Trung, T. Q.; Lee, N. E., Recent progress on stretchable electronic devices with intrinsically stretchable components. *Advanced Materials* **2017,** *29* (3), 1603167.

214. Cai, G.; Wang, J.; Qian, K.; Chen, J.; Li, S.; Lee, P. S., Extremely stretchable strain sensors based on conductive self-healing dynamic cross-links hydrogels for human-motion detection. *Advanced Science* **2017,** *4* (2), 1600190.

215. Lee, W.; Kim, H.; Kang, I.; Park, H.; Jung, J.; Lee, H.; Park, H.; Park, J. S.; Yuk, J. M.; Ryu, S., Universal assembly of liquid metal particles in polymers enables elastic printed circuit board. *Science* **2022,** *378* (6620), 637-641.

216. Liu, S.; Shah, D. S.; Kramer-Bottiglio, R., Highly stretchable multilayer electronic circuits using biphasic gallium-indium. *Nature Materials* **2021,** *20* (6), 851-858.

217. Tutika, R.; Haque, A. T.; Bartlett, M. D., Self-healing liquid metal composite for reconfigurable and recyclable soft electronics. *Communications Materials* **2021,** *2* (1), 64.

218. Yuan, J.; Zhang, Y.; Li, G.; Liu, S.; Zhu, R., Printable and stretchable conductive elastomers for monitoring dynamic strain with high fidelity. *Advanced Functional Materials* **2022,** *32* (34), 2204878.

219. Ohm, Y.; Pan, C.; Ford, M. J.; Huang, X.; Liao, J.; Majidi, C., An electrically conductive silver–polyacrylamide–alginate hydrogel composite for soft electronics. *Nature Electronics* **2021,** *4* (3), 185-192.

220. Araby, S.; Meng, Q.; Zhang, L.; Zaman, I.; Majewski, P.; Ma, J., Elastomeric composites based on carbon nanomaterials. *Nanotechnology* **2015,** *26* (11), 112001.

221. Singh, M.; Vander Wal, R. L., Nanostructure quantification of carbon blacks. *C* **2018,** *5* (1), 2.

222. Sheka, E.; Golubev, Y. A.; Popova, N., Raman Scattering by sp $^ 2$ Amorphous Carbons. *arXiv preprint arXiv:2002.09913* **2020**.

223. Khodabakhshi, S.; Fulvio, P. F.; Andreoli, E., Carbon black reborn: Structure and chemistry for renewable energy harnessing. *Carbon* **2020,** *162*, 604-649.

224. Neffati, R.; Brokken-Zijp, J., Electric conductivity in silicone-carbon black nanocomposites: percolation and variable range hopping on a fractal. *Materials Research Express* **2019,** *6* (12), 125058.

225. Huang, Y.; Kormakov, S.; He, X.; Gao, X.; Zheng, X.; Liu, Y.; Sun, J.; Wu, D., Conductive polymer composites from renewable resources: an overview of preparation, properties, and applications. *Polymers* **2019,** *11* (2), 187.

226. Gabbett, C.; Kelly, A. G.; Coleman, E.; Doolan, L.; Carey, T.; Synnatschke, K.; Liu, S.; Dawson, A.; O'Suilleabhain, D.; Munuera, J., Understanding how junction resistances impact the conduction mechanism in nano-networks. *Nature Communications* **2024,** *15* (1), 4517.

227. Bozó, É.; Ervasti, H.; Halonen, N.; Shokouh, S. H. H.; Tolvanen, J.; Pitkanen, O.; Jarvinen, T.; Palvolgyi, P. S.; Szamosvolgyi, A.; Sápi, A., Bioplastics and carbon-based sustainable materials, components, and devices: toward green electronics. *ACS applied materials & interfaces* **2021,** *13* (41), 49301-49312.

228. Coupette, F.; Zhang, L.; Kuttich, B.; Chumakov, A.; Roth, S. V.; González-García, L.; Kraus, T.; Schilling, T., Percolation of rigid fractal carbon black aggregates. *The Journal of Chemical Physics* **2021,** *155* (12), 124902.

229. Gao, Q.; Liu, J.; Liu, X., Electrical conductivity and rheological properties of carbon black based conductive polymer composites prior to and after annealing. *Polymers and Polymer Composites* **2021,** *29* (9_suppl), S288-S295.

230. Du, J.; Cheng, H. M., The fabrication, properties, and uses of graphene/polymer composites. *Macromolecular Chemistry and Physics* **2012,** *213* (10-11), 1060-1077.

231. Rwei, S.-P.; Ku, F.-H.; Cheng, K.-C., Dispersion of carbon black in a continuous phase: Electrical, rheological, and morphological studies. *Colloid and Polymer Science* **2002,** *280* (12), 1110-1115.

232. Bauhofer, W.; Kovacs, J. Z., A review and analysis of electrical percolation in carbon nanotube polymer composites. *Composites Science and Technology* **2009,** *69* (10), 1486-1498.

233. Subramanian, S.; Øye, G., Aqueous carbon black dispersions stabilized by sodium lignosulfonates. *Colloid and Polymer Science* **2021**, 1-14.

234. Kreyenschulte, H.; Richter, S.; Götze, T.; Fischer, D.; Steinhauser, D.; Klüppel, M.; Heinrich, G., Interaction of 1-allyl-3-methyl-imidazolium chloride and carbon black and its influence on carbon black filled rubbers. *Carbon* **2012,** *50* (10), 3649-3658.

235. Chossat, J.-B.; Park, Y.-L.; Wood, R. J.; Duchaine, V., A soft strain sensor based on ionic and metal liquids. *Ieee sensors journal* **2013,** *13* (9), 3405-3414.

236. Lyu, Q.; Gong, S.; Yin, J.; Dyson, J. M.; Cheng, W., Soft wearable healthcare materials and devices. *Advanced healthcare materials* **2021,** *10* (17), 2100577.

237. Xu, L.; Gutbrod, S. R.; Bonifas, A. P.; Su, Y.; Sulkin, M. S.; Lu, N.; Chung, H.-J.; Jang, K.-I.; Liu, Z.; Ying, M., 3D multifunctional integumentary membranes for spatiotemporal cardiac measurements and stimulation across the entire epicardium. *Nature communications* **2014,** *5* (1), 3329.

238. Liu, H.; Li, Q.; Zhang, S.; Yin, R.; Liu, X.; He, Y.; Dai, K.; Shan, C.; Guo, J.; Liu, C., Electrically conductive polymer composites for smart flexible strain sensors: a critical review. *Journal of Materials Chemistry C* **2018,** *6* (45), 12121-12141.

239. Yu, Y.-H.; Ma, C.-C. M.; Teng, C.-C.; Huang, Y.-L.; Lee, S.-H.; Wang, I.; Wei, M.-H., Electrical, morphological, and electromagnetic interference shielding properties of silver nanowires and nanoparticles conductive composites. *Materials Chemistry and Physics* **2012,** *136* (2-3), 334-340.

240. Della Gaspera, E.; Tucker, R.; Star, K.; Lan, E. H.; Ju, Y. S.; Dunn, B., Copper-based conductive composites with tailored thermal expansion. *ACS applied materials & interfaces* **2013,** *5* (21), 10966-10974.

241. Klos, M. A.; González-García, L.; Kraus, T., Mechanically Robust, Inkjet-Printable Polymer Nanocomposites with Hybrid Gold Nanoparticles and Metal-like Conductivity. *ACS Applied Materials & Interfaces* **2024,** *16* (24), 31576-31585.

242. Araki, T.; Nogi, M.; Suganuma, K.; Kogure, M.; Kirihara, O., Printable and stretchable conductive wirings comprising silver flakes and elastomers. *IEEE Electron Device Letters* **2011,** *32* (10), 1424-1426.

243. Zhang, L.; Schmidt, D. S.; González-García, L.; Kraus, T., Microscopic Softening Mechanisms of an Ionic Liquid Additive in an Electrically Conductive Carbon-Silicone Composite. *Advanced Materials Technologies* **2022,** *7* (11), 2101700.

244. Shin, M. K.; Oh, J.; Lima, M.; Kozlov, M. E.; Kim, S. J.; Baughman, R. H., Elastomeric conductive composites based on carbon nanotube forests. *Advanced materials* **2010,** *22* (24), 2663-2667.

245. Tarhini, A.; Tehrani-Bagha, A.; Kazan, M.; Grady, B., The effect of graphene flake size on the properties of graphene-based polymer composite films. *Journal of Applied Polymer Science* **2021,** *138* (6), 49821.

246. Biccai, S.; Boland, C. S.; O'Driscoll, D. P.; Harvey, A.; Gabbett, C.; O'Suilleabhain, D. R.; Griffin, A. J.; Li, Z.; Young, R. J.; Coleman, J. N., Negative gauge factor piezoresistive composites based on polymers filled with MoS2 nanosheets. *Acs Nano* **2019,** *13* (6), 6845-6855.

247. Ma, C.; Ma, M. G.; Si, C.; Ji, X. X.; Wan, P., Flexible MXene-based composites for wearable devices. *Advanced Functional Materials* **2021,** *31* (22), 2009524.

248. Lux, F., Models proposed to explain the electrical conductivity of mixtures made of conductive and insulating materials. *Journal of materials science* **1993,** *28*, 285-301.

249. Masouras, K.; Silikas, N.; Watts, D. C., Correlation of filler content and elastic properties of resin-composites. *Dental Materials* **2008,** *24* (7), 932-939.

250. Coupette, F.; Schilling, T., Universal Approach to Critical Percolation. *arXiv preprint arXiv:2308.16757* **2023.**

251. Nan, C.-W.; Shen, Y.; Ma, J., Physical properties of composites near percolation. *Annual Review of Materials Research* **2010,** *40* (1), 131-151.

252. Schueler, R.; Petermann, J.; Schulte, K.; Wentzel, H. P., Agglomeration and electrical percolation behavior of carbon black dispersed in epoxy resin. *Journal of applied polymer science* **1997,** *63* (13), 1741-1746.

253. Topcu, G.; Arenas, D. R.; McNally, T.; Becer, C. R., Microphase separation assisted reduction in the percolation threshold of MWCNT/block polymer composites. *Soft Matter* **2023,** *19* (6), 1109-1114.

254. Prabhakar, O. P.; Sahu, R. K., Effects of soft and hard fillers on electromechanical properties and performance of polydimethylsiloxane elastomer for actuator applications. *Journal of Applied Polymer Science* **2023,** *140* (38), e54434.

255. Schmidt, D. S.; Kraus, T.; González-García, L., Electrofluids with Tailored Rheoelectrical Properties: Liquid Composites with Tunable Network Structures as Stretchable Conductors. *ACS Applied Materials & Interfaces* **2024,** *16* (33), 43942-43950.

256. McClements, D. J., *Food emulsions: principles, practices, and techniques*. CRC press: 2004.

257. Koos, E., Capillary suspensions: Particle networks formed through the capillary force. *Current opinion in colloid & interface science* **2014,** *19* (6), 575-584.

258. Bhagavathi Kandy, S.; Simon, G. P.; Cheng, W.; Zank, J.; Joshi, K.; Gala, D.; Bhattacharyya, A. R., Effect of incorporation of multiwalled carbon nanotubes on the microstructure and flow behavior of highly concentrated emulsions. *ACS omega* **2018,** *3* (10), 13584-13597.

259. Mazurek, P.; Hvilsted, S.; Skov, A., Green silicone elastomer obtained from a counterintuitively stable mixture of glycerol and PDMS. *Polymer* **2016,** *87*, 1-7.

260. Dapčević Hadnađev, T.; Dokić, P.; Krstonošić, V.; Hadnađev, M., Influence of oil phase concentration on droplet size distribution and stability of oil-in-water emulsions. *European Journal of Lipid Science and Technology* **2013,** *115* (3), 313-321.

261. Sullivan, A. P.; Kilpatrick, P. K., The effects of inorganic solid particles on water and crude oil emulsion stability. *Industrial & engineering chemistry research* **2002,** *41* (14), 3389-3404.

262. de Souza, T. A.; Scheer, A. d. P.; Khalil, M. C.; Yamamoto, C. I.; Luz Jr, L. F. d. L., Emulsion inversion using solid particles. *Journal of Petroleum Science and Engineering* **2012,** *96*, 49-57.

263. Pal, R., Rheology of simple and multiple emulsions. *Current opinion in colloid & interface science* **2011,** *16* (1), 41-60.

264. Macosko, C. W., Rheology principles. *Measurements and Applications* **1994**.

265. Shi, S.; Wang, Y.; Liu, Y.; Wang, L., A new method for calculating the viscosity of W/O and O/W emulsion. *Journal of Petroleum Science and Engineering* **2018,** *171*, 928-937.

266. Bullard, J. W.; Pauli, A. T.; Garboczi, E. J.; Martys, N. S., A comparison of viscosity–concentration relationships for emulsions. *Journal of colloid and interface science* **2009,** *330* (1), 186-193.

267. Lago-Garrido, S.; Schmidt, D. S.; Martín-Alfonso, M. J.; González-García, L., Multi-Walled Carbon Nanotubes Suspensions as Liquid Conductors: Electrical and Mechanical Network Interplay. *Advanced Electronic Materials* **2025**, 2400917.

268. Jiang, Y.; Cui, Y.; Li, Y.; Liu, Z.; Ness, C.; Seto, R., Filled colloidal gel rheology: Strengthening, stiffening, and tunability. *Journal of Rheology* **2025,** *69* (1), 35-44.

269. Lee, J. H.; Gwon, S.; Shin, M., Effect of filler particle characteristics on yield stress and viscosity of fresh sulfur composites. *journal of materials research and technology* **2021,** *12*, 2138-2152.

270. Zhou, Z.; Solomon, M. J.; Scales, P. J.; Boger, D. V., The yield stress of concentrated flocculated suspensions of size distributed particles. *Journal of Rheology* **1999,** *43* (3), 651-671.

271. Hyun, K.; Kim, S. H.; Ahn, K. H.; Lee, S. J., Large amplitude oscillatory shear as a way to classify the complex fluids. *Journal of Non-Newtonian Fluid Mechanics* **2002,** *107* (1-3), 51-65.

272. Haridas, H.; Kontopoulou, M., Effect of specific surface area on the rheological properties of graphene nanoplatelet/poly (ethylene oxide) composites. *Journal of Rheology* **2023,** *67* (3), 601-619.

273. Zhang, A.; Zhu, C.; Pan, D.; Lin, Y., Study on strain stiffening of non-colloidal suspension in oscillating shear by a subsequent steady shear test. *Colloids and Surfaces A: Physicochemical and Engineering Aspects* **2021,** *618*, 126401.

274. Kim, H.; Esser-Kahn, A. P.; Rowan, S. J.; Jaeger, H. M., Stress-activated friction in sheared suspensions probed with piezoelectric nanoparticles. *Proceedings of the National Academy of Sciences* **2023,** *120* (49), e2310088120.

275. Seto, R.; Mari, R.; Morris, J. F.; Denn, M. M., Discontinuous shear thickening of frictional hard-sphere suspensions. *Physical review letters* **2013,** *111* (21), 218301.

276. Hermes, M.; Clegg, P. S., Yielding and flow of concentrated Pickering emulsions. *Soft Matter* **2013,** *9* (31), 7568-7575.

277. Hong, J. S.; Kong, H. J.; Hyun, K.; Bergfreund, J.; Fischer, P.; Ahn, K. H., Rheological analysis of oil–water emulsions stabilized with clay particles by LAOS and interfacial shear moduli measurements. *Rheologica Acta* **2019,** *58* (8), 453-466.

278. Mudeme, S.; Masalova, I.; Haldenwang, R., Kinetics of emulsification and rheological properties of highly concentrated explosive emulsions. *Chemical Engineering and Processing: Process Intensification* **2010,** *49* (5), 468-475.

279. Kim, H.; Ahn, K. H.; Lee, S. J., Conductive poly (high internal phase emulsion) foams incorporated with polydopamine-coated carbon nanotubes. *Polymer* **2017,** *110*, 187-195.

280. Princen, H.; Kiss, A., Rheology of foams and highly concentrated emulsions: III. Static shear modulus. *Journal of colloid and interface science* **1986,** *112* (2), 427-437.

281. Malkin, A. Y.; Masalova, I.; Slatter, P.; Wilson, K., Effect of droplet size on the rheological properties of highly-concentrated w/o emulsions. *Rheologica Acta* **2004,** *43*, 584-591.

282. Lacasse, M.-D.; Grest, G. S.; Levine, D.; Mason, T.; Weitz, D., Model for the elasticity of compressed emulsions. *Physical review letters* **1996,** *76* (18), 3448.

283. Masalova, I.; Malkin, A. Y., Peculiarities of rheological properties and flow of highly concentrated emulsions: the role of concentration and droplet size. *Colloid Journal* **2007,** *69* (2), 185-197.

284. Mougel, J.; Alvarez, O.; Baravian, C.; Caton, F.; Marchal, P.; Stébé, M.-J.; Choplin, L., Aging of an unstable w/o gel emulsion with a nonionic surfactant. *Rheologica acta* **2006,** *45* (5), 555-560.

285. Peralta-Martínez, M. V.; Arriola-Medellín, A.; Manzanares-Papayanopoulos, E.; Sánchez-Sánchez, R.; Palacios-Lozano, E. M., Influence of the speed mixing-on viscosity and droplet size of oil in water emulsions. *Petroleum science and technology* **2004,** *22* (7-8), 1035-1043.

286. Sharu, B.; Simon, G. P.; Cheng, W.; Zank, J.; Bhattacharyya, A. R., Development of microstructure and evolution of rheological characteristics of a highly concentrated emulsion during emulsification. *Colloids and Surfaces A: Physicochemical and Engineering Aspects* **2017,** *532*, 342-350.

287. Arganda-Carreras, I.; Kaynig, V.; Rueden, C.; Eliceiri, K. W.; Schindelin, J.; Cardona, A.; Sebastian Seung, H., Trainable Weka Segmentation: a machine learning tool for microscopy pixel classification. *Bioinformatics* **2017,** *33* (15), 2424-2426.

288. Li, J.; Liu, Y.; Zhao, K.; Guo, C.; Ye, C., Liquid metal hybrid: Structural engineering toward strain-insensitive stretchable conductors. *Materials Today Chemistry* **2025,** *49*, 103042.

289. Gui, Q.; He, Y.; Wang, Y., Soft electronics based on liquid conductors. *Advanced Electronic Materials* **2021,** *7* (1), 2000780.

290. Hautz, N.; González-García, L., Direct Ink Writing of Carbon-Based Electrofluids for Soft Electrical Component Manufacturing. *Advanced Materials Technologies* **2025**, e02012.

291. Naguib, M.; Kurtoglu, M.; Presser, V.; Lu, J.; Niu, J.; Heon, M.; Hultman, L.; Gogotsi, Y.; Barsoum, M. W., Two-dimensional nanocrystals: two-dimensional nanocrystals produced by exfoliation of Ti3AlC2 (Adv. Mater. 37/2011). *Advanced Materials* **2011,** *23* (37), 4207-4207.

292. Park, J. Y.; Lee, W. J.; Kwon, B.-S.; Nam, S.-Y.; Choa, S.-H., Highly stretchable and conductive conductors based on Ag flakes and polyester composites. *Microelectronic Engineering* **2018,** *199*, 16-23.

293. Osman, A.; Elhakeem, A.; Kaytbay, S.; Ahmed, A., A comprehensive review on the thermal, electrical, and mechanical properties of graphene-based multi-functional epoxy composites. *Advanced Composites and Hybrid Materials* **2022,** *5* (2), 547-605.

294. Wang, X.; Xing, W.; Feng, X.; Song, L.; Hu, Y., MoS2/polymer nanocomposites: preparation, properties, and applications. *Polymer Reviews* **2017,** *57* (3), 440-466.

295. Anasori, B.; Gogotsi, Y., Introduction to 2D transition metal carbides and nitrides (MXenes). In *2D Metal Carbides and Nitrides (MXenes) Structure, Properties and Applications*, Springer: 2019; pp 3-12.

296. Stoller, M. D.; Park, S.; Zhu, Y.; An, J.; Ruoff, R. S., Graphene-based ultracapacitors. *Nano letters* **2008,** *8* (10), 3498-3502.

297. Candan, S.; Barton, V.; Yang, H.; López-Cámara, C. F.; Fortugno, P.; Wiggers, H.; Eriten, M.; Andrews, J.; Notbohm, J.; Franck, C., Design of a Simple and Rugged Soft

Polydimethylsiloxane-Carbon Nanotube-Graphene-Based Composite Sensor. *Advanced Materials Technologies* **2025**, e70009.

298. Guo, W.; Yin, Y.-X.; Xin, S.; Guo, Y.-G.; Wan, L.-J., Superior radical polymer cathode material with a two-electron process redox reaction promoted by graphene. *Energy & Environmental Science* **2012,** *5* (1), 5221-5225.

299. Sahu, D.; Sahu, R. K.; Patra, K., In-plane actuation performance of graphene oxide filled VHB 4910 dielectric elastomer. *Journal of Applied Polymer Science* **2022,** *139* (5), 51594.

300. Partoens, B.; Peeters, F., From graphene to graphite: Electronic structure around the K point. *Physical Review B—Condensed Matter and Materials Physics* **2006,** *74* (7), 075404.

301. Abdelkader, A.; Cooper, A.; Dryfe, R. A.; Kinloch, I., How to get between the sheets: a review of recent works on the electrochemical exfoliation of graphene materials from bulk graphite. *Nanoscale* **2015,** *7* (16), 6944-6956.

302. López-Cámara, C.-F.; Fortugno, P.; Asif, M.; Musikhin, S.; Prindler, C.; Wiggers, H.; Endres, T.; Eaves, N.; Daun, K. J.; Schulz, C., Evolution of particle size and morphology in plasma synthesis of few-layer graphene and soot. *Combustion and Flame* **2023,** *258*, 112713.

303. Dato, A., Graphene synthesized in atmospheric plasmas—A review. *Journal of Materials Research* **2019,** *34* (1), 214-230.

304. Wu, Y.-S.; Hsieh, C.-Y.; Peng, C.-S.; Chen, J.-R.; Lin, J.-M.; Lin, G.-W., Method for the preparation of graphene. Google Patents: 2014.

305. Marchesini, S.; Turner, P.; Paton, K. R.; Reed, B. P.; Brennan, B.; Koziol, K.; Pollard, A. J., Gas physisorption measurements as a quality control tool for the properties of graphene/graphite powders. *Carbon* **2020,** *167*, 585-595.

306. Peigney, A.; Laurent, C.; Flahaut, E.; Bacsa, R.; Rousset, A., Specific surface area of carbon nanotubes and bundles of carbon nanotubes. *Carbon* **2001,** *39* (4), 507-514.

307. Ferrari, A. C.; Meyer, J. C.; Scardaci, V.; Casiraghi, C.; Lazzeri, M.; Mauri, F.; Piscanec, S.; Jiang, D.; Novoselov, K. S.; Roth, S., Raman spectrum of graphene and graphene layers. *Physical review letters* **2006,** *97* (18), 187401.

308. Kim, K.; Coh, S.; Tan, L. Z.; Regan, W.; Yuk, J. M.; Chatterjee, E.; Crommie, M.; Cohen, M. L.; Louie, S. G.; Zettl, A., Raman spectroscopy study of rotated double-layer graphene: misorientation-angle dependence of electronic structure. *Physical review letters* **2012,** *108* (24), 246103.

309. Lenski, D. R.; Fuhrer, M. S., Raman and optical characterization of multilayer turbostratic graphene grown via chemical vapor deposition. *Journal of Applied Physics* **2011,** *110* (1).

310. Garlow, J. A.; Barrett, L. K.; Wu, L.; Kisslinger, K.; Zhu, Y.; Pulecio, J. F., Large-area growth of turbostratic graphene on Ni (111) via physical vapor deposition. *Scientific reports* **2016,** *6* (1), 19804.

311. Fortugno, P.; Sahinovic, A.; Wilson, N.; Tuling, J.; López-Cámara, C.-F.; Pentcheva, R.; Wiggers, H., Microwave plasma synthesis of freestanding sulfur-doped few-layer graphene and the impact of the dopant on the electrical transport properties: Experiment and simulation. *Carbon* **2025**, 120815.

312. Fröhlich, J.; Niedermeier, W.; Luginsland, H.-D., The effect of filler–filler and filler–elastomer interaction on rubber reinforcement. *Composites Part A: Applied Science and Manufacturing* **2005,** *36* (4), 449-460.

313. Choi, H.-J.; Kim, M. S.; Ahn, D.; Yeo, S. Y.; Lee, S., Electrical percolation threshold of carbon black in a polymer matrix and its application to antistatic fibre. *Scientific reports* **2019,** *9* (1), 6338.

314. Zhang, B.; Yu, Y.; Liu, Y.; Huang, Z.-D.; He, Y.-b.; Kim, J.-K., Percolation threshold of graphene nanosheets as conductive additives in Li 4 Ti 5 O 12 anodes of Li-ion batteries. *Nanoscale* **2013,** *5* (5), 2100-2106.

315. Yuan, H.; Chen, H.; Li, M.; Liu, L.; Liu, Z., Percolation threshold and electrical conductivity of conductive polymer composites filled with curved fibers in two-dimensional space. *Soft Matter* **2023,** *19* (37), 7149-7160.

316. Zare, Y.; Rhee, K. Y.; Hui, D., Modeling of electrical conductivity for graphene-based systems by filler morphology and tunneling length. *Diamond and Related Materials* **2023,** *134*, 109782.

317. Kislenko, V. A.; Pavlov, S. V.; Kislenko, S. A., Influence of defects in graphene on electron transfer kinetics: The role of the surface electronic structure. *Electrochimica Acta* **2020,** *341*, 136011.

318. Zhong, J.-H.; Zhang, J.; Jin, X.; Liu, J.-Y.; Li, Q.; Li, M.-H.; Cai, W.; Wu, D.-Y.; Zhan, D.; Ren, B., Quantitative correlation between defect density and heterogeneous electron transfer rate of single layer graphene. *Journal of the American Chemical Society* **2014,** *136* (47), 16609-16617.

319. Pargoletti, E.; Scavini, M.; Santangelo, S.; Consolati, G.; Cerrato, G.; Longoni, M.; Patané, S.; Longhi, M.; Cappelletti, G., Tuning the Interlayer Distance of Graphene Oxide as a Function of the Oxidation Degree for o-Toluidine Removal. *Advanced Materials Interfaces* **2023,** *10* (21), 2300179.

320. Precha-Atsawanan, S.; Uttapap, D.; Sagis, L. M., Linear and nonlinear rheological behavior of native and debranched waxy rice starch gels. *Food Hydrocolloids* **2018,** *85*, 1-9.

321. Mezger, T. G., The rheology handbook 4th edition. *For users of rotational and oscillatory rheometers, Hanver, Germany* **2014**.

322. Perius, D.; Engstler, M.; Blum, S.; González-García, L.; Kraus, T., Reconstruction of 3D Conductive Networks in Metal-Filled Elastomer Composites Indicates Dominance of Contact Resistances. *Small Structures* **2025,** *6* (10), 2500234.

323. Chen, X.; Yi, C.; Ke, C., Bending stiffness and interlayer shear modulus of few-layer graphene. *Applied Physics Letters* **2015,** *106* (10).

324. Lin, A. Y.; Yu, X.-x.; Dato, A.; Krauss, G.; Marks, L. D., In situ observations of graphitic staples in crumpled graphene. *Carbon* **2018,** *132*, 760-765.

325. Zhu, J.; Wei, S.; Yadav, A.; Guo, Z., Rheological behaviors and electrical conductivity of epoxy resin nanocomposites suspended with in-situ stabilized carbon nanofibers. *Polymer* **2010,** *51* (12), 2643-2651.

326. Liu, Y.; Wilkinson, A., Rheological percolation behaviour and fracture properties of nanocomposites of MWCNTs and a highly crosslinked aerospace-grade epoxy resin system. *Composites Part A: Applied Science and Manufacturing* **2018,** *105*, 97-107.

327. Lago-Garrido, S.; Schmidt, D. S.; Martín-Alfonso, M. J.; González-García, L., Multi-Walled Carbon Nanotubes Suspensions as Liquid Conductors: Electrical and Mechanical Network Interplay. *Advanced Electronic Materials* **2024**, 2400917.

328. Wang, M.-J.; Wolff, S.; Tan, E.-H., Filler-elastomer interactions. Part VIII. The role of the distance between filler aggregates in the dynamic properties of filled vulcanizates. *Rubber chemistry and technology* **1993,** *66* (2), 178-195.

329. Johnson, L. C.; Zia, R. N.; Moghimi, E.; Petekidis, G., Influence of structure on the linear response rheology of colloidal gels. *Journal of Rheology* **2019,** *63* (4), 583-608.

330. Menut, P.; Seiffert, S.; Sprakel, J.; Weitz, D. A., Does size matter? Elasticity of compressed suspensions of colloidal-and granular-scale microgels. *Soft Matter* **2012,** *8* (1), 156-164.

331. Vialetto, J.; Ramakrishna, S. N.; Isa, L.; Laurati, M., Effect of particle stiffness and surface properties on the non-linear viscoelasticity of dense microgel suspensions. *Journal of Colloid and Interface Science* **2024,** *672*, 814-823.

332. Liu, H.; Li, Y.; Dai, K.; Zheng, G.; Liu, C.; Shen, C.; Yan, X.; Guo, J.; Guo, Z., Electrically conductive thermoplastic elastomer nanocomposites at ultralow graphene

loading levels for strain sensor applications. *Journal of Materials Chemistry C* **2016,** *4* (1), 157-166.

333. Hur, O.-N.; Ha, J.-H.; Park, S.-H., Strain-sensing properties of multi-walled carbon nanotube/polydimethylsiloxane composites with different aspect ratio and filler contents. *Materials* **2020,** *13* (11), 2431.

334. Hu, G.; Zhao, C.; Zhang, S.; Yang, M.; Wang, Z., Low percolation thresholds of electrical conductivity and rheology in poly (ethylene terephthalate) through the networks of multi-walled carbon nanotubes. *Polymer* **2006,** *47* (1), 480-488.

335. Park, J.; You, I.; Shin, S.; Jeong, U., Material approaches to stretchable strain sensors. *ChemPhysChem* **2015,** *16* (6), 1155-1163.

336. Natarajan, T. S.; Eshwaran, S. B.; Stöckelhuber, K. W.; Wießner, S.; Pötschke, P.; Heinrich, G.; Das, A., Strong strain sensing performance of natural rubber nanocomposites. *ACS applied materials & interfaces* **2017,** *9* (5), 4860-4872.

337. Ke, K.; Pötschke, P.; Wiegand, N.; Krause, B.; Voit, B., Tuning the network structure in poly (vinylidene fluoride)/carbon nanotube nanocomposites using carbon black: toward improvements of conductivity and piezoresistive sensitivity. *ACS applied materials & interfaces* **2016,** *8* (22), 14190-14199.

338. Falvo, M. R.; Clary, G. J.; Taylor, R. M.; Chi, V.; Brooks Jr, F.; Washburn, S.; Superfine, R., Bending and buckling of carbon nanotubes under large strain. *Nature* **1997,** *389* (6651), 582-584.

339. Shi, X.; Sun, S.; Zhao, A.; Zhang, H.; Zuo, M.; Song, Y.; Zheng, Q., Influence of carbon black on the Payne effect of filled natural rubber compounds. *Composites Science and Technology* **2021,** *203*, 108586.

340. Yang, J.; Han, C.-R., Dynamics of silica-nanoparticle-filled hybrid hydrogels: nonlinear viscoelastic behavior and chain entanglement network. *The Journal of Physical Chemistry C* **2013,** *117* (39), 20236-20243.

341. Rendek, M.; Lion, A., Strain induced transient effects of filler reinforced elastomers with respect to the Payne-Effect: experiments and constitutive modelling. *ZAMM-Journal of Applied Mathematics and Mechanics/Zeitschrift für Angewandte Mathematik und Mechanik: Applied Mathematics and Mechanics* **2010,** *90* (5), 436-458.

342. Zhao, A.; Shi, X.-Y.; Sun, S.-H.; Zhang, H.-M.; Zuo, M.; Song, Y.-H.; Zheng, Q., Insights into the Payne effect of carbon black filled styrene-butadiene rubber compounds. *Chinese Journal of Polymer Science* **2021,** *39* (1), 81-90.

343. Rickaby, S.; Scott, N., A cyclic stress softening model for the Mullins effect. *International Journal of Solids and Structures* **2013,** *50* (1), 111-120.

344. Lozano-Pérez, C.; Cauich-Rodríguez, J.; Avilés, F., Influence of rigid segment and carbon nanotube concentration on the cyclic piezoresistive and hysteretic behavior of multiwall carbon nanotube/segmented polyurethane composites. *Composites Science and Technology* **2016,** *128*, 25-32.

345. Zhang, R.; Deng, H.; Valenca, R.; Jin, J.; Fu, Q.; Bilotti, E.; Peijs, T., Strain sensing behaviour of elastomeric composite films containing carbon nanotubes under cyclic loading. *Composites Science and Technology* **2013,** *74*, 1-5.

346. Mewis, J.; Wagner, N. J., Thixotropy. *Advances in colloid and interface science* **2009,** *147*, 214-227.

347. Wang, Y.; Ewoldt, R. H., New insights on carbon black suspension rheology—Anisotropic thixotropy and antithixotropy. *Journal of Rheology* **2022,** *66* (5), 937-953.

348. Chang, C.; Smith, P. A., Flow-induced structure in a system of nuclear waste simulant slurries. *Rheologica acta* **1996,** *35* (4), 382-389.

349. Macdonald, J. R.; Barlow Jr, C. A., Relaxation, retardation, and superposition. *Reviews of Modern Physics* **1963,** *35* (4), 940.

Appendix

Methods used for General Discussion

This section contains information about the methods used for some data that has not been previously described in **Chapters 3-5**.

Strain-softening

Amplitude sweeps for the three selected electrofluids were performed on a stress-controlled Anton-Paar MCR302e (Anton-Paar, Austria) rheometer in a 25 mm plate-plate configuration at 25 °C. All samples were pre-sheared for 2 min at a shear rate of 10 s^{-1} and rested for 15 min. A fixed angular frequency of 10 rad/s was used, and strain sweeps from 0.001 to 100% were applied. For the reversibility test, the strain was subsequently swept back from 100 to 0.001% without any additional step in between. This was repeated a total of 10 times. The electrical signal was recorded with a Keysight E4980A LCR-meter (Keysight, USA). For each rheological measurement point, the electrical resistance was measured.

Stress-softening

Tensile tests were performed on a Hegewald & Peschke Inspect 5 tensiometer (Hegewald & Peschke, Germany). Selected electrofluids were filled into elastomeric tubes made from EcoFlex silicone polymer. The samples were mounted at an initial length of 30 mm and pre-stretched to a length of 39 mm. All samples were cycled at 10% strain at a strain rate of 10 %/s. The electrical resistance was recorded with a Keithley DMM6500 Digit Multimeter (Tectronix, USA).

Non-linear, intracycle resistance responses

Intracycle resistance responses under uniaxial tensile tests for Galinstan were performed analogously to the stress-softening experiments described above. The rheological measurements were performed on a strain-controlled Anton-Paar MCR702e MultiDrive (Anton-Paar, Austria) rheometer in a 25 mm plate-plate configuration at 25 °C. A constant strain of either 0.04% (SAOS) or 100% (LAOS) was applied at a fixed angular frequency of 10 rad/s. The electrical resistance was recorded with a Keithley DMM6500 Digit Multimeter (Tectronix, USA).

Thixotropy

Step-down shear rate experiments were performed on a strain-controlled Anton-Paar MCR702e MultiDrive (Anton-Paar, Austria) rheometer in a 25 mm plate-plate configuration at 25 °C. A shear rate of 100 s^{-1} was applied for 2 min. Afterwards, the shear rate was reduced to 80 s^{-1} and held constant for 30 min. Between every step-down interval, the sample was sheared again at 100 s^{-1} for 2 min.

Creep

All creep tests were performed on a stress-controlled Anton-Paar MCR302e (Anton-Paar, Austria) rheometer in a 25 mm plate-plate configuration at 25 °C. Each sample was pre-sheared at 10 s^{-1} for 2 min with a subsequent rest of 15 min. Stress values were held constant for 2500 s, and the subsequent relaxation was recorded for 3400 s. Simultaneous electrical resistance measurements were carried out with a Keysight E4980A LCR-meter (Keysight, USA).

Stress Relaxation

All stress relaxation tests were performed on a strain-controlled Anton-Paar MCR702e MultiDrive (Anton-Paar, Austria) rheometer in a 25 mm plate-plate configuration at 25 °C. Each sample was pre-sheared at 10 s^{-1} for 2 min with a subsequent rest of 15 min. A step strain deformation was applied, and the relaxation of the stress was recorded. Simultaneous electrical resistance measurements were carried out with a Keysight E4980A LCR-meter (Keysight, USA)